In situ Monitoring of Electrochemical Interfaces by Reflection Anisotropy Spectroscopy

Dissertation

der Mathematisch-Naturwissenschaftlichen Fakultät

der Eberhard Karls Universität Tübingen

zur Erlangung des Grades eines

Doktors der Naturwissenschaften

(Dr. rer. nat.)

vorgelegt von

M. Eng. Margot Guidat

aus Nancy, Frankreich

Tübingen

2024

Gedruckt mit Genehmigung der Mathematisch-Naturwissenschaftlichen Fakultät der Eberhard Karls Universität Tübingen.

Tag der mündlichen Qualifikation: 28.06.2024

Dekan:	Prof. Dr. Thilo Stehle
1. Berichterstatter:	Dr. Matthias M. May
2. Berichterstatter:	Prof. Dr. Udo Weimar

To Omar Khaled
because this dream
now achieved
was for you

This doctoral thesis was produced in the group of Dr. Matthias M. May, started at the Institute of Theoretical Chemistry at the University of Ulm in November 2020 and finalized at the Institute of Physical and Theoretical Chemistry at the University of Tübingen in April 2024.

Acknowledgment

From the work side: First, I would like to specially thank you Dr. Matthias May for your trust and for allowing me to do my PhD in your group. It has been a pleasure to work under your close supervision. I am grateful for your support, your patience, your good temper and your good communication. Also thank you for giving me liberty and flexibility in my work. All these ways of work have established a very nice working group atmosphere, and it helped me a lot in making a successful PhD.

Thank you Prof. Dr. Udo Weimar for accepting to be the second reviewer of my thesis. Thank you Prof. Dr. Alfred Meixner for your being my second supervisor. Thank Dr. Heiko Peisert for accepting to be my oral examiner.

During the first half of my PhD in Ulm, I specially thank Mario Löw for his kindness and close work collaboration. Thank Vibhav and Krish who brought me a lot, work-wise and personally. From the theoretical institute of Ulm and POLiS, I am thankful to have met Manuel, Johannes, Kanchan, Katharina, Mohsen, and Jack. Thank you for your friendship, your advices and the good time we spent at the coffee break.

Thank you Moritz for your precious insight and guidance. It has been a pleasure to work with you and to host you in Tübingen.

During the second half of my PhD in Tübingen, thank my students Florian, Anna-Lena, and Marco for their great work and their good mood. In general thank the all working group: Erica, Daniel, Vibhav, Holger, Maxi, Marco, Mihnea, Anna-Lena, Miriam, and Jongmin. It has been a great pleasure to get to know you and work with you.

For the revision of this Manuscript, big thank Holger, thank Maxi, Erica, and David .

Un grand merci à toi Holger, roi des princesses. All my gratitude for all the time you spent helping me on the interpretation of my results and the revision of my manuscripts/thesis. Les cafés franco-allemand ainsi que ta complicité ont été très importants pour moi.

Finally, I would like to thank you my dear colleague and friend Erica A. Schmitt Gaalad, for making this adventure beautiful. If I say that the most difficult thing in this PhD is to leave you, my holy grail, I think that there is nothing else to add.

From the relatives side: Merci à ma famille et en particulier à mes parents pour votre amour, votre bonne éducation et votre support. Merci d'avoir rendu ce rêve réalisable.

Thank to you David, my dear Love, for your priceless presence in my life and your spiritual support. I am very happy and thankful to have made this journey by your side.

List of Abbreviations

AFM	atomic force miscroscopy. 55
AWM	anti-wobble mirror. 35
BG	band gap. 8, 9, 10, 11
CA	chromoamperometry. 24, 32, 44, 45
CB	conduction band. 8, 9, 10, 11
CE	counter electrode. 15
CP	colourplot. 29, 58, 60
CV	cyclic voltammetry. 23, 24, 32, 33, 34, 41, 45, 46, 47, 48, 59, 60
DFT	density functional theory. 28
EC	electrochemical. 23, 30, 31, 32, 33, 34, 39
EDL	electrochemical double layer. xv, 17, 18, 19, 31, 32
EMW	electromagnetic wave. 6, 7
FFT	fast Fourier transform. 59, 60
GB	glovebox. 35, 44, 45, 46
GHG	green house gases. 1
HHL	Helmholtz layer. 17
LEED	low energy electron diffraction. 33
LEO	linear electro-optic effect. 18, 47
OCP	open circuit potential. 40, 41, 43, 44, 45, 46, 47
PEC	photoelectrochemical. 1, 34, 35, 54
PEM	photo-elastic modulator. 7, 26
PS	photoelectrochemical Schlenk. 35, 43, 44, 52, 54
PV	photovoltaic. 53
QM	quantum mechanics. 8

RAS reflection anisotropy spectroscopy. 3, 26, 27, 28, 29, 30, 31, 32, 33, 34, 35, 54, 55, 56, 57, 58, 59, 60, 61
RCB remaining carbon budget. 1
RE reference electrode. 16
RIE reactive ion etching. 29, 30

SEM scanning electron microscopy. 23, 58
S-L solid-liquid. 13, 21, 31, 33, 46, 53
S-M semiconductor-metal. 12, 13
SEI solid electrolyte interphase. 2, 33
STM scanning tunneling microscopy. 33, 34

UHV ultra-high vacuum. 5, 31, 39, 44

VB valence band. 8, 9, 10, 11

WE working electrode. 15, 16

XPS X-ray photoelectron spectroscopy. 23, 45, 46

List of Symbols

$\underline{n}$	Complex refractive index
k	Wave vector
$\underline{r}$	Complex Fresnel reflection coefficient
k_B	Boltzmann constant
T	Temperature
E_F	Fermi level
E_g	Band gap
E_{CB}	Conduction band
E_{VB}	Valence band
E_{imp}	Impurity state
n_h	Concentration of holes
n_e	Concentration of electrons
${}^*E_{Fn}$	Quasi-Fermi level of electrons
${}^*E_{Fp}$	Quasi-Fermi level of holes
ϕ_m	Metal work function
ϕ_s	Solution work function
ϕ_{SB}	Schottky barrier
$\Delta_r G$	Reaction free energy
$\bar{\mu}$	Electrochemical potential
μ	Chemical potential
μ°	Standard chemical potential
F	Faraday constant
R	Gas constant
θ	Surface coverage
N_a	Avogadro constant
ϵ_{ads}	Formation energy of the adsorption of an isolated ion
R	Fresnel reflection amplitude
z	Charge number
e	Elementary charge
λ	Wavelength
ϵ	Complex dielectric function

List of Publications

A. Review Papers and Book Chapters

A1.

Guidat, M.; Löw, M.; Kölbach, M.; Kim, J.; May, M. M. Experimental and Computational Aspects of Electrochemical Reflection Anisotropy Spectroscopy: A Review. ChemElectroChem 2023, 10 (8), e202300027.

Conceptualization: MMM, **MG (50%)**, and MK. Formal analysis and experiments: ML, **MG (40%)**, JK, and MMM. Writing-Original Draft preparation: **MG (70%)**, JK, ML, and MK. Writing-Review: **MG (50%)**, JK, ML, MK, and MMM. Supervision: MMM.

A2.

Hajduk, A.; Zare Pour, M. A.; Paszuk, A.; **Guidat, M.**; Löw, M.; Ullmann, F.; Moritz, D. C.; Hofmann, J. P.; Krischok, S.; Runge, E.; Schmidt, W. G.; Jaegermann, W.; May, M. M.; Hannappel, T. (Photo-)Electrochemical Reactions on Semiconductor Surfaces, Part B: III-V Surfaces–Atomic and Electronic Structure. In Encyclopedia of Solid-Liquid Interfaces (First Edition); Wandelt, K., Bussetti, G., Eds.; Elsevier: Oxford, 2024; pp 120–156.

Section "III-V based liquid electrolyte contacts for H_2O splitting"

Research Papers

B1.

Löw, M.; **Guidat, M.**; Kim, J.; May, M. M. The Interfacial Structure of InP(100) in Contact with HCl and H_2SO_4 Studied by Reflection Anisotropy Spectroscopy. RSC Adv. 2022, 12 (50), 32756–32764.

Conceptualization: MMM, ML, and **MG**. Formal analysis and experiments: ML, **MG**, JK, and MMM. Writing-Original Draft preparation: ML. Writing-Review: ML, **MG**, JK, and MMM. Supervision: MMM.

B2.

Schmitt, E. A.; **Guidat, M.**; Nusshör, M.; Renz, A.-L.; Möller, K.; Flieg, M.; Lörch, D.; Kölbach, M.; May, M. M. Photoelectrochemical Schlenk Cell Functionalization of Multi-Junction Water-Splitting Photoelectrodes. Cell Reports Physical Science 2023, 4 (10), 101606.

Conceptualization: MK, ES, **MG**, and MMM. Formal analysis and experiments: ES, MK, **MG**, A-LR, MN, MF, DL, and MMM. Writing-Original Draft preparation: ES, and **MG (20%)**. Writing-Review: ES, **MG (10%)**, and MMM. Supervision: MK, and MMM.

B3.

Guidat, M.; Rahide, F.; Löw, M.; Kim, J.; Ehrenberg, H.; Dsoke, S.; May, M. M. In Situ Monitoring of the Al(110)-[EMImCl]:$AlCl_3$ Interface by Reflection Anisotropy Spectroscopy. Batteries & Supercaps 2023, e202300394.

Conceptualization: FR, **MG**, SD, and MMM. Formal analysis and experiments: **MG**, FR, ML, and JK. Writing-Original Draft preparation: **MG**, FR, and JK. Writing-Review: **MG)**, FR, ML, HE, SD, and MMM. Supervision: SD, and MMM.

B4.

Guidat, M.; Flieg, M; Fuchs, S; Loew, M; Buchner, F; Euchner, H; Behm, R. J.; May, M. M. Atomically well-ordered InP-electrolyte interfaces enabled by optical *in situ* spectroscopy. The Physical Chemistry C. 2024 (in preparation)

Conceptualization: **MG**, and MMM. Formal analysis and experiments: **MG**, MF, SF, ML, HE, and FB. Writing-Original Draft preparation: **MG**, SF, and HE. Supervision: HE, JRB, and MMM.

Abstract

Shifting from fossil fuels to renewable energy sources necessitates the development of diverse electrochemical devices for energy storage and production of fuels, driving the demand for innovative materials and interfaces. However, understanding and controlling these interfaces remains challenging due to the lack of suitable *in situ* and *operando* characterization techniques. Due to the sometimes harsh reaction conditions, surfaces can undergo e.g. restructuring and corrosion only visible during the process. In this case, *in situ* and *operando* measurements can provide the missing link to the full understanding of a system. This thesis explores the potential of Reflection Anisotropy Spectroscopy (RAS) as an *in situ* optical probe for studying crystalline solid-liquid interfaces in electrochemical environments. By combining RAS with electrochemical methods, particularly under external bias (EC-RAS), this research investigates the dynamic evolution of optical properties at interfaces. Together with complementary computational RAS and other *ex situ* techniques, EC-RAS provides a comprehensive understanding of the observed phenomena. Through experimental method development, the dissertation emphasizes the capability of EC-RAS, a rather novel technique, in identifying crucial interface behaviors such as surface reconstructions, ion adsorption/desorption, and thin film formation. Time-resolved measurements offer insights into etching processes, interface restructuring, interface degradation, and adsorption kinetics. The first EC-RAS case studies involving III-V heterojunction solar cells in etching solution, semiconductor-aqueous electrolytes, and non-aqueous battery systems demonstrate the versatility of the method across various electrochemical scenarios. This research paves the way for routine (photo)electrochemical interface monitoring using *in situ* RAS, contributing to the advancement of renewable energy technologies.

Zusammenfassung

Damit erneuerbare Energiequellen anstelle von fossilen Brennstoffen genutzt werden können, ist es weiterhin nötig, vielfältige elektrochemische Prozesse zur Energiespeicherung zu entwickeln, wodurch die Nachfrage an neuen innovativen Materialien und Grenzflächen groß ist. Es ist eine herausfordernde Aufgabe, diese neuen Systeme zu verstehen und zu kontrollieren, da es an passenden *in situ* und *operando* Techniken zur Charakterisierung fehlt. Augrund der manchmal harschen Reaktionsbedingungen, denen die Materialien ausgesetzt sind, kann es zu z.B. Korrosion und Restrukturierungen der Oberflächen kommen, die nur während des Experiments beobachtbar sind. In solchen Fällen können *in situ* und *operando* Messungen die Informationen liefern, welche fehlen, um das System vollständig zu verstehen. Vor diesem Hintergrund wird in dieser Arbeit das Potenzial von Reflektions-Anisotropie Spektroskopie (RAS) als eine *in situ* Methode, um kristalline fest-flüssig-Grenzfläche in einer elektrochemischen Umgebung zu studieren, erörtert. Indem RAS mit elektrochemischen Methoden, vor allem computergestütztem RAS (computational RAS) und *ex situ* Techniken kombiniert wird, ist EC-RAS in der Lage, ein vollständiges Verständnis von den beobachteten Phänomenen aufzubauen. Durch experimentelle Methodenentwicklung, diese Dissertation betont insbesondere die Fähigkeit von EC-RAS, das kritische Grenzflächenverhalten zu identifizieren. Dazu gehört beispielsweise Oberflächenrestrukturierung, Ionen Adsorptions- und Desorptionsprozesse und die Bildung von dünnen atomaren Filmen auf der Oberfläche. Zeitabhängige Messungen gehen noch einen Schritt weiter und können Einsichten in Ätzprozesse, Grenzflächenrestrukturierung, Grenzflächendegradierung und der Adsorptionskinetik geben. Anhand der Untersuchung des Ätzverhaltens von Solarzellen auf Basis von III-V Halbleitern, von Halbleiter-Elektrolyt Wechselwirkungen in wässrigen Medien und von nicht-wässrigen Batteriesystemen wird die Vielseitigkeit von EC-RAS in vielen elektrochemischen Szenarien aufgezeigt. Diese Arbeit ebnet den Weg für photoelektrochemsiches Routinemonitoring von Grenzflächen mit Hilfe von in situ RAS, welches Chancen für entscheidende Fortschritte in erneuerbaren Energietechnologien möglich machen könnte.

Contents

1 Motivation

Climate change is one of the triggers of the ecological disaster currently unsettling our planet's balance. It is important to keep in mind that climate change is only one part of the ecological disaster, that the root of the latter is rather an antropogenic than a technical issue and it will therefore not be solved by science alone [1]. Nevertheless, as the topic of my thesis is fundamental science, I will here introduce some areas where science can contribute to limit climate change. The primary contribution to anthropogenic climate change is the exhaustion of green house gases (GHG) consisting mainly of CO_2, CH_4 and NO_2. According to the 6th IPCC synthesis report, there has been a 0.99℃ increase in global surface temperature during the first two decades of the 21^{st} century compared to the pre-industrial era [2]. The newest numbers from the world meteorological organization even show that the average temperature over the last years was 1.45℃ higher than expected. This global temperature rise leads to various consequences, such as extreme weather events, water shortages, and the elevation of the global sea level [3]. Climate models indicate that global warming will keep increasing in the near future due to the increasing cumulative CO_2 emissions [2]. A recent study demonstrated that the remaining carbon budget (RCB) for a 50% chance of limiting warming to 1.5℃ (corresponding to the target of the Paris agreement for 2030) is only 250 Gt [4]. It corresponds to 6 years left before complete exhaustion of the RCB if the current global trend of 40 Gt of CO_2 emitted per year is maintained [4]. Furthermore, a recent report from the UN indicates that with the current engagements taken by the governments, a decrease of only 2% of GHG emissions will occur instead of 43% required to respect the Paris agreement. It becomes evident that reaching the targets from the Paris agreement will only be possible by a drastic cut in CO_2 emissions and their capture from the atmosphere. CO_2 emissions are significantly originating from burning fossil fuels to produce energy for buildings, and power and transport industry [5]. Therefore, fossil fuels have to be replaced by renewable energies, whose production relies on energy conversion and storage systems. Among them are electrochemical systems such as batteries [6] , supercapacitors [7], electrolyzers [8], photoelectrochemical (PEC) [9] as well as photocatalytic water splitting [10]. The present thesis focuses on systems for solar water splitting and battery applications.

Batteries are already well-developed, world-wide used, and are becoming a key technology in

our societies [11, 12]. The current battery market for car and telephone industries is dominated by lithium ion technology [13]. However, the earth abundance of Li is insufficient to cover the battery demand in the next decades [14]. Furthermore, its extraction from the earth's crust damages and pollutes the environment. Therefore, more earth abundant elements, involving more eco-friendly refining and mining processes, are being intensively investigated as possible post-lithium technologies for applications like stationary devices [13]. The specifications of (post-lithium) batteries include five main criteria: power density, energy density, safety, life cycle, and low cost. Depending on the application, the priorities between these requirements and their expected value differ [15]. Although new material and electrolyte development is the main challenge to reach the targeted performance criteria, the design and the exploration of metal-electrolyte interfaces remains at the heart of all battery systems. More specifically, the solid–liquid phase boundary determines many of the relevant properties, as ion transport can be blocked by a solid electrolyte interphase (SEI) or dendrite formation can induce detrimental conduction pathways [16, 17].

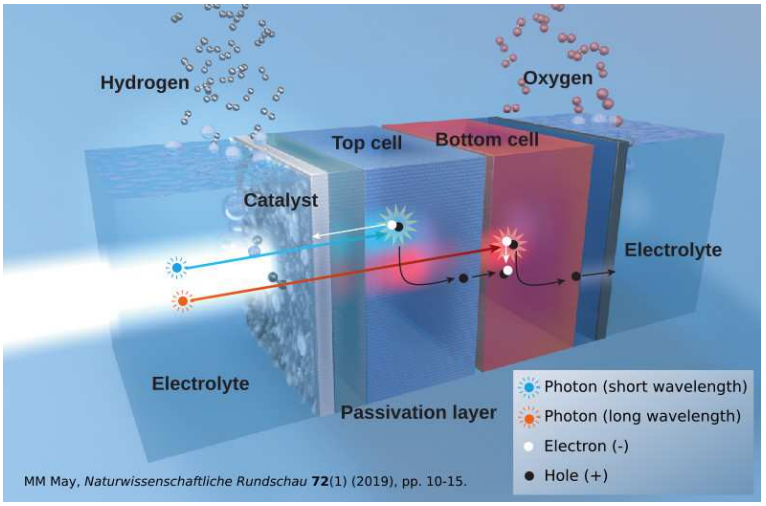

Figure 1.1: Principle of solar water splitting with a tandem absorber. Hydrogen is produced on the left side, where light shines on. Oxygen is produced on the other side.

Electrical energy can be stored and used in a sustainable way using batteries but also fuels. Since, unlike for fossil fuels, the combustion of hydrogen and its derivatives releases harmless components for the environment, it has been regarded as a suitable fuel for the future. Hydrogen has a higher gravimetric energy density compared to batteries [18]. However, hydrogen is difficult to transport and to store, limiting the competitiveness of fuel cells with respect to batteries to stationary application and heavy-duty vehicles. It can be obtained from a variety of sources, but remains up to now mainly produced by thermochemical routes, in which CO_2 is the by-product. Only less that 1% of the global hydrogen is currently produced from renewable energy, like with

electrolyzers [19]. Hence, renewable energy technologies for hydrogen production must become more attractive and competitive. Direct solar-water-splitting devices represent a promising, but also challenging approach for green hydrogen production. As illustrated in Figure 1.1, they are highly integrated systems with a solar cell immersed in aqueous ion-conductive solution. In other words, they combine an electrolyzer and a photo-voltaic cell in a single device [20]. To generate both sufficient potential and current to split water into hydrogen and oxygen, the solar cell must be comprised of ideally two semiconductors of different bandgaps. For high-efficiency absorbers in operation, the low stability of the top-most semiconductor layer in contact with an electrolyte and a catalyst is currently the biggest bottleneck to achieve longer lifetime and optimized performance of the device [21]. Therefore, fundamental understanding at an atomistic level is also required to design the solid-liquid interface in a way that prevents corrosion processes while absorbing enough light.

Implementing (photo)electrochemical surface conditioning for photoelectrodes could enable novel process routes at potentially low costs, but the understanding and control of the related interface (electro)chemistry is so far limited [21]. Nevertheless, such surface functionalization approaches already demonstrated their use for achieving highest solar-to-hydrogen efficiencies by effective surface protection against corrosion [21, 22]. The main limitation in the investigation of these interfaces is the lack of characterization technique that can monitor in real time the solid-liquid interface while an external potential is applied. In this regard, reflection anisotropy spectroscopy (RAS), with its straightforward set-up operating at near-normal incidence configuration, represents a tool for the in situ/operando monitoring of (photo)electrochemical surface passivation with a sub-nanometer control of surface modifications. Although RAS has the advantage to operate in electrochemical environments, it is restricted to single crystalline surfaces. Nevertheless, surfaces and interfaces play an important role in numerous phenomena like semiconductor/metal junctions, corrosion, and catalysis. To understand the mechanism of these processes, it is relevant to first study well-defined crystalline plane surfaces with low Miller indexes to determine their structures and their physical-chemical properties in different environments. This doctoral thesis demonstrates the potential of application of RAS in electrochemistry with the study of different single crystalline surfaces in different electrochemical environments. More specifically, RAS on InP(100) in acidic aqueous solution first serves as a demonstrator system for the development of the method. Then, RAS on AlInP/GaAs in etching solution and in acidic aqueous electrolyte extends the applicability of the technique to more advanced solar water splitting systems. Finally, the interface of Al(110) in ionic liquid is investigated by RAS for post-lithium battery technology.

2 Background

2.1 Light Interacting with Crystals

2.1.1 Crystal and Surface Reconstruction

A crystal is a solid whose micro-structure is ordered over its whole volume. Depending on the crystallization conditions, either a poly-crystal or a single-crystal is formed. A poly-crystal is composed of ordered little crystallites (or grains) with the same structure but with different orientations, whereas a single crystal is an identically oriented solid over its entire volume, meaning that no grain boundaries exist in the crystal lattice. The continuous and unbroken crystal lattice of single-crystals confers them unique mechanical and electrical properties. Among these noteworthy properties is the optical anisotropy, which will be discussed in the following section.

Theoretically, a surface is obtained by sectioning a crystal and is defined as the ensemble of atomic layers modified by the cut. The unmodified part of the crystal is referred to as the bulk. In an ideal case, due to the cut, the top-most atoms of the surface loose some of their chemical bonds and rearrange themselves to reach a new energetical equilibrium position. The obtained surface is called a reconstructed surface [23]. Since the spontaneous transition into the reconstructed phase is often kinetically hindered at room temperature, the surface is annealed in an inert environment at high temperature (usually two third of its melting point) to overcome the activation barrier [24]. However, in reality, unless if the crystal is in a ultra-high vacuum (UHV) environment, it is exposed to other atoms from its surrounding. After cleaving or sawing the crystal, these "ad-atoms" can deposit on the surface and form new chemical bonds while preserving the 2D-periodicity of the surface. Surfaces can be distinguished by their crystalline orientation. When a crystal is cut through a given plane (referenced as (hkl) with the Miller indexes notation) and the cut does not change the position of the atoms, it is possible to determine a surface mesh defined as the section of the volume of a crystal lattice through this plane (hkl). Figure 2.1a illustrates the most commonly studied surfaces with low Miller indexes from a cubic crystal. For reconstructed surfaces, the notation (hkl) (pXq) Rα is used, where p and q are the factors linking the base vectors (a_1,b_1) from the surface mesh before and after the reconstruction

(a_2,b_2). α is the angle between the base vectors (a_2,b_2). Figure 2.1b displays a scheme of a (5X20) reconstructed Au(100) surface after a thermally-induced reconstruction process.

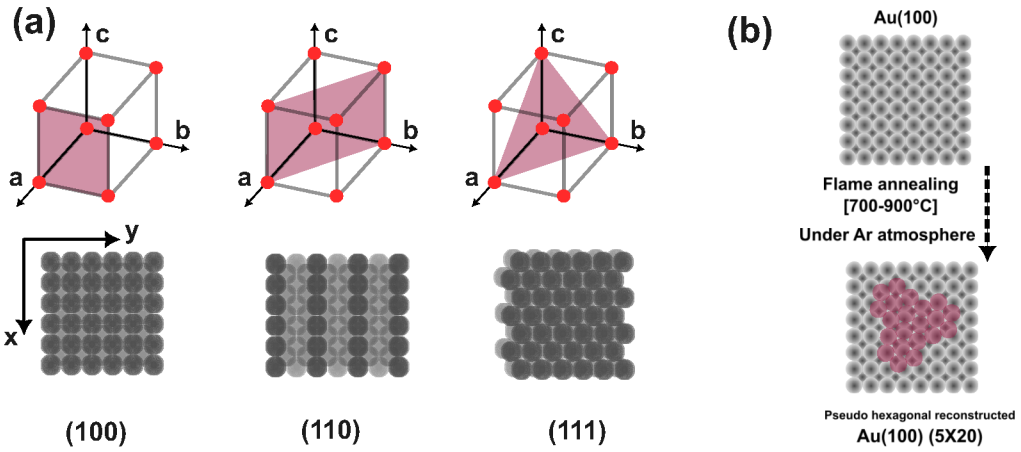

Figure 2.1: (a) (100),(110), and (111) planes in a cubic crystal (b) Au(100) surface before and after annealing under Ar flow. Adapted from [24].

2.1.2 Anisotropic Properties of Crystals

Since different crystal orientations and reconstructions result in different physical properties, e.g. catalysis or electron/hole affinity, it is very important to study surface and interface effects [25, 26]. Figure 2.1 illustrates an important aspect of single crystals which is the anisotropy of crystalline surfaces. The lattice parameters in the x and y axes of a (110) surface differ, resulting in different optical properties along x and y, and therefore in different responses of an electromagnetic wave (EMW) propagating in or reflecting on the crystal. Using the fact that anisotropic surfaces have different optical properties along their x and y axes is a way to access interfacial properties. These optical properties can be determined by studying the polarization of light upon reflection on an anisotropic surface.

2.1.3 Light Polarization upon Reflection on an Anisotropic Material

The polarization of an EMW is described by its electric field. The latter can be decomposed into two components obtained by projection on two orthogonal directions x and y of the plane perpendicular to the propagation direction z of the wave, as shown in Equations (2.1) and (2.2).

$$E_x(z,t) = E_{x0}\cos(wt - kz) \tag{2.1}$$

$$E_y(z,t) = E_{y0}\cos\left(wt - kz + \alpha\right) \tag{2.2}$$

The response of a solid medium of an incoming EMW is described by the complex refractive index $\underline{n}$ according to Equation (2.3). The real and imaginary parts of $\underline{n}$ represent, respectively, refraction and attenuation of the wave by the medium. Equation (2.3) shows that $\underline{n}$ is related to the extinction coefficient k and is a function of its frequency w.

$$\underline{n}(w) = n(w) - ik(w) \tag{2.3}$$

When a linearly polarized EMW, of which the direction of the electric field's vector is constant, is incident on a crystalline surface, the polarization state of the reflected wave is affected by the different optical properties along the different crystallographic axes of the surface. When the wave interacts with a surface, the anisotropy of the surface causes a constant phase shift between $E_x(z,t)$ and $E_y(z,t)$ after being reflected. This phase difference causes a rotation of the polarization direction of the reflected wave, resulting in an elliptical polarization state. The degree of ellipticity depends on the anisotropy of the surface and the angle of incidence of the wave. For near-normal incidence, since the polarization direction of the light is parallel to the surface, only anisotropies in planes parallel to the surface plane affect the change in light polarization upon reflection on the surface. Therefore, the Fresnel reflection coefficient $\underline{r}$ can then be expressed according to Equation (2.4). Note that for isotropic surfaces, no phase shift is introduced between $E_x(z,t)$ and $E_y(z,t)$, and the light remains linearly polarized.

$$|\underline{r}| = |\frac{\underline{E_r}}{\underline{E_i}}| = \frac{\underline{n_i} - \underline{n_t}}{\underline{n_i} + \underline{n_t}} \tag{2.4}$$

Hence, measuring the polarization of the light along x and y after its reflection on a solid medium allows determining the Fresnel reflection coefficients r_x and r_y along x and y. The difference between r_x and r_y gives direct information about the surface's anisotropy. However, it requires decomposing the polarization of the light to access r_x and r_y separately. This can be done by the use of a photo-elastic modulator (PEM) or a rotating analyzer, and will be detailed in the characterization technique (chapter 3). The anisotropy, and more generally the optical properties of a crystal and its surface can also be predicted by determining their electronic structures with numerous theoretical approaches.

2.2 Physics of Semiconductors

For a more complete understanding of the physical properties of crystals and surfaces, it is very helpful to look at solids from a quantum mechanical point of view. These properties can be derived by calculating the band structure of crystalline solids, comprised of the arrangement and distribution of different energy states that electrons can take. In short, the band structure is determined with quantum mechanics (QM) by solving the Schrödinger equation assuming single electron wave functions. Detailed information of the theory of QM can be found elsewhere [27, 28].

2.2.1 Electronic Band-Structure of Solids

The probability f that an electron occupies a state E, depending on the temperature T, is described by the Fermi-Dirac-distribution function given in Equation (2.5), where k_B is the Boltzmann constant. At 0 K, all states up to the Fermi level E_F are occupied while all states above E_F are unoccupied. Increasing the temperature above 0 K allows electrons to leave states below E_F and to occupy states above E_F.

$$f(E) = \frac{1}{\exp \frac{E-E_F}{k_B T+1}} \tag{2.5}$$

The highest energy band occupied by electrons (valence band level E_{VB}) is separated from the lowest unoccupied band (conduction band level E_{CB}) by an energy gap E_g. E_g determines the electric properties between solids and classifies them in 3 different categories: namely metallic conductors, semiconductors and insulators.

In a metallic conductor, the Fermi level E_F, i.e. the electrochemical potential of electrons, lies within a continuous energy band. Hence, there is no band gap (BG) between the conduction band (CB) and the valence band (VB), and electrons can transit from a confined state in the VB to a mobile state in the CB without needing to overcome an energy barrier. This transition of electrons from the VB to the CB generates electron-hole pairs, which are delocalized within the VB, i.e. electrons are mobile over the whole CB resulting in metallic conductivity. As described by the Fermi-Dirac distribution function, this process leads to a high density of intrinsic charge carriers (electrons in the CB n_e and holes in the VB n_h) at room temperature, thereby facilitating favorable electrical conductivity. Unlike metallic conductors, insulators have no significant electric conductivity at room temperature because E_g is too high to be exclusively overcome by thermal energy. As a consequence, electrons remain confined in the VB and no mobile electron-hole-pairs are generated. Semiconductors are between metals and insulators: they have a E_g

that is too high to spontaneously generate electron-hole pairs, yet it is still sufficiently small to be overcome by thermal excitation [29].

2.2.2 Optical Transitions

In addition to predicting the electrical conductivity of solids, the BG also determines their photoabsorption characteristics. In a photoabsorption process, electrons are excited from their ground state to excited CB states via the absorption of photons from a light source, generating an electron hole in the VB and thus forming a so-called electron-hole pair (e-h pair).

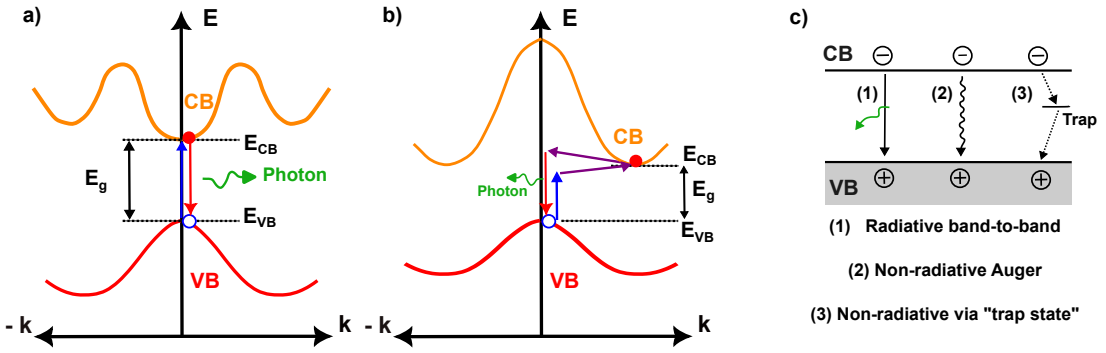

Figure 2.2: E-k diagram of a semiconductor with (a) a direct BG and (b) an indirect BG. The blue and red arrows indicate the absorption and emission of a photon, respectively, while the purple arrows refer to phonon absorption and emission (c) Different recombination mechanisms. Adapted from [30].

Measuring the absorption properties of a material allows determining its band structure. The latter can be represented in an energy-momentum diagram (E-k diagram), where k refers to the momentum of the electrons in the crystal lattice. One can distinguish between two characteristic band structure types depending on the position of the VB maximum and the CB minimum with respect to each other. If the former and the latter are aligned on the E-k diagram, the photoabsorption process only involves radiative transition of electrons between the ground state and the excited states (see Figure 2.2a). The semiconductor is then qualified as direct semiconductor. If now the VB maximum and the CB minimum are not aligned in the reciprocal k-space, the electron has to pick-up momentum from a lattice vibration (phonon) to conserve its momentum when transiting from CB to VB.

the photo-absorption process is then a three-particle-process (photon-electon-phonon) combining radiative and non-radiative processes, i.e. the process undergoes thermal losses and the absorption probability goes down. In this case, illustrated on Figure 2.2b, the semiconductor

has an indirect BG. In opto-electronic devices, direct semiconductors are preferred over indirect semiconductors because the probability of absorbing photons is higher. Hence, the penetration depth of light in the material is small. Consequently, a solar cell made of direct semiconductor materials does not have to be thicker than a few µm while for indirect semiconductor materials, the thickness should be typically higher than 100 µm [29].

Unless the generation of an e-h pair is extracted from the photo-absorber and for instance stored as chemical energy in a battery or directly used in catalysis, its lifetime is very short (<10^{-3} s) and the charge carriers recombine [31]. More specifically, after the thermal radiation is converted into chemical energy of e-h pairs (absorption, 10^{-14} s), the charge-carrier cools down, hereby heating the crystal during thermalization, i.e. a rapid equilibration with lattice phonons (10^{-12} s). Then, the e-h pairs recombine. In addition to the radiative and non-radiative recombination processes described in Figure 2.2a-b and represented again on Figure 2.2c (1) and (2); non-radiative recombination via impurities/defects (3) can also occur and is in fact the predominant recombination process in solar cells. The presence of impurities leads to "impurity states" lying within the BG. If an electron in the CB is in the proximity of a capture cross section occupied by a hole in the VB, they can recombine in an impurity state. Alternatively, electrons or holes can be trapped in impurity states. Electrons trapped in impurity states that are not located in the vicinity of the CB or the VB but in the middle of the BG are unlikely to be released because the energy barriers between E_{CB} and E_{imp} or E_{VB} and E_{imp} is too high, and the charge carriers are considered as "lost". Hence, impurities in semiconductors are undesired since they reduce the concentration of charge carriers available for radiative absorption. Impurities in the bulk can be minimized by optimizing and controlling the growth process of a semiconductor. However, after the manufacturing process, its surface gets in contact with impurities and humidity from the ambient air, e.g. H_2O and O_2. The latter can be adsorbed at the surface and induce a surface reconstruction and/or corrode/passivate the surface, which can lead to undesirable surface states. Therefore, recombination induced by impurities is often happening at the surface of the material and is difficult to prevent. Besides semiconductor-liquid/gaseous contacts, semiconductor/metal contacts also constitute effective recombination centers since the metal has countless energetic states between the E_{VB} and E_{CB} of the semiconductors.

2.2.3 Charge Carriers and Doping

Varying the concentration of holes (n_h) and the concentration of electrons (n_e) in a semiconductor is a way to tune its electrical properties. For intrinsic semiconductors, n_e being equal to n_h, E_F always lies in the middle or close to the middle of the BG. Intrinsic semiconductors have a low electrical conductivity at room temperature due to low concentration of free charge carriers

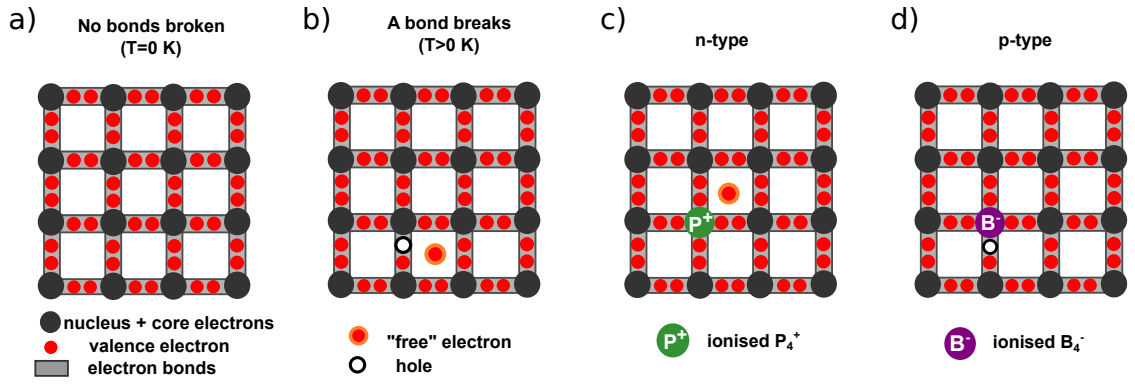

Figure 2.3: **The doping process illustrated using the bonding model for c-Si**. (a) No bonds are broken. (b) A bond between two Si atoms is broken resulting in a free electron and hole. (c) A phosphorus (P) atom replaces a Si atom in the lattice resulting in the positively-ionized P atom and a free electron. (d) A boron (B) atom replaces a Si atom resulting in the negatively ionized B atom and a hole. Taken from [30].

and low carriers mobility. Therefore, as illustrated in Figure 2.3a and b, generating charge carriers requires thermal excitation. Nonetheless, it is possible to create donors or acceptor states within the BG by introducing impurities in the crystal with a process called doping [29]. In this process, as displayed in Figure 2.3c-d, the introduction of hetero-atoms into the solid that either have one valence electron more (donors) or less (acceptors) than the semiconductor atoms allows generating free electrons or holes in the lattice that occupy energy states in the CB and the VB, respectively. A semiconductor doped with donor or acceptor atoms is categorized as a n-type or p-type conductor, respectively. The doping level plays a major role in the electronic structure of semiconductors because E_F depends on n_e and n_h (see Equation (2.6) for n_e).

$$E_F = E_{CB} - k_B T ln(\frac{N_{CB}}{n_e}) \tag{2.6}$$

Hence, for a n-type conductor, E_F is near the CB while for a p-type conductor, E_F is close to the VB. Note that mid-gap bulk or surface states originating both from defects or doping can have detrimental effect and act as recombination centers [32].

2.2.4 Solar Cell

In a so-called "pn-junction" solar cell, shown schematically in Figure 2.4, an n-type and a p-type semiconductor are stacked together. Due to the difference in Fermi levels between the n and p-type regions, electrons diffuse from the n-doped into the p-doped region to equalize the elec-

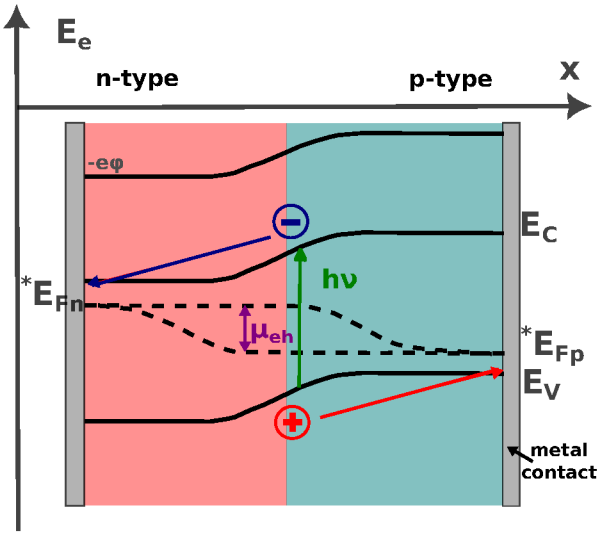

Figure 2.4: Potential distribution in an illuminated pn-junction solar cell. μ_{eh} is the internal photovoltage and -eϕ is the electrical potential energy of electrons. Adapted from [29, 33].

trochemical potentials, establishing a built-in potential across the junction even in the absence of external bias [34]. This built-in potential creates an electric field, causing electrons to migrate to the n-doped region and holes to migrate to the p-doped region when the cell is illuminated. This spatial separation of charge carriers prevents their recombination, allowing the maintenance of a photovoltage μ_{eh} across the junction, which can be harnessed to generate electrical power. To describe the charge carrier concentration under light exposure, the use of a single E_F is no longer appropriate. Instead, the specific quasi-Fermi energy ${}^*E_{Fn}$ and ${}^*E_{Fp}$ for electrons and holes is used, respectively (see Figure 2.4). As mentioned previously, the higher the doping level, the higher the recombination rate, whereas the lower the doping level, the lower the electrical conductivity of the material at room temperature. Thus, choosing adequate doping concentrations is a delicate matter. To give some order of magnitude, heavily doped semiconductors have a doping concentration of about 10^{19} cm^{-3}, while low doped semiconductors have a doping concentration of about 10^{13} cm^{-3}. To collect the photocurrent produced by the solar cell, the latter must be connected to an external electrical circuit (see Figure 2.4), which requires a direct contact between the metals and the semiconductors at the extremities of the cell. The properties of the S-M contacts must be controlled to ensure a sufficient carrier exchange and will be discussed in the following section.

2.2.5 Semiconductor-Metal Contact

When a metal (M) is brought into physical contact with a semiconductor (S), an interface forms between the two solids [35]. Understanding the mechanism of this interface formation is of great importance in the field of photo-chemical processes because semiconductor-metal (S-M) junctions are similar to S-L junctions. Schottky and Mott initially introduced the concept of band bending to elucidate the rectifying behavior observed in S-M contacts [36]. In Figure 2.5a, one can observe the theoretical energy band diagrams for a n-type semiconductor and a metal junction before contact. When these materials come into contact, there is a transfer of free electrons between them due to differences in their work functions (the energy needed to bring an electron from E_F to the vacuum energy level E_{vac}). In the case of a metal's work function (ϕ_m) higher than the one of the semiconductor (ϕ_s), as depicted on Figure 2.5b, electrons migrate from the semiconductor to the metal until the Fermi levels of both the metal (E_{FM}) and the semiconductor (E_{FS}) align. In an equilibrium state, the charge redistribution that forms at the S-M interface creates a negative charge on the metal and induces a positive charge on the semiconductor's surface through electrostatic effects. Because the semiconductor contains a low concentration

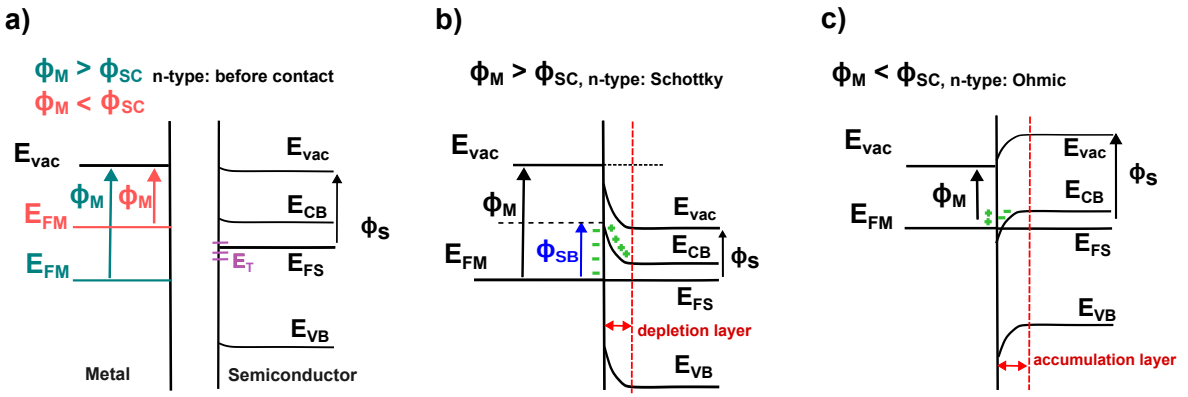

Figure 2.5: Metal-semiconductor a) before contact b) after contact (Schottky type) c) after contact (Ohmic type). Adapted from [36]

of free charge carriers, it cannot effectively screen the electric field between the semiconductor and the metal interfaces. Consequently, this results in a depletion of free charge carriers near the semiconductor surface compared to the bulk, forming what's known as the space-charge region. For a n-type semiconductor (where electrons are the majority charge carriers), the configuration $\phi_m > \phi_s$ leads to an electrons flow from the semiconductor to the metal. The depletion of electrons in the space charge region is called depletion layer. Conversely, when $\phi_m < \phi_s$, as shown on Figure 2.5c, electrons are transferred from the metal to the semiconductor. Hence, they accumulate in the space charge region, forming an accumulation layer. In the space charge

region of the semiconductor, the shifting of the energy band edges due to the electric field originating from charge transfer between the semiconductor and the metal is referred to as band bending. When $\phi_m > \phi_s$, the energy bands bend upwards towards the interface, whereas when $\phi_m < \phi_s$, the edges bend downwards towards the interface. If $\phi_m > \phi_s$ for a n-type conductor, the energy barrier formed at the S-M interface, called the Schottky barrier (ϕ_{SB}), induces a rectifying behavior of the interface. When $\phi_m < \phi_s$, there is no Schottky barrier and the S-M contact shows an ohmic behavior, i.e. the current over the interface follows a linear relation upon the applied voltage. For S-M interfaces, ohmic contacts are preferred because the resistance to current in both voltage polarities is very low.

Note that in Figure 2.5a, a band bending is already present at the semiconductor-vacuum interface before contact with the metal. This is due to the presence of surface states near E_F (symbolized E_T on the Figure) formed by the termination of the periodic crystal, which creates electron transfer from the bulk to the the surface in order to achieve electronic equilibrium [35]. If the surface states are not entirely filled before the junction of a semiconductor and a metal, the band bending will remain unaffected upon contact. Consequently, the Schottky barrier remains unchanged if some electrons are transferred from the surface to the metal. The Fermi level is then "pinned" at the surface state energy, resulting, for most semiconductors, in a large Schottky barrier height for the majority charge carriers. It is empirically possible to transform a Schottky contact into an ohmic contact - where the Fermi level is almost unpinned and thus allows easy majority charge carrier transfer across the interface - by surface doping or by inserting an interlayer at the interface, creating new contact properties

Elucidating the electronic structure of metals and opto-electronic devices is a prerequisite to study their behavior in an electrochemical environment. As a matter of fact, introducing an electrochemical environment increases the level of complexity, especially for semiconductors, as will be discussed in the following section.

2.3 Physical Chemistry of Electrochemical Solid-Liquid Interfaces

Electrochemistry is the study of oxidation and reduction reactions involving charge transfer. Redox reactions are used in electrochemical systems to convert chemical energy in electrical energy and vice versa. A simple picture of an electrochemical system consists of an electron conductor called electrode immersed in an ion conductor named electrolyte. Both electrode and electrolyte can be liquid or solid. Let's consider two metal electrodes M1 and M2 immersed in liquid electrolyte solutions and separated by an electrolytic junction, constituting an electrochemical cell, as illustrated in Figure 2.6a. The charge transfer through the electrode/electrolyte interface generates a current I, which is delivered to an external load at a cell voltage E determined by the redox couples involved. Consequently, the cell supplies electrical power P to the final recipient. We can picture the electron exchange between the oxidants and the reductants in the Equations (2.7), (2.8), (2.9). At the anode, the metal M_1^{y-} is oxidized into a metallic cation $M_1^{(y-n)-}$, while at the cathode, the reverse transformation of M_2^{x+} reduced to $M_2^{(x-n)+}$ takes place.

$$M_1^{y-} \rightarrow M_1^{(y-n)-} + ne^- \tag{2.7}$$

$$M_2^{x+} + ne^- \rightarrow M_2^{(x-n)+} \tag{2.8}$$

$$M_1^{y-} + M_2^{x+} \rightarrow M_1^{(y-n)-} + M_2^{(x-n)+} \tag{2.9}$$

The value of current flowing through the system is in addition determined by the kinetics of the redox reactions involved.

The reaction free energy delivered by the redox process $\Delta_r G$, involving an exchange of n electrons between the two redox couples can be expressed as function of the potential difference ΔE between them, with F being the Faraday constant, i.e. the charge of one mole of electrons [37].

$$\Delta_r G = -nF\Delta E \tag{2.10}$$

The closest definition of the potential of a single electrode corresponds to the equilibrium difference of the potential at the electrode/electrolyte interface [37]. However, it has a physical meaning and can be measured when related to the potential of a second electrode/electrolyte interface. To accurately measure the potential of an electrode of interest (working electrode, WE) while a current flows through an electrochemical system, usually a 3 electrodes setup is introduced, as schematized in Figure 2.6b. Here, a third electrode, called counter electrode (CE), allows that a current flows though the WE without passing through a second electrode, called

reference electrode (RE). The potential difference between the latter and the WE can then be precisely controlled and measured. When the potential difference is measured in "standard conditions", e.g. with the standard hydrogen electrode (SHE) as RE and at 25℃, it is called standard electrode potential. Determining a scale of standard potentials with common redox couples allows predicting the oxidizing/reducing character between them. The redox couples at higher potential are able to oxidize those at lower potentials, e.g. in Equation (2.9), $M_1^{y-}/M_1^{(y-n)-}$ belongs to the couple with the higher potential, while $M_2^{(x-n)+}/M_2^{x+}$ belongs to the couple with the lower potential.

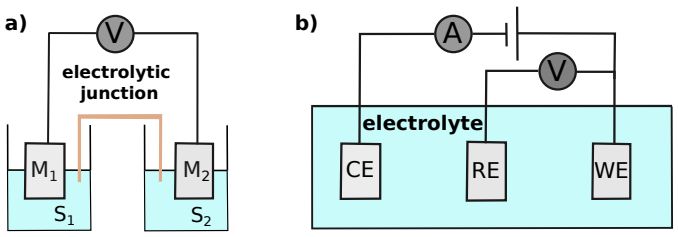

Figure 2.6: a) 2 electrodes system and b) 3 electrodes system. WE, RE, and CE stand for working, reference, and counter electrode, respectively.

The electrochemical potential $\bar{\mu}$ of a species is defined as its molar free energy (chemical potential, μ), adjusted to include the contribution from electrostatic interactions. Here, z represents the charge of the species, F is the Faraday constant, and Φ is the electrostatic potential affecting the species.

$$\bar{\mu} = \mu + zF\phi \tag{2.11}$$

Let's consider a generic redox reaction taking place between species at the electrode/electrolyte interface (Equation (2.12)). n is the number of electrons e^- exchanged, and ν_O and ν_R are the stoichiometric coefficient of the oxidant Ox, and the reductant Red, respectively.

$$\nu_O Ox + ne^- \rightleftharpoons \nu_R Red \tag{2.12}$$

When the conditions of the electrode potential or the chemical potential deviate from the standard conditions, respectively E and μ, and depends on the activity of the redox species at the interface, they can be expressed as in Equations (2.13) and (2.14), respectively. Equation (2.14) is the so-called Nernst Equation, where a_{Ox}, a_{Red}, R, and T denote the activities of the oxidant and the reductant, the perfect gas constant, and the temperature, respectively.

$$\mu = \mu^{\circ} + RT * \ln \frac{a_{Ox}}{a_{Red}} \tag{2.13}$$

$$E = E^{\circ} + \frac{RT}{nF} * \ln \frac{a_{Ox}}{a_{Red}} \tag{2.14}$$

The electrochemical reaction in Equation (2.12) considers an electron transfer at the interface between an electrode and an electrolyte, leading to a change in the chemical composition of the latter. In this case, the process is Faradic, meaning that the amount of substance converted by the electrochemical reaction is proportional to the amount of electricity that has passed through the interface. However, when the polarisation at the interface involves a charge redistribution without electron transfer between the electrode and the electrolyte, the process is non-Faradic. Although non-Faradic processes are not associated with redox reactions, the potential of an electrode is influenced by the charge distribution at its interface with an electrolyte. To understand this influence, a nano-scale picture of the interface has proven to be very helpful.

2.3.1 Electrochemical Double Layer (EDL)

This subsection is taken from the publication A1 [1].

Figure 2.7 shows a schematic structure of a semiconductor surface in contact with an electrolyte solution in the dark, forming so-called "electrochemical double layers" (EDL). Solvent species (H_2O) are represented with blue spheres. The electrolyte solution is composed of solvent molecules, solvated positive ions (cations, pink spheres) and negative ions (anions, yellow spheres). When a metal or a semiconductor is brought in contact with an electrolyte, different processes are taking place, in particular under electrical potential control.

Semiconductor-electrolyte contacts are much more complex than metal-electrolyte contacts. One factor is certainly the reduced structural stability against electrochemical corrosion of most semiconductors when compared to many (noble) metals. Furthermore, the interfacial energetics are altered, as semiconductor-electrolyte interfaces have additional potential drops compared to metal-electrolyte interfaces, whose potential drop region is limited (mainly) to the Helmholtz layer (HHL). Like for S-M contact, when a semiconductor is in contact with an electrolyte, the charges in the solid need to be redistributed to reach an equilibrium due to the Fermi level E_F differences between the solution and the electrode. The E_F of the semiconductor aligns with the E_F of the red-ox species resulting in a band bending of the E_{CB} and E_{VB}, forming in this case with a downward band-bending of a p-type semiconductor, a depletion layer. Therefore, it is not

[1] see list of publications above

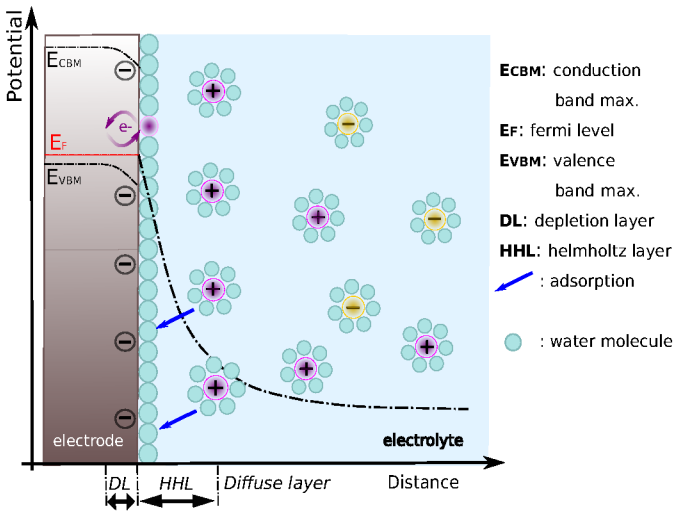

Figure 2.7: Electrochemical interface of a p-type semiconductor with an electrolyte forming a depletion layer in the dark after equilibrium. The positive and negative charge on the electrolyte side account for solvated ions. Inspired by Gerischer [38].

possible to neglect the tunneling process as for metal electrodes [39, 40]. As sketched in Figure 2.8, the band bending, which depends on the externally applied voltage/irradiation, the red-ox potential from the electrolyte, and the doping level of the substrate, can shift electronic states of the surface across E_F. Thus, charge transfer between the electrode and the ions adsorbed at the surface can occur via conduction/valence band and via surface states [41].

As described in section 2.2.5, the band bending arises from an electric charge exchange between the bulk and the surface (states) of the semiconductor. The resulting electric field modifies the dielectric function of such a material and can impact the surface's anisotropic properties [42]. This effect, called the linear electro-optic effect linear electro-optic effect (LEO), may have different origins. On the electrode side, the electric field is influenced by the doping level of the substrate, while in the space-charge layer on the electrolyte side, it depends on molecular dipoles and their orientation with respect to the surface, but also on the ion distribution. An electric dipole within an adsorbed molecular film can also affect the integrated electric field. External parameters that impact the electric field are certainly the applied voltage, but also the irradiation in case of a photoabsorber. The development of an illumination-induced photovoltage adds another layer of complexity. At a given light intensity, the photovoltage also depends on the charge-carrier recombination, which can in most cases change upon corrosion or potential-induced restructuring of the interface [41]. Taken together, these specificities of the EDL of

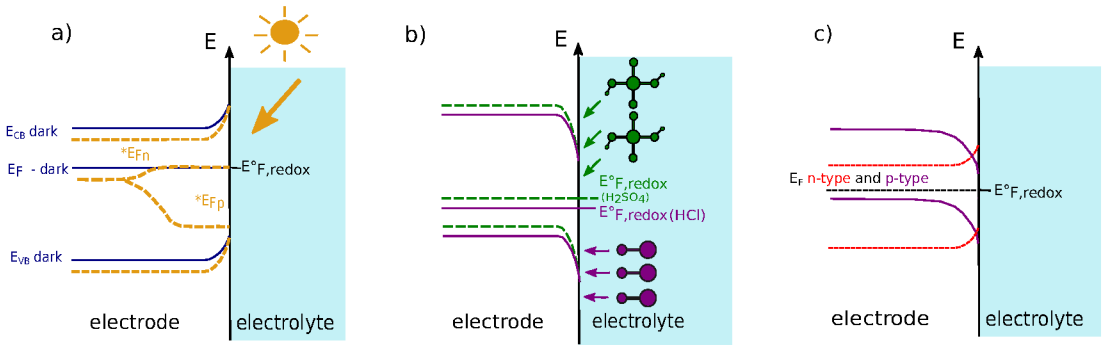

Figure 2.8: **Energy band diagrams showing the influence of the irradiance, the doping type, and the electrolyte on the EDL and the optical properties of an idealized semiconductor-liquid interface (no surface passivation/corrosion)**. The electrode is considered as photo-cathode for solar water splitting, and H^+/H_2 is the most active redox couple. Interfacial layers and charge-carrier recombination [41] are ignored for the sake of simplicity. a) dark and illuminated (dotted line) EDL of n-type semiconductor. b) EDL of p-type semiconductor influenced by the charging effect of H_2SO_4 (dotted lines) and HCl electrolytes (0.01 M). c) EDL for n and p-type semiconductors.

the semiconductor-electrolyte system show that these interfaces can be more complex than for metals, which also impacts spectroelectrochemistry. The configuration and the composition of the EDL impacts the relationship between the amount of ions or molecules adsorbed onto a solid surface. The involved adsorption processes can be characterized and understood using tools called adsorption isotherms, described in the following section.

2.3.2 Adsorption Isotherms

The process by which molecules, ions or atoms adhere to the surface of a solid material is called adsorption. It is not to be confused with absorption which happens when a particle or a fluid penetrate the entire volume of an other substance. Desorption refers to the the reverse process of adsorption, i.e. molecules, ions or atoms are released from the solid surface into the surrounding fluid or vacuum [43]. The amount of adsorbed species is usually given in terms of the coverage θ. For systems in which the adsorbate can form a full monolayer, θ is defined as the ratio of the amount of adsorbate present on the surface to the maximum amount that can be adsorbed. Depending on the nature of the interaction between the adsorbate and the surface,

the adsorption process can be categorized as physisorption or chemisorption. Physisorption involves weak van der Waals forces between the adsorbate and the surface, such as solvent molecule acting as dipoles on the surface. The adsorption of electrolyte ions on the electrode's surface is usually a chemisorption, meaning that strong interactions (several hundred kJ/mol) are involved, which mainly depend on the type of adsorbates, the electronic properties of the substrates, and the structure of the surface. These strong interactions lead to local changes in the geometric, electronic and vibrational structure of the substrate and the adsorbates [44]. Species can chemisorb at different sites on the electrode, e.g. on top of certain atoms, on bridge position between two atoms, on steps/vicinity for structurally in-homogeneous surfaces and on different elements for alloy surfaces. Therefore, adsorption studies are often conducted on single crystals of which the surface is well-defined [43].

For electrochemical systems, the external potential, the temperature, the bulk concentration of adsorbed species in solution, the nature of the interactions between adsorbates and surface and the adsorbate-adsorbate interaction also influence the adsorption. For instance, when applying an external electric field to the electrode, there is an enhanced tendency towards surface restructuring upon interaction with adsorbates (adsorbate induced restructuring). Bringing the electrode to low negative potentials can lead to adsorbed cations that may then desorb from the surface when letting the system evolve to thermodynamic equilibrium. Figure 2.9 illustrates the adsorption of chlorine ions from an aqueous electrolyte on an In-riched, InP surface depending on the applied potential at the electrode. On Figure 2.9c, one over two In sites is occupied by a chlorine atom, which thus translates to θ = 0.5.

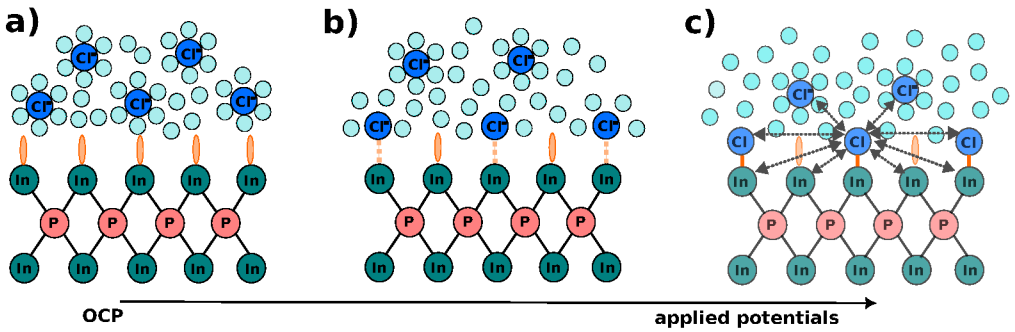

Figure 2.9: a) In-rich, InP surface in contact with chlorine ions solvated by water molecules at OCP. b) Under applied potentials, Cl^- start to strip their water sheaths and to adsorb on the surface. c) At even higher potentials, the adsorbed Cl^- form chemical bonds with the surface. The dashed gray arrows represent the interactions between a reference Cl^- and its surrounding. The oval, dashed and full orange lines represent the type of In bonding with Cl^- (no interaction, weak interaction, chemisorption, respectively).

When studying adsorption and desorption processes of solid-liquid (S-L) system, the ad/desorption kinetics, ad/desorption equilibrium, substrate-adsorbate interactions, and surface diffusion are the most relevant phenomena to take into account. As a refinement, the adsorbate-adsorbate interactions are also important to be considered since they can modify the free reaction enthalpy of the adsorption process [44].

The chemisorption process of an adsorbate A in solution on the vacant sites S of a surface in dynamic equilibrium with the product AS, is given in Equation (2.15). k_a and k_d are the adsorption and desorption reaction rate constants, respectively.

$$A_{solution} + S_{surface} \underset{k_d}{\overset{k_a}{\rightleftharpoons}} AS \tag{2.15}$$

The simplest description of a chemisorption is the Langmuir model, which considers a uniform surface where all the adsorption sites are equivalent, and the ability of a species to absorb at a given site is independent of the occupation of neighboring sites. The rate of a such a reaction process can be expressed by the rate of change of the surface coverage θ, i.e. the variation over time of the ratio of the number of occupied adsorption sites M to the number of available adsorption sites N. Hence, the rate of adsorption r_a, proportional to the available sites, and the rate of desorption r_d, proportional to the occupied sites, can be expressed as function of θ and the concentration C_A of the adsorbate in solution, as described in Equation (2.16) and (2.17), respectively.

$$r_a = \frac{d\theta}{dt} = k_a C_A (N - M) = k_a C_A N (1 - \theta) \tag{2.16}$$

$$r_d = \frac{d\theta}{dt} = -k_d M = -k_d N \theta \tag{2.17}$$

The chemisorption kinetics can thus be determined by studying the variation of θ with the concentration at a chosen temperature, called adsorption isotherm. In this case, the equality of Equation (2.16) and (2.17) at equilibrium yields the Langmuir adsorption isotherm expressed in Equation (2.18), where $K = k_a/k_d$.

$$\frac{\theta}{1 - \theta} = K C_A \tag{2.18}$$

When the adsorbed ions interact oŕ when the adsorption sites are not equivalent, i.e., some sites are energetically more favorable for the adsorption, the adsorption enthalpy can vary with the coverage. In this case, the Langmuir model is no longer valid and more complex, often empirical models must be established [44, 45]. Among them, the Temkin isotherm describes a linear

dependency between the coverage and the adsorption enthalpy (Equation (2.19)), whereas in the Freundlich isotherm, the adsorption enthalpy varies logarithmically with the coverage (Equation (2.20)). In both cases, c_1 and c_2 are specific empirical constants related to the adsorption system.

$$\theta = c_1 \ln c_2 C_A \tag{2.19}$$

$$\theta = c_1 C_A^{\frac{1}{c_2}} \tag{2.20}$$

2.3.3 Electro-adsorption Isotherm under Cyclic Potential

If the applied potential is swept at the electrode with a very low speed in a given potential range, it can be assumed that the system reaches an equilibrium at each potential of the scan. Using thermodynamic and statistic principles, the electrochemical potential of the adsorbate $\tilde{\mu}_{ad}$ can be expressed as function of the coverage and the adsorption energy per adsorbate ϵ_{ads} (Equation (2.21)) [43]. The electrochemical potential of the adsorbate species in solution $\tilde{\mu}_{sol}$ is given in Equation (2.22). ϕ_{ads} and ϕ_{sol} are the local electrostatic potentials.

$$\tilde{\mu}_{ad} = N_a \epsilon_{ads} + RT \ln \left(\frac{\theta}{1-\theta}\right) + zF\phi_{ads} \tag{2.21}$$

$$\tilde{\mu}_{sol} = \mu^{\circ}_{sol} + RT \ln \frac{C_A}{C_0} + zF\phi_{sol} \tag{2.22}$$

At equilibrium, $\tilde{\mu}_{sol}$ and $\tilde{\mu}_{ad}$ are equal. Using this equality, it is then possible to establish the potential ($\Delta\phi$) dependent Langmuir isotherms, given in Equation (2.23). The term ϵ_{ads} contains the formation energy of the adsorption of an isolated ion. However, this model neglects interactions between the adsorbates. The latter can be taken into account by adding latter interaction parameter g to Equation (2.23) (positive if the adsorbed particles repel, and negative if they attract each other), leading to the Frumkin isotherm (2.24) [43, 46]. When the values of θ are in the intermediate range 0.2 to 0.8, the term $\frac{\theta}{1-\theta}$ varies little with θ in comparison to the exponential term $\exp(g\theta)$ with θ. In this case, the Frumkin isotherm can be simplified to the Temkin isotherm shown in Equation (2.25).

$$\frac{\theta}{1-\theta} = \exp\left(zF\frac{\phi_{sol} - \phi_{ads}}{RT}\right) \exp\left(\frac{\mu^{\circ}_{sol} - N_a * \epsilon_{ads}}{RT}\right) \tag{2.23}$$

$$\frac{\theta}{1-\theta} = \exp\left(zF\frac{\phi_{sol} - \phi_{ads}}{RT}\right) \exp\left(\frac{\mu^{\circ}_{sol} - N_a * \epsilon_{ads}}{RT}\right) \exp\left(-g\theta\right) \tag{2.24}$$

$$\exp\left(g\theta\right) = \exp\left(zF\frac{\phi_{sol} - \phi_{ads}}{RT}\right) \exp\left(\frac{\mu^{\circ}_{sol} - N_a * \epsilon_{ads}}{RT}\right) \tag{2.25}$$

3 Characterization Techniques

The basic principles of X-ray photoelectron spectroscopy (XPS) and scanning electron microscopy (SEM) can be found in the Appendix, sections 7.1 and 7.2, respectively.

3.1 Electrochemical (EC) Measurements

3.1.1 Cylcic Voltammetry

Cyclic voltammetry (CV) is an EC technique used to investigate the current generated within an EC cell when a potential ramp at a scanning speed v is applied to the electrode of interest (the working electrode). The process can be understood as follows: in a 3-electrodes setup, the potential of the working electrode is measured in relation to a reference electrode, which maintains a constant potential. This setup results in an excitation signal vs. time, as depicted in Figure 3.1a.

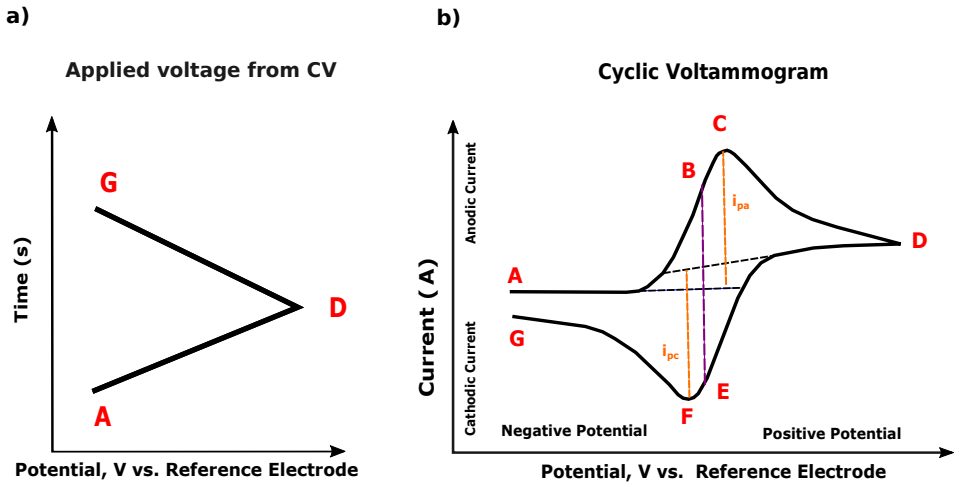

Figure 3.1: a) Applied voltage extracted from the voltammogram. b) Voltammogram of a reversible single electron oxidation-reduction. Adapted from [47] and [48].

In the forward phase (oxidation), the scan starts at a potential where no reaction occurs (point A), goes through the redox potential of the redox couple present in solution, and ends at a potential that exceeds this redox potential (point D) [47]. In the backward scan (reduction), the reverse process occurs from D to G, where the potential goes from higher potential to lower potentials. A cyclic voltammogram is obtained by measuring the current flow between the working electrode and the counter electrode (the third electrode of the setup) during the potential scans. Figure 3.1b shows a cyclic voltammogram representing the reversible redox reaction from the generic Equation (2.12). It also illustrates a typical oxidation process taking place from A to D and a reduction process from D to G. This cyclic process can be repeated, and the speed at which the potential is scanned can be adjusted. The slope of the excitation signal indicates the scan rate employed during the experiment. Note that the CV does not have to start with the oxidation process followed by the reverse reduction process but can also be the other way around.

At the beginning of the oxidation process, the concentration of the reactant (the reductant) is sufficiently high so that the Faradic current is limited by the kinetics of the electrode and increases as the potential increases. Then, as the solution in the vicinity of the electrode is progressively depleted in reductant, the Faradic current grows much more slowly than electrode kinetics alone would allow. At point C, it becomes limited by mass transport phenomena (diffusion, in most of the cases) and it starts to decrease. The current that emerges from this oxidation process is called the anodic current. The coordinate of point C are referred as anodic peak potential ($E_{p,a}$) and the anodic peak current ($i_{p,a}$). At the switching potential D, the solution in the vicinity of the electrode is now more rich in oxidant. The potential is subsequently scanned in the cathodic direction, moving from D to G. This results in a cathodic current corresponding to a reduction process. At position F, one encounters the cathodic peak potential ($E_{p,c}$). C and F are shifted with respect to each other on the potential scale due to the diffusion of the oxidant/reductant to and from the electrode. Note that in addition to Faradic current (involving electrons transfer from redox reactions), non-Faradic current can also contribute to the overall current of the cyclic voltammogram. Non-Faradic processes involve charge redistribution at the interface without electron transfer and depend on the scan speed.

3.1.2 Chronoamperometry

Chronoamperometry (CA) is a simpler technique that consists of imposing a potential step at time t=0 s between two potentials framing the redox potential of the system under consideration [49]. Here again, the final potential is often chosen to be sufficiently far from the initial potential to generate a total reaction at the electrode, but this is not obligatory. Figure 3.2b shows the current plotted as a function of time in the case of a diffusion-controlled current. After taking a

very high value at the start of the reaction, it decreases in $t^{-1/2}$ throughout the experiment.

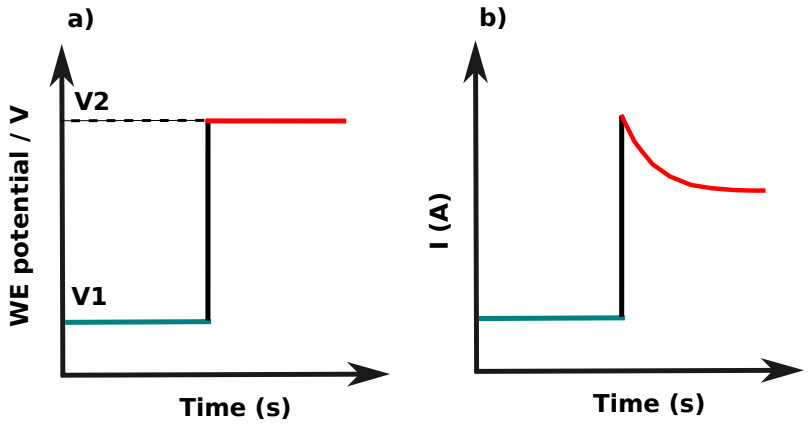

Figure 3.2: a) Potential step from a potential V1, where no reaction occurs, to a potential V2, at which a redox reaction begin. b) Chronoamperogram showing the resulting diffusion-limited current. Taken from [49].

3.2 Reflection Anisotropy Spectroscopy (RAS)

this section contains several parts of the publication A1 [1].

3.2.1 Principle

RAS is a linear, differential optic probe that measures the difference in reflectivity of near-normal incident light between two orthogonal directions of the surface normalized by the overall reflectivity. The definition of the RAS signal is given in equation (3.26). r_x and r_y are the Fresnel reflection coefficients along the two axes x and y in the surface plane. In case of an anisotropic surface, r_x and r_y have different values and their difference normalized by the average reflectivity represents the optical anisotropy of the sample [50]. While both real and imaginary part are measured, experimental literature typically refers to the real part, a convention that we will also employ for the spectra displayed in the following sections.

$$\text{RAS} = \frac{\Delta r}{r} = 2 \cdot \frac{r_x - r_y}{r_x + r_y} \tag{3.26}$$

It is noteworthy to mention that one can also probe the anisotropy of the reflectance, i.e. the (real) square of the Fresnel reflection amplitude, $R = |r|^2$. This case is then referred to as reflectance anisotropy spectroscopy, where the relation $\mathrm{Re}(\frac{\Delta r}{r}) \approx \frac{1}{2}\frac{\Delta R}{R}$ holds true for $\Delta r \ll r$ [51, 52]. The basic working principle of RAS and the configuration used in this study are illustrated in Figure 3.3. A more detailed description of the working principle of RAS can be found elsewhere [53].

When linearly polarized light in the UV-visible range is reflected by an anisotropic crystalline surface, the polarization becomes elliptic and reaches the photo-elastic modulator (PEM) of the spectrometer. Due to its birefringent property, the PEM induces a retardation between the two components of the elliptic polarization along the x and y surface crystal direction. By periodically switching the PEM off and on at its resonance frequency, it acts as a switchable λ/2 plate [55]. It means that the component of the elliptic polarization that is aligned with the direction to be transmitted by the analyzer varies periodically. Hence, the ellipticity of the polarization, which is related to the difference in reflectance r_x - r_y, can be determined. After the modulated polarized light has passed through an analyzer, its intensity (I) now depends on the polarization state of the light, the retardation, and the modulation frequency ω of the PEM. This signal is then detected by a photomultiplier and demodulated by a lock-in amplifier. The intensity ratio between

[1] see list of publications above

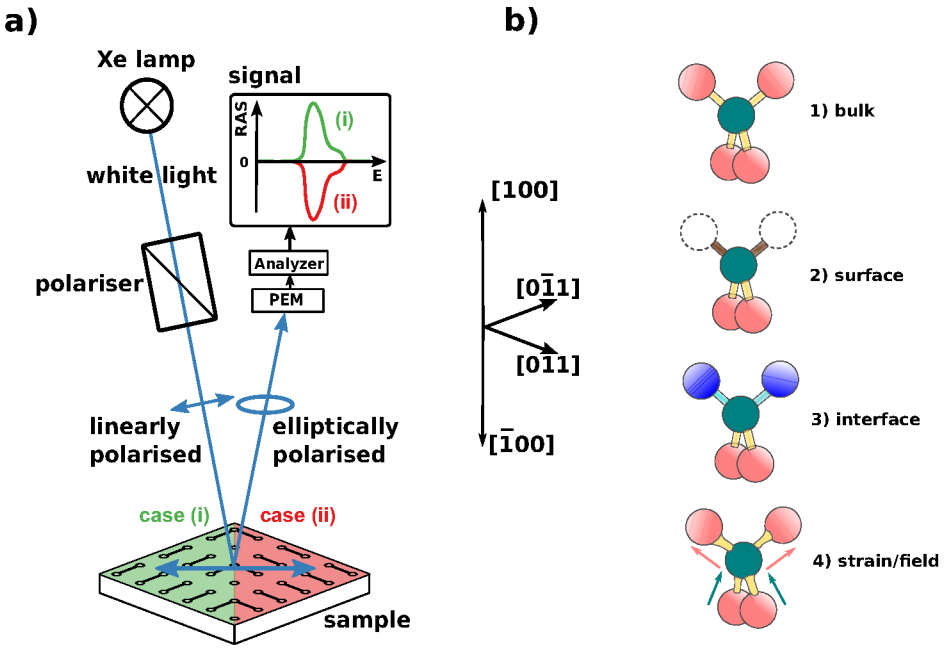

Figure 3.3: a) **General principle of RAS** for the case of a dimerized, cubic (100) surface. The rotation of the dimers by 90° (case i, green vs. case ii, red) switches the sign of their contribution to the spectrum. Adapted from Ref.[54] with permission from the ACS. Further re-use subject to permission by ACS. b) **Contributions to the RAS signal** of a zincblende compound in (001) orientation (Source: M. Pristovsek, Habilitation, Technische Universität, Berlin, 2012, slightly edited).

the oscillatory ($I_{2\omega}$) and the time-independent (I_0) contributions, given in Equation (3.27), is thus proportional to the optical ratio shown in the Equation (3.26) [50].

$$\mathrm{Re}\left(\frac{\Delta r}{r}\right) = \frac{\sqrt{2}I_{2\omega}}{I_0} \tag{3.27}$$

To allow sufficiently high reflectivity and to limit the complexity of the anisotropic signal, RAS is mainly restricted to single crystals with very low surface roughness (<10 nm). The anisotropy of the signal can arise from both the surface and the bulk of the sample due to the relatively large penetration depth of light. To get a signal exclusively from the surface, the symmetry of the bulk in the plane of the surface must be isotropic (Figure 3.3b 1)) whereas the symmetry of the surface must be anisotropic. At surfaces, different surface reconstructions can occur to minimize surface energy. The broken symmetry of the reconstructions can result in anisotropy (Figure 3.3b 2)). For instance, cubic systems with (100) and (111) surface orientation have isotropic symmetry and in principle should give a zero RAS signal. However, they can undergo a surface reconstruction. For example, annealing Au(100) allows obtaining a pseudo hexagonal recon-

structed Au(100)-(5×20) surface which breaks the symmetry between the bulk and the surface and gives a RAS signal exclusively from the surface. For alloys like InP, their surface typically reconstruct in dimer rich surfaces which present some anisotropy. For cubic systems with (110) surfaces, the RAS signal is more complex because the signal is also arising from the bulk. However, a break in the symmetry between the bulk and the surface gives different contribution to the RAS signal and surface evolution can be monitored. For instance, it is possible to distinguish a (1×2) from a (1×1) or (1×3) reconstruction of Au(110). Yet for example in the case of cubic (100) surfaces, whose bulk is isotropic, it is possible to exclusively get information about the surface. Two other factors can contribute to anisotropy of the signal. First, the environment with which the surface is in contact with dictates preferential orientations of bonds at the interface, which can result in a RAS signal (Figure 3.3b 3)). When a relatively thick surface film forms or in case of heteroepitaxial sample, interface anisotropies can only contribute to the RAS signal if the layers above the interface are transparent enough to allow that a sufficient amount of light reaches it [51]. Second, anisotropy can also be the result of an electric field or an internal strain that cause differences in the bond lengths, resulting in bulk anisotropy (Figure 3.3b 4)). A strain, for example, can be caused by changes in the lattice constant in the case of a heteroepitaxial sample, while field effects can be the result of high doping [56]. In solutions, layers of electrolyte or water can also generate an electric field at the surface resulting in surface anisotropy [57]. Since, in general, several effects can contribute to a RAS signal, RAS can only be used as a surface-sensitive technique when the contributions of the interfaces or the bulk are significantly smaller than the sample's surface contribution. This is usually true for homoepitaxial samples with an isotropic bulk. On the contrary, the RAS signals of heteroepitaxial samples, like InP, can be rather complex, even if the bulk crystal structure is isotropic.

3.2.2 Computational RAS

Computational modelling enables interpreting and having an atomistic understanding of the experimental RA-spectra. It involves the determination of ground state electronic structure via density functional theory (DFT) calculation as a starting point, followed by computational spectroscopy [58]. To consider possible surface reconstructions observed experimentally, a slab of a couple of atomic layers is constructed with vacuum on top [59]. The number of atomic layers to be used and the amount of vacuum above and below the slab is decided based on the results obtained by convergence calculations. Since a single-crystalline electrode surface is periodic, it is sufficient to simulate a surface cell. The calculations are carried out under periodic boundary conditions, which reduces the computational costs while providing a good approximation of the structure. The cell size must be carefully chosen to allow enough degree of freedom of the atoms at the surface. To model the surface reconstruction, the desired atoms are positioned

or removed from the top and bottom-most layers of the slab. Then, geometry optimization is performed to minimize the total energy. With the obtained different surface reconstructions, a phase diagram is determined to know which surfaces are the most stable ones. The suitable surfaces can then be used for further investigations involving for instance adsorbed hydrogen, oxygen, or water, to mimic an electrode surface in contact with an aqueous electrolyte solution. Ultimately, the obtained stable surfaces can be used as input for the computation RA-spectra.

From a computational approach, the RAS signal can be computed with the dielectric function, according to Equation (3.28) [50, 52].

$$\frac{\Delta R}{R} = \frac{4\pi d}{\lambda} \operatorname{Im}\left[\frac{\Delta\varepsilon_s}{\varepsilon_b - 1}\right] \tag{3.28}$$

Here, ε_s and ε_b represent the complex dielectric functions ($\varepsilon = \varepsilon' + i\varepsilon''$) of the surface and the bulk, respectively, and λ is the wavelength of the light. The dielectric tensor, which is the crucial component of this Equation, can be computed via the random phase approximation-independent particle approach (RPA-IP approach). The latter is a coarse approximation used to compute excited states. Details of this approach can be found elsewhere [60].

3.2.3 History and Development

Established in the 1980s by Aspnes et al., RAS was first developed as an *in situ* optical probe to achieve a layer-by-layer surface control in III–V semiconductor growth systems as for example molecular beam epitaxy (MBE) [61, 62] or metal-organic vapor phase epitaxy (MOVPE) [63]. Since then, the technique has been widely used for the study of semiconductor surfaces and interfaces in growth environments. In particular, RAS studies on GaAs have not only demonstrated how the spectroscopy can be used to control epitaxial growth and the preparation of specific surface reconstructions, but also the possibility to investigate layer-by-layer removal of GaAs as a protective cap layer for the preparation of fresh surfaces was shown [64–66]. More recently, Sombiro et al. have pointed out the utilization of RAS to extract etching rate and etch-depth resolution from the analysis of Fabry-Pérot oscillations generated by reactive ion etching (RIE) of GaAs/AlGaAs multi-layer structures [67]. Figure 3.4 illustrates the RAS measurements that can be obtained during such an experiment [67]: Figure 3.4a corresponds to a continuous spectra measurement, denoted as colourplot (CP), recorded during the etching of the multi-layer structure. The CP presents oscillations that partly depend on the wavelength and the refractive indexes of the layers. They originate, upon etching, from interference phenomenon between the ever-shrinking topmost layer surface and the underlying interfaces of the structure.

Time-resolved measurements, also named transients, allow a better visualization of Fabry-Pérot oscillations at a specific energy, as depicted in Figure 3.4c. Note that here the reflectivity signal is shown and not the anisotropy. To observe differences in the spectral fingerprints of the layer stack, single spectra taken are extracted from the CP at different time of the etching process and plotted on Figure 3.4b, thus corresponding to the anisotropy of different layers. Along with the

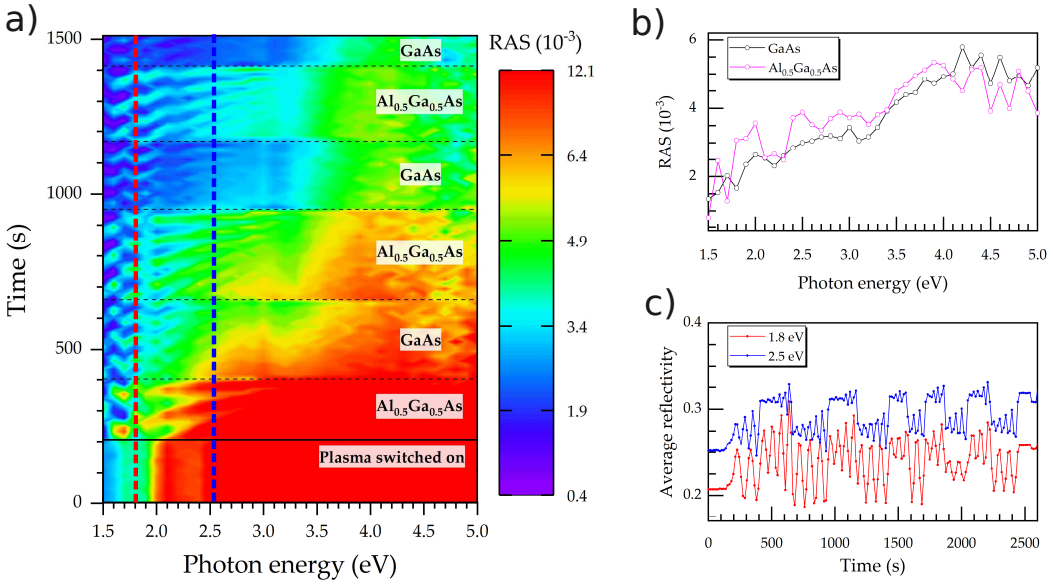

Figure 3.4: a) CP acquired during RIE of a GaAs/AlGaAs multi-layer structure. b) RAS spectra extracted from CP at t = 1007 s (GaAs) and t = 1243 (AlGaAs). c) Reflectively signals acquired at 1.8 and 2.5 eV during the same process than a). The signals would correspond to the reflectivity of transients extracted on the CP (marked by red and blue vertical dotted lines). Taken from [67].

work from Sombiro et al., dry etching in hydrogen ambient was studied by Brückner et al.[68], who have reported that RAS reveals a layer-by-layer removal from Si(100) single-crystals in H_2 atmosphere at elevated temperatures. The etching of single Si layers is identified in transients that oscillate between one dimer orientation to another, which would correspond to switching between spectra (i) and (ii) in Figure 3.3a. These studies demonstrate that RAS is a relevant tool for the development of direct growth processes of III-V/Si solar cells, since well-defined monolayer etching allows single domain preparation. In principle, the fitting methods used to determine growth rate, etching rate, and etch-depth resolution from transients in dry processes can be adapted for transients measured during chemical and EC processes.

In addition to growth process monitoring, RAS is sensitive to the surface coverage and provides a surface fingerprint for instance caused by molecular adsorption. Thus, RAS can be used to characterize adsorption processes in a quantitative manner. In vacuum, studies have already

established a linear dependency between the RAS signal of Si(100) at around 3.5 eV and the amount of dangling bonds/hydrogen coverage at the surface [68, 69]. In particular, Witkowski and al. have demonstrated that the adsorption of different molecules on a chosen surface can give a similar RA-spectral signature, such as benzene and hydrogen adsorbed on Si(100) [69]. In this case, unsaturated and saturated hydrogen spectra can constitute a reference to determine the coverage of benzene on Si(100) depending on the ratio of the measured spectrum over the reference spectrum. Investigations on the adsorption of constituents of an electrolyte – typically water – with RAS can serve as an intermediate step between UHV and gas-phase studies on the one side and the full EC environment with the solid/liquid phase boundary on the other side [54, 69–72]. The great advantage of such a type of study is that the surface stays in inert gas or vacuum conditions prior to and after water adsorption, which allows to precisely characterise and control the initial surface configuration by standard surface science tools. This can help to understand, for instance, the impact of step edges on the reactivity of a given surface [72] or derive activation energies [69]. The downside of such a type of experiment is that the comparability with the realistic EC environment is limited at best. Low-temperature water adsorption from the gas phase [71] allows to adsorb multi-layer water (ice) on a surface, but reactivity of the interface might be qualitatively different from the ambient temperatures of a typical EC experiment. Adsorption at ambient temperatures, on the other hand, limits the maximum water layer thickness typically to a sub-monolayer [54, 70].

A solution to bridge the knowledge gap between gas-phase studies and EC S-L interfaces is to use the established RAS technique to directly probe real S-L interfaces. In this regard, with its straightforward set-up operating at near-normal incidence configuration (Figure 3.3), RAS represents a potential tool for the in situ/operando monitoring of EC S-L interfaces with a sub-nano- meter control of surface modifications.

3.2.4 Important Aspects of the EDL

As a proof of principle that RAS can be developed to probe the EDL, the different contributions to the electric field described in section 2.3.1 are investigated by RAS. Figure 3.5 compares their different impacts on the EDL and on the optical properties of semiconductors. The orange and red spectra, respectively corresponding to n-type with and without additionnal illumination, are almost identical. It indicates that additional illumination, in the considered situation, has hardly any influence on the optical properties of the interface. In this case, n-type InP is acting as a photo-cathode for the reduction of protons. Hence, as showed on Figure 2.8(a), the redox potential aligns with the the quasi-fermi level of the electrons ($^*E_{Fn}$), resulting in a minor increase of the photo-voltage. Similarly to the spectra with and without additional illumination, the spectra

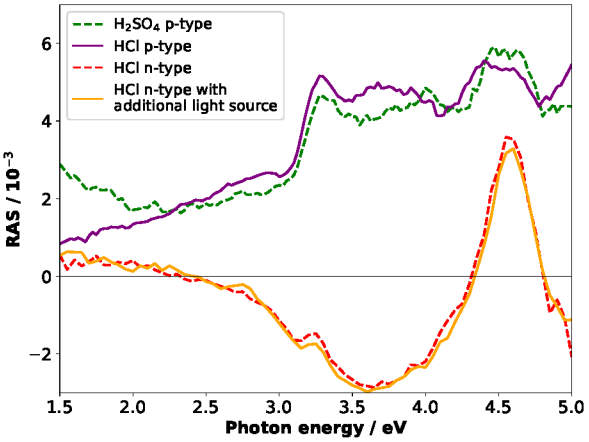

Figure 3.5: RA spectra of InP(100) for different conditions (different wafer doping, different electrolyte, different illumination conditions, see Figure 2.8). Here, the doping shows a major effect, the electrolyte a minor effect, and the bias illumination essentially none. Taken from publication A1

associated to p-InP-HCl and p-InP-H_2SO_4 interfaces (purple and green spectra, respectively) resemble each other. The electrolytes have the same concentration but different counter ions and slightly different pH, which influence the redox potential of H^+/H_2 and therefore slightly modify the position of the fermi level and the band bending (see Figure 2.8(b)). For this reason, the type of electrolyte has a minor effect on the related RA spectra. The most noticeable changes between the RA spectra provided by Figure 3.5 are in fact due to a difference in doping levels. Since E_{CB}, E_{VB} and E_F depend on the charge carriers concentrations, the doping level strongly impacts the electronic structure and therefore the optical properties at the interface.

3.2.5 Applications of RAS in Electrochemistry

RAS can be used as probe of the EDL and can easily be coupled with intrinsically EC characterization methods such as CA and CV. The correlation between RA spectra and cyclic voltammogramms can complement the understanding of EC processes from CV by providing access to charge, potentials, and chemical species with a sub-nanometer spatial resolution in the surface normal. For instance, some surface reconstructions are not distinguishable on the cyclic voltammogramm, because they involve non-Faradic process with very small change in capacitance of the EDL (see Fig. 2.7) and therefore very small charging currents. Thanks to RAS, the different surface reconstructions and surface steps are observable and distinguishable [73]. In this regard, since the first RAS implementation, there has been a rapid growth of the field, especially for RAS studies on metallic systems in EC environments or molecular films on metals. First ap-

plications of EC-RAS were dedicated to the study of different gold single-crystalline surfaces in aqueous electrolytes. These studies have outlined the relationship between surface charge and surface reconstruction and steps by measuring RA spectra for interfaces between Au(110) and aqueous electrolytes while potentials were applied to Au(110) [74–76]. Furthermore, RAS has allowed elucidating the impact of surface phases transition and surface roughening of Au(110) in sulfuric acid under applied voltage on the electronic structure [77]. In addition to the determination of surface states, surface roughness and surface phase transitions, it is possible to deeply investigate surface transformations, ion adsorption, and SEI formation processes by evaluating the spectral features during the transition from clean to adsorbate-covered surfaces in both liquid and non-liquid environments.

3.2.6 RAS and Adsorption Coverage

As shown in section 3.2.4, RAS probes the fingerprint of a S-L interface, for instance caused by the adsorption of anions from the electrolyte. Thus, the adsorption studies in a vacuum described in section 3.2.3 can be transferred to EC systems, e.g. electro-adsorption kinetics can be determined by fitting RA-transients measured at suitable energies with adsorption isotherm models. Under the assumption of a Langmuir-type adsorption process, the time-dependent adsorption coverage is proportional to the time-dependent RAS signal, following Equation (3.29) [72].

$$\theta(t) \propto \frac{RAS_{initial} - RAS(t)}{RAS_{initial} - RAS_{sat}} \propto 1 - \exp(\frac{-t}{\tau}) \tag{3.29}$$

The evolution of the literature on adsorption kinetics from gas-phase systems to EC systems studied by RAS is best illustrated by the case of copper. Extensive research on the Cu(110) surface has shown the sensitivity of RAS to molecular adsorbates orientation [78, 79], and its potential as a surface analytic tool for kinetic studies of molecule adsorption and desorption, as well as their memory effect on the surface [80–82]. Later on, the study of ad/desorption of molecules in the gas phase on Cu(110) has been extended to EC environments [83–85]. All studies have mainly investigated chlorine ions adsorption on Cu(110) in hydrochloric acid. Goletti et al. used EC-RAS together with EC-scanning tunneling microscopy (STM) and *ex situ* low energy electron diffraction (LEED) to identify the two-step process in the anodic and cathodic region of the CV [84]. They have ruled out the adsorption (desorption) of two different anions and have demonstrated that chlorine anions are involved in one adsorption (desorption) process followed by a surface reconstruction (deconstruction). The latter study on copper has performed EC-RAS on the same system with slightly different potential range and also shows together with

EC-STM the reversible formation of stripes and channels induced by chlorine ad/desorption [85]. In EC environment, when potentials are swept to the electrode at a speed that is low enough to not hinder any kinetic processes, very often, specific spectral features of RAS are directly correlated with the surface coverage. By fitting transient measurements with adsorption isotherm models, it is then possible to access kinetic and thermodynamic quantities [72, 85]. Vazquez-Miranda et al. have particularly demonstrated the extraction of the formation energy of adsorption of chlorine ions and lateral interaction parameter from a transient by fitting it with Frumkin-type isotherms [46, 85]. Furthermore, by correlating the current peaks measured in CV with the derivative of the RAS-transients, they could derive the dependency between applied potential duration and copper/chlorine chemical reactions.

3.2.7 EC-RAS setup

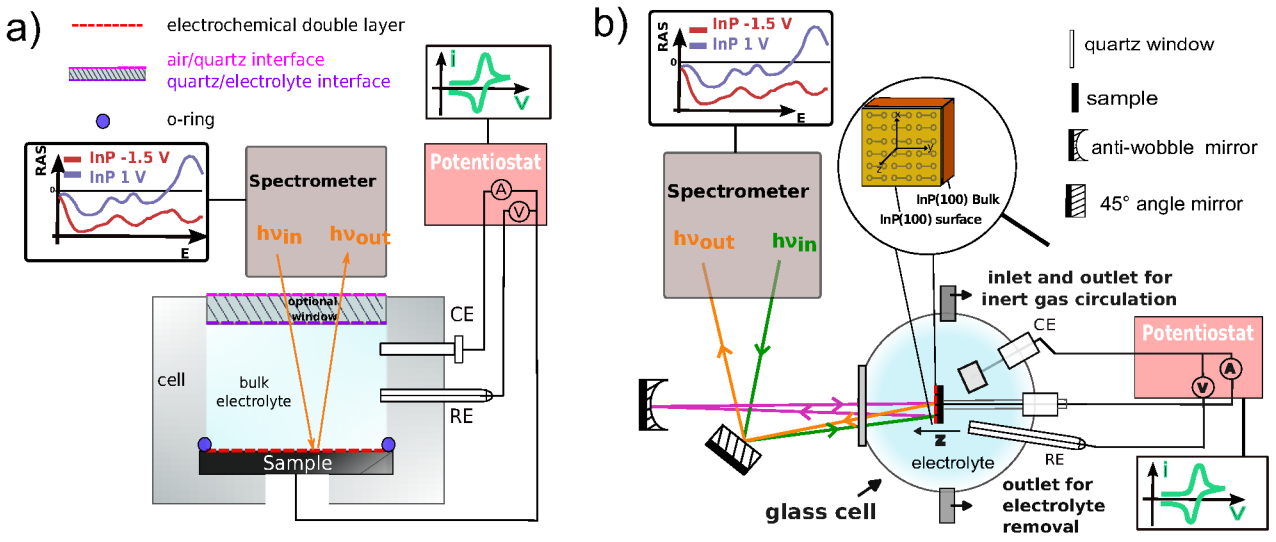

Figure 3.6: a) Cross-section of a horizontal EC-RAS setup. CE and RE refer to counter and reference electrode, respectively. Adapted from the publication A1 (Ref. [86]). b) Cross-section of a vertical EC-RAS setup, where the electrodes are inserted in a glass Schlenk cell. Adapted from the publication B2 (Ref. [87])

Figure 3.6a shows a typical horizontal EC-RAS setup, where the single-crystal, mounted horizontally in the cell, is in contact with the liquid electrolyte. The sample of interest (working electrode) is mounted together with a counter electrode and an optional reference electrode in a PEC cell filled with an electrolyte. Compared to conventional RAS setups, additional potential measurement artefacts in the RA spectrum have to be carefully considered in this configuration, e.g. artefacts from the liquid medium, as the setup now comprises media of at least three

different refractive indices, as opposed to two for a vacuum or gas-phase setup. If a quartz window is present in the PEC cell, as indicated in Figure 3.6a, it affects the refraction angle of the light at the air-quartz and quartz-electrolyte interfaces due the different refractive indexes of the media. Hence, the optical path between the spectrometer and the sample has to be carefully adjusted. Furthermore, if non-homogeneous mechanical stress is applied to the window, its dielectric tensor is no longer scalar, leading to a stress-induced contribution of the window to the signal. In principle, the PEC cell can also be used without a quartz window. The air-electrolyte interface, however, still changes the refraction angle of the light and hence modifies the light focal point. Also vibration damping might be needed in this case, as vibrations disturb the electrolyte interface and hence the optical path. Baseline effects can be largely compensated by adequate baseline correction using an optically isotropic standard such as an oxidised Si(100) sample, a reference of well-defined anisotropy such as Si(110), or the sum of two spectra where the sample has been rotated by 90° in between. Figure 3.6b shows a slightly different setup compared to the one of Figure 3.6a. Here, the sample is mounted vertically in a glass Schlenk cell. The advantage of the vertical setup over the horizontal setup is the possibility to work in clean condition and under inert gas circulation, and the ability to remove the electrolyte while a potential is applied to the electrode. Hence, electrochemically prepared surfaces whose lifetime in aqueous solution is very short can be stabilized in the photoelectrochemical Schlenk-cell setup (PS-cell setup), and be reliably transferred for further surface characterization in an inert glovebox(GB) atmosphere or a UHV chamber. To perform RAS measurement, a mirror is placed below the spectrometer at an angle of 45° and in front of the sample. The incoming linearly polarized light is reflected on the mirror and reaches the sample (green light path). After the first reflection on the surface, the light reaches the anti-wobble mirror (AWM) (pink light path) for correction of an eventual imperfect vertical position of the sample. After the second reflection on the electrode, the light is reflected again on the 45° angle mirror and reaches the detector of the spectrometer (orange light path).

4 Objectives

Reference Systems for Method Development

The first objective of this thesis is to develop EC-RAS as a reliable probe of the EDL, unravelling processes occurring at the very solid–liquid interface. The method will first be demonstrated on noble metal-aqueous electrolyte interfaces (see publication A1), and then be extended to semiconductor-electrolyte interfaces. For the former, gold-acidic electrolyte interfaces are investigated to reproduce previous studies and to establish the experimental setup (see publication A1). Concerning the latter, well-defined surfaces of wafer-based semiconductors in aqueous electrolytes are used as a starting point. To establish the experimental setup and a reference basis for further more complex systems, the semiconductors InP(100) is first investigated in acidic aqueous electrolytes. The adequate parameters of the system required to prove that surface ordering can be conserved during electrochemical etching/deposition are determined.

To find out the configuration of a semiconductor surface in contact with electrolyte under applied potential, the experimental spectra are correlated with computational spectra for an atomistic view. Additionally, XPS is used as an *ex situ* characterization techniques to verify the surface composition. This constitutes a basis to understand the origin of the anisotropy oscillation of InP in contact with an electrolyte [86] . Time-resolved measurement under different applied potential are deeply analyzed to disentangle the different processes occurring at the EDL such as ion adsorption, LEO, and surface reconstruction with a sub-nanometer spatial resolution and time resolution of about 10 ms. Ultimately, to show that RAS, as a linear optical technique, can quantify processes at the semiconductor-electrolyte interfaces, time-resolved measurements under applied potential are fitted with adsorption isotherm models.

Hence this section shows that EC-RAS can monitor *in situ* surface corrosion processes and electrochemical surface passivation processes, also called “surface functionalization”.

Application for more Complex III-V Semiconductor Compounds

To transfer the applicability of RAS to more complex semiconductor-liquid systems used for solar-water-splitting applications, the wet etching of a protective GaAs layer on top of an AlInP layer is controlled with *in situ* RAS in a well-ordered, precise and reproducible manner. Oscillations of the time-resolved RAS during wet etching are used as an etch depth and etch rate indicator. Furthermore, the presence of the oscillation emphasizes the possibility for a layer-by-layer etching/deposition control during (photo)-electrochemical conditioning of the solid-liquid interface with *in situ* RAS.

With the reference system established in the previous section, EC-RAS is used to study the initial corrosion and interaction with ions of more advanced material systems, i.e. AlInP in HCl and in aqueous $RhCl_3$. Especially, elucidating the nature of the III-V oscillations during open circuit measurements in acidic electrolyte and under external illumination is expected to help improving the surface design of solar cells for solar water splitting, and to promote the understanding of corrosion processes [21].

Thus, thanks to RAS, an approach for the first steps of the *in situ* preparation of ordered surfaces in aqueous electrolyte is provided. These ordered surfaces are required for RAS studies, ease the comparability with the model, and serve as a starting point for further surface modifications.

Potential Tool for Battery

in situ EC-RAS combined with non-aqueous systems is more challenging than for semiconductor-aqueous electrolytes because the interface is very often not well-defined, inhomogeneous, and extended to a solid electrolyte interphase (SEI). Furthermore, the chemical nature and the electric double layers of the electrolytes used in batteries are more complex than the aqueous electrolytes used in the previous sections. Nevertheless, the solid–liquid phase boundary also determines many of the relevant properties. For instance, ion adsorption can be blocked by SEI or dendrite (undesired extra growth) formation can induce detrimental conduction pathways. In the case of non-aqueous Al batteries, the presence of the native oxide layer on top of the Al anode currently limits the choice of electrolytes to highly corrosive ionic liquids, mainly [EMImCl]:$AlCl_3$. To develop and understand, respectively, the design and the properties of the Al-[EMImCl]:$AlCl_3$ interface with and without applied potentials, the latter is studied by *in situ* EC-RAS.

5 Results and Discussion

5.1 EC-RAS Method Development

The results from this section are partially taken from the publication B1 and the manuscript in preparation B4.

RAS has already proven to be an essential instrument for the preparation of well-defined surfaces in epitaxial growth chambers and the study of water adsorption in UHV experiments [54]. Currently, its application is being extended to the scrutinizing of electrochemical processes in realistic environments. Since only few studies have reported RAS fingerprints of metals in acidic aqueous electrolytes, an adequate reference system must first be chosen to establish the method for semiconductor-aqueous electrolyte systems. InP is an important material for optoelectronic devices, and a major component of III-V semiconductor absorbers in multi-junction solar cells used for solar water splitting [88, 89]. While its high electron velocity renders it attractive over other III-V semiconductors, InP is also subject to corrosion, which hinders its performance as a photo-cathode for photoelectrochemical applications. Therefore, prior to its use in solar water-splitting devices, its surface must be protected against corrosion, a current challenge that is being addressed e.g. by electrochemical surface designs [88]. Regarding the implementation of EC-RAS, the reactivity of InP in electrochemical environments and its availability in wafer quantities makes it a suitable candidate. A previous study on *in situ* electronical and electrochemical passivation of InP surfaces and derived compounds for water splitting electrodes have shown that the interfaces formed are usually amorphous and present a thickness of about 10 nm [21]. Nevertheless, the limit in time resolution and the lack of structural information leaves room of improvement in precise control and comprehension of the electrochemical interface in real-time with EC-RAS. For this purpose, the potential-dependent structural changes of the InP–HCl and InP–H_2SO_4 interfaces are monitored *in situ* with RAS.

Figure 5.1 displays the fingerprints of InP(100) immersed in low concentration of HCl and H_2SO_4. The red spectra correspond to the epi-ready InP(100) surfaces, i.e. the surfaces before electrochemical treatment that are terminated with an epitaxially grown oxide. Two characteristic peaks at 3.25 eV and 4.55 eV can be observed, originating from surface-modified bulk trans-

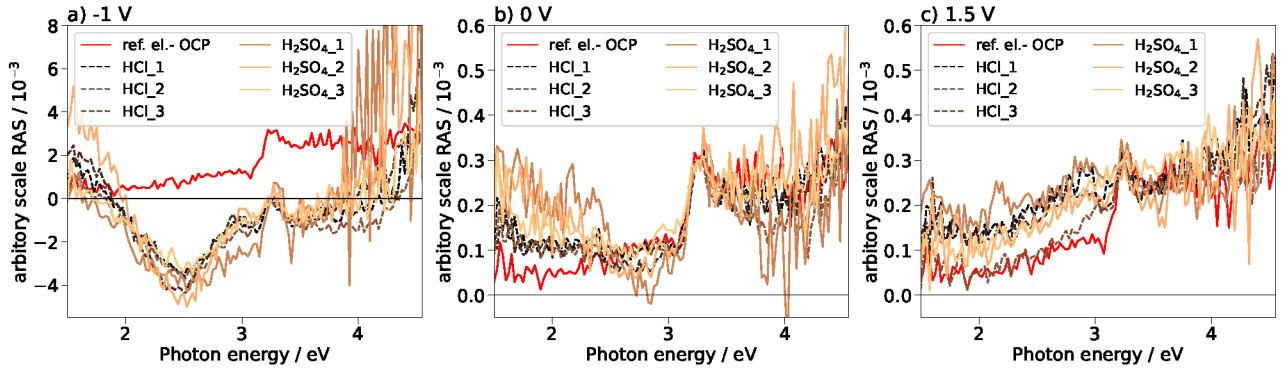

Figure 5.1: RAS spectra at -1 V (a), 0 V (b), and 1.5 V (c) of the InP(100) surface in 0.01 M HCl (dashed line) and 0.01 M H_2SO_4 (solid line) solution, normalized to the peak at 3.25 eV. The red spectrum corresponds to the epi-ready InP(100) immersed in 0.01 M HCl at open-circuit potential.

itions [54]. The anisotropy at lower energies is usually more surface sensitive [90–92]. The low signal-to-noise ratio at high energies (>4 eV) is due to light absorption from the electrolyte at high energies and the slight differences between the two red spectra is caused by an imperfect setup alignment/baseline correction and/or by the influence of the electrolyte (see section 3.2.7). To understand both the influence of the potential and the influence of the counter ion on the anisotropy, the two InP-electrolyte systems are studied under potentiostatic conditions, i.e. at -1 V, then 0 V, and finally 1.5 V vs. Ag/AgCl. The resulting spectra are plotted in Figure 5.1 together with the reference spectra described above. The spectra are normalized with respect to the anisotropy at 3.25 eV to bypass imperfect baseline correction and thus to observe differences only arising from the electrolytes. The qualitative comparison of the spectra in Figure 5.1a-c leads to the conclusion that both electrolytes give similar spectral signatures. Therefore, either the applied potential and the hydrogen adsorption play a dominant role in the obtained surface structures, or the adsorption of the counter ions lead to similar RAS fingerprints. Since a peak starts to build at around 2.5 eV at 0 V only in H_2SO_4, it indicates that at this potential, the different adsorption behavior due to the different nature of the two anions (Cl^- and SO_4^{2-}) is detectable with RAS.

Comparing the spectra without differentiating the electrolytes, the RAS spectra taken at a cathodic potential (-1V) develop a pronounced negative peak for photon energies below 3 eV and for higher energies the spectra shift to slightly more negative anisotropies. Additionally, the peak at 4.55 eV is much more intense at -1 V than at OCP, whereas the spectra taken under 0 and -1.5 V are hardly different from InP(100) at OCP conditions. Interestingly, the noticeable ordered surface structure at cathodic potential does not exactly correspond to the spectral shape of the main characteristic surface reconstructions of InP(100), e.g. the ‘P-rich’ p(2 × 2)/c(4 × 2) re-

construction or the mixed-dimer 'In-rich' (2 × 4) reconstruction. While reconstructed InP(100) surfaces prepared in metal organic vapor phase epitaxy (MOVPE) reactors exhibit a negative anisotropy at around 1.8-2 eV, associated with intradimer electronic transitions, here the negative anisotropic peak at cathodic potentials is located at about 2.5 eV. Therefore, the surface phase is expected to involve adsorbed ions from the electrolyte.

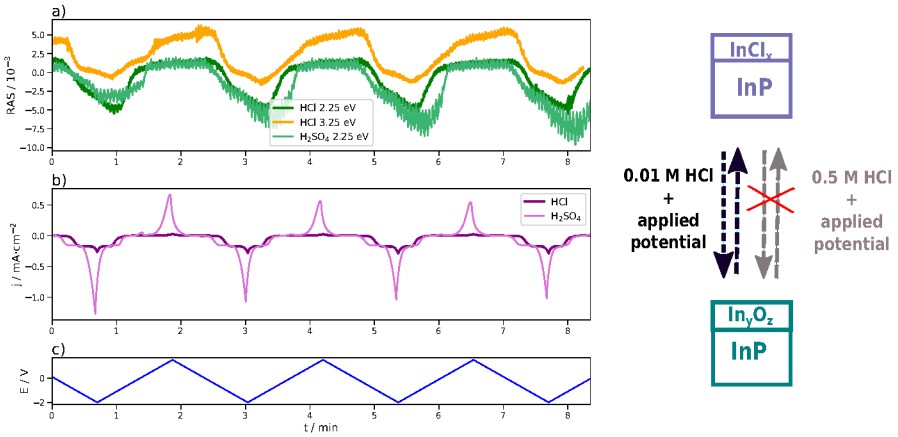

Figure 5.2: (a) Transients acquired upon CV of InP(100) in 0.01 M HCl and in 0.01 M H_2SO_4, (b) current from CV over the time (c) Potential plotted against Ag/AgCl over the time. Scan from OCP towards -2 V and than to 1.5 V for 3 cycles, with a scan rate of 50 mV/s.

The first question arising from the previous results is whether the interfacial restructuring is reversible or not. To that extend, time-resolved measurements (i.e. transients) are acquired at specific energies during cyclic voltammetry (CV) measurements and are shown in Figure 5.2. Both InP-HCl and InP-H_2SO_4 present oscillating transients whose period matches the one of the potential displayed in Figure 5.2c. In particular, the emergence of an anisotropy at 2.25 eV in the cathodic potential range that has been observed in the RAS spectra also clearly appears on the transient and is reversible. However, when going from cathodic toward anodic potentials during the first cycle, the anisotropic values at 3.25 eV are higher than the initial values. This suggests that after its dissolution in the electrolyte from OCP to negative potentials, the surface oxide layer is reformed, potentially with a higher degree of ordering. Furthermore, although the RAS spectra and transients of InP-HCl and InP-H_2SO_4 systems under electrochemical conditions evolve very similarly, the InP-HCl electrochemical interface shows a higher degree of reversibility: the oscillations of the transient at 2.25 eV remain identical over the cycles in HCl, whereas in H_2SO_4, the anisotropy at cathodic potentials increases over the cycles. When correlating the transient with the current density in Figure 5.2b, there is hardly any oxidation peak in HCl, while in H_2SO_4 one can see a small oxidation peak in the first cycle followed by a very pronounced oxidation peak, present on all other cycles. Previous studies showed that in H_2SO_4, InP is more

prone to form metallic In in the cathodic region, which is additionally passivated with phosphate species in the anodic region [93, 94]. In HCl, In further reacts with chloride in the cathodic region to form $InCl_x$, which then partially dissolves in the electrolyte at anodic potentials. At a high concentration (0.5 M HCl), this process is no longer reversible, the reflectivity decreases, and a decreased interface ordering with ongoing cycles appears on the transients due to the formation of an amorphous, thicker and opaque $InCl_x$ surface film (see publication B1). In contrast, since the process is fully reversible in 0.01M HCl, it involves the building and complete removal of a monolayer upon electrochemical cycling.

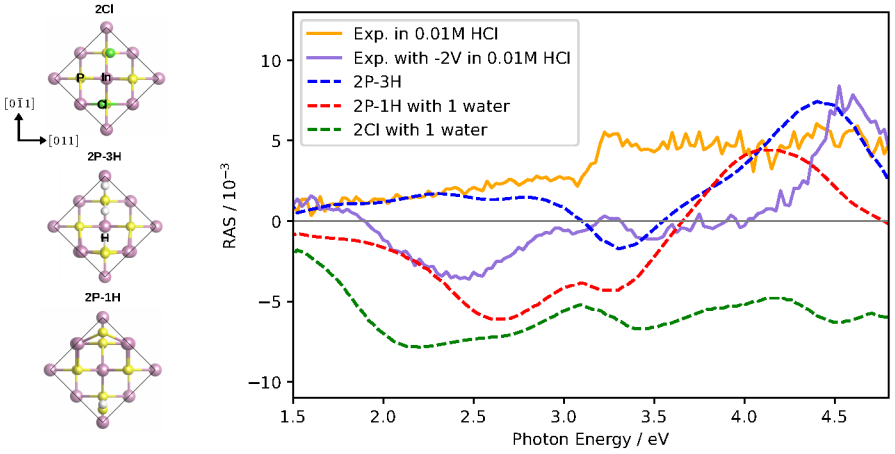

Figure 5.3: Left: Top view of the fully Cl-covered surface, as well as the surface with one and three adsorbed hydrogen atoms on top of InP(100) (2Cl, 2P-1H, 2P-3H, respectively). The black line indicates the surface unit cell. Right: Computed (dashed lines) and experimental (solid lines) RAS of the InP(100) in contact with 0.01 M HCl solution under the applied potential of -2 V.

Thus, due to a higher reversibility of the process, HCl is a more suitable electrolyte to investigate the well-ordered interface formed in the cathodic region, where chloride ions and protons are the main species involved from the electrolyte side. Furthermore, chloride ions are less complex to compute than sulfate ions, which is an important argument since the interpretation of experimental spectra requires their comparison with theoretical spectra. Thus, computational RAS spectra of InP surfaces with different chloride and hydrogen coverage are determined and displayed in Figure 5.3. No theoretical spectrum reproduces the experimental ones perfectly (purple curve). The latter is rather a superposition of the green and red curve. This suggests that the experimental spectrum obtained at cathodic potential corresponds the best to an In-rich surface decorated by chloride and hydrogen atoms. However, in contrast to the ideal computed model, the electrochemical system involves a higher degree of complexity due to the applied potential and the bulk electrolyte, that can influence the anisotropic properties at the interface. Besides, minor discrepancies between the experiment and calculations in terms of the peak

energies have to be expected due to the underestimation of the band gap usually observed in DFT [95]. Furthermore, defects, oxidation, and domain boundaries on the surface are neglected in computational RAS. An additional important issue is that contributions from distinct processes such as surface reconstruction, ion adsorption and surface film formation can lead to similar RAS spectral signatures. Therefore, unraveling the connection between each process and its spectral signature is crucial to fully interpret a RA-spectrum originating from an electrochemical interface [96]. Especially for ultra-thin interface layers, it is important to understand to what extent the surface created at a certain potential can be stabilized in the absence of applied potential and/or electrolyte. Hence, a second question arises concerning the stability

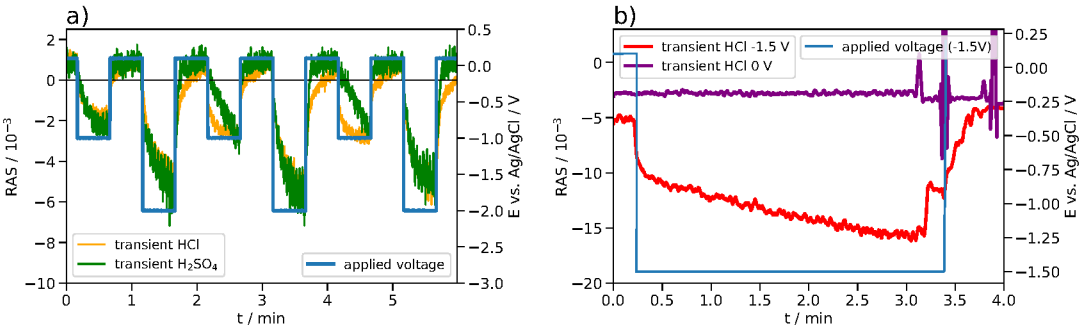

Figure 5.4: a) Potential-steps and transient measurements at 2.25 eV of InP(100) in 0.01 M HCl and in 0.01 M H_2SO_4. b) transients taken in 0.01 M HCl at 2.25 eV under a step potential from OCP to 0 V (purple curve) and OCP to -1.5 V (red curve). The potential is plotted against Ag/AgCl.

of ordered interfaces, which is investigated by acquiring transients at 2.25 eV during potential pulses measurements, as shown in Figure 5.4. The experiment demonstrates that when a cathodic potential-step is applied, the RAS amplitudes of the transient spectrum decrease toward a negative extremum in equilibrium, but with different time constants for the different electrolytes and applied potentials. Especially for HCl at -1 V, there appears to be a fast process in addition to a slower signal decrease, while the transient in H_2SO_4 decreases more slowly. After setting the potential back to OCP, the anisotropy in H_2SO_4 changes back to the original value at OCP, while the process is slower in HCl. One of the two processes observed in HCl could be related to the formation and dissolution of the above-mentioned $InCl_x$ layer, which is not present for the H_2SO_4 case. Yet, this layer involves a very fast desintegration process. Consequently, as soon as the externally applied potential is switched off, the interface disintegrates in the electrolyte and cannot be further characterized by *ex situ* techniques. To overcome this problem, a PS-cell setup combined with the RAS setup presented in Figure 3.2.7b of section 3.2.7, is used, allowing (photo)electrochemical surface functionalization under optical *in situ* control (see section 3.2.7). For this application, the main advantage of such a cell is the ability to remove the

electrolyte while a potential is applied to the electrode and under inert gas circulation. Hence, electrochemically prepared surfaces whose lifetime in aqueous solution is very short can be stabilized in the PS-cell setup, and be reliably transferred for further surface characterization in an inert glovebox (GB) atmosphere or a UHV chamber.

For this purpose, the following protocol, under constant RAS monitoring via time-resolved measurements is selected: first, the InP electrodes are pre-cycled in 0.01 M HCl at 20 mV/s for 10 cycles in the PS-cell (Figure 5.7a). A subsequent fixed potential (chronoamperometry (CA)) is applied (-1.5 or 0 V vs. Ag/AgCl) to the electrode. The transition in potential from the open circuit potential (OCP) to -1.5 or 0 V is illustrated by the red curve in Figure 5.4b, occurring approximately at 0.20 minutes. After 3 minutes of maintaining the fixed applied potential, the electrolyte is purged from the cell under nitrogen gas circulation while maintaining the potential. Upon the cessation of contact between the InP electrode surface and the solution, the CA measurement is terminated. This is observable on the red curve of Figure 5.4b, occurring at around 3.15 minutes. The decrease in the RAS signal indicates that the surface film already starts to disintegrate in the PS-cell.

Immediately after electrolyte removal, the electrochemical cell, filled with nitrogen gas, is transferred to a GB for subsequent *ex-situ* RAS and XPS characterizations of the InP surfaces. The InP surfaces prepared under different applied potentials and transferred to the GB are first analyzed by RAS. Figure 5.5a contrasts the RAS spectra acquired in the GB from the surfaces after electrochemical preparation with a reference spectrum from an as-received InP wafer. The spectra are vertically offset to facilitate their comparison. The spectrum of InP prepared at 0 V is very similar to the reference spectrum, whereas that prepared at -1.5 V exhibits deviations from the reference spectrum, notably featuring an anisotropic peak at approximately 2.5 eV.

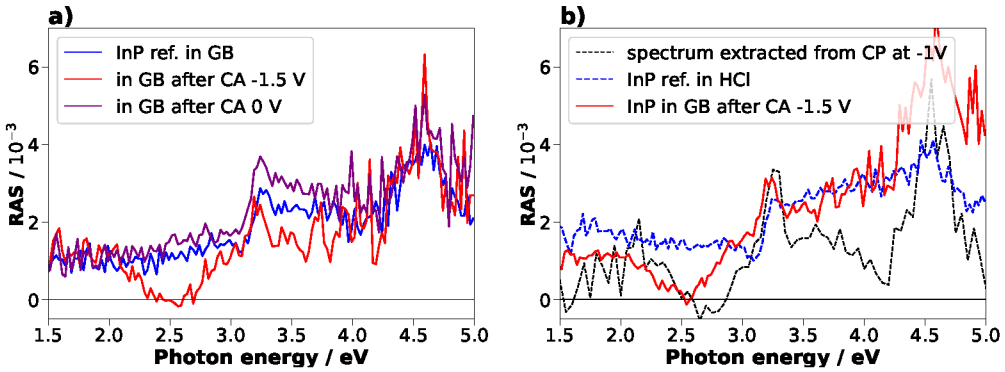

Figure 5.5: RAS spectra of InP surface before, during (PS-cell), and after (GB) electrochemical preparation.

Since the OCP values before CA measurements were between -70 and -30 mV, an applied

potential of 0 V is located at the beginning of the anodic region. In this region, the $InCl_x$ film is expected to not be stable and to dissolve in the electrolyte, leaving behind an InP surface that re-oxidizes. This would explain why the purple spectrum taken at 0 V vs. OCP resembles the reference spectra taken in GB and in HCl. Concerning the InP surface prepared at -1.5 V, where the $InCl_x$ film is assumed to be formed, the corresponding spectrum taken in GB resembles the black spectrum taken in the electrolyte when the applied potential is about -1 V. It indicates that the ordered interfacial film formed at cathodic potential during the CV and the CA could be partially preserved during and after the transfer to the GB. The InP surfaces are further characterized by XPS to verify the interpretation of the RAS spectra.

Figure 5.6 compares the XPS spectra of In3d, P2p and Cl2p core levels of the InP surfaces: without any electrochemical treatment ((a), InP ref, treated in HCl and cathodically polarised at -1.5 V vs OCP (sample (b)), and treated in HCl and anodically polarised at 0 V vs OCP (sample (c)). Figure 5.6a shows that the oxide layer covering the InP reference spectrum is $InPO_4$. Since its RAS spectrum in GB (Figure 5.5a, blue spectrum) and in the electrolyte at OCP (Figure 5.3, orange spectrum) are very similar, the $InPO_4$ is expected to be conserved when InP wafers are immersed in solution, before any electrochemical treatment is done. The peaks of the different core levels are qualitatively similar for samples (b) and (c) compared to the reference sample (a), i.e. the peak responsible for $InPO_4$ observed on (a) vanished on (b) and (c), and a peak corresponding to $InCl_x$ formed. To understand why samples (b) and (c) present different RAS spectral signatures, a quantitative analysis of the XPS spectra is required. For this purpose, Table 5.1 shows the relative areas of the XPS peaks normalized to the In3d peak.

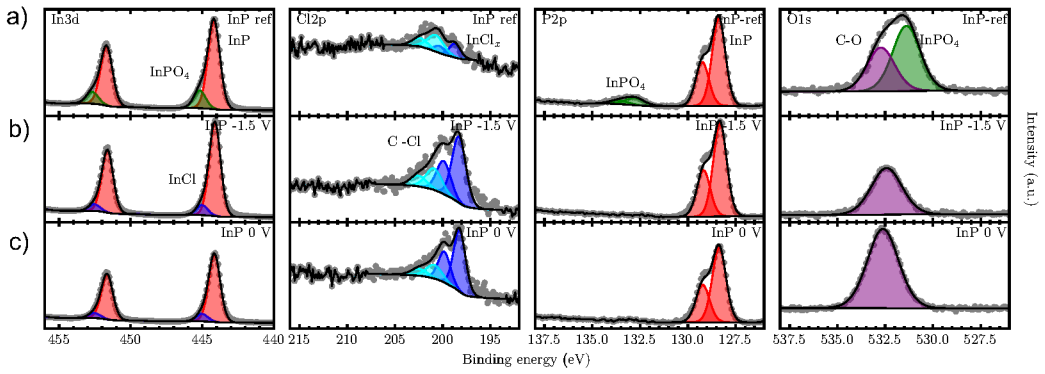

Figure 5.6: XPS analysis of In3d, P2p, and Cl2p core levels for InP electrodes a) without any electrochemical treatment (InP ref), b) treated in HCl and cathodically polarised at -1.5 V (InP -1.5 V) and c) treated in HCl and anodically polarised at 0 V (InP 0 V). *The XPS results are conducted by Stefan Fuchs from the group of Prof. Fichtner in the POLiS cluster at the University of Ulm.*

The spectra of sample (c) show an increase in P, O, and Cl content compared to sample (b).

Table 5.1: Relative peak areas of the XPS peaks normalized to the peaks of In3d

	InP-ref	InP -1.5 V	InP 0 V
O1s	1.20	0.66	1.41
In3d	1	1	1
P2p	0.98	1	1.17
Cl2p	0.05	0.13	0.19

In addition, the peak ratio is exactly P2p/In3d=1 for sample (b), and 1.17 for sample (c). It suggests, that applying a potential either at -1.5 V or at 0 V right after performing CV partially preserves the surface ($InCl_x$) created during the CV, but not to the same degree depending on the condition of the CA. At 0 V, not only an $InCl_x$ phase is present, but eventually also a P-Cl or a P-O-Cl phase, whereas at 1.5 V, only a $InCl_x$ phase may be formed. Translated to the RAS spectra, the occurrence of the anisotropic peak at 2.5 eV in the cathodic region that could be conserved after transfer to the GB may originate from the formation of an ordered and stabilized phase of adsorbed chloride ions. In the anodic region, the surface does not recover back to its initial phase $InPO_4$, but the disintegration of the anisotropic peak at 2.5 eV implies a partial dissolution of the $InCl_x$ phase, associated with the occurrence of a P-Cl or a P-O-Cl phase which is either amorphous or isotropic.

The XPS results confirm that RAS probes the fingerprint of an electrochemical S-L interface, for instance caused by the chemisorption of electrolyte species. Thus, under equilibrium conditions at for instance certain applied potentials/concentrations, the anisotropy profile can be fitted with the adsorption isotherm models presented in section 2.3.2. This can provide information about the adsorption energy of an isolated ion and the character of the lateral interactions between the adsorbed ions. Once the adequate adsorption model is found, process lifetimes at the interface can also be assessed by fitting time-resolved RAS measurements with kinetic models. The latter are derived from adsorption isotherm models, allowing the determination of kinetic parameters, as shown in section 3.2.6. Since sweep rates between 5 mV/s and 20 mV/s give qualitatively similar current and transient profiles (see appendix, Figure 7.3), no processes are completely kinetically hindered at a scan rate of 20 mV/s. Hence, the data fitting is applied to a transient recorded upon CV measured at a scan rate of 20 mV/s. 2.25 eV is selected because at this energy, the anisotropy is the highest when a cathodic potential is applied to the InP sample. Furthermore, according to the RAS calculation, the chlorinated In-rich InP(100) and P-H-terminated In-rich InP (100) surfaces develop a peak anisotropy around 2.1 eV and around 2.6 eV, respectively (Figure 5.3). Besides, previous studies have claimed that surface-related features are observed in the lower energy region of the RAS spectra [90–92].

As previously demonstrated, when the potential is swept from OCP towards a more negative

potential (-0.553 V vs Ag/AgCl) at low HCl concentration (0.01 M HCl), InP is reduced to Indium metal, which then reacts with chloride to form $InCl_x$. However, in the cathodic potential range of the CV shown in figure 5.7a, chloride adsorption is expected to compete with hydrogen adsorption. The theoretical phase diagram of an InP(100) surface in HCl at pH=2, displayed in Figure 7.4 in the Appendix, provides which phase is the most stable at a certain applied potential. It attests that $InCl_x$ is present at the surface from 1 V to about -0.55 V vs. Ag/AgCl. Around this potential, a clear transition between chloride and hydrogen covered surface occurs. When increasing the potential from -0.55 V further in the cathodic direction, hydrogen adsorption starts. The fact that the anisotropy increases at 2.5 eV when the applied voltage is more negative suggests an incremental LEO from the charging of the EDL. This LEO can arise from the electric field generated by the potential itself in the material (bulk LEO) and the ion adsorption resulting from this potential. Consequently, it is assumed that surface coverage θ increases as cathodic potentials increase. HCl is a strong acid that dissociates almost completely in water. Therefore, at the surface, HCl does not undergo a dissociative adsorption but hydrogen and chloride are adsorbed as single entities on the surface. Given that $InCl_x$ forms experimentally on InP(100), chloride is expected to adsorb preferentially on In sites [97], whereas the stable hydrogenated phase in the theoretical phase diagram (Figure 7.4, Appendix) shows that hydrogen preferably adsorbs on P sites. Therefore, in this case study, and according to the theoretical phase diagram, protons and chloride are considered to adsorb on the P and In sites of the surface, respectively. Furthermore, to simplify the the adsorption isotherm models, the concentrations of the bulk is regarded as constant, and the presence of the solvent is not considered.

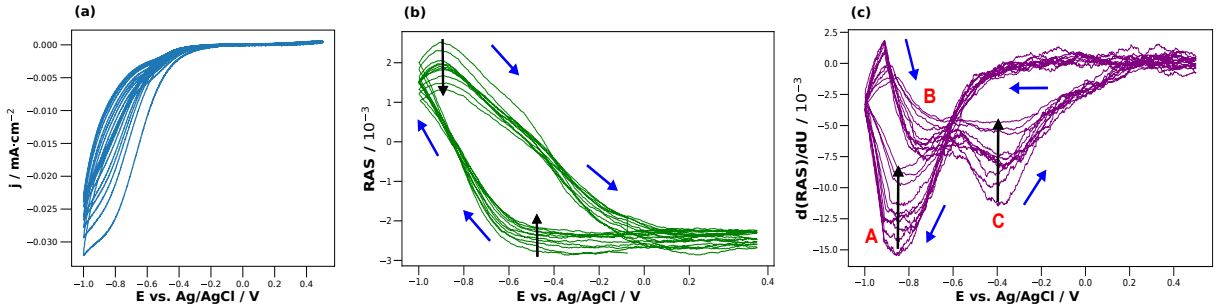

Figure 5.7: (a) CV of InP(100) in 0.01 M HCl. The potential is plotted against Ag/AgCl, and scanned from OCP towards -1 V, then to 0.5 V and back to OCP, for 10 cycles, with a scan rate of 20 mV/s. (b) Cyclic transient and (c) cyclic transient derivative measured at 2.6 eV in parallel to the CV. The anisotropic values are filtered with a Savitzky-golay filter to increase the signal-to-noise ratio. The blue arrows indicate the scan direction while the black arrows indicate the increasing cycle number.

A recent study showed that to decouple the different Faradic processes involved during a CV measurement, the derivative of the transient with respect to the potential (cyclic transient de-

rivative) should be considered rather than the cyclic transient (transient measured during CV), because the RAS an the RAS derivative are directly proportional to the charge and the current delivered during the CV, respectively [85]. The cyclic transient and its derivative measured during the CV shown in Figure 5.7a are displayed in Figure 5.7b and c, respectively. The processes occurring during the reduction scan are associated with only one strong anisotropy peak (peak A, Figure 5.7a) on the transient derivative and one reduction peak on the CV, while during the back scan, the CV shows one peak with a small shoulder at around -0.55 V and 2 noticeable peaks (B and C, Figure 5.7c-d) are present on the cyclic transient derivative. The fact that peaks are present on the RAS derivative and not clearly visible on the CV indicates that some Faradic processes are better observed on the transient derivative. The characteristics of the transient derivative can be associated with the one of the phase diagram: the onset of peak A (0.4 V) should correspond to chloride desorption, peak A to hydrogen adsorption, peak B to hydrogen desorption and peak C to chloride adsorption. ad-/desorption occurring in the cathodic direction appear as a one-step process whereas ad-/desorption in the reverse cathodic direction involves a two-step process. Thus, the RAS-potential region of each peak are fitted separately with the Langmuir, Frumkin, and Temkin electro-adsorption isotherms presented in section 2.3.2.

Table 5.2: Resulting values from the fit of the last cycle from the cyclic transient shown in Figure 5.8

		restricted		
	peak A (Frumkin)	peak A (Temkin)	peak B (Temkin)	peak C (Temkin)
ϵ_{ads}(meV)	-303	-387	-317	-329
error ϵ_{ads} (meV)	0.8	0.8	2	1
g (meV)	262	437	354	354
error g (meV)	25	1	1	2

The fits of the adsorption process, depicted in Figure 5.8a yield to a Frumkin type behavior over the all cathodic curve (between -1 and -0.2 V). Assuming that mid-values of θ are obtained for a restricted cathodic potential range, the transient data should follow a Temkin isotherm is in this range. This is confirmed in Figure 5.8b, where the Temkin model fits closer to the transient data than the Frumkin one between -1 and -0.55 V. The two-step desorption processes (peaks B and C), shown in Figure 5.8c-d, clearly correspond to Temkin isotherms. Hence, the data fitting shows that all processes are more complex than a simple Langmuir process, and involves adsorbate interactions. For each process, the energy of adsorption of an ion lies between -400 and -300 eV, and the lateral interactions are repulsive. Interestingly, the energy of the lateral interactions for the Temkin fits is stronger than ϵ_{ads}, meaning that the former interactions are stronger than the interaction of the ions with the surface. This could potentially limit the applic-

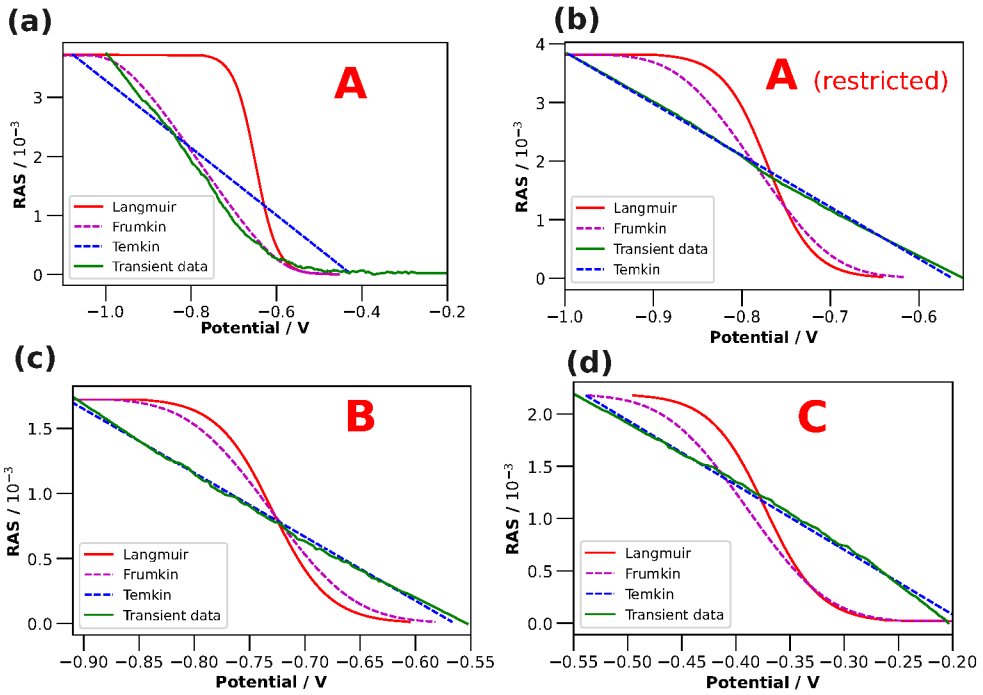

Figure 5.8: Zone A with all adsorption range (a), zone A with restricted adsorption range (b), zone B (c), and Zone C (d) of the last cycle of the cyclic transient shown in Figure 5.7b fitted with Langmuir, Frumkin, and Temkin adsorption isotherms given in Equations (2.23),(2.24), and (2.25), respectively. The Transient data are y-shifted to start or end at 0. Furthermore, they are filtered with a Savitzky-Golay filter.

ability of the Frumkin and Temkin models in this study case. Alternative models that account better for strong interactions or specific ion adsorption mechanisms might be more appropriate for fitting the experimental data.

As a result, in equilibrium conditions and within a potential range of -1 to -0.2 V, the anisotropy of the InP(100) surface in 0.01 M HCl exhibits non-Langmuir behavior. This indicates that kinetic models derived from non-Langmuir isotherms are necessary to analyze time-resolved RAS measurements conducted under constant applied potentials, thereby operating under non-equilibrium conditions. However, deriving such non-Langmuir models, such as Frumkin and Temkin, is more specialized and less common compared to the derivation of models based on Langmuir isotherms. Consequently, for the subsequent experiment, a Langmuir model is applied. Figure 5.9a shows transient measurements at 2.25 eV recorded during CA measurements (Figure 5.9b-c) at -0.75 V and -1 V. More precisely, the OCP was first measured for 60 s, followed by 1100 s of CA measurement, and finally the OCP was measured again for 800 s. In

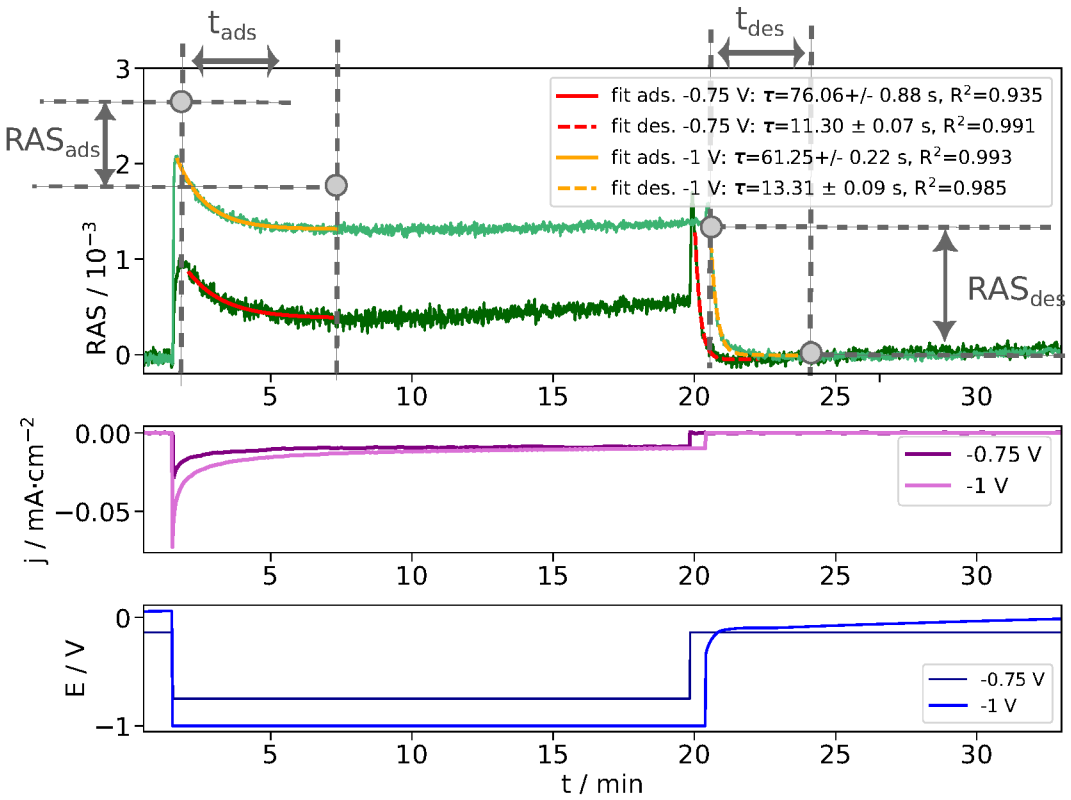

Figure 5.9: CA and transient measurements at 2.25 eV in 0.01 M HCl. The anisotropy values are filtered with a Savitzkys-Golay filter and shifted on the y-axis to start at 0. Parts of the transients are fitted with Equation-type (3.2.6). *Masterthesis of Marco Flieg [98].*

Figure 5.9a, as soon as the potential is switched on, the RAS values jump to higher numbers

and then decrease slowly until reaching a plateau. This exponential decay of the anisotropy corresponds to the adsorption process. When the potential is switched off, the transient values first drop steeply before decreasing slowly until reaching a second plateau, which corresponds to the desorption process. By measuring transients under short potential-pulses (see Figure 7.5 in the Appendix), it is possible to de-convolute the anisotropy originating from the bulk LEO and the anisotropy originating from the adsorption/desorption process. This shows how soon the adsorption/desorption process actually begins after the potential is switched on/off. The transient-potential pulses measurement indicates that the first 1.5 seconds of applied voltage lead to a rather symmetric spike on the transient, attributed to a charging of the electrode (bulk LEO). The adsorption process, identifiable when the spike gets asymmetric, starts about 2 s after the potential was switched on. The zone from the beginning of the adsorption to the RAS value where the derivation of the transient is zero, is defined as ΔRAS_{ads}, and the time in between is denoted as t_{ads}.

For the desorption, disentangling applied potential and the actual start of the desorption is more complex. Nevertheless, it is understandable as followed: the steep anisotropy fall occurring when the potential is switched off is associated with a discharging of the electrode (bulk LEO). Then, the adsorbates start to desorb and the transient values decrease more slowly. The first steep fall will therefore not be taken into account for the determination of the desorption. To determine the actual onset of the desorption, the values are fitted with a linear function. The beginning of the desorption is determined when the linear regression coefficient of the fit becomes lower than 0.995. With the ongoing desorption, the transient values decrease slowly until the final RAS value is reached. The period between the beginning of the desorption and the RAS value where the derivation of the transient is zero is defined as t_{des}, and the corresponding zone on the y-axis is defined as ΔRAS_{des}.

Concerning the adsorption part, the higher the potential, the higher the RAS jump, and the higher ΔRAS_{ads}. For the desorption, similar to the adsorption, the higher the potential difference between applied potential and OCP, the higher the RAS drop, and the higher ΔRAS_{des}. Interestingly, the shape of the transient closely resembles the shape of the current, but the applied potentials of -1 and -0.75 V lead to different anisotropy plateaus, while the current densities converge to the same value. As an example, transient data corresponding to the adsorption and desorption parts are fitted with pseudo-first order kinetic model derived from a Langmuir isotherm (3.2.6). The adsorption fits yield rate constants of 0.013 s^{-1} for -0.75 V and 0.016 s^{-1} for -1 V, whereas the desorption fits yield rate constant of 0.088 s^{-1} for -0.75 V and 0.075 s^{-1} for -1 V. Hence, the desorption rates are higher than the adsorption one, which can be explained by the adsorbate-adsorbate interaction strength: in the potential region between -1 and -0.55 V, the fit of the desorption process leads to weaker adsorbate-adsorbate interactions than the one of the adsorption process (see Table 5.2). Thus, the desorption is expected to be faster than the

adsorption. Furthermore, the potential-steps of -0.75 and -1 V result in slightly different values of the desorption and the adsorption lifetimes. It indicates that a more cathodic potential leads to a faster adsorption process and a slower desorption process. In conclusion, while the Langmuir model shows promise in evaluating kinetic parameters, there is a need for further refinement through the exploration of alternative models such as Freundlich and Temkin.

In summary, this section demonstrates that EC-RAS detects *in situ* changes in the surface structure and surface chemistry of electrochemical systems. The interfacial re-structuring of p-type InP(100) in contact with HCl and H_2SO_4 demonstrates that at low concentration, it is possible to maintain highly ordered interfaces in an aqueous electrolyte in a reversible manner. The interfacial film formed at cathodic potential shows short life-time in the electrolyte in absence of potential, which renders its stabilization and characterization challenging. Due to the implementation of a PS cell, the surface film can be partially stabilized to perform *ex situ* XPS measurements. Computational RAS and *ex situ* XPS indicate that the potential-induced formation of well-ordered InP–electrolyte interface in the cathodic region is associated with a well-ordered $InCl_x$ phase and hydrogen adsorption. Hence, probing surface fingerprints with RAS allows *in situ* monitoring of electrochemical interface design, which can contribute the performance improvement of solar-water splitting and battery devices. Furthermore, information about ad-/desorption kinetics can be extracted by fitting time-resolved measurements with electroadsorption isotherms. It evidences that adsorption processes at the InP(100)-0.01M HCl interface in a low cathodic potential range follow a non-Langmuir behavior with highly repulsive adsorbate-adsorbate interactions. The latter may impact the adsorption and desorption kinetics and explain why the desorption process is faster than the adsorption process.

5.2 EC-RAS for more Complex III-V Semiconductor Compounds

The results from this section are partially taken from the publication B2. All the results have been obtained in close collaboration with Erica A. Schmitt.

As already mentioned in Chapter 1, developing a photoelectrochemical cell that converts solar energy into chemical energy, specifically by producing hydrogen, represents a promising strategy for advanced photoelectrochemical water splitting devices. These integrated systems, utilizing III-V photoelectrodes, offer the potential for reduced overall costs compared to traditional PV-electrolysis setups, while also demonstrating high efficiency [20, 21]. A dual-junction photoabsorber made of GaInP/GaAs is a suitable candidate to generate both sufficient potential and optimized current output to split water into hydrogen and oxygen from absorption of the sunlight. Recently, attempts to use materials that are more abundant than III-V elements are implemented by integrating Silicon as a bottom substrate for III-V/Si tandem cells [99]. Figure 5.10a and d present drawings of the above mentioned cells. The cell in Figure 5.10a (sample A) is provided by the company Azur Space and the one in Figure 5.10d (sample B) is provided by Jonas Grutke from Fraunhofer ISE, Freiburg. For matter of confidentiality, details of the cell designs are omitted.

The solar cells are initially terminated with an AlInP window layer and a GaAs or a GaAsP cap layer on top. The purpose of the cap layer is to protect the solar absorber from damage due to moisture or mechanical influence prior to processing, Therefore, it needs to be removed before operating the PEC cell. In the case of a photovoltaic solar cell, the cap layer additionally forms a barrier between the electronic front contact and the AlInP window layer, preventing metal diffusion towards the bulk, forming undesired alloys. The thickness of the cap layer differs from 20 nm as a protection layer to 250 nm in a photovoltaic solar cell. The most common way to achieve the removal of this cap layer is wet-chemical etching. After the etching process, to turn the dual-junction photoabsorber with an AlInP window layer into an efficient photoelectrode, two other process steps must follow: the passivation of the window layer, and the decoration of the surface with a co-catalyst. To allow a control and homogeneous photoelectrochemical deposition of the catalyst on the surface of the photoabsorber, the protective cap layer must be removed in a manner that leaves a well-defined and homogeneous surface [21]. This implies firstly a careful choice of the etching solution to realise an isotropic and a highly selective etching, i.e. the etching rate ratio of the topmost layer to the layer below must typically be greater than five, which minimises etching into the underlying window layer [100]. Secondly, this implies the need of real-time *in situ* monitoring of the etching process. For a well-defined control of the S-L interface evolution, the characterisation technique considered should be surface-sensitive, non-

destructive and offer a reasonable time resolution to observe the transition from one material layer to another. Reflection anisotropy spectroscopy falls within the available techniques that fulfill these requirements [101, 102].

The present work focuses on the first process step, more specifically on the etching process optimisation via real-time *in situ* RAS monitoring. To combine wet-chemical etching with optical *in situ* control, PEC functionalization, and PEC characterization, the PS-cell setup combined with the RAS setup presented in section 3.2.7 is employed. Etching solutions composed of H_2O_2, NH_4OH and H_2O are widely used for a selective removal of GaAs [100]. In a previous related work, a 1:1:10 (H_2O_2: NH_4OH:H_2O) volume ration was used to etch the GaAs cap layer within 5 s [21]. For the preparation of the etching solution, aqueous solutions of H_2O_2 and NH_3 are used and the stated concentration of NH_4OH refers to the initial concentration of NH_3 before any protonation has occurred. The etching process is believed to consist of two steps: the oxidation of GaAs by the oxidising agent H_2O_2 and the dissolution of the oxides by the dissolving agent NH_4OH [103]. Therefore, the etching solution must have a pH value between 10.1 and 12 to ensure that no residual Ga oxides are present on the surface after etching (pH < 10.1) and to prevent H_2O_2 dissociation (pH > 12). Furthermore, the time of etching should be long enough to be resolved by the optical *in situ* probe. Hence, the volume ratio of the etching solution of 1:1:200 (H_2O_2:NH_4OH:H_2O) was chosen to fulfill these two conditions.

First, the etching process is performed with sample A, whose cap layer thickness is very low (<50 nm). The RAS spectra of the solar absorber in water, prior to and after the etching process, are shown in Figure 5.10b. The orange and green spectra correspond to GaAs and AlInP, respectively. The GaAs spectrum resembles an n-type, oxidised GaAs(100) surface [64, 104]. The main features of the GaAs RA-spectrum are found at the E1 and E1 + δ E1 critical points at around 2.6 and 3.2 eV, respectively. The AlInP spectrum resembles a 2D-2H terminated AlInP surface with a Cu Pt-B type ordering [105]. The peak at 2.6 eV is attributed to intradimer electronic transitions, localized at the P dimers. The AlInP spectrum is well-distinguishable from the one of GaAs, especially around 2.6 and 3.7 eV, where it shows two main characteristic peaks. For this reason, to control the etching process, a transient is measured at 2.6 eV, where the anisotropy is expected to significantly drop. The etch monitoring is illustrated in Figure 5.10c. The high signal-to-noise ratio of the time-resolved anisotropy and the large anisotropy drop between 20 and 35 s allow for a well-defined etching process monitoring with RAS. The artefact present at around 15 s corresponds to the addition of etching solution from the bottom to the top of the sample. To facilitate fitting of the transient with a higher precision, the latter is smoothed with a Savitzky-Golay filter.

The transient is then fitted with a sigmoid function given in Equation (5.30), adapted from Ref.[106], and the etching time is determined with Equation (5.31). τ is a time constant and

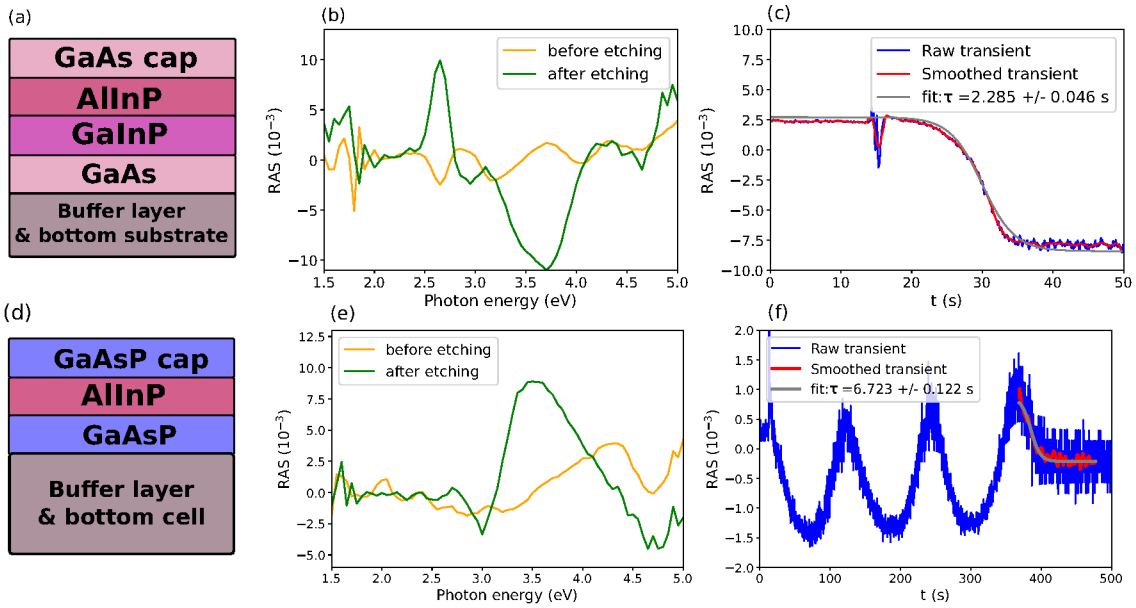

Figure 5.10: Schemes of the solar cells from Azur Space (a), denoted sample A, and Fraunhofer ISE (d) denoted sample B. RAS spectra of sample A b) and B e) before and after etching. The orange and green curves correspond to cap layer and AlInP termination, respectively. c) Transient at 2.6 eV of sample A during etching and corresponding curve fit to determine the etch time. f) Transient at 2.0 eV of sample B during etching and corresponding curve fit to determine the etch time.

t_0 is defined as the time of the inflection point of the transient. RAS_i and RAS_f are the anisotropy values at the beginning and the end of the etching process, respectively.

$$f(t) = \frac{\mathrm{RAS}_i - \mathrm{RAS}_f}{1 + \exp(\frac{t-t_0}{\tau})} + \mathrm{RAS}_f \tag{5.30}$$

The etching time is then defined as the time at which the growth rate of the function f is less than 97%:

$$\frac{f(t) - f(t_i)}{f(t_\infty) - f(t_i)} \leq 0.97 \tag{5.31}$$

Over five different etched samples, a mean etching time of 14.8 s with a standard deviation of 1.6 s is determined, and a smooth surface with less than 20 nm roughness is obtained (see atomic force miscroscopy (AFM) images in Figure 7.6, Appendix). It is therefore possible to precisely control the removal of the GaAs cap layer in the time domain by *in situ* RAS monitoring without the requirement of time-consuming *ex situ* analysis.

Beyond determining the etching time, the evaluation of the etching rate and etching depth is possible if particular conditions are met. For a well-ordered etching process of a sample with

a sufficiently thick cap layer and an adequate refractive index, measuring the anisotropy at the cap layer-etching media interface produces a Fabry-Pérot oscillation for sufficiently long wavelengths [106]. This oscillations result from an interference phenomenon, and are building up on a RAS-transient from etching of the cap layer and hence, its ever-shrinking thickness. While Fabry-Pérot oscillations have been observed on RAS with dry etching process (reactive-ion etching) [106, 107], it has not yet been demonstrated with wet etching. Here, anisotropy oscillation during chemical etching is shown with sample B, whose cap layer is about 250 nm thick. A similar etching procedure than for sample A is followed and illustrated on the RAS spectra and the RAS-transient in Figure 5.10e and f, respectively.

The significant differences in spectral fingerprints between sample A and B, before and after etching may originate form various factors: the layer composition (e.g. GaAsP for sample B vs. GaAs for sample A), the layer compound ratio (i.e. the Al content in $Al_xIn_{1-x}P$), the surface termination, and the different interfaces of the underlying layers that can also contribute to the RAS spectra. On this last point, it implied that if interference phenomena are observed on RAS spectra or on transients, they do not necessarily originate from the very first interfaces, but can also be an overlap of interference between more than 2 interfaces. The transient in Figure 5.10f displays 3 oscillations followed by a anisotropic plateau. The transition between the oscillations and the plateau indicates a passage from the cap layer and the AlInP layer. The etching time can therefore be determined in the same way as for sample A, and is estimated to be about 398 seconds. From the number of oscillations k observed during etching, knowing the refractive index n of the top-most layer and the wavelength λ, it is possible to deduce the etch depth using Equation (5.32).

$$d = \frac{k\lambda}{2n} \tag{5.32}$$

Hence, for a transient including 3 oscillations and measured at 2.0 eV on a GaAsP surface with a refractive index of 3.88, the etch depth is 240 nm. This result is close to the expected thickness of the cap layer (about 250 nm). Improvement on the etch depth precision can be done by analysing oscillations at several energies [106]. Finally, knowing the etch depth and the etching time, the etching rate is estimated to amount to 0.6 nm/s, which is in the order of magnitude of a layer-by-layer etching.

In summary, this section shows that RAS provides a surface fingerprint upon wet-etching that varies depending on the structure, the composition, and the quality of the surface. To precisely control the etching process and the resulting interfacial properties, evaluating both, spectra and time resolved signals, is desirable. Here, the measured transients upon etching attest for a well-defined etching process and allow determining the etching time. Furthermore, the case

study presents the first application of Fabry-Pérot oscillations during wet-etching with *in situ* RAS. If oscillations are building-up on time-resolved RAS measurement from a layer-by-layer wet-etching, it suggests that the method could also be instrumental for a (photo)electrochemical layer-by-layer deposition/etching control.

5.3 EC-RAS: a Potential Tool for Battery

The results from this section are taken from the publication B3.

The present section reports the first application of RAS as an in situ characterization technique for non-aqueous battery systems, investigating an Al(110)-based model system for Al-batteries (AlBs). In AlBs, Al and [EMImCl]:$AlCl_3$ (1:1.5) ionic liquid (IL) are commonly used as anode material and electrolyte, respectively. The porous and in-homogeneous native oxide layer (Al_2O_3) present on th Al anode surface currently hinders the development of more sustainable and less corrosive electrolytes than [EMImCl]:$AlCl_3$, because Al_2O_3 acts as an insulator and blocks Al electrochemical plating and stripping. With *in situ* RAS, the Al surface pre-treatment in IL for a partial oxide layer removal before electrochemical cycling as well as its effect on the electrochemical performance in IL is investigated. Thanks to the peak at 1.5 eV in the Al(110) RAS spectrum which is sensible to the surface oxide coverage, it is possible to monitor the Al-IL interface during pre-treatment and cycling.

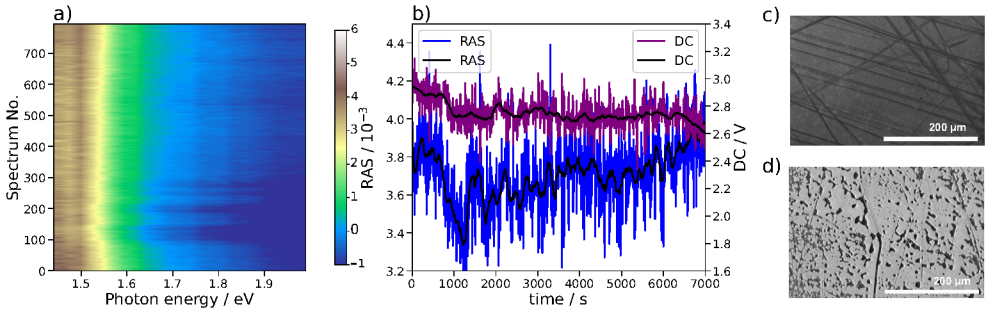

Figure 5.11: (a) Colourplot (CP) of Al(110) upon immersion in IL for 2 h. (b) Transient at 1.49 eV extracted from the CP. The purple and black curves correspond to the evolution of the anisotropy and the reflectance over the time, respectively. (c) and (d) provide the SEM pictures taken before and after pre-treatment, respectively.

For this purpose, multiple RAS spectra are recorded during the 2h of immersion pre-treatment in IL, displayed in a colourplot (CP) in Figure 5.11a. The width of the peak at 1.5 eV is conserved, but its anisotropy drops in the first phase before increasing slightly above its initial value. The evolution of the anisotropic values at 1.5 eV can be better observed on the transient extracted from the CP in Figure 5.11b. It indicates that, during pre-treatment, the Al(110) surface passivation film is modified. While the anisotropy globally increases, the DC signal (Figure 5.11b, purple curve) keeps decreasing over the entire pre-treatment. This means that the Al surface progressively deteriorates due to IL electrolyte decomposition, but some regions of the surface get more well-defined. Comparison of the surface before and after pre-treatment with post-mortem SEM/EDX analysis allows deducing a combination of a partial decrease in the Al_2O_3

passivation layer thickness and the appearance of active sites with an overall increase in surface roughness/in-homogeneities (SEM: Figure 5.11c-d, EDX: Appendix Figure 7.7 and Table 7.1). The dark areas in Figure 5.11d are due to electrolyte decomposition which generates an organic layer on top of the inorganic oxide layer. The emergence of actives site (grey matrix in Figure 5.11d) indicates an efficient pre-treatment of Al in IL for subsequent electrochemical cycling, since the redox active species from the electrolyte ($Al_2Cl_7^-$ and $AlCl_4^-$) are, via the active sites, in direct contact with the Al metal.

As shown by the black arrows in Figure 5.12a-b, the CVs of the pre-treated Al(110) electrode exhibit a faster stabilization of Al plating and stripping peaks compared to those of untreated Al(110). This observation suggests that for an Al crystal with a (110)- orientation, the pre-treatment has a positive effect on the Al plating and stripping performance. Over the experimental series, the stripping peak on the CV around 0.28 V vs. Al gets more pronounced, as depicted in Figure 5.12c. This phenomenon is attributed to a progressive Al plating and stripping from nanocrystalline to microcrystalline form of Al, i.e. the surface is getting rougher.

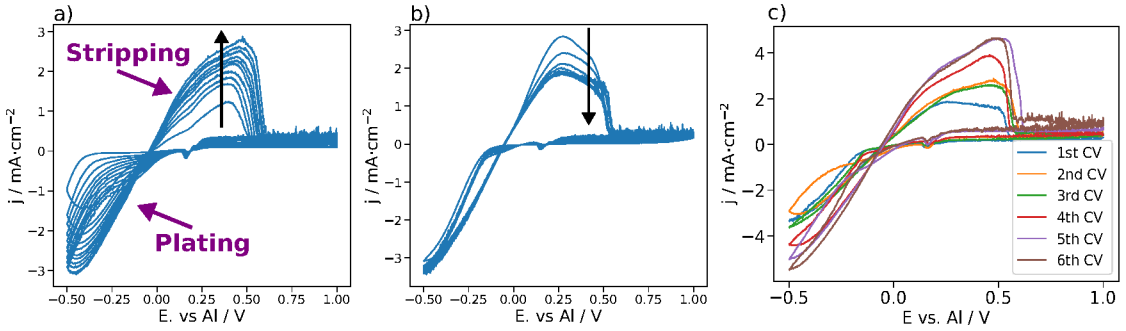

Figure 5.12: Recorded CV for (a) unpre-treated and (b) pre-treated Al(110) in IL measured between -0.5 to 1 V vs. Al at 20 mV/s for 10 cycles. The direction of the black arrows indicate the increase or the decrease of the current density with increasing number of cycles. (c) Last cycles of 6 CV experiments

Lowering the scan rate and the potential window of the CV allows recording spectra in parallel with a reasonable time resolution, as shown in Figure 5.13a-b. Thus, recording structural changes during plating and stripping with RAS becomes possible. The signal-to-noise ratio of the transients data still being very low, the latter must be further processed by fast Fourier transform (FFT) in order to evaluate a trend between the RA-values and the electrochemical cycles. Upon electrochemical cycling, applied potential-dependent oscillations of the anisotropy are observed from the FFT-filtered transients. Cycling in a potential range (-0.25 and 0.25 V) where Al plating and stripping in the nanocrystalline form is predominant occurs in a more defined manner than cycling in a potential range (-0.5 and 0.5 V) where Al plating and stripping in the microcrystalline form is pre-ponderant.

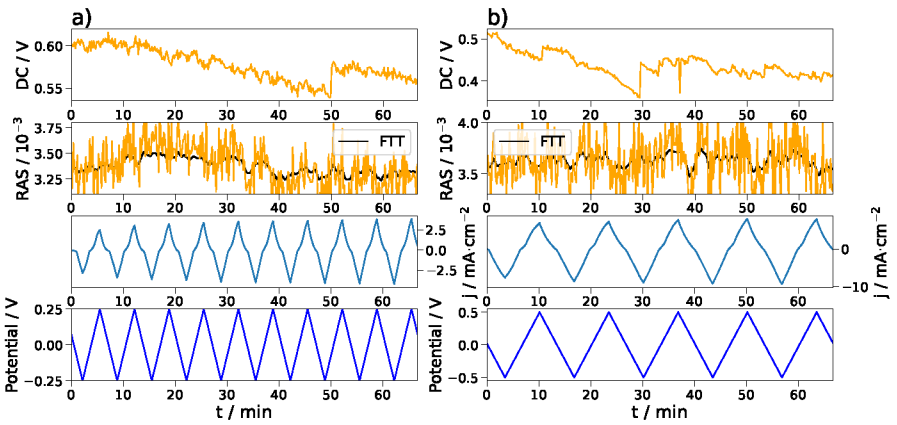

Figure 5.13: DC signal and transients at 1.49 eV extracted from a CP measured during (a) CV between -0.25 and 0.25 V at a scan speed of 2.5 mV/s for 10 cycles and (b) CV between -0.5 and 0.5 V at 2.5 mV/s for 5 cycles. The black curves correspond to the FFT-filtered transients.

In summary, this section demonstrates the applicability of RAS in electrochemical environments containing organic electrolyte to monitor phenomena such as plating/stripping, SEI formation, and surface passivation in real-time. It suggests that the formation of dendrites, i.e. the passage from 2D metal surfaces to locally 3D metal surfaces should be identifiable by RAS.

6 Conclusion

This thesis endeavors to delve into the properties of solid-liquid electrolyte interfaces at an atomistic level. Due to the presence of the electrolyte and the need for an applied potential at the electrode, the number of *in situ* and *operando* techniques and studies reported in the literature is currently insufficient to bridge the gap between the performance limitation of a device and the physico-chemical processes occurring at its interfaces. To address this gap, this study employs reflection anisotropy spectroscopy (RAS), a highly surface-sensitive optical method, in an electrochemical environment (EC-RAS).

In the investigation of noble metal (Au)-aqueous electrolyte interfaces, RAS successfully distinguishes anisotropy features arising from potential-induced surface reconstruction and ion adsorption, complementing traditional techniques like cyclic voltammetry (CV). The restructuring and adsorption processes identified with RAS could be further complemented with EC-STM to gain further insights into surface morphological changes (stripes/grooves, faceting). This approach holds promise for advancing battery research, particularly for metal-anode batteries.

The study extends to non-aqueous battery interfaces, exemplified by examining the Al(110) surface evolution during treatment and electroplating/stripping in [EMImCl]:$AlCl_3$ (1:1.5). Despite the complexity of the interphases formed, RAS, coupled with computational techniques and SEM/EDX analysis, enables the tracking of surface roughness, homogeneity, and oxide layer evolution. Additionally, transient measurements reveal the initial evidence of Al plating and stripping, crucial for SEI and dendrite formation monitoring. This study emphasizes that RAS is a potential tool to follow the build-up of a conductive and protective film which is required for the implementation of non-acidic, non-aqueous electrolytes. Since SEI and dendrite formation produce inhomogeneous interphases, it suggests future integration with Reflection Anisotropy Microscopy (RAM) for enhanced spatial resolution (up to few µm). Additionally, the use of more advanced light sources with higher luminosity would allow a temporal resolution to the µs scale.

For well-ordered III-V semiconductors systems, the origin of potential-induced anisotropy oscillations of InP(100) in a 0.01M HCl system is now clarified. The reversible build-up of anisotropy in the cathodic region is partly originating from a restructuring of the interface with the formation of a thin, well-ordered $InCl_x$ surface film, evidenced by computational RAS and *ex situ*

XPS. Potential pulse measurements combined with a computational study revealed that the anisotropy is in fact an overlap of the applied potential-induced LEO, and adsorbed hydrogen/-chloride. Kinetic parameters such as ionic adsorption formation energy, adsorption lifetime and adsorbate-adsorbate interaction type are determined by fitting time-resolved measurements with adsorption isotherm models. In this case study, non-Langmuir-like behavior and strongly repulsive adsorbate-adsorbate interactions are demonstrated for the ad-/desorption process in the cathodic region. Overall, this work establishes EC-RAS as a reliable technique *in situ* technique for the structure-potential relationship of semiconductor-aqueous electrolyte interfaces. As a continuation of this work, the kinetic studies of InP in HCl combined with noble metal-aqueous electrolyte investigation would allow fundamental studies with an easier study case, and would increase the robustness of time-resolved RAS measurements fitting with adsorption isotherm models. Along with these kinetic studies, in-depth investigation of the LEO through the analysis of potential-pulse measurements could be done. A progression of this work is comparing the experimental spectra of the InP(100)-HCl system under applied potential with the computational spectra of the stable phases observed in the theoretical phase diagram obtained in similar conditions (same pH and applied potentials). Ultimately, coupling EC-RAS with ambient-pressure XPS could provide a direct structural and compositional picture of the formed interfaces.

Expanding to more complex III-V semiconductor systems, RAS facilitates improvements in the first step of the surface preparation of III-V photocathodes. The association of RAS with a photo-electrochemical cell avoids the use of glovebox or clean room facilities, enables well-controlled conditions and further improves repeatability and quantification of sample to sample variation. More specifically, real-time monitoring of the chemical etching process of GaAs semiconductor cap layers on solar cells makes it possible to determine the adequate etching solution ratio and the required etching time. The appearance of Fabry-Pérot oscillations on time-resolved measurements during etching indicates a well-ordered process and provides information on etch depth and etch rate. AFM measurements confirm the RAS results, showing that the surface obtained after etching is very smooth (<20 nm roughness). The control of the electrochemical passivation of the InP(100) surface and Fabry-Pérot oscillations during GaAs wet etching suggest that layer-by-layer electrochemical etching/deposition processes can be implemented with the help of *in situ* EC-RAS. This would allow the preparation of more robust passivation layers on III-V photo-electrodes.

In conclusion, this study underscores the versatility and potential of RAS in elucidating complex interfacial processes across various material systems. Future endeavours should focus on expanding the application of RAS in advancing electrochemical and semiconductor technologies.

7 Appendix

7.1 Basic Principles of X-ray Photoelectron Spectroscopy (XPS)

XPS is a surface sensitive analytical technique that probes the core electrons of the sample atoms. It allows not only accessing the elementary composition at the sample surface (all elements are detectable expect H and He), but also the chemical environment of the elements (their oxidation state) [108]. Additionally, by analysing XPS spectra, mixed compounds of surface layers can be quantified with a detection limit of ∼0.3 to 0.03 at.-%., and the thickness of surface film in the nm range can be determined.

XPS is based on the photoelectric effect illustrated in Figure 7.1, in which short-wavelength light can lead to the emission of photo-electrons from metal or semiconductor surfaces. The property of the photoelectrons measured by the detector is the kinetic energy E_{kin}, related to the binding energy of the electron E_B, the photon energy $h\nu$, and the spectrometer work function ϕ (Equation 7.33).

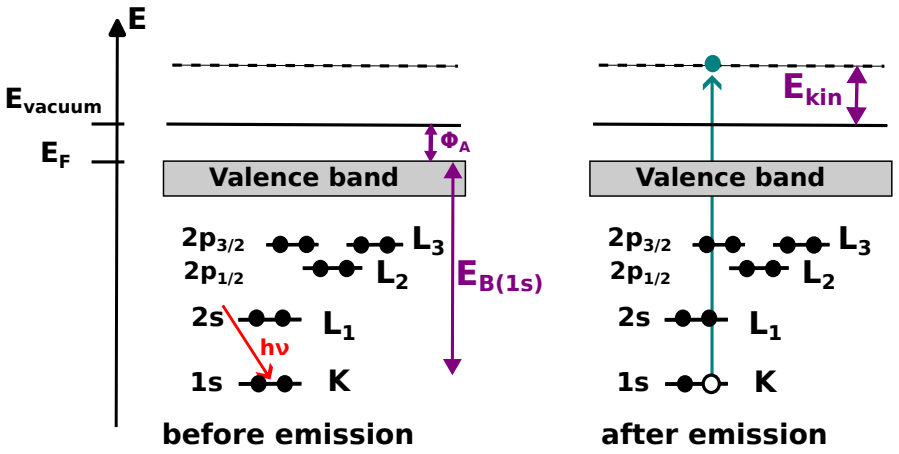

Figure 7.1: Energy scheme illustrating the principle of photoemission for a solid metal. Adapted from [108]

$$E_{kin} = h\nu - E_B - \phi \tag{7.33}$$

Since a set of core levels with characteristic binding energies exists for every element, a spectrum of the intensity of each element as function of E_B of its core electrons is obtained upon XPS measurements. The surface sensitivity is determined by the short inelastic mean free path of the photoelectrons in solids (95% of the intensity comes from the first 5 nm of the surface sample). However, for quantitative analysis, the surface sensitivity can be increased by increasing the angle of detection relative to the sample surface normal.

An example of XPS spectra is shown in Figure 7.2 for Cu. In characteristic peak pattern, the peak nomenclature nlj is used, where n is the principal quantum number (QN), l the angular QN, and j the total angular momentum QN. The peak (core levels) with l>=1 are split into doublets due to spin-orbit coupling, i.e. p, d, and f states are split. A background is present in the peak pattern due to inelatstically scattered electrons. Additionally, Auger electrons may lead to features, like the LMM peak in Figure 7.2. Depending on the bonding environment around the atom, small chemical shifts (ΔE_B = 5 eV) occur as a function of the charge state (oxidation state) of an atom.

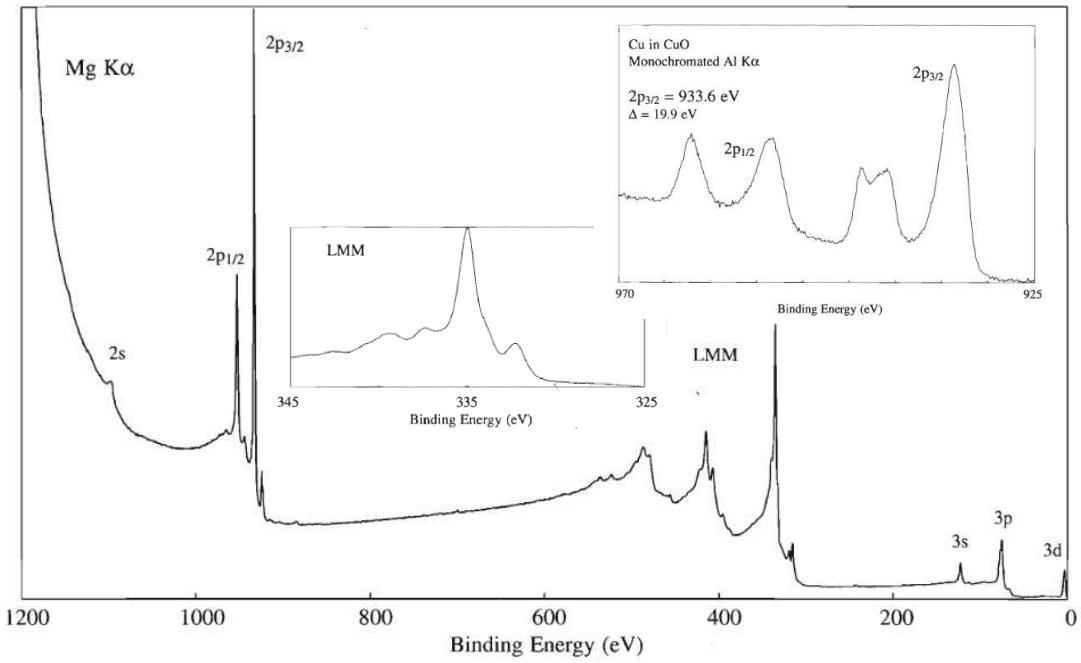

Figure 7.2: XPS spectrum of Copper. Taken from [109]

XPS measurements have to be conducted in a UHV chamber at a pressure of 10^{-8} mbar or better. This enables undisturbed travel of the photoelectrons. It also ensures to keep the sample

surface clean, and to protect the X-ray source and the analyser. The standard X-ray source usually contains Al and Mg anode. To generate X-rays, electrons are accelerated from a filament to the anode. Usually, a monochromator is placed on the electron path between the source and the sample to remove satellites/background, and to improve peak resolution. Then, the impact of the high energy electrons on the sample causes X-ray emission. In order to replace the photoelectrons that left the sample, a flood of low-energy electrons is directed to the latter thanks to an electron flood gun. Before reaching the detector, the electrons passes through a concentric hemispherical analyser. The analyser separates the photoelectrons according to their kinetic energy and their angle of incidence. Analogue to an optical lens system, it acts as an electron lens systems.

7.2 Basic Principles of Scanning Electron Microscopy (SEM)

SEM is an electron microscopy technique for obtaining topographic images of surfaces. Just as lenses and a camera are used in optical microscopy to focus light and generate an image of a sample, SEM uses electromagnetic fields to focus electrons and specific detectors to collect electrons emitted from a sample, thus forming an image [110]. Electron scanning enables features to be observed down to a few nm in size, while light detection enables features to be observed down to only a few hundred nm in size.

For similar reasons to XPS, SEM measurements are carried out in a vacuum. The pressure in the chamber is generally between 10^{-7} and 10^{-8} mbar. To produce a beam of electrons, called primary electrons, a high voltage is applied to a filament. Since electrons are charged particles, the electron beam can be directed and focused by the application of electromagnetic fields, acting as electromagnetic lenses. In the electromagnetic field, electrons are subject to the Lorentz force $\vec{F}$ given in equation 7.34, which depends on the electromagnetic field ($\vec{B}$, $\vec{E}$), the velocity $\vec{v}$ and the charge e of the electrons. The electron beam is accelerated by applying an acceleration voltage (EHT), leading to wavelengths of the electrons of about 10^{-11} m, thus allowing for nm spatial resolution.

$$\vec{F} = e.(\vec{E} + \vec{v} * \vec{B}) \tag{7.34}$$

Among the charged particles/radiations that are generated from the interactions of the electron beam with atoms at various depths within the sample's surface, secondary electrons (SE) are of main interest in SEM because the low mean free path of SE in solid limits their escape from the top few nanometers of the surface. SE are ejected from conduction or valence bands of

the specimen atoms by inelastic scattering interactions with beam electrons. The probability p of an excited electron to be emitted from the sample can be approximated by Equation 7.35, where z represents the depth of the sample where the electron was excited and λ represents the mean free path of the excited electron. The value of the mean free path is generally between 1 nm (metals) and 20 nm (insulators). The emission rate of SE is also determined by the specimen's surface composition and topography allowing for imaging a surface by varying SE signal intensities.

$$p \approx \exp \frac{-z}{\lambda} \tag{7.35}$$

Inelastic scattering interactions between the primary electrons and the sample also leads, from the relaxation of an electron to replace an ejected orbital electron, to the generation of X-rays. When the SEM setup is equipped with a X-ray detector, the determination of the chemical composition of a material is possible. This characterization is commonly called EDX. Like XPS, EDX provides the elementary composition at sample surface. However, in contrast to XPS, in EDX the incident probes are electrons and X-ray radiations are emitted. It is less surface sensitive than XPS (0.1 mm depth) but has a higher spatial resolution (10 nm). It provides elemental analysis but no information about the chemical environment.

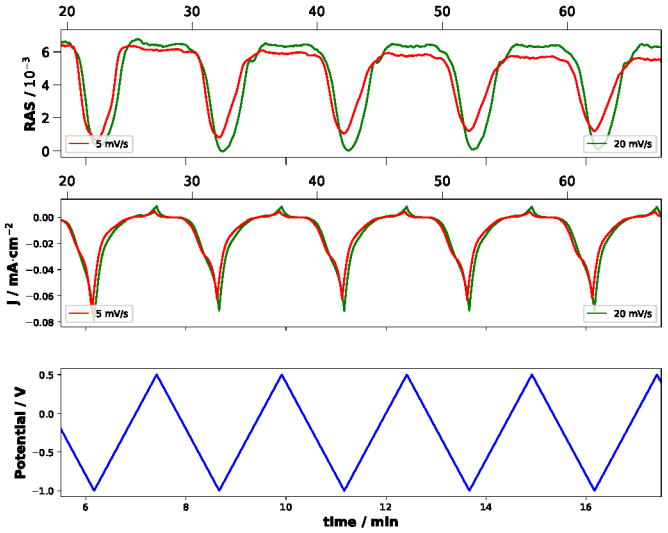

Figure 7.3: influence of the scan rate (5 mV/s vs. 20 mV/s) on the current from CV measurement and on the transient at 2.25 eV measured in parallel of the CV.

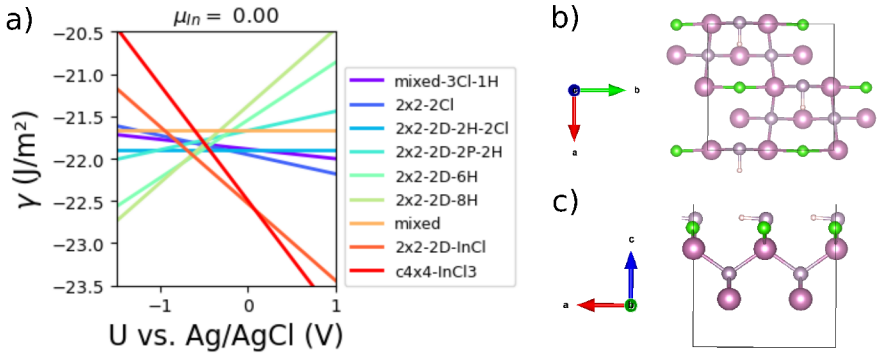

Figure 7.4: a) Theoretical phase diagram of InP(100) in HCl at pH=2. As an example, top view (b) and side view (c) of the 2x2-2D-2H-2Cl phase is depicted. Green atoms: Cl, white atoms: H, dark pink atoms: In, and light pink atoms: P. Calculation made by Dr. Holger Euchner at the University of Tübingen.

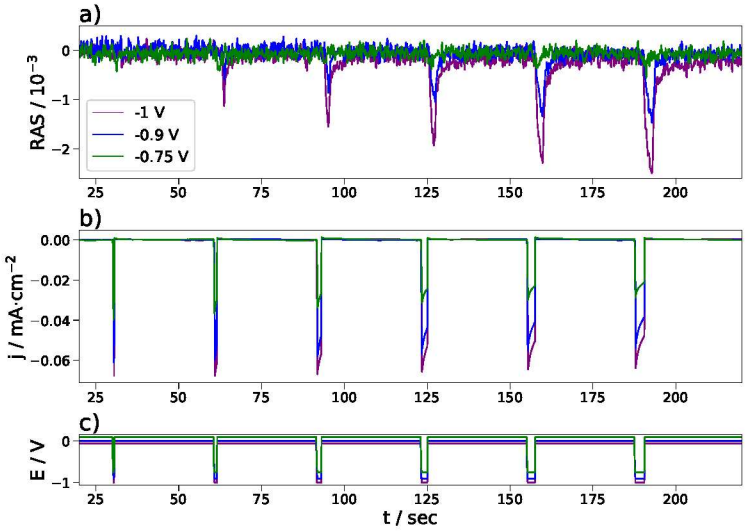

Figure 7.5: Transients at 2.25 eV recorded under potential pulses conditions. The measurement was conducted in 0.01 M HCl for 3 different potentials with 6 time pulses (0.5 s, 1.0 s, 1.5 s, 2.0 s, 2.5 s, and 3 s), and with OCP measurements between the pulses.

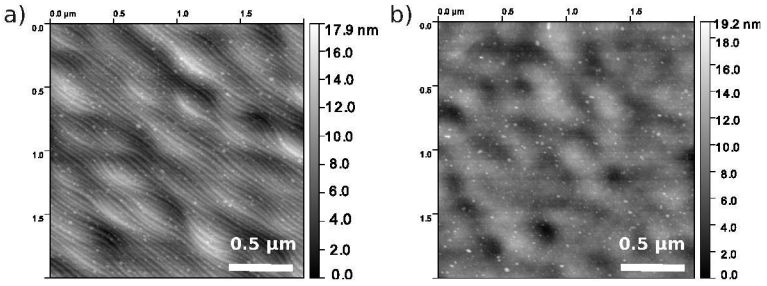

Figure 7.6: AFM images of sample A before a) and after b) etching.

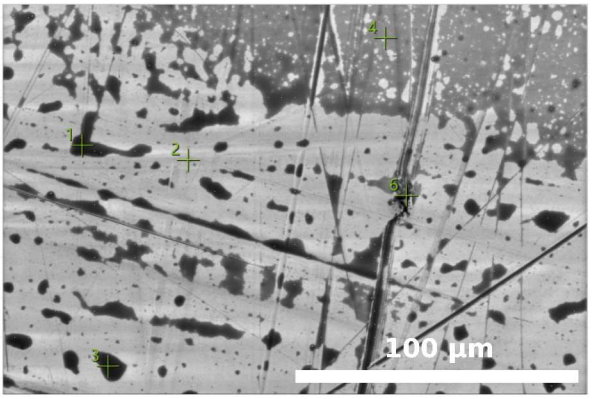

Figure 7.7: SEM picture of the Al(110) surface after treatment.

Table 7.1: Table of the atomic weight percent of the elements at different points of the SEM picture from Figure 7.7.

	Atomic %				
Element	Point 1	Point 2	Point 3	Point 4	Point 6
C	13.3	1.6	13.9	2.3	11.6
N	4.2	0.1	4.1	0.3	3.8
O	5.7	0.9	4.7	1.2	8.3
Al	73.5	97.0	74.1	95.8	70.3
Si	0.0	0.0	0.0	0.0	1.0
Cl	3.3	0.4	3.1	0.4	5.1

Bibliography

[1] A. Barrau, *L'Hypothèse K: La science face à la catastrophe écologique*, Grasset, **2023**.

[2] J. Shukla, P. R.; Skea, R. Slade, Working Group III Contribution to the Sixth Assessment Report of the Intergovernmental Panel on Climate Change, en, IPCC, **2022**.

[3] A. Mikhaylov, N. Moiseev, K. Aleshin, T. Burkhardt, *JESI* **2020**, *7*, 2897–2913.

[4] R. D. Lamboll, Z. R. J. Nicholls, C. J. Smith, J. S. Kikstra, E. Byers, J. Rogelj, *Nat. Clim. Chang.* **2023**, *13*, 1360–1367.

[5] K. O. Yoro, M. O. Daramola, *CO2 emission sources, greenhouse gases, and the global warming effect*, Elsevier, **2020**, pp. 3–28.

[6] J. Popovic, *Nat. Commun.* **2021**, *12*, 1–5.

[7] J. Sun, B. Luo, H. Li, *Adv. Sustain. Syst.* **2022**, *3*, 2100191.

[8] M. Chatenet, B. G. Pollet, D. R. Dekel, F. Dionigi, J. Deseure, P. Millet, R. D. Braatz, M. Z. Bazant, M. Eikerling, I. Staffell, P. Balcombe, Y. Shao-Horn, H. Schäfer, *Chem. Soc. Rev.* **2022**, *51*, 4583–4762.

[9] K. Sivula, R. van de Krol, *Nat. Rev. Mater.* **2016**, *1*, 1–16.

[10] Q. Wang, K. Domen, *Chem. Rev.* **2020**, *120*, 919–985.

[11] B. Dunn, H. Kamath, J.-M. Tarascon, *Science* **2011**, *334*, 928–935.

[12] J. B. Goodenough, *Energy Environ. Sci.* **2014**, *7*, 14–18.

[13] F. Duffner, N. Kronemeyer, J. Tübke, J. Leker, M. Winter, R. Schmuch, *Nat. Energy* **2021**, *6*, 123–134.

[14] D. B. Agusdinata, W. Liu, H. Eakin, H. Romero, *Environ. Res. Lett.* **2018**, *13*, 123001.

[15] D. Muñoz-Torrero, J. Palma, R. Marcilla, E. Ventosa, *Dalton Trans.* **2019**, *48*, 9906–9911.

[16] M. Jäckle, K. Helmbrecht, M. Smits, D. Stottmeister, A. Groß, *Energy Environ. Sci.* **2018**, *11*, 3400–3407.

[17] S. K. Das, S. Mahapatra, H. Lahan, *J. Mater. Chem. A* **2017**, *5*, 6347–6367.

[18] J. Andrews, B. Shabani, *Int. J. Hydrogen Energy* **2012**, *37*, 1184–1203.

[19] J. M. Bermudez, S. Evangelopoulou, F. Pavan, IEA (2022) Hydrogen, IEA, Paris.

[20] W.-H. Cheng, M. H. Richter, M. M. May, J. Ohlmann, D. Lackner, F. Dimroth, T. Hannappel, H. A. Atwater, H.-J. Lewerenz, *ACS Energy Lett.* **2018**, *3*, 1795–1800.

[21] M. M. May, H.-J. Lewerenz, D. Lackner, F. Dimroth, T. Hannappel, *Nat. Commun.* **2015**, *6*, 8286.

[22] B. L. Pearce, S. J. Wilkins, T. Paskova, A. Ivanisevic, *J. Mater. Res.* **2015**, *30*, 2859–2870.

[23] C. Malgrange, C. Ricolleau, F. Lefaucheux, *Symétrie et propriétés physiques des cristaux*, EDP SCIENCES, **2011**.

[24] L. A. Kibler, Preparation and Characterization of Noble Metal Single Crystal Electrode Surfaces, **2003**, `http://www.uni-ulm.de/echem/ekat/kibler_single_crystals_2003.pdf`.

[25] J. Geiger, M. Sprik, M. M. May, *The Journal of Chemical Physics* **2020**, *152*, 194706.

[26] S. Kashiwaya, T. Toupance, A. Klein, W. Jaegermann, *Advanced Energy Materials* **2018**, *8*, _eprint: https://onlinelibrary.wiley.com/doi/pdf/10.1002/aenm.201802195, 1802195.

[27] C. Kittel, *Introduction to solid state physics*, 8th ed, Wiley, Hoboken, NJ, **2005**.

[28] S. O. Kasap, *Principles of electronic materials and devices*, Fourth edition, McGraw-Hill, a business unit of The McGraw-Hill Companies, Inc, New York, NY, **2018**.

[29] P. Würfel, *Physics of Solar Cells: From Principles to New Concepts*, 1st ed., Wiley, **2005**.

[30] A. Smets, K. Jäger, O. Isabella, R. v. Swaaij, M. Zeman, *Solar Energy: The Physics and Engineering of Photovoltaic Conversion, Technologies and Systems*, UIT Cambridge, **2016**.

[31] S. Corby, R. R. Rao, L. Steier, J. R. Durrant, *Nat Rev Mater* **2021**, *6*, 1136–1155.

[32] *Photoelectrochemical Hydrogen Production*, (Eds.: R. Van De Krol, M. Grätzel), Springer US, Boston, MA, **2012**.

[33] P. K. Nayak, G. Garcia-Belmonte, A. Kahn, J. Bisquert, D. Cahen, *Energy Environ. Sci.* **2012**, *5*, 6022.

[34] M. Schleuning, I. Y. Ahmet, R. van de Krol, M. M. May, *Sust. En. Fuels* **2022**, 3701–3716,

[35] R. Memming in *Semiconductor Electrochemistry*, John Wiley & Sons, Ltd, **2015**, Chapter 2, pp. 23–47.

[36] Z. Zhang, J. T. J. Yates, *Chem. Rev.* **2012**, *112*, 5520–5551.

[37] F. Nobili, R. Marassi, Fundamental Principles of Battery Electrochemistry, en, (Eds.: A. J. Bard, M. Stratmann, E. Gileadi, M. Urbakh, E. J. Calvo, P. R. Unwin, G. S. Frankel, D. Macdonald, S. Licht, H. J. Sch¿fer, G. S. Wilson, I. Rubinstein, M. Fujihira, P. Schmuki, F. Scholz, C. J. Pickett, J. F. Rusling), **2020**.

[38] H. Gerischer, *Electrochim. Acta* **1990**, *35*, 1677–1699.

[39] P. P. Notten, *Electrochemical study of the etching of III-V semiconductors*, Technische Universiteit Eindhoven, **1989**.

[40] H.-J. Lewerenz, I. D. Sharp, *Chapter 1. Concepts of Photoelectrochemical Energy Conversion and Fuel Generation*, Royal Society of Chemistry, **2018**, pp. 1–42.

[41] M. M. May, W. Jaegermann, *Curr. Opin. Electrochem.* **2022**, *34*, 100968.

[42] S. E. Acosta-Ortiz, A. Lastras-Martínez, *Phys. Rev. B* **1989**, *40*, 1426–1429.

[43] W. Schmickler, E. Santos, *Interfacial Electrochemistry*, Springer Berlin Heidelberg, Berlin, Heidelberg, **2010**, pp. 51–64.

[44] P. Atkins, J. D. Paula, J. Keeler, *Atkins' Physical Chemistry*, 12th ed., Oxford University Press, **2022**, pp. 916–925.

[45] S. Kalam, S. A. Abu-Khamsin, M. S. Kamal, S. Patil, *ACS Omega* **2021**, *6*, 32342–32348.

[46] G. Jerkiewicz, *Electrocatal* **2010**, *1*, 179–199.

[47] N. Elgrishi, K. J. Rountree, B. D. McCarthy, E. S. Rountree, T. T. Eisenhart, J. L. Dempsey, *J. Chem. Educ.* **2018**, *95*, 197–206.

[48] S. Vázquez Miranda, PhD thesis, Autonomous University of San Luis Potosi, San Luis Potosí, **2020**.

[49] F. Miomandre, S. Sadki, P. Audebert, R. Méallet-Renault, *Électrochimie - 2e éd.: Des concepts aux applications*, Dunod, **2011**.

[50] P. Weightman, D. S. Martin, R. J. Cole, T. Farrell, *Rep. Prog. Phys.* **2005**, *68*, 1251–1341.

[51] O. Supplie, M. M. May, S. Brückner, N. Brezhneva, T. Hannappel, E. V. Skorb, *Adv. Mater. Interfaces* **2017**, *4*, 1601118.

[52] W. G. Schmidt, *Phys. Status Solidi B* **2005**, *242*, 2751–2764.

[53] K. Haberland, P. Kurpas, M. Pristovsek, J.-T. Zettler, M. Weyers, W. Richter, *Appl. Phys. A* **1999**, *68*, 309–313.

[54] M. M. May, H.-J. Lewerenz, T. Hannappel, *The Journal of Physical Chemistry C* **2014**, *118*, 19032–19041.

[55] H. Fouckhardt, J. Richter, C. Doering, J. Strassner, *Adv. Mater. Sci. Eng.* **2023**, *2023*, (Ed.: I. J. Ferrer), 1–12.

[56] H. Döscher, T. Hannappel, *J. Appl. Phys.* **2010**, *107*, 123523.

[57] M. M. May, M. Sprik, *New J. Phys.* **2018**, *20*, 033031.

[58] F. Jensen, *Introduction to computational chemistry*, 2nd ed, John Wiley & Sons, Chichester, England, **2007**, pp. 232–264.

[59] W. Schmidt, *Appl. Phys. A: Mater. Sci. Process.* **2002**, *75*, 89–99.

[60] G. P. Chen, V. K. Voora, M. M. Agee, S. G. Balasubramani, F. Furche, *Annu. Rev. Phys. Chem.* **2017**, *68*, 421–445.

[61] D. E. Aspnes, A. A. Studna, *Phys. Rev. Lett.* **1985**, *54*, 4.

[62] B. A. Joyce, *Rep. Prog. Phys.* **1985**.

[63] M. Behet, R. Hövel, A. Kohl, A. M. Küsters, B. Opitz, K. Heime, *Microelectronics J* **1996**, *27*, 297–334.

[64] Z. Sobiesierski, D. I. Westwood, M. Elliott, *Phys. Rev. B* **1997**, *56*, 15277–15281.

[65] J. Ortega-Gallegos, L. Guevara-Macías, A. Ariza-Flores, R. Castro-García, L. Lastras-Martínez, R. Balderas-Navarro, R. López-Estopier, A. Lastras-Martínez, *Appl. Surf. Sci.* **2018**, *439*, 963–967.

[66] G. Hughes, C. Springer, U. Resch, N. Esser, W. Richter, *J. Appl. Phys.* **1995**, *78*, 1948–1952.

[67] G. Sombrio, E. Oliveira, J. Strassner, C. Doering, H. Fouckhardt, *J. Vac. Sci. Technol. B* **2021**, *39*, 052204.

[68] S. Brückner, P. Kleinschmidt, O. Supplie, H. Döscher, T. Hannappel, *New J. Phys.* **2013**, *15*, 113049.

[69] N. Witkowski, R. Coustel, O. Pluchery, Y. Borensztein, *Surf. Sci.* **2006**, *600*, 5142–5149.

[70] M. M. May, O. Supplie, C. Höhn, R. v. d. Krol, H.-J. Lewerenz, T. Hannappel, *New J. Phys.* **2013**, *15*, 103003.

[71] A. Baghbanpourasl, W. G. Schmidt, M. Denk, C. Cobet, M. Hohage, P. Zeppenfeld, K. Hingerl, *Surf. Sci.* **2015**, *641*, 231–236.

[72] M. M. May, H. Stange, J. Weinrich, T. Hannappel, O. Supplie, *SciPost Phys.* **2019**, *6*, 58.

[73] C. I. Smith, N. J. Almond, P. Weightman, *J. Electrochem. Soc.* **2007**, *154*, F90.

[74] C. I. Smith, P. Harrison, T. Farrell, P. Weightman, *J. Phys.: Condens. Matter* **2012**, *24*, 482002.

[75] P. Harrison, C. I. Smith, Y. Gründer, C. A. Lucas, S. D. Barrett, P. Weightman, *Phys. Chem. Chem. Phys.* **2016**, *18*, 24396–24400.

[76] V. Mazine, *phys. stat. sol.* **1999**, 6.

[77] B. Sheridan, D. S. Martin, J. R. Power, S. D. Barrett, C. I. Smith, C. A. Lucas, R. J. Nichols, P. Weightman, *Phys. Rev. Lett.* **2000**, *85*, 4.

[78] T. Yamada, K. Shirasaka, A. Takano, M. Kawai, *Surf. Sci.* **2004**, *561*, 233–247.

[79] P. D. Lane, G. E. Isted, R. J. Cole, *Phys. Status Solidi B* **2010**, *247*, 1969–1973.

[80] X. F. Jin, M. Y. Mao, S. Ko, Y. R. Shen, *Phys. Rev. B* **1996**, *54*, 7701–7704.

[81] L. Sun, M. Hohage, P. Zeppenfeld, R. Balderas-Navarro, K. Hingerl, *Phys. Rev. Lett.* **2003**, *90*, 106104.

[82] C. Punckt, F. S. Merkt, H. H. Rotermund, *New J. Phys.* **2007**, *9*, 213–213.

[83] G. Barati, V. Solokha, K. Wandelt, K. Hingerl, C. Cobet, *Langmuir* **2014**, *30*, 14486–14493.

[84] C. Goletti, G. Bussetti, A. Violante, B. Bonanni, M. Di Giovannantonio, G. Serrano, S. Breuer, K. Gentz, K. Wandelt, *J. Phys. Chem. C* **2019**, *119*, 1782–1790.

[85] S. Vazquez-Miranda, V. Solokha, R. E. Balderas-Navarro, K. Hingerl, C. Cobet, *J. Phys. Chem. C* **2020**, *124*, 5204–5212.

[86] M. Löw, M. Guidat, J. Kim, M. M. May, *RSC Adv.* **2022**, *12*, 32756–32764.

[87] E. A. Schmitt, M. Guidat, M. Nusshör, A.-L. Renz, K. Möller, M. Flieg, D. Lörch, M. Kölbach, M. M. May, *Cell Reports Physical Science* **2023**, 101606.

[88] J. Tournet, Y. Lee, S. K. Karuturi, H. H. Tan, C. Jagadish, *ACS Energy Lett.* **2020**, *5*, 611–622.

[89] J. L. Young, M. A. Steiner, H. Döscher, R. M. France, J. A. Turner, T. G. Deutsch, *Nat. Energy* **2017**, *2*, 17028.

[90] C. Noguez, *Phys. Rev. B* **2000**, *62*, Publisher: American Physical Society, 2681–2685.

[91] P. Monachesi, M. Palummo, R. D. Sole, R. Ahuja, O. Eriksson, *MRS Online Proceedings Library* **1999**, *579*, 59–63.

[92] W. G. Schmidt, N. Esser, A. M. Frisch, P. Vogt, J. Bernholc, F. Bechstedt, M. Zorn, T. Hannappel, S. Visbeck, F. Willig, W. Richter, *Phys. Rev. B* **2000**, *61*, R16335–R16338.

[93] A. Goryachev, L. Gao, R. P. J. van Veldhoven, J. E. M. Haverkort, J. P. Hofmann, E. J. M. Hensen, *Phys. Chem. Chem. Phys.* **2018**, *20*, 14242–14250.

[94] H.-J. Lewerenz, K. Schulte, *Electrochim. Acta* **2002**, *47*, 2639–2651.

[95] C. Hogan, R. Del Sole, G. Onida, *Phys. Rev. B* **2003**, *68*, 035405.

[96] F. Deißenbeck, S. Wippermann, *J. Chem. Theory Comput.* **2023**, *19*, 1035–1043.

[97] V Montgomery, R. H. Williams, R. R. Varma, *J. Phys. C: Solid State Phys.* **1978**, *11*, 1989–2000.

[98] M. Flieg, masterthesis, University of Tübingen, Tübingen, **2024**.

[99] M. Yamaguchi, K.-H. Lee, K. Araki, N. Kojima, *J. Phys. D: Appl. Phys.* **2018**, *51*, 133002.

[100] A. Clawson, *Mater. Sci. Eng. R-Rep.* **2001**, *31*, 1–438.

[101] W. Richter, J.-T. Zettler, *Appl. Surf. Sci.* **1996**, *100-101*, 465–477.

[102] M. Guidat, M. Löw, M. Kölbach, J. Kim, M. M. May, *ChemElectroChem* **2023**, *10*, e202300027.

[103] C. Bryce, D. Berk, *Ind. Eng. Chem. Res.* **1996**, *35*, 4464–4470.

[104] A. Acosta-Ortiz, S.& Lastras-Martínez, *Solid State Commun.* **1987**, *64*, 809–811.

[105] I. A. Ruiz Alvarado, M. A. Zare Pour, T. Hannappel, W. G. Schmidt, *Phys. Rev. B* **2023**, *108*, 045410.

[106] G. Sombrio, E. Oliveira, J. Strassner, J. Richter, C. Doering, H. Fouckhardt, *Micromachines* **2021**, *12*, 502.

[107] C. Doering, J. Strassner, H. Fouckhardt, *AIP Adv.* **2019**, *9*, 075116.

[108] J. F. Watts, J. Wolstenholme, *An introduction to surface analysis by XPS and AES*, J. Wiley, Chichester, West Sussex, England ; New York, **2003**.

[109] *Handbook of X-ray photoelectron spectroscopy: a reference book of standard spectra for identification and interpretation of XPS data*, Update, (Eds.: J. F. Moulder, J. Chastain), Perkin-Elmer Corporation, Eden Prairie, Minn, **1992**.

[110] In *Principles of SEM*, John Wiley & Sons, Ltd, **2008**, pp. 17–62.

ChemElectroChem

Review
doi.org/10.1002/celc.202300027

Chemistry Europe
European Chemical Societies Publishing

www.chemelectrochem.org

Special Collection

Experimental and Computational Aspects of Electrochemical Reflection Anisotropy Spectroscopy: A Review

Margot Guidat,[a, b] Mario Löw,[b] Moritz Kölbach,[a] Jongmin Kim,[a, b] and Matthias M. May*[a, b]

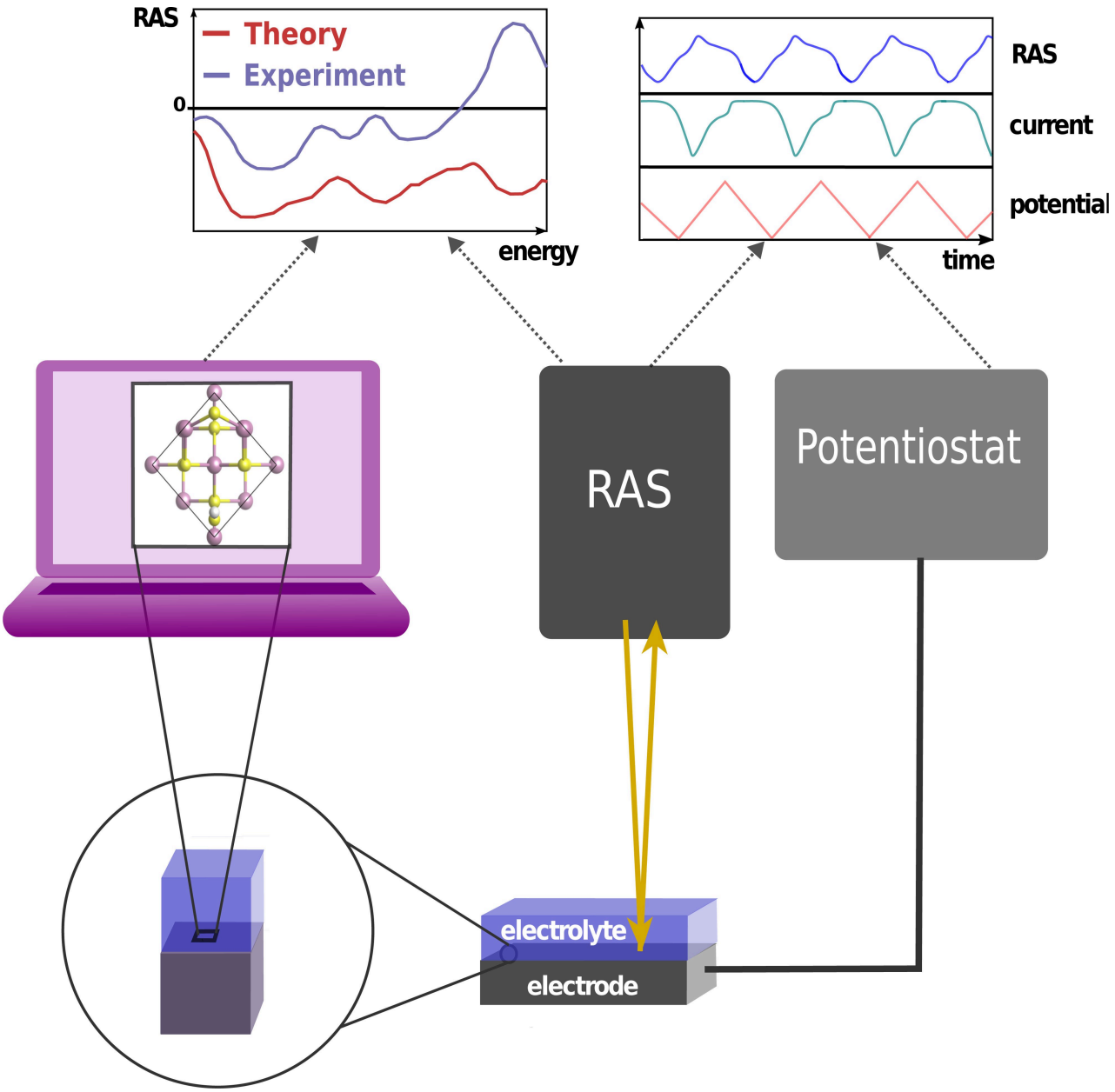

Electrode/electrolyte interfaces play a crucial role in many electrochemical energy conversion and storage technologies. Hence, a deep understanding of the interfacial structure, energetic alignment and processes is of high relevance and has triggered the development of a number of in situ and operando techniques. One approach for gaining information about the change in surface chemistry and structure on an atomic scale is reflection anisotropy spectroscopy (RAS). This review presents and discusses the continuing effort to develop RAS as an in situ optical probe for solid-liquid interfaces under applied potentials. Experimental and computational basic principles are presented and key challenges of electrochemical RAS are highlighted. Furthermore, we exemplarily demonstrate the potential of the method for spectroelectrochemistry, focusing on indium phosphide- and gold-aqueous electrolyte interfaces as exemplary case studies, and outline research directions for battery systems.

1. Introduction

Electrochemical energy conversion and storage is expected to play a crucial role in a global sustainable energy system based on renewable energy. Potential applications are for example electrolyzers,[1] photoelectrochemical (PEC)[2] as well as photocatalytic water splitting,[3] batteries[4], supercapacitors,[5] and carbon dioxide removal.[6] At the heart of any of such electrochemical energy conversion and storage systems is the electrode/electrolyte interface. Even though this interface is an essential aspect of improving these devices, the physical and chemical processes occurring at electrochemical interfaces still lack fundamental understanding for most systems.[7] Changes in the chemistry, morphology and homogeneity of the surface structure of electrodes caused by corrosion, oxidation, and ion ad-/desorption processes can hinder the efficiency and the durability of electrochemical devices.[8] A microscopic understanding and ultimately controlling and designing the relevant interfaces of (photo)electrodes are hence of particular importance.

Interface and surface phenomena have been widely investigated in ultra-high vacuum (UHV), with techniques such as ex situ X-ray photoelectron spectroscopy (XPS)[9] and ex situ secondary ion mass spectrometry (SIMS).[10] However, these methods fail to account for the electrochemical environment and the applied potential at the electrode. An intermediate approach towards a realistic electrochemical environment are emersion-type experiments, where electrodes are exposed to an electrolyte or water film under inert gas conditions, which has to be removed before transfer to an adjacent analysis chamber.[11] Although recent efforts are focused to further close these gaps by developing techniques such as near-ambient pressure XPS and in situ SIMS,[12,13] significant challenges remain. Specifically, the short inelastic path of photoelectrons in the electrolyte limits studies to thin film of electrolyte in the case of ambient pressure XPS, while the utilization of a traditional time-of-flight mass analyzer in SIMS limits the mass resolution.[14] A deep understanding of the interfacial structure, energetics and processes, however, requires analysis with (close-to) atomic resolution in realistic environments, i.e. with the presence of a thick electrolyte allowing sufficient mass transport for the (photo)currents of a working device.[15]

The electrochemical double layer (EDL), i.e. the charge distribution at the electrode/electrolyte interface, plays a key role in designing efficient electrodes for electrochemical energy conversion devices. Gaining insight into the EDL requires electrochemical characterization methods with both high time (100 ms or better) and spatial (Å-nm) resolution. The limitation of several techniques with respect to their resolution and the type of information they can provide is described by Esposito et al. in detail.[8] In short, most experimental methods fall into the two categories of scanning probe measurements (SPM) and pump-probe techniques. The former allow high spatial resolution, but are restricted in temporal resolution. Scanning photocurrent microscopy[16] and optical spectroscopies (Raman,[17] Infrared,[18] UV-visible) are hindered by their optical diffraction resolution ranges and their long acquisition time. The techniques with a higher spatial resolution, i.e. with atomic resolution, are also limited by long acquisition times and by the nature of the interaction, physical by the contact of a tip for atomic force miscroscopy (AFM)[19–21] and electrical by the applied voltages for electrochemical scanning tunneling microscopy (ECSTM).[22] These interactions can alter the surface and hence decrease the reliability of the obtained data. Nevertheless, the time acquisition of scanning probe microscopy techniques can be extended to the millisecond range with video-rate measurements.[23] Pump-probe techniques consist of ultrafast spectroscopic techniques with a fs-ns time scale for the investigation of electronic processes such as interfacial transfer of charge carriers and lifetimes of electronic and vibrational states.[24,25] Such techniques show high temporal resolution, but the information is typically non-local.

Another category of techniques that is worth to be mentioned are synchrotron-based X-ray techniques, where the in situ evolution of structural changes of electrodes can be monitored.[26–28] In addition to be non-destructive, and to have high penetration depth of hard X-rays into liquid electrolytes, surface resonant X-ray diffraction (SRXRD) has the advantage to access the atomic structure of both the electrode and the adsorbate adlayers with a reasonable temporal resolution. Combining these diffraction techniques with additional spec-

[a] M. Guidat, Dr. M. Kölbach, J. Kim, Dr. M. M. May
Institute of Physical and Theoretical Chemistry, Tübingen D-72076, Germany
E-mail: matthias.may@uni-tuebingen.de
[b] M. Guidat, M. Löw, J. Kim, Dr. M. M. May
Universität Ulm, Institute of Theoretical Chemistry, Ulm D-89081, Germany

Special Collection An invited contribution to the Electrochemical Nibbles for Computational Chemists Special Collection

troscopies can give further insight into chemical composition and charge distribution at the electrochemical interface. However, the need to set wavelength and/or polarization state of the X-rays at sufficiently high intensities requires a synchrotron facility. In this review, however, we will focus on lab-based techniques that at least have the potential for a higher sample-throughput and refer the reader to the extensive literature in this field.[26,27]

In addition to the methods mentioned above, reflection anisotropy spectroscopy (RAS) is a surface-sensitive method that has the potential to help understanding the structure and the fundamental properties of electrochemical interfaces at an atomistic level with an adequate time resolution (down to a few milliseconds).[29] In short, RAS probes the difference in reflectivity of broad band light at near-normal incidence between two orthogonal directions of a single-crystal surface plane, scaled with the overall reflectivity. An adequate interpretation of experimental RAS data does, however, require both experimental and theoretical considerations to derive a comprehensive understanding of the structure-property relationship of solid-liquid interfaces. To compute the surface optical properties, the surface dielectric function determined from density-functional theory (DFT) is considered.[30] Some previous studies[31–33] have already determined the surface optical properties from first principles for the study of surface structure and surface reconstruction in vacuum. In particular, Schmidt et al. have performed many RAS investigations on III–V(100) surfaces in vacuum with quantitative and qualitative analysis.[34–38] From an electrochemical perspective, however, this approach neglects effects from the solid surfaces in contact with molecules from a realistic bulk electrolyte.[39] It is challenging to accurately calculate theoretically derived RAS, since DFT for the underlying ground-state does, in a purely surface-science approach involving vacuum, not necessarily describe the electrode-electrolyte interaction comprehensively. One fundamental challenge consists in including the polarization generated by mobile ions to preserve electric boundary condition from the supercell to the ionic solution.[40] The main constraints are the simulation of applied electric field and the simulation of realistic electrolyte, limited at best to a mono-layer for large supercells. Model systems with simplified, few-monolayer approximations for electrolytes can, however, be a bridge towards more realistic electrochemical systems.[39]

In this review, we present and discuss the technique of RAS, with a focus on its development towards an in situ/operando spectroscopy in electrochemical environments. In this regard, the need of method development from an experimental and a computational point of view using well-defined reference systems is highlighted. As case studies, we demonstrate the application of electrochemical RAS for aqueous electrolyte systems with the interfacial structures of indium phosphide and gold in contact with acidic electrolytes. Moreover, we discuss potential applications of RAS to investigate the solid-electrolyte interphase in battery systems.

Margot Guidat is currently a PhD student in physical chemistry at Tübingen University. She received her M.Sc. in chemical engineering from ENSCR at Rennes university in 2020. Her research interests include in situ/operando spectroscopic techniques for elucidating electrochemical processes at solid-liquid interfaces of both solar-water-splitting and aluminum battery systems.

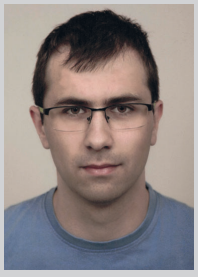

Mario Löw is currently a PhD student at Ulm University. He received his M.Sc. in chemistry from Ulm University in 2021. His research interests include the operando investigation of the interface in rechargeable magnesium batteries.

Jongmin Kim did his PhD studies Humboldt-University of Berlin. He currently holds a postdoctoral position at Tübingen University, where his research focuses on computational investigation of electrochemical interfaces in water–splitting devices as well as further method development within density-functional theory.

Matthias M. May studied physics in Stuttgart, Grenoble, and Berlin, with a focus on condensed matter and computational physics. His PhD studies (2011–2015) at Humboldt-Universität zu Berlin and Helmholtz-Zentrum Berlin targeted III–V semiconductors for solar water splitting. He spent two years as postdoctoral fellow at the Chemistry Department of the University of Cambridge, funded by the German Academy of Sciences Leopoldina. He leads an Emmy-Noether group at the Institute of Physical and Theoretical Chemistry at Tübingen University. His scientific interests lie in the area of photoelectrochemical energy conversion and solid-liquid interfaces.

2. From epitaxial growth to electrochemical interface monitoring

RAS is a linear, differential optic probe that measures the difference in reflectivity of normal incident light between two orthogonal directions of the surface normalized by the overall reflectivity. The definition of the RAS signal is given in equation 1. r_x and r_y are the complex eigenvalues of the Fresnel reflection coefficient tensor along the two axes x and y in the surface plane. In case of an anisotropic surface, r_x and r_y have different values and their difference normalized by the average reflectivity represents the optical anisotropy of the sample.[41] While both real and imaginary parts are measured, experimental literature typically refers to the real part, a convention that we will also employ for the spectra displayed in the following sections.

$$\mathrm{RAS} = \frac{\Delta r}{r} = 2 \cdot \frac{r_x - r_y}{r_x + r_y} \tag{1}$$

It is noteworthy to mention that one can also probe the anisotropy of the reflectance, i.e. the (real) square of the Fresnel reflection amplitude, $R = |r|^2$. This case is then referred to as reflectance anisotropy spectroscopy, where the relation $\mathrm{Re}\left(\frac{\Delta r}{r}\right) \approx \frac{1}{2}\frac{\Delta R}{R}$ holds true for $\Delta r \ll r$.[42,43]

2.1. Experimental realization

The basic working principle of RAS and the configuration used in this study are illustrated in Figure 1. For a more detailed description of the working principle of RAS, we refer the reader to the work of Haberland et al.[45] When linearly polarized light in the UV-visible range is reflected by an anisotropic crystalline surface, the polarization becomes elliptic and reaches the photoelastic modulator (PEM) of the spectrometer. Due to its birefringent property, the PEM induces a retardation between the two components of the elliptic polarization along the x and y surface crystal direction, resulting in an oscillating signal. After the modulated polarized light has passed through an analyzer, its intensity (I) now depends on the polarization state of the light, the retardation, and the modulation frequency ω of the PEM. This is then detected by a photomultiplier and demodulated by a lock-in amplifier. The intensity, given in equation 2, is thus proportional to the optical ratio shown in the equation 1.[41]

$$\mathrm{Re}\left(\frac{\Delta r}{r}\right) = \frac{\sqrt{2} I_{2\omega}}{I_0} \tag{2}$$

To allow sufficiently high reflectivity and to limit the complexity of the anisotropic signal, RAS is restricted to single crystals with very low surface roughness (< 10 nm). The anisotropy of the signal can arise from both the surface and the bulk of the sample due to the relatively large penetration depth

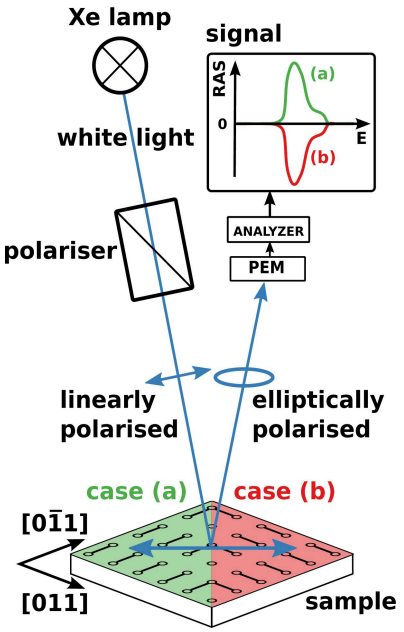

Figure 1. General principle of RAS for the case of a dimerized, cubic (100) surface. The rotation of the dimers by 90 (case a, green vs. case b, red) switches the sign of their contribution to the spectrum. Adapted from Ref. [44] with permission from the ACS. Further re-use subject to permission by ACS.

of light. To get a signal exclusively from the surface, the symmetry of the bulk in the plane of the surface must be isotropic whereas the symmetry of the surface must be anisotropic. Cubic systems with (100) and (111) surfaces orientation have isotropic symmetry and in principle should give a zero RAS signal. However, they can undergo a surface reconstruction. For example, annealing Au(100) allows obtaining a pseudo hexagonal reconstructed Au(100)-(5 × 20) surface which breaks the symmetry between the bulk and the surface and gives a RAS signal exclusively from the surface. For alloys like InP, their surface typically reconstruct in dimer-rich surfaces which present some anisotropy. For cubic systems with (110) surfaces, the RAS signal is more complex because the signal is also arising from the bulk. However, a break in the symmetry between the bulk and the surface gives different contribution to the RAS signal and surface evolution can be monitored. For instance, it is possible to distinguish a (1 × 2) from a (1 × 1) or (1 × 3) reconstruction of Au(110). Yet for example in the case of cubic (100) surfaces, whose bulk is isotropic, it is possible to exclusively get information about the surface.

Several related optical methods currently exist for the study of surface structure and chemistry with a sub-nanometer surface sensitivity. Table 1 shows a summary of the most common of these techniques to distinguish and clarify their differences and similarities with RAS. Surface differential reflectivity (SDR) is very similar, also by name to RAS because the information extracted from both measurements are very similar. However, SDR is applicable for both isotropic and anisotropic surfaces. Since the technique consists of measuring the reflectivity of a sample's surface before and after exposure

Table 1. Main differences between RAS and other related spectroscopic techniques.

Method	RAS	SE[a]	SDR[b]	ER[c]	RAIRS[d]
Principle	$2 \cdot \frac{r_x - r_y}{r_x + r_y}$	$\frac{r_p}{r_s}$	$\frac{R_{clean}(E) - R_{ox}(E)}{R_{ox}(E)}$	$a\Delta\varepsilon' + b\Delta\varepsilon''$	$\int_\nu \ln\left(\frac{R_0}{R_{adsorbates}}\right) d\nu$
Time resolution	few ms	few fs	few ms	few ms	< 1 s
sample type	single-crystal with anisotropic surface	thin film	single-crystal	thin film	single-crystal
typical energy range (eV)	1.5–5	1–6	0.5–5	0.5–5	0.05–0.5
1 or 2 step measurement ?	1 step	1 step	2 steps	2 steps	2 steps

[a] spectroscopic ellipsometry. [b] surface differential reflectivity. [c] electroreflectance. [d] reflection-absorption infrared spectroscopy.

(E) to an external gas (here oxygen as an example in Table 1), the acquisition of one spectrum requires two different experimental conditions. The variation in reflectivity between clean surface and surface after exposure can arise from surface electronic states, electric fields, or optical properties of the growing oxide layer.[46] Note that although SDR resembles RAS, the type of provided information is different, i.e. SDR allows learning about molecular adsorption, but not about surface ordering and reconstructions.

Spectroscopic ellipsometry (SE) is based on the same principle as RAS. It measures the change of polarization state between the incident and reflected light on a surface. However, while RAS is operating at near-normal incidence, SE is measured at oblique incidence. Therefore, the polarized light is composed of components parallel (rp) and perpendicular (rs) to the plane of incidence. Since the set-up is commonly oriented at 45 from the incidence plane, a signal is emerging from measurements also for isotropic surfaces.[47,48] This technique is mainly used to determine the dielectric function and the thickness of thin films.[49]

First introduced by Seraphin,[50] electroreflectance (ER) is used for the determination of internal parameters of thin-film solar cells such as the internal electric field and the band gaps of the different junctions.[51] RAS, on the other hand, is a "static" reflection technique which allows accessing the real part of the optical response. While in ER spectroscopy, in addition to the set-up illustrated in Figure 1, an external AC voltage is applied between the backside and the front side of the p-n junction. This applied AC voltage allows accessing both real and imaginary parts of the optical response of the interface, respectively, represented by the real and imaginary part ε' and ε'' of the dielectric function in Table 1. Thus, the AC voltage "modulates" the reflection, amplifying the response generated by the electric field and suppressing the constant background of reflection.

Finally, reflection-absorption infrared spectroscopy (RAIRS) measures the difference in reflectivity of the surface with ($R_{adsorbates}$) and without (R_0) adsorbed molecules.[52,53] Studying adsorbed monolayer and submonolayer on metal surfaces by RAIRS allows accessing information about their molecular structure, their chemical identity and adsorption site.

2.2. Computational aspects

The great challenge for RAS is that, without correlation to other complementary experimental methods, it is not a straightforward quantitative technique. Yet this correlation with other techniques is certainly time-consuming, but sometimes not possible at all. For this reason, complimentary computational efforts are a viable alternative. The following section is not an in-depth picture as can be found in references [41] and [43], but gives a first overview of computational RAS.

Reflection anisotropy is associated with the dielectric response function of a semi-infinite system. According to the three-phase model devised by McIntyre and Aspnes,[54] the dielectric response function can be described by dielectric functions of bulk and vacuum layers and a surface layer with thickness *d*.

Equation 1 can be rewritten in the following manner.[41,43]

$$\frac{\Delta R}{R} = \frac{4\pi d}{\lambda} \mathrm{Im}\left[\frac{\Delta\varepsilon_s}{\varepsilon_b - 1}\right], \tag{3}$$

where $\boldsymbol{\varepsilon}_s$ and $\boldsymbol{\varepsilon}_b$ represent complex dielectric functions ($\varepsilon = \varepsilon' + i\varepsilon''$) of the surface and bulk, respectively, and λ is the wavelength of the light. When the first energy derivative of $\boldsymbol{\varepsilon}_b$ is employed in this model, it yields to the subsequent equations:

$$\frac{\Delta R}{R} = \frac{4\pi d}{\lambda}\left[A\Delta\varepsilon_s'' - B\Delta\varepsilon_s'\right], \tag{4}$$

where

$$A = \frac{\varepsilon_b' - 1}{(1 - \varepsilon_b')^2 + (\varepsilon_b'')^2}, \tag{5}$$

and

$$B = \frac{\varepsilon_b''}{(1 - \varepsilon_b')^2 + (\varepsilon_b'')^2}. \tag{6}$$

By using the half-slab polarizability α^{hs}, equation 3 transforms into[55,56]

$$\frac{\Delta R}{R}(\omega) = \frac{4\omega}{c}\mathrm{Im}\left[\frac{4\pi(\alpha_{xx}^{hs}(\omega) - \alpha_{yy}^{hs}(\omega))}{\varepsilon_b(\omega) - 1}\right]. \quad (7)$$

Likewise, the half-slab polarizability can be applied to equation 4.

For a symmetric slab, α^{hs} can be calculated within the independent-particle random phase approximation (IP-RPA) that neglects the local field effect:[31]

$$\mathrm{Im}\left[4\pi\,\alpha_{xx}^{hs}(\omega)\right] = \frac{4\pi^2 e^2}{m^2\omega^2 A}\sum_{\mathbf{k}}\sum_{v,c}|P^x_{v\mathbf{k},c\mathbf{k}}|^2 \times\delta(E_{c\mathbf{k}} - E_{v\mathbf{k}} - \hbar\omega). \quad (8)$$

In equation 8, $P_{v,c}$ is the transition matrix element of the momentum operator, and A is the surface area. Calculating this polarizability requires the Kohn-Sham (KS) single-particle eigenvalues and wave-functions. The eigenvalues and wave-functions need to be calculated from DFT or other quantum chemistry methods to be used as an input in the IP-RPA scheme. Unfortunately, this IP-RPA scheme underestimates excitation energies due to the underestimated KS eigenvalues, since the unphysical self-interaction and the derivative discontinuity in the exchange-correlation functional result in an incorrect band gap for semiconductors or insulators. A simple way for correcting this limitation is to consider a scissors shift operator.[31] This technique is useful for semiconductors or insulators. However, it does not apply to materials where many-body effects are crucial, such as metallic and low-dimensional systems or oxides.

If the slab is nonsymmetric, a real-space cutoff approach to capture the actual surface response is needed. By considering the cutoff θ, modified matrix elements are constructed as follows[31]

$$\tilde{P}^x_{v\mathbf{k},c\mathbf{k}} = -i\int d\mathbf{r}\psi^*_{v\mathbf{k}}(\mathbf{r})\theta(z)\frac{\partial}{\partial r_x}\psi_{c\mathbf{k}}(\mathbf{r}), \quad (9)$$

and the corresponding polarizability becomes

$$\mathrm{Im}\left[4\pi\alpha_{xx}^{hs}(\omega)\right] = \frac{8\pi^2 e^2}{m^2 w^2 A}\sum_{\mathbf{k}}\sum_{v,c}\left[P^x_{v\mathbf{k},c\mathbf{k}}\right]^*\tilde{P}^x_{v\mathbf{k},c\mathbf{k}} \times\delta(E_{c\mathbf{k}} - E_{v\mathbf{k}} - \hbar\omega)\,. \quad (10)$$

A typical computational workflow to compute equation 7 using equations 9 and 10, which was for instance employed in Refs. [39] and [57], is to start with the structural optimizations of slabs on a DFT level, for instance with the CP2K code,[58] using the generalized gradient approximation as parameterized by Perdew-Burke-Ernzerhof for the exchange-correlation functional.[59] The Yambo code[60,61] readily provides a module for computational RAS in the IP-RPA approach, providing the reflectance, i.e. $\Delta R/R$. Underestimated bandgaps for semiconductors can be corrected by a scissor operator. Using Yambo does, however, require a ground-state calculation in QUANTUM ESPRESSO[62] as an intermediate step. For the bulk dielectric function, either experimental or computational input can be employed.

2.3. Application of RAS in surface science

RAS was first developed by Aspnes et al. in the 1980s[63] to establish an in situ optical probe to achieve a layer-by-layer surface control in III–V semiconductor growth systems as for example molecular beam epitaxy (MBE)[64] or metal-organic vapor phase epitaxy (MOVPE).[65] Since then, the technique has been widely used for the study of semiconductor surfaces and interfaces in growth environments. In particular, RAS studies on GaAs have not only demonstrated how the spectroscopy can be used to control epitaxial growth and the preparation of specific surface reconstructions, but also the possibility to investigate layer-by-layer removal of GaAs as a protective cap layer for the preparation of fresh surfaces was shown.[66–68] More recently, Sombiro et al. have pointed out the utilization of RAS to extract etching rate and etch-depth resolution from the analysis of Fabry-Pérot oscillations generated by reactive ion etching of GaAs/AlGaAs multi-layer structures.[69] Also dry etching in hydrogen ambient was studied by Brückner et al.,[70] who report that RAS reveals a layer-by-layer removal from Si(100) single-crystals in H_2 atmosphere at elevated temperatures. This study suggests that RAS is a relevant tool for the development of direct growth processes of III–V/Si solar cells, since well-defined monolayer etching allows single domain preparation. In principle, the fitting methods used to determine growth rate, etching rate, and etch-depth resolution from transients in dry processes can be adapted for transients measured during electrochemical processes.

Investigations on the adsorption of constituents of an electrolyte – typically water – can serve as an intermediate step between UHV and gas-phase studies on the one side and the full electrochemical environment with the solid/liquid phase boundary on the other side.[44,71–74] The great advantage of such a type of study is that the surface stays in inert gas or vacuum conditions prior to and after water adsorption, which allows to precisely characterize and control the initial surface configuration by standard surface science tools. This can help to understand, for instance, the impact of step edges on the reactivity of a given surface[74] or derive activation energies.[71] The downside of such a type of experiment is that the comparability with the realistic electrochemical environment is limited at best. Low-temperature water adsorption from the gas phase[73] allows to adsorb multi-layer water (ice) on a surface, but reactivity of the interface might be qualitatively different from the ambient temperatures of a typical electrochemical experiment. Adsorption at ambient temperatures, on the other hand, limits the maximum water layer thickness typically to a sub-monolayer.[44,72] For comprehensive overviews about the application of RAS in a number of fields during the past decades, we refer the reader to the reviews by Weigthman et al.[41] and Supplie et al.[42] which focus mainly on applications in surface science.

3. Emergence, principles, and application of electrochemical RAS

Implementing (photo)electrochemical surface conditioning for photoelectrodes could enable novel process routes at potentially low costs, but the understanding and control of the related interface (electro)chemistry is so far limited.[75] Nevertheless, such surface functionalization approaches already demonstrated their use for achieving highest solar-to-hydrogen efficiencies by effective surface protection against corrosion.[75,76] In this regard, with its straightforward set-up operating at near-normal incidence configuration (Figure 2), RAS represents a potential tool for the in situ/operando monitoring of (photo)electrochemical surface passivation with a sub-nanometer control of surface modifications.

More generally, RAS can be developed as probe of the electrochemical double layer and can easily be coupled with intrinsically electrochemical characterization methods such as chronoamperometry (CA) or cyclic voltammetry (CV). The correlation between RA spectra and cyclic voltammogramms can complement the understanding of electrochemical processes from CV by providing access to charge, potentials, and chemical species with a sub-nanometer spatial resolution in the surface normal. For instance, some surface reconstructions are not distinguishable on the cyclic voltammogramm, because they involve non-Faradic processes with very small change in capacitance of the EDL (see Figure 3) and therefore very small charging currents. Thanks to RAS, the different surface reconstructions and surface steps are observable and distinguishable.[77] In this regard, since the first RAS implementation, there has been a rapid growth of the field and RAS was used on metallic systems in electrochemical environments or molecular films on metals.

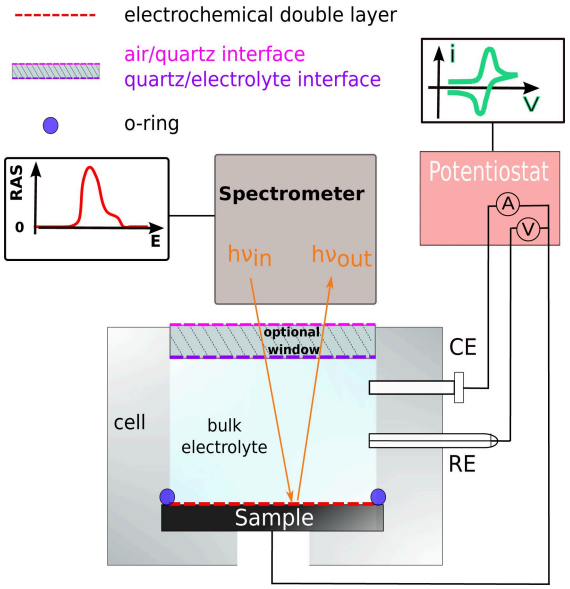

Figure 2. Cross-section of a typical cell setup for electrochemical RAS. CE and RE refer to counter and reference electrode, respectively. Adapted from Ref. [57] with permission from the Royal Society of Chemistry.

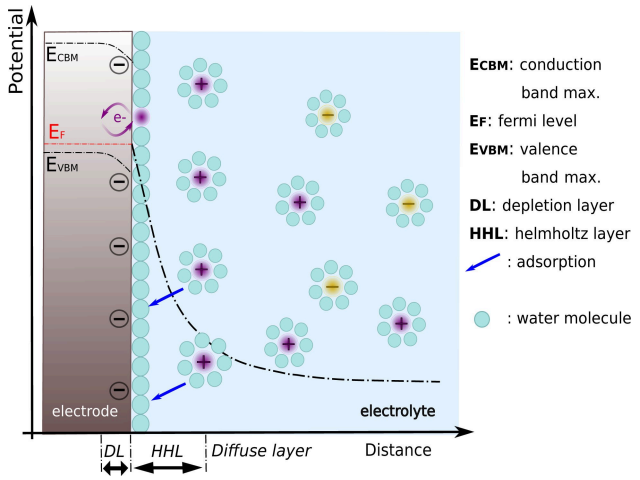

Figure 3. Electrochemical interface of a p-type semiconductor with an electrolyte forming a depletion layer in the dark after equilibrium. The positive and negative charge on the electrolyte side account for solvated ions. Inspired by Gerischer.[78]

3.1. Application of RAS in electrochemistry

Here, we now follow the literature on first "electrochemical RAS" (EC-RAS) applications, i.e. RAS applied in electrochemical environments. First applications of EC-RAS were dedicated to the study of different gold single-crystalline surfaces in aqueous electrolytes. These studies have outlined the relationship between surface charge and reconstruction by measuring RA spectra for interfaces between Au(110) and aqueous electrolytes while potentials were applied to Au(110).[79,80] Yet, their investigation focused exclusively on experimental EC-RAS and were corroborating previous findings evidenced by STM. Similarly, Sheridan et al. have combined experimental RAS with the modelling of the surface optical response – not full ab initio computational spectroscopy – to investigate the impact of surface phases transition and surface roughening of Au(110) in sulfuric acid under applied voltage on the electronic structure.[81] Again, to support their findings, the authors refer to results from other studies on the same system, for instance with EC-STM and ex situ low-energy electron diffraction (LEED).[82,83] This emphasizes that RAS, at least in the initial phase of system exploration, is not a high-throughput technique and that it in principle needs to be supplemented by other surface-sensitive techniques. In such an exploratory phase, it is typically not possible to identify chemical species directly from the spectra. After correlation with complementary experimental techniques or computational spectroscopy, however, an assignment of spectral features to chemical species is often possible.

Mazine et al. combined experimental and computational RAS – the latter for a slab in vacuum – with EC-STM in their study on interfaces of gold with aqueous electrolytes.[84,85] Correlating STM images and RA spectra show the relationship between surface charge and surface reconstruction and steps, while attempts on including local field effects on theoretical

RAS are made to enlighten the origin of the transitions obtained for the different reconstructions.

In addition to the determination of surface states, surface roughness and surface phase transitions, it is possible to deeply investigate surface transformations, ion adsorption, and solid electrolyte interphase formation processes by evaluating the spectral features during the transition from clean to adsorbate-covered cubic surfaces in both liquid and non-liquid environments. Extensive research on the Cu(110) surface has shown the sensitivity of RAS to molecular adsorbate orientation,[86,87] and its potential as a surface analytic tool for kinetic studies of molecule adsorption and desorption, as well as their memory effect on the surface.[88–90] Later on, the study of ad/desorption of molecules in the gas phase on Cu(110) has been extended to electrochemical environments.[91–93] All studies have mainly investigated chlorine ion adsorption on Cu(110) in hydrochloric acid. Goletti et al. used EC-RAS together with EC-STM and ex situ LEED to identify the two-step process in the anodic and cathodic region of the CV.[92] They have ruled out the adsorption (desorption) of two different anions and have demonstrated that chlorine anions are involved in one adsorption (desorption) process followed by a surface reconstruction (deconstruction). The latter study on copper has performed EC-RAS on the same system with slightly different potential range and also show together with EC-STM the reversible formation of stripes and channels induced by chlorine ad/desorption.[93] Very often, specific spectral features of RAS are directly correlated with the surface coverage. By fitting transient measurements with adsorption isotherm models, it is then possible to access some kinetic and thermodynamic quantities.[74,93] Vazquez-Miranda et al. have particularly demonstrated the extraction of the formation energy of adsorption of chlorine ions and lateral interaction parameter from a transient by fitting it with Frumkin-type isotherms.[93,94] Furthermore, by correlating the current peaks measured in CV with the derivative of the RAS-transients, they could derive the dependency between applied potential duration and copper/chlorine chemical reactions.

Recently, the use of RAS in combination with AFM and CV has unraveled the mechanism responsible for porphyrin dissolution in acidic media,[95] a more complex system involving organic molecules. In their approach, several types of porphyrin nanocrystals were vacuum-deposited on graphite substrates and cycled in sulfuric acid. The correlation of RAS with the current density revealed that the single electron transfer involved in the oxidation of porphyrin in a more cationic form is the precursor of its dissolution. The study of porphyrin-liquid interfaces is relevant for energy-storage systems such as post-lithium batteries, where battery based on an alkyne-substituted-porphyrin complex are under development.[96]

3.2. EC-RAS setup

Figure 2 shows a typical electrochemical RAS setup, where the single-crystal is in contact with the liquid electrolyte. The sample of interest (working electrode) is mounted together with a counter electrode and an optional reference electrode in a photoelectrochemical cell filled with an electrolyte. Compared to conventional RAS setups, additional potential measurement artefacts in the RA spectrum have to be carefully considered in this configuration, e.g. artefacts from the liquid medium, as the setup now comprises media of at least three different refractive indices, as opposed to two for a vacuum or gas-phase setup. If a quartz window is present in the photoelectrochemical cell, as indicated in Figure 2, it affects the refraction angle of the light at the air-quartz and quartz-electrolyte interfaces due the different refractive indexes of the media. Hence, the optical path between the spectrometer and the sample has to be carefully adjusted. Furthermore, if non-homogeneous mechanical stress is applied to the window, its dielectric tensor is no longer scalar, leading to a stress-induced contribution of the window to the signal. In principle, the photoelectrochemical cell can also be used without a quartz window. The air-electrolyte interface, however, still changes the refraction angle of the light and hence modifies the light focal point. Also vibration damping might be needed in this case, as vibrations disturb the electrolyte surface and hence the optical path. Baseline effects can be largely compensated by adequate baseline correction using an optically isotropic standard such as an oxidized Si(100) sample, a reference of well-defined anisotropy such as Si(110), or the sum of two spectra where the sample has been rotated by 90 in between.

3.3. Important aspects of the EDL

Literature on electrochemical RAS has so far mainly been limited to metallic systems. This is most likely due to the additional complexity introduced by semiconductor-electrolyte contacts. One factor is almost certainly the reduced structural stability against electrochemical corrosion of most semiconductors when compared to many (noble) metals. Furthermore, the interfacial energetics are altered, as semiconductor-electrolyte interfaces have additional potential drops compared to metal-electrolyte interfaces whose potential drop region is limited (mainly) to the Helmholtz layer (HHL). Figure 3 illustrates a simple case of the electrochemical double layer of solid-liquid interfaces for a semiconductor electrode in the dark. When the semiconductor is in contact with an electrolyte, the charges in the solid need to be redistributed to reach equilibrium due to the Fermi level E_F differences between solution and electrode. The E_F of the semiconductor aligns with the E_F of the red-ox species resulting in a band bending of the conduction and valence band energies (respectively denoted E_{CB} and E_{VB}) forming in this case with a downward band-bending of a p-type semiconductor a depletion layer. Therefore, it is not possible to neglect the tunneling process as for metal electrodes.[98,99] As sketched in Figure 4, the band bending, which depends on the externally applied voltage/irradiation, the red-ox potential from the electrolyte, and the doping level of the substrate, can shift electronic states of the surface across E_F. Thus, charge transfer between the electrode and the ions adsorbed at the surface can occur via conduction/valence band and via surface states.[97]

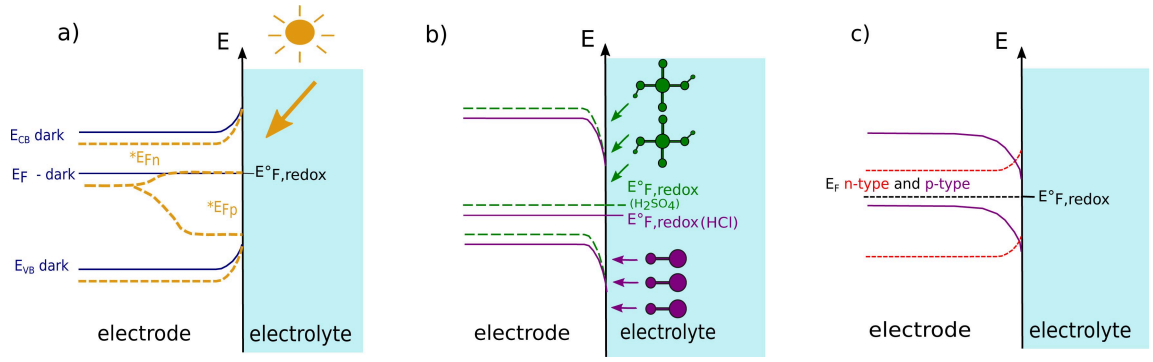

Figure 4. Energetic band diagrams showing the influence of the irradiance, the doping type, and the electrolyte on the EDL and the optical properties of an idealized semiconductor-liquid interface (no surface passivation/corrosion). The electrode is considered as photo-cathode for solar water splitting, and H^+/H_2 is the most active redox couple. Interfacial layers and charge-carrier recombination[97] are ignored for the sake of simplicity. a) dark and illuminated (dotted line) EDL of n-type semiconductor. b) EDL of p-type semiconductor influenced by the charging effect of H_2SO_4 (dotted lines) and HCl electrolytes (0.01 M). c) EDL for n and p-type semiconductors.

Band bending arises from an electric charge exchange between the bulk and the surface (states) of the semiconductor. The resulting electric field modifies the dielectric function of such a material and therefore contributes to the anisotropy of the associated RA spectrum, making it an indirect probe of interfacial electric fields.[100] This effect, called the linear electro-optic effect, may have different origins. On the electrode side, the electric field is influenced by the doping level of the substrate, while in the space-charge layer on the electrolyte side, it depends on molecular dipoles and their orientation with respect to the surface, but also on the ion distribution. An electric dipole within an adsorbed molecular film can also affect the integrated electric field. External parameters that impact the electric field are certainly the applied voltage, but also the irradiation of the system. The development of an illumination-induced photovoltage adds another layer of complexity. At a given light intensity, the photovoltage also depends on the charge-carrier recombination, which can, and in most cases will, change upon corrosion or potential-induced restructuring of the interface.[97] Yet as RAS is an optical technique, a minimum level of illumination by the measurement spot cannot be avoided.

Investigating these different contributions of the electric field by RAS can help elucidate surface reconstructions during molecular chemisorption processes and study preferential adsorption sites from the evidence of adsorbed molecular films.[101] Taken together, these specifics of the EDL of the semiconductor-electrolyte system show that these interfaces can be more complex than for metals, which also impacts spectroelectrochemistry. Figure 5 compares their different impact on the EDL and on the optical properties of semiconductors. The orange and red spectra, respectively corresponding to n-type with and without additionnal illumination, are almost identical. It indicates that additional illumination, in the considered situation, has hardly no influence on the optical properties of the interface. In this case, n-type InP is acting as a photo-cathode for the reduction of protons. Hence, as showed on Figure 4 (a), the redox potential aligns with the the quasi-Fermi level of the electrons ($^*E_{Fn}$), resulting in a minor increase

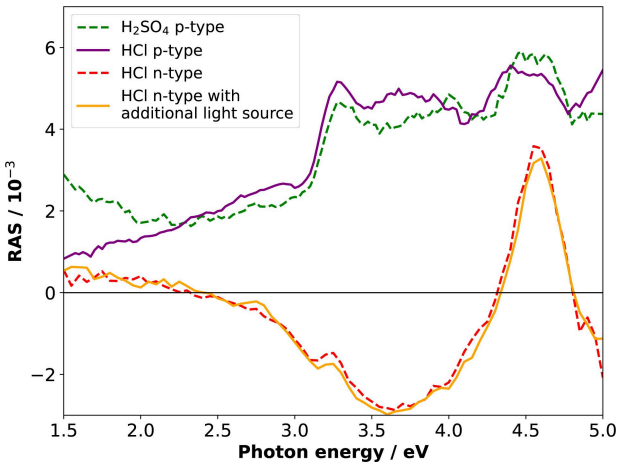

Figure 5. RA spectra of InP(100) for the different conditions a), b) and, c) illustrated on Figure 4. Here, the doping shows a major effect, the electrolyte a minor effect, and the bias illumination essentially none.

of the photovoltage. Similarly to the spectra with and without additional illumination, the spectra associated to p-InP-HCl and p-InP-H_2SO_4 interfaces (purple and green spectra, respectively) resemble each other. The electrolytes have the same concentration, but different pH, which influence the redox potential of H^+/H_2 and therefore modify the position of the Fermi level and the band bending (see Figure 4 (b)). For this reason, the type of electrolyte has a minor effect on the related RA spectra. The most noticeable changes between the RA spectra provided by Figure 5 are in fact due to a difference in doping levels. Since E_{CB}, E_{VB} and E_F depend on the charge carriers concentrations, the doping level strongly impacts the electronic structure and therefore the optical properties at the interface.

3.4. Aqueous electrolyte systems I: InP(100)

As a first example for the application of electrochemical RAS, we present an investigation of the interfacial structure of InP(100) in contact with 0.01 M hydrochloric acid (HCl). Such

III–V semiconductor/electrolyte interfaces play a crucial role in high-efficiency direct PEC solar water-splitting devices. These systems produce hydrogen via combining water electrolysis and solar energy harvesting in a single process and have been shown to achieve highest solar-to-hydrogen efficiencies.[75] However, even though significant progress has been made in improving the stability of III–V semiconductors in aqueous electrolytes, corrosion is still preventing practical applications.[76] Hence, a detailed understanding of the processes at the solid/electrolyte interface is crucial for the realization of a viable solar-water splitting technology based on III–V semiconductors. Therefore, we have chosen InP(100) as a first case study for an electrochemical RAS analysis, as it is available in high single-crystalline quality, but also subject to rapid electrochemical corrosion. A more detailed investigation with experimental details can be found in our recent publication.[57]

Figure 6 (a) presents a 2D color-coded graphic (colorplot) showing continuously acquired RA spectra in situ under CV conditions. The starting point were samples prepared from *epi-ready* InP(100) wafers, but without pre-treatment of the surface prior to immersion into the electrolyte. The corresponding applied potential as a function of time, and the cyclic voltammogramm are shown on the right-hand side of Figure 6 (a) and in Figure 6 (b), respectively. Note that a baseline correction is applied to all the spectra using the signal of an optically isotropic Si(100) crystal in water. Such a continuous type of measurement is helpful for the exploration of a novel system, giving a broad spectral overview at the expense of temporal resolution.

In Figure (b), the cathodic current for the corresponding CV in the voltage range between −0.4 V to −1.3 V can be ascribed to the reduction of InP into phosphine and metallic In. The latter can then further react with HCl to form an InCl interfacial film starting from potentials lower than −0.4 V vs. (Ag/AgCl).[57] The cathodic current density starting from around −0.4 V and reaching a plateau at −1.3 V is associated with the hydrogen evolution reaction. Here, the current density is limited in rate by the low overall photocurrent from the incident light of the spectrometer, while below −1.7 V, the hydrogen production is no longer photo-current limited.[57] This highlights again the challenge that for a semiconductor, the optical probe can impact the photoelectrochemical response of the system under investigation.

The formation and disintegration of the InCl film strongly depends on the electrolyte concentration. The literature shows that for high HCl concentration (0.5 M), in the anodic region,

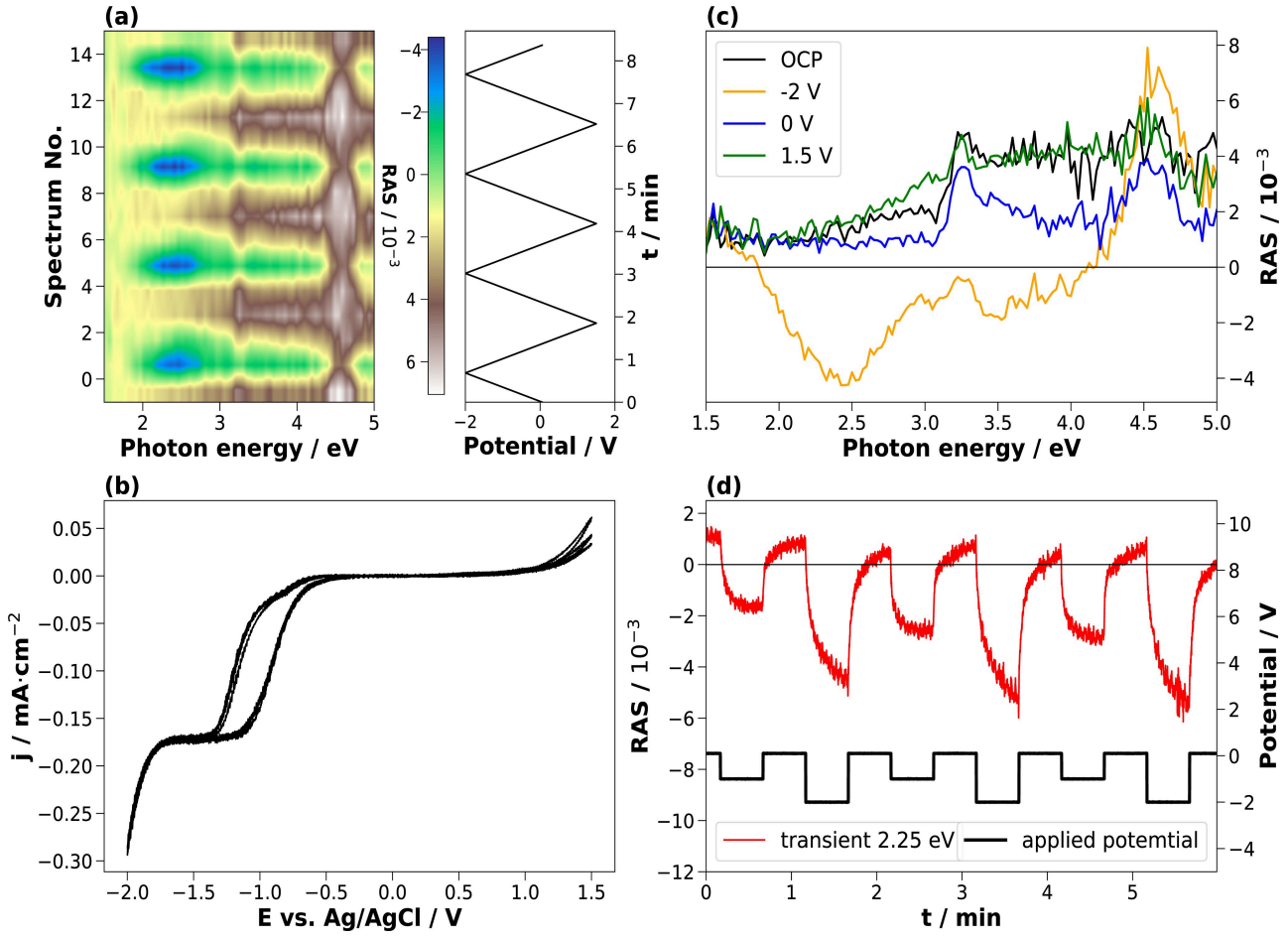

Figure 6. P-type InP(100) in contact with 0.01 M HCl. Left: Colorplot (a) of the InP(100) surface in contact with the electrolyte under cyclic voltammetry conditions (b), scan from open-circuit potential (OCP) towards −2 V and then to 1.5 V for 3 cycles, with a scan rate of 50 mV s^{-1}. Right: RA spectra in the electrolyte (c) at OCP and during chronoamperometry, and transient at 2.25 eV (d) acquired while potential steps are applied.

InCl then only partially dissolves into In^{3+} and Cl^- at −0.3 V vs. (Ag/AgCl). Therefore, the formation of InCl is non-reversible, and a several nm-thick passivation layer builds up over the cycles.[102–104]

In the case of 0.01 M HCl, however, the CV shows, in terms of the interfacial structure, fully reversible cathodic and anodic processes. The reversibility of the processes is also observed on the colorplot (CP) by a reversible build-up of characteristic anisotropies in the cathodic and anodic potential ranges. The strong anisotropic features shown in Figure 6 (c) indicate well-ordered interfacial structures. A reference spectrum acquired at OCP (around 0.2 V vs. Ag/AgCl) in the electrolyte is plotted together with three spectra measured in 0.01 M HCl at different constant applied potentials. The spectral signature of the reference spectrum exhibits two peaks at around 3.25 and 4.55 eV, respectively, due to surface-modified bulk transitions.[44] The strong features at about 2.25 and 4.5 eV at −2 V indicate that when scanning to negative potentials, the epi-ready oxide layer present on the epi-ready InP(100) wafer dissolves in the acidic electrolyte, leading to a well-ordered, oxide-free layer. At 0 V and anodic potentials, the spectra are again very similar to the one at OCP, suggesting the re-formation of an oxide layer very similar to the initial epi-ready oxide, accompanied by chlorine-InP interactions.[103,104] To better understand the involved interfacial structure and chemistry, computational RAS is performed.

Computational RA spectroscopy first requires setting up an adequate selection of structural models for the system under investigation. In this case, the ingredients In, P, O, Cl, and H span a large parameter space of potential structures. Our starting point here was guided by the findings discussed above. For a comparison of computed RA spectra with the experimental spectrum of InP(100) in 0.01 M HCl under the applied potential of −2 V, we consider three structures: the fully Cl^- covered InP(100) surface in which an InCl layer is formed (2Cl), and one and three hydrogen atoms adsorbed on the InP(100) surface (2P-1H and 2P-3H, respectively). Furthermore, we investigate how sensitive the calculated spectrum is to the adsorption of one and two water molecules on the 2Cl and 2P-1H surfaces. Figure 7 displays the computed spectra of all investigated systems as well as the experimental spectrum. Our calculations reveal that the theoretically derived RA spectra of the 2Cl, 2P-1H, and 2P-3H surfaces are similar to the experimental spectrum. In the 2Cl case, two main negative peaks around 2.2 and 3.8 eV are revealed. The positions of these peaks are slightly changed when the additional one water molecule is adsorbed. The spectral shape, however, remains conserved. The spectrum for two water adsorbed 2Cl surface is considerably up-shifted compared to that of one water adsorbed surface. Interestingly, a positive anisotropy at 4.5 eV, which is observed in the experiment, is not shown. This suggests that the real interface is more complex than a simplified model with a highly ordered supercell and in the absence of oxygen molecules. Similar to the 2Cl structure, we can find the two notable negative anisotropies around 2.5 eV and 3.3 eV in the calculated spectrum of 2P-1H. In contrast to 2Cl, the 2P-1H surface exhibits a strong positive feature at 4.0 eV. This shows a redshift of around 0.55 eV compared to the main positive peak shown in the experiment. The adsorption of water molecules results in a slight blueshift and an increase in the minimum peak. Our calculation of the 2P-3H surface displays a constantly positive feature until 3 eV, a negative anisotropy, and a pronounced positive anisotropy at 3.4 and 4.4 eV, respectively. The corresponding maximum anisotropy in the computed spectrum is similar to that in the experiment. Based on these results, we can anticipate that H-terminated and Cl-terminated surfaces coexist. This hypothesis will have to be tested in future work where applied potentials and more structures are be considered.

While the results from computational RAS already help to form a first atomistic picture of the studied electrochemical system, they do not yet show the high degree of quantitative agreement with experiment as often established for many vacuum-based systems. This demonstrates the above-mentioned challenges of the large chemical parameter space resulting in many structures to be considered as well as the

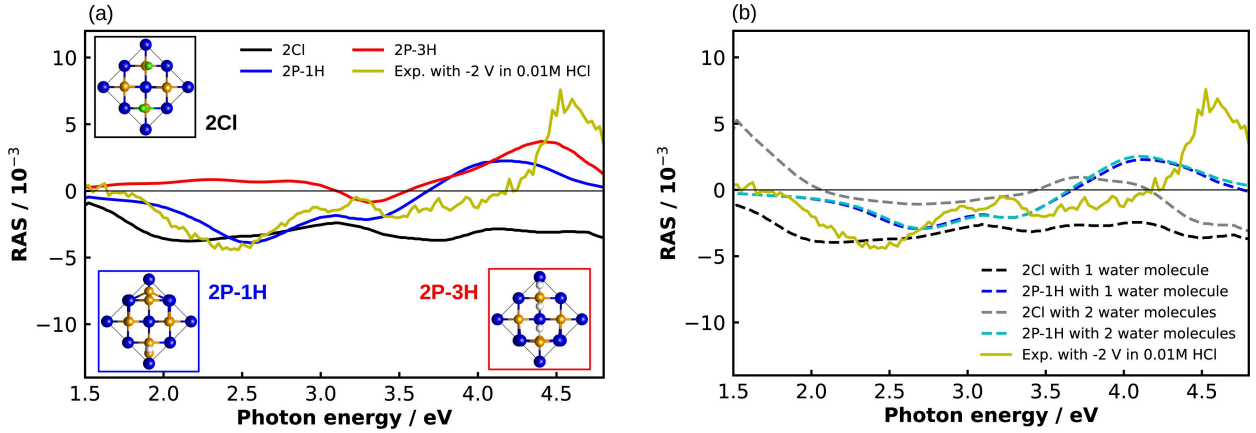

Figure 7. (a) Calculated and experimental (yellow) RA spectra of the InP(100) surface covered with Cl atoms and adsorbed with one and three H atoms. The injects are the top view of corresponding structures. Green-, blue-, orange-, and white-colored balls represent Cl, P, In, and H atoms, respectively. (b) Computed RA spectra of one water molecule adsorbed on 2Cl and 2P-1H.

methodological uncertainty on how to best treat applied potentials in a bulk electrolyte.

Further testing of the validity of the structural model derived from the data above should, in principle, be enabled by complementary XPS, probing the chemical composition of the surface. Yet such an analysis requires the transfer to ultra-high vacuum, where the electrolyte layer has to be removed before the measurement. Yet here, the question arises, if the interfacial layer persists under this change of external conditions. Time-resolved measurements that assess the kinetic stability of a given interface can help to estimate the experimentally available time-window between breaking of the potential control and establishing a dry surface in UHV. Figure 6 (d) shows a transient, where the optical anisotropy is acquired at a fixed photon energy of 2.25 eV, while potential steps at −1 V and −2 V are applied. The fast and reversible change in the anisotropy suggests that if a thin InCl layer builds up in the cathodic region, it immediately dissolves when setting the potential back to OCP. Therefore, at low HCl concentration, the hypothetically formed InCl is unstable and unlikely to be accessible for further analysis by other techniques, where no potential can be applied in an electrolyte, such as XPS in vacuum.

To summarize, in situ electrochemical RAS enabled to identify electrochemical conditions with respect to potentials and electrolyte concentration, under which highly ordered InP-electrolyte interfaces can be prepared. Alas, the observed surface layer generated is not stable when the applied voltage is set back to OCP, which renders complementary analysis for the identification of the exact chemical composition by XPS challenging. The results clearly demonstrate the potential of electrochemical RAS for the monitoring of well-defined (photo)electrochemical etching or layer deposition for III–V semiconductors, especially relevant for solar water splitting applications. In order to computationally identify the real surface structure formed by different potentials, complex surface phase diagram of various surface structures have to be investigated. To do so, molecular dynamics and calculations with applied potentials, followed by excited state calculations can be performed, but the computational effort is significant.

3.5. Aqueous systems II: Au(110)

Understanding electrochemical interfaces implies the ability to distinguish between chemical and physical processes occurring between the electrode surface and the electrolyte. Noble metals such as gold, inert in most acidic and alkaline media, allow focusing on the physical and chemical adsorption of molecules from the electrolyte on the metal surface by preventing or at least – compared to semiconductors – reducing chemical side reactions. Changes in the interaction between the electrolyte's dipoles and electrode surface under applied potentials can also lead to surface structural changes. Insights from these processes on gold can then be ideally transferred to more complex electrochemical systems.

The interfacial structure of gold single-crystals in contact with electrolytes has been experimentally widely investigated by STM, CV, and RAS.[105,106] Additionally, ex-situ RHEED and LEED have been used in UHV to verify the surface reconstruction after annealing prior to electrochemical cycling.[107] In particular, Mazine et al. have reported on the reconstruction of Au(110) in sulfuric acid under different applied potentials observed by RAS.[84] Initially possessing a reconstructed annealed Au(110)(1 × 2) surface, the crystal adopts an unreconstructed (1 × 1) surface upon immersion in H_2SO_4. Starting from an Au(110)(1 × 1) surface in H_2SO_4 at OCP, RAS measurements trace the electrochemically induced surface reconstruction below 0.05 V vs. SCE (0.018 V vs. Ag/AgCl) reference corresponding to a (1 × 2) missing row. The charge-distribution organization at the electrode surface depends on the applied potential. Hence, tuning the applied potential modifies surface-ion interactions, which play an essential role in the reconstruction/deconstruction.

At room temperature, the unreconstructed Au surface is in a metastable state. Applying a negative electrode potential with respect to the potential of zero charge (pzc) reduces the activation barrier for the reconstruction,[108] and therefore allows the transition from the (1 × 1) to the (1 × 2) surface. When applying potentials above 0.25 V vs. SCE (0.218 V vs. Ag/AgCl), the electrode is charged positively. Adsorption of the anions of the electrolyte (sulfate ions) on the Au surface lifts the reconstruction and the unreconstructed (1 × 1) surface is restored.

Here, we show typical electrochemical RAS experiments with Au(110) in low concentrations of both sulfuric and hydrochloric acid. Prior to the electrochemical RAS experiment, the crystal is flame-annealed to prepare a reconstructed (1 × 2) surface.[79,81,84,108] A baseline correction is applied to all the spectra using the spectrum of Au(110) in the electrolyte at OCP and its inverted spectrum, which was obtained by rotating the sample by 90 . The RA spectra obtained in H_2SO_4 and HCl are presented in Figure 8 (a) and (b), respectively. After annealing, Au(110) RA spectra exhibit a "W"- like shape. Contributions to the complex dieletric function arise both from the bulk and the surface. The slight differences between the spectra are due to different interband transitions from different Fermi level positions.[80] In general, the results in sulfuric acid (H_2SO_4) agree with those of Mazine et al.[84] The blue curve was recorded under open-circuit potential and shows a characteristic RA spectrum of well-ordered unreconstructed (1 × 1) Au(110) in an acidic environment.[84] The spectra obtained under applied potentials exhibit similar features as the spectrum measured in H_2SO_4. Below OCP, an Au(110) (1 × 2) reconstruction (−0.15 V, orange spectra) is observed with a pronounced shoulder at about 2 eV. In the range from OCP to 0.6 V, an Au(110) (1 × 1) unreconstructed (0.3 V, green spectra) surface is existent. This shows that the different surface reconstructions are associated with distinct optical signatures, hence at this stage providing a similar type of information as the diffraction patterns from LEED, which is limited to UHV.

Interestingly, when increasing the potential to values higher than 0.6 V, a positive anisotropic peak develops around 2.3 eV

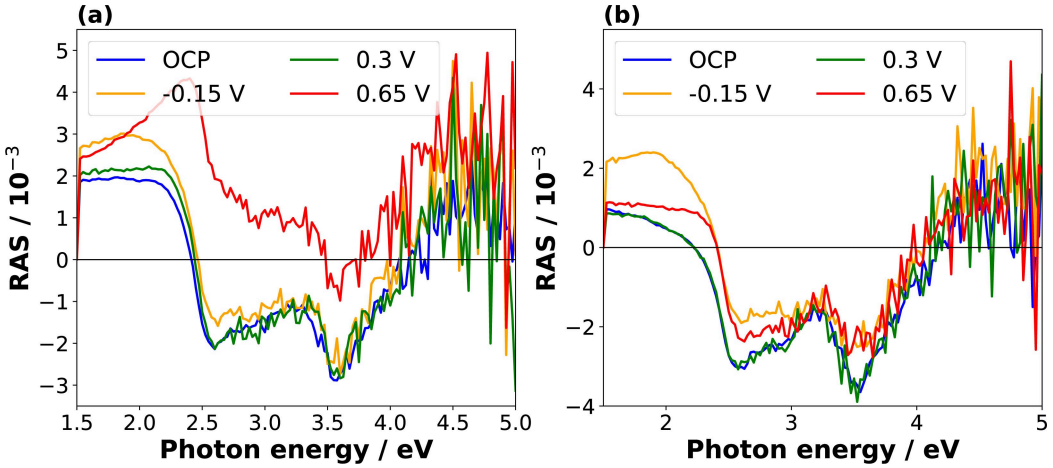

Figure 8. RA spectra of annealed Au(110) in different electrolytes under applied potentials. (a) in 0.1 M HCl and (b) in 0.1 M H_2SO_4 under different applied potentials vs. Ag/AgCl and at OCP. At the beginning of the experiments, the OCP values of Au(110) in 0.1 M HCl in 0.1 M H_2SO_4 were 164 mV and 367 mV, respectively. The orange spectra correspond to the Au(110) (1×2) reconstruction while the green spectra correspond to the unreconstructed Au(110) (1×1) surface.

in HCl (0.65 V, red spectrum). This peak was not observed in the spectrum measured in H_2SO_4 (see Figure 8 a) and, to the best of our knowledge, has not been reported in the literature. With no computational spectroscopy available at this point, the interpretation of this spectral feature has to rely on literature data. Yet for a metal, this task should be, due to the absence of a photovoltage adding uncertainty to actual potential at the surface as discussed above, a more reliable undertaking.

Some previous studies of gold/acidic electrolyte interfaces have shown that the screening of anions depends on the charge of the surface.[77,109–111] In particular, Shi et al. have reported that applying a potential above 0.7 V vs. SCE (0.668 V vs. Ag/AgCl) to the Au(111)/HCl interface leads to a change in the polarity of the chemisorption bond between gold and chloride, forming an ordered ($p \times \sqrt{3}$) overlayer of adsorbed chloride.[111] A polarity drop between Cl-anions and the gold surface could generate a linear electro-optic effect at the Au(110)/HCl interface and could explain the presence of the shoulder on the RA spectrum at 2.3 eV. Furthermore, the formation of an ordered overlayer could explain why the optical anisotropy of the interface is significantly increased. The observed optical anisotropy could therefore be the signature of an ordered Cl^- overlayer, formed in the anodic region above 0.7 V vs. SCE (0.668 V vs. Ag/AgCl).

The distinction between anisotropic features responsible for surface reconstructions and electrode/electrolyte electrostatic interactions and the reversibility of these processes can be readily observed in the transient illustrated in Figure 9 (a). The transient corresponds to Au(110) in 0.1 M HCl under CV conditions. Here, the transient was recorded at 2.3 eV because at this energy both features responsible for surface reconstruction/deconstruction and adsorbed anions overlayer are present. The CV, illustrated in Figure 9 (c), was performed between −0.25 V and +0.6 V (vs. Ag/AgCl) with a scan rate of 20 mV/s, starting from −0.25 V for 4 cycles. The current density and the potential from the CV are plotted separately as function of the

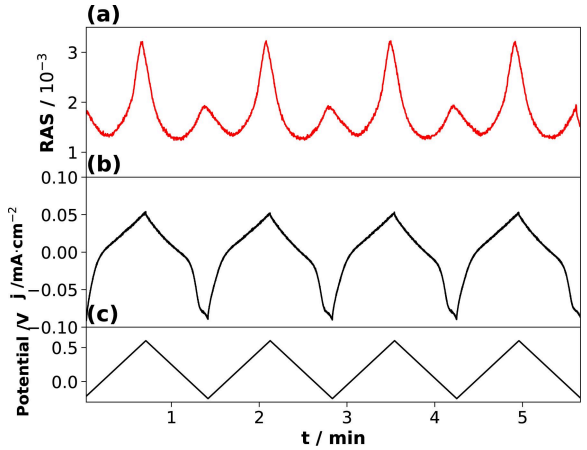

Figure 9. Time-resolved correlation between RAS and CV for Au(110). (a) Transient of Au(110) in 0.1 M HCl at 2.3 eV after annealing, during cycling voltammetry conditions (−0.25 to 0.6 V vs. Ag/AgCl reference electrode for 4 cycles with 20 mV/s scan rate.) (b) and (c) respectively correspond to the current and the voltage as function of the time from the CV.

time on Figure 9 (b) and (c), respectively. Such a plot type allows easier correlation between faradaic processes and changes in optical properties at the interface. The small time shift between the maxima of the current density and the transient is, in this case, an artifact from imperfect temporal alignment of CV and RAS measurements.

Figure 9 (a) shows the first maximum anisotropic peak corresponding to a voltage of 0.6 V and is a signature of the change in chloride adsorption. The second maximum anisotropic peak corresponds to a voltage of −0.25 V and indicates the reconstruction. On the CV, the reconstruction is associated with a progressive decline of the current density from 0.6 to −0.25 V marked by a shoulder at around 0.018 V (vs. Ag/AgCl). Whereas in the same potential range, the anisotropy first decreases until it reaches a minimum at around 0.2 V (beginning of the anion adsorption) and then rises again. The reverse

trend is observed during the deconstruction. Yet, while the transient peaks are almost symmetric around the extrema of the applied potential, the current cycles from the CV show a pronounced asymmetry around the cathodic extremum. After the formation of the reconstruction (below 0.018 V), the slope of the current decrease is reduced towards −0.2 V. This could be attributed either to the onset of a (1×3) surface reconstruction[112] or a change of the charging current of the EDL. A more detailed analysis of transients during potential steps, also including isotherms[94] would be needed to clarify this.

In summary, we showed that the well-known, potential-dependent re-ordering of the Au-electrolyte interface is associated with distinct optical anisotropies and can therefore be monitored in a time-resolved manner by electrochemical RAS. This demonstrates how RAS can complement CV, in which the distinction between surface reconstruction and chemical processes is not straightforward. Although electrochemical RAS is more developed for metallic systems than for III–V semiconductors systems – or semiconductors in general – mentioned in the previous section, it still needs significant input to become a well-establish method. In this regard, RAS represents an excellent complementary method to scanning tunneling measurements (STM) when investigating single-crystalline metals at different potentials.[107] It could also be used in the currently field of battery research, especially for metal-anode batteries, as we will briefly discuss in the following.

3.6. Outlook for battery systems

Metal electrodes like magnesium or aluminium are expected to play an essential role in next-generation battery technologies.[113] Especially for novel material combinations and novel electrolytes, often very little is known about the electrode-electrolyte interface's atomistic structure at operation conditions. Nevertheless, this knowledge is crucial for developing and benchmarking new and sustainable batteries. From this, RAS can potentially be used for battery research on the anode and the cathode, as outlined in the following.

Two aspects are crucial for the investigation of the anode: the solid-electrolyte interphase (SEI) and stripping and plating. For alkali and alkaline earth metals anode batteries, an SEI is formed on the battery's anode in contact with the liquid electrolyte's salts, solvents, additives, or impurities, consisting of different components in either a mosaic, homogeneous or even artificially created form.[4,114] In addition to the already existing ex situ and in situ/operando techniques for interfaces in batteries,[115] RAS could be highly beneficial when creating an artificial SEI because it allows controlling the growth process in the same way it monitors the growth process of semiconductors.[48] The other point worth considering on the anode side is stripping and plating. Here RAS can investigate changes in the surface anisotropy during metal deposition in analogy to epitaxial growth studies in gas-phase ambient.[48] The technique should also allow the detection of nuclei that lead to dendrite formation. Such investigations are especially relevant for lithium metal batteries. However, they should also be addressed for multivalent metal batteries (e.g. Al and Mg batteries).[116]

For the cathode, RAS also promises to benefit battery research: despite a large number of cathode materials for rechargeable magnesium batteries being investigated,[117] only little is known about the cathode-electrolyte interface (CEI). This is because mostly the intercalation into the cathode is investigated rather than the interphase.[118] RAS could close the knowledge gap and help develop high-performance batteries by highlighting an often overlooked topic.

However, there are also some challenges when investigating metal electrodes for batteries with RAS, both from an experimental and computational perspective. The first challenge comes with the electrolyte used in batteries, which might be, as in the case of Grignard, optically active.[119] The consequence is that the probing light is absorbed, which leads to a low signal-to-noise ratio in the RA spectra. Furthermore the surface preparation is quite challenging as alkali and earth-alkaline metals are highly reactive with oxygen and water. Therefore polishing and annealing must be done in a glove box.[120] This, however, allows for the direct observation of the crystal surface quality without transfer to UHV.

For theoretical investigations, battery electrolytes are also challenging because the number of atoms increases compared to aqueous electrolytes by a factor of ten when using highly advanced electrolytes like $Mg[B(hfip)_4]_2$ for magnesium batteries.[121] Furthermore, for metallic systems, a higher number of **k**-points are generally demanded to describe partially occupied bands of the systems. These combined effects lead to high computational costs.

As we have outlined, electrochemical RAS for battery applications will be a significant challenge; however, it can open up a new way to investigate the anode and cathode surface operando with a reduced or even without the requirement of correlation with other experimental techniques.

4. Conclusion and Outlook

The present review outlined the potential and current state of RAS as an emerging optical technique for exploring electrochemical interfaces. Probing the polarization state of light reflected at crystalline surfaces, EC-RAS detects changes in the surface structure and surface chemistry of electrochemical systems in situ/operando with a sub-monolayer resolution and on a reasonably fast time scale with standard light sources. The use of more advanced light sources with higher luminosity, hitherto barely explored, could further improve time resolution to the μs range.

Outlining the theory behind computational RAS, we briefly showed that standard DFT on a PBE level together with IP-RPA for the excited states can already provide reasonable, quantitative results for some systems. While in general, the computational method is relatively well-established for semiconductors, it remains challenging for metallic systems, whereas for electrochemical experiments, the study of metals dominates. Further-

more, the exploration of best practices for computational RAS of electrochemical systems has just begun. This explains why most EC-RAS applications on metallic systems in the literature combined their studies with other experimental techniques such as STM, but none used computational RAS.

We presented typical experimental approaches and results for the metallic system Au(110) and the semiconductor InP(100). For the former, RA spectra under applied potentials show that RAS is a powerful tool to visualize changes in surface reconstruction and in ions adsorption at the interface. For the latter, we also show first steps for the interpretation of experimental signatures aided by computational spectra derived from a DFT ground-state structure. This already allowed to determine experimental parameters with respect to applied potential and electrolyte composition, at which ordered surfaces of InP can be stabilized in the electrolyte, providing a starting position for further (photo)electrochemical surface processing. Yet the many constituents of the interface in addition to the requirement to apply an electrode potential in a realistic manner renders the configuration space to be probed by DFT large and the overall computational effort significant.

Time-resolved potential steps measurements allow to quantify the time-window available between breaking of the potential control and complete removal of the electrolyte for transfer to complementary UHV-based analysis. This is highly relevant to assess the transferability decoupled electrochemical experiments followed by surface science analysis in vacuum. Furthermore, fitting time-resolved measurements with adsorption isotherm models gives more quantitative insights into interfacial processes by the determination of kinetic and thermodynamic parameters. Also quantitative measures for the surface quality prior to or during an electrochemical experiment can be derived. When comparing a specific spectrum with a reference spectrum for the same surface, it is possible to quantitatively assess the quality of a given surface, i.e. which fraction of the surface actually shows a given reconstruction. Similarly, the quantity of a specific chemical species or ion on a well-ordered interface can be assessed, as soon as the corresponding spectral signature has been identified from complementary experiments or computational spectroscopy. Finally, RAS also has the potential to make an impact in battery research, giving insides into SEI formation, metal stripping and plating, as well as ion transport processes.

Experimental Section

InP samples were prepared from p-doped InP(100) (Zn-doping of $4 \cdot 10^{18}$ cm^{-3}), single-crystalline wafers with an offcut of (0 ± 0.5) from CrysTec. The wafers with an epi-ready surface were cleaved and used without further pre-treatment. For the RAS measurement, the InP samples were mounted into a photoelectrochemical cell (PECC) from Zahner without an optical window. The back-side of the samples were contacted with a copper wire, fixed with a silver paste (Ferro GmbH), and with GaIn eutectic (Sigma Aldrich). Pt and Ag/AgCl electrodes were used as counter and reference electrodes, respectively.

A gold single crystal was purchased from Mateck (purity 99,999 %), polished on one side to a roughness below 0.01 μm and an orientation accuracy better than 0.1 . Before electrochemical RAS measurements, the crystal was flame-annealed with the following procedure. The crystal was placed on a ceramic plate and flamed annealed with a bunsen burner gun to about 100 C below the melting temperature for about 5 minutes until the edge of the crystal turned red. The crystal was cooled down under Argon flow for about 10 min.[122] The annealed crystal was then transferred to the PECC equiped with an optical window. Pt and Ag/AgCl electrodes were used as counter and reference electrodes, respectively.

The PECC was filled with the HCl and H_2SO_4 electrolytes (VWR Chemicals, reagent grade). The RA spectra were measured with an RA-Spectrometer (EpiRAS from Laytec) equipped with a Xenon light source. The electrochemical measurements were done with a potentiostat (Versa STAT 3F from AMETEK). Further details of the experimental procedure can be found elsewhere.[57]

For structural optimizations of slabs of the electronic structure model, DFT calculations were performed using the CP2K code.[58] The code employs the gaussian and plane waves scheme. The generalized gradient approximation (GGA) as parameterized by Perdew-Burke-Ernzerhof (PBE) for the exchange-correlation functional was used.[59] A plane-wave cutoff of 800 Ry was set. We adopted Goedecker-Teter-Hutter (GTH) pseudopotentials. Ground-state properties were computed with QUANTUM ESPRESSO.[62] Here, we employed optimized norm-conserving vanderbilt pseudopotentials.[123] The sampling of Brillouin zone (BZ) was carried out with a $10 \times 10 \times 1$ **k**-grid, and an energy cutoff was set to 60 Ry. For computational RAS, we used the IP-RPA approach implemented in Yambo.[60,61] We applied a scissor operator to correct the underestimated band gap.

Acknowledgements

The following organizations are thanked for financial support: DFG (Deutsche Forschungsgemeinschaft) under Germany's Excellence Strategy – EXC 2154 – Project number 390874152 as well as DFG project number 434023472. Computational resources were provided by the state of Baden-Württemberg, through bwHPC, and DFG through grant no. INST 40/575-1 FUGG (JUSTUS 2 cluster). We thank Krishnaveni Palanisamy for discussions on the experimental approach to anneal the gold crystals.

Conflict of Interest

The authors declare no conflict of interest.

Data Availability Statement

The data used to generate the plots for this review (section 3) are openly available on Zenodo[124] and the NOMAD Repository.[125]

Keywords: electrochemistry · interfaces · time-resolved spectroscopy · computational chemistry · surface chemistry

[1] M. Chatenet, B. G. Pollet, D. R. Dekel, F. Dionigi, J. Deseure, P. Millet, R. D. Braatz, M. Z. Bazant, M. Eikerling, I. Staffell, P. Balcombe, Y. Shao-Horn, H. Schäfer, *Chem. Soc. Rev.* **2022**, *51*, 4583.
[2] K. Sivula, R. van de Krol, *Nat. Rev. Mater.* **2016**, *1*, 15010.
[3] Q. Wang, K. Domen, *Chem. Rev.* **2020**, *120*, 919.
[4] J. Popovic, *Nat. Commun.* **2021**, *12*, 6240.
[5] J. Sun, B. Luo, H. Li, *Adv. Sustainable Syst.* **2022**, *3*, 2100191.
[6] M. M. May, K. Rehfeld, *Adv. Energy Mater.* **2022**, *12*, 2103801.
[7] M. Wang, Z. Feng, *Chem. Commun.* **2021**, *57*, 10453.
[8] D. V. Esposito, J. B. Baxter, J. John, N. S. Lewis, T. P. Moffat, T. Ogitsu, G. D. O'Neil, T. A. Pham, A. A. Talin, J. M. Velazquez, B. C. Wood, *Energy Environ. Sci.* **2015**, *8*, 2863.
[9] M. Bozorgchenani, F. Buchner, K. Forster-Tonigold, J. Kim, A. Groß, R. J. Behm, *Langmuir* **2018**, *34*, 8451.
[10] C. R. Brundle, Ultra-High Vacuum Techniques of Surface Characterization, in *Industrial Applications of Surface Analysis*, volume 199 of *ACS Symposium Series*, pages 13–32, American Chemical Society **1982**.
[11] A. Hajduk, M. V. Lebedev, B. Kaiser, W. Jaegermann, *Phys. Chem. Chem. Phys.* **2018**, *20*, 21144.
[12] D. M. Itkis, J. J. Velasco-Velez, A. Knop-Gericke, A. Vyalikh, M. V. Avdeev, L. V. Yashina, *ChemElectroChem* **2015**, *2*, 1427.
[13] Z. Wang, Y. Zhang, B. Liu, K. Wu, S. Thevuthasan, D. R. Baer, Z. Zhu, X.-Y. Yu, F. Wang, *Anal. Chem.* **2016**, *89*, 960.
[14] M. Favaro, B. Jeong, P. N. Ross, J. Yano, Z. Hussain, Z. Liu, E. J. Crumlin, *Nat. Commun.* **2016**, *7*, 12695.
[15] S. Axnanda, E. J. Crumlin, B. Mao, S. Rani, R. Chang, P. G. Karlsson, M. O. M. Edwards, M. Lundqvist, R. Moberg, P. Ross, Z. Hussain, Z. Liu, *Sci. Rep.* **2015**, *5*, 9788.
[16] D. V. Lang, C. H. Henry, *Solid-State Electron.* **1978**, *21*, 1519.
[17] R. Paul, G. Safa, G. Dina, *J. Raman Spectrosc.* **2016**, *6*, 16.
[18] W. S. Lau, *Infrared Characterization for Microelectronics*, World Scientific **1999**.
[19] D. Cao, Y. Song, J. Peng, R. Ma, J. Guo, J. Chen, X. Li, Y. Jiang, E. Wang, L. Xu, *Front. Chem.* **2019**, *7*, 626.
[20] Y. Gan, G. V. Franks, *J. Phys. Chem. B* **2005**, *109*, 12474.
[21] A. Jarzembski, C. Shaskey, K. Park, *Front. Energy* **2018**, *12*, 43.
[22] M. Aliofkhazraei, *Modern Electrochemical Methods in Nano, Surface and Corrosion Science*, IntechOpen, Rijeka **2014**.
[23] O. M. Magnussen, *Chem. Eur. J.* **2019**, *25*, 12865.
[24] M. Maiuri, M. Garavelli, G. Cerullo, *J. Am. Chem. Soc.* **2020**, *142*, 3.
[25] T. Elsaesser, *Chem. Rev.* **2017**, *117*, 10621.
[26] H. Khan, A. S. Yerramilli, A. D'Oliveira, T. L. Alford, D. C. Boffito, G. S. Patience, *The Canadian Journal of Chemical Engineering* **2020**, *98*, 1255.
[27] B. F. Baggio, Y. Gründer, *Annual Rev. Anal. Chem.* **2021**, *14*, 87.
[28] K. A. Stoerzinger, W. T. Hong, E. J. Crumlin, H. Bluhm, Y. Shao-Horn, *Acc. Chem. Res.* **2015**, *48*, 2976.
[29] R. J. Gale (Editor), *Spectroelectrochemistry*, Springer US **1988**.
[30] A. Groß, *Theoretical Surface Science*, Springer, Berlin, Heidelberg **2009**.
[31] C. Hogan, R. Del Sole, G. Onida, *Phys. Rev. B* **2003**, *68*, 035405.
[32] C. Hogan, E. Ferraro, N. McAlinden, J. F. McGilp, *Phys. Rev. Lett.* **2013**, *111*, 087401.
[33] C. Hogan, R. Magri, R. Del Sole, *Phys. Rev. B* **2011**, *83*, 155421.
[34] W. G. Schmidt, K. Seino, P. H. Hahn, F. Bechstedt, W. Lu, S. Wang, J. Bernholc, *Thin Solid Films* **2004**, *455–456*, 764.
[35] W. G. Schmidt, J. L. Fattebert, J. Bernholc, F. Bechstedt, *Surf. Rev. Lett.* **1999**, *06*, 1159.
[36] W. G. Schmidt, A. Hermann, F. Fuchs, M. Preuss, *Large-Scale Simulations for Understanding Surface Optical Spectra*, Springer-Verlag **2006**.
[37] W. G. Schmidt, F. Bechstedt, J. Bernholc, *J. Vac. Sci. Technol. B* **2000**, *18*, 2215.
[38] W. G. Schmidt, N. Esser, A. M. Frisch, P. Vogt, J. Bernholc, F. Bechstedt, M. Zorn, T. Hannappel, S. Visbeck, F. Willig, W. Richter, *Phys. Rev. B* **2000**, *61*, R16335.
[39] M. M. May, M. Sprik, *New J. Phys.* **2018**, *20*, 033031.
[40] C. Zhang, T. Sayer, J. Hutter, M. Sprik, *J. Phys. E* **2020**, *2*, 032005.
[41] P. Weightman, D. S. Martin, R. J. Cole, T. Farrell, *Rep. Prog. Phys.* **2005**, *68*, 1251.
[42] O. Supplie, M. M. May, S. Brückner, N. Brezhneva, T. Hannappel, E. V. Skorb, *Adv. Mater. Interfaces* **2017**, *4*, 1601118.
[43] W. G. Schmidt, *Phys. Status Solidi B* **2005**, *242*, 2751.
[44] M. M. May, H.-J. Lewerenz, T. Hannappel, *J. Phys. Chem. C* **2014**, *118*, 19032.
[45] K. Haberland, P. Kurpas, M. Pristovsek, J.-T. Zettler, M. Weyers, W. Richter, *Appl. Phys. A* **1999**, *68*, 309.
[46] A. Cricenti, *J. Phys. Condens. Matter* **2004**, *16*, S4243.
[47] A. Rothen, *Rev. Sci. Instrum.* **1945**, *16*, 26.
[48] J.-T. Zettler, *Prog. Cryst. Growth Charact. Mater.* **1997**, *35*, 27.
[49] S. Richter, O. Herrfurth, S. Espinoza, M. Rebarz, M. Kloz, J. A. Leveillee, A. Schleife, S. Zollner, M. Grundmann, J. Andreasson, R. Schmidt-Grund, *New J. Phys.* **2020**, *22*, 083066.
[50] B. O. Seraphin, *Optical Properties of Solids: Papers from the NATO Advanced Study Institute on Optical Properties of Solids*, Springer US **1969**.
[51] C. Huber, C. Krämmer, D. Sperber, A. Magin, H. Kalt, M. Hetterich, *Phys. Rev. B* **2015**, *92*, 075201.
[52] P. Hollins, *Infrared Reflection–Absorption Spectroscopy*, John Wiley & Sons, Ltd, Chichester, UK **2006**.
[53] K. Mudiyanselage, D. J. Stacchiola, *In-situ Infrared Spectroscopy on Model Catalysts*, John Wiley and Sons, Inc. **2013**.
[54] J. McIntyre, D. Aspnes, *Surf. Sci.* **1971**, *24*, 417.
[55] R. del Sole, *Solid State Commun.* **1981**, *37*, 537.
[56] F. Manghi, R. Del Sole, A. Selloni, E. Molinari, *Phys. Rev. B* **1990**, *41*, 9935.
[57] M. Löw, M. Guidat, J. Kim, M. M. May, *RSC Adv.* **2022**, *12*, 32756.
[58] T. D. Kühne, M. Iannuzzi, M. D. Ben, V. V. Rybkin, P. Seewald, F. Stein, T. Laino, R. Z. Khaliullin, O. Schütt, F. Schiffmann, D. Golze, J. Wilhelm, S. Chulkov, M. H. Bani-Hashemian, V. Weber, U. Borštnik, M. Taillefumier, A. S. Jakobovits, A. Lazzaro, H. Pabst, T. Müller, R. Schade, M. Guidon, S. Andermatt, N. Holmberg, G. K. Schenter, A. Hehn, A. Bussy, F. Belleflamme, G. Tabacchi, A. Glöß, M. Lass, I. Bethune, C. J. Mundy, C. Plessl, M. Watkins, J. VandeVondele, M. Krack, J. Hutter, *J. Chem. Phys.* **2020**, *152*, 194103.
[59] J. P. Perdew, K. Burke, M. Ernzerhof, *Phys. Rev. Lett.* **1996**, *77*, 3865.
[60] A. Marini, C. Hogan, M. Grüning, D. Varsano, *Comput. Phys. Commun.* **2009**, *180*, 1392.
[61] D. Sangalli, A. Ferretti, H. Miranda, C. Attaccalite, I. Marri, E. Cannuccia, P. Melo, M. Marsili, F. Paleari, A. Marrazzo, G. Prandini, P. Bonfà, M. O. Atambo, F. Affinito, M. Palummo, A. Molina-Sánchez, C. Hogan, M. Grüning, D. Varsano, A. Marini, *J. Condens. Matter Phys.* **2019**, *31*, 325902.
[62] P. Giannozzi, S. Baroni, N. Bonini, M. Calandra, R. Car, C. Cavazzoni, D. Ceresoli, G. L. Chiarotti, M. Cococcioni, I. Dabo, A. D. Corso, S. de Gironcoli, S. Fabris, G. Fratesi, R. Gebauer, U. Gerstmann, C. Gougoussis, A. Kokalj, M. Lazzeri, L. Martin-Samos, N. Marzari, F. Mauri, R. Mazzarello, S. Paolini, A. Pasquarello, L. Paulatto, C. Sbraccia, S. Scandolo, G. Sclauzero, A. P. Seitsonen, A. Smogunov, P. Umari, R. M. Wentzcovitch, *J. Phys. Condens. Matter* **2009**, *21*, 395502.
[63] D. E. Aspnes, A. A. Studna, *Phys. Rev. Lett.* **1985**, *54*, 4.
[64] B. A. Joyce, *Rep. Prog. Phys.* **1985**.
[65] M. Behet, R. Hövel, A. Kohl, A. M. Küsters, B. Opitz, K. Heime, *Microelectronics J* **1996**, *27*, 297.
[66] Z. Sobiesierski, D. I. Westwood, M. Elliott, *Phys. Rev. B* **1997**, *56*, 15277.
[67] J. Ortega-Gallegos, L. Guevara-Macías, A. Ariza-Flores, R. Castro-García, L. Lastras-Martínez, R. Balderas-Navarro, R. López-Estopier, A. Lastras-Martínez, *Appl. Surf. Sci.* **2018**, *439*, 963.
[68] G. Hughes, C. Springer, U. Resch, N. Esser, W. Richter, *J. Appl. Phys.* **1995**, *78*, 1948.
[69] G. Sombrio, E. Oliveira, J. Strassner, C. Doering, H. Fouckhardt, *J. Vac. Sci. Technol.* **2021**, *39*, 052204.
[70] S. Brückner, P. Kleinschmidt, O. Supplie, H. Döscher, T. Hannappel, *New J. Phys.* **2013**, *15*, 113049.
[71] N. Witkowski, R. Coustel, O. Pluchery, Y. Borensztein, *Surf. Sci.* **2006**, *600*, 5142.
[72] M. M. May, O. Supplie, C. Höhn, R. van de Krol, H.-J. Lewerenz, T. Hannappel, *New J. Phys.* **2013**, *15*, 103003.
[73] A. Baghbanpourasl, W. G. Schmidt, M. Denk, C. Cobet, M. Hohage, P. Zeppenfeld, K. Hingerl, *Surf. Sci.* **2015**, *641*, 231.
[74] M. M. May, H. Stange, J. Weinrich, T. Hannappel, O. Supplie, *SciPost Phys.* **2019**, *6*, 58.
[75] M. M. May, H.-J. Lewerenz, D. Lackner, F. Dimroth, T. Hannappel, *Nat. Commun.* **2015**, *6*, 8286.
[76] B. L. Pearce, S. J. Wilkins, T. Paskova, A. Ivanisevic, *J. Mater. Res.* **2015**, *30*, 2859.
[77] C. I. Smith, N. J. Almond, P. Weightman, *J. Electrochem. Soc.* **2007**, *154*, F90.
[78] H. Gerischer, *Electrochim. Acta* **1990**, *35*, 1677.
[79] C. I. Smith, P. Harrison, T. Farrell, P. Weightman, *J. Phys. Condens. Matter* **2012**, *24*, 482002.
[80] P. Harrison, C. I. Smith, Y. Gründer, C. A. Lucas, S. D. Barrett, P. Weightman, *Phys. Chem. Chem. Phys.* **2016**, *18*, 24396.

[81] B. Sheridan, D. S. Martin, J. R. Power, S. D. Barrett, C. I. Smith, C. A. Lucas, R. J. Nichols, P. Weightman, *Phys. Rev. Lett.* **2000**, *85*, 4.
[82] O. Magnussen, J. Wiechers, R. Behm, *Surf. Sci.* **1993**, *289*, 139.
[83] R. Michaelis, D. Kolb, *Surf. Sci.* **1990**, *234*, L281.
[84] V. Mazine, Y. Borensztein, *Phys. Rev. Lett.* **2002**, *88*, 147403.
[85] V. Mazine, *Phys. Status Solidi* **1999**, *6*.
[86] T. Yamada, K. Shirasaka, A. Takano, M. Kawai, *Surf. Sci.* **2004**, *561*, 233.
[87] P. D. Lane, G. E. Isted, R. J. Cole, *Phys. Status Solidi B* **2010**, *247*, 1969.
[88] X. F. Jin, M. Y. Mao, S. Ko, Y. R. Shen, *Phys. Rev. B* **1996**, *54*, 7701.
[89] L. Sun, M. Hohage, P. Zeppenfeld, R. Balderas-Navarro, K. Hingerl, *Phys. Rev. Lett.* **2003**, *90*, 106104.
[90] C. Punckt, F. S. Merkt, H. H. Rotermund, *New J. Phys.* **2007**, *9*, 213.
[91] G. Barati, V. Solokha, K. Wandelt, K. Hingerl, C. Cobet, *Langmuir* **2014**, *30*, 14486.
[92] C. Goletti, G. Bussetti, A. Violante, B. Bonanni, M. Di Giovannantonio, G. Serrano, S. Breuer, K. Gentz, K. Wandelt, *J. Phys. Chem. C* **2019**, *119*, 1782.
[93] S. Vazquez-Miranda, V. Solokha, R. E. Balderas-Navarro, K. Hingerl, C. Cobet, *J. Phys. Chem. C* **2020**, *124*, 5204.
[94] G. Jerkiewicz, *Electrocatal* **2010**, *1*, 179.
[95] R. Yivlialin, C. Filoni, F. Goto, A. Calloni, L. Duò, F. Ciccacci, G. Bussetti, *Molecules* **2022**, *27*, 8010.
[96] Z. Chen, P. Gao, W. Wang, S. Klyatskaya, Z. Zhao-Karger, D. Wang, C. Kübel, O. Fuhr, M. Fichtner, M. Ruben, *ChemSusChem* **2019**, *12*, 3737.
[97] M. M. May, W. Jaegermann, *Curr. Opin. Electrochem.* **2022**, *34*, 100968.
[98] P. P. Notten, *Electrochemical study of the etching of III–V semiconductors*, Technische Universiteit Eindhoven **1989**.
[99] H.-J. Lewerenz, I. D. Sharp, *Chapter 1. Concepts of Photoelectrochemical Energy Conversion and Fuel Generation*, Royal Society of Chemistry **2018**.
[100] S. E. Acosta-Ortiz, A. Lastras-Martínez, *Phys. Rev. B* **1989**, *40*, 1426.
[101] T. Bruhn, B.-O. Fimland, M. Kneissl, N. Esser, P. Vogt, *Phys. Rev. B* **2011**, *83*, 045307.
[102] A. Goryachev, L. Gao, R. P. J. van Veldhoven, J. E. M. Haverkort, J. P. Hofmann, E. J. M. Hensen, *Phys. Chem. Chem. Phys.* **2018**, *20*, 14242.
[103] K. Schulte, H. Lewerenz, *Electrochim. Acta* **2002**, *47*, 2633.
[104] H. Lewerenz, K. Schulte, *Electrochim. Acta* **2002**, *47*, 2639.
[105] C. I. Smith, P. Harrison, C. A. Lucas, Y. Grunder, S. D. Barrett, P. Weightman, *J. Phys. Condens. Matter* **2016**, *28*, 015005.
[106] B. M. Ocko, A. Gibaud, J. Wang, *J. Vac. Sci. Technol.* **1992**, *10*, 3019.
[107] D. M. Kolb, J. Schneider, *Electrochim. Acta* **1986**, *31*, 929.
[108] D. Kolb, *Prog. Surf. Sci.* **1996**, *51*, 109.
[109] I. R. de Moraes, F. C. Nart, *J. Electroanal. Chem.* **1999**, *461*, 110.
[110] O. M. Magnussen, J. Hageböck, J. Hotlos, R. J. Behm, *Faraday Discuss.* **1992**, *94*, 10.
[111] Z. Shi, J. Lipkowski, *J. Electroanal. Chem.* **1996**, *403*, 225.
[112] C. I. Smith, A. Bowfield, N. J. Almond, C. P. Mansley, J. H. Convery, P. Weightman, *J. Phys. Condens. Matter* **2010**, *22*, 392001.
[113] A. El Kharbachi, O. Zavorotynska, M. Latroche, F. Cuevas, V. Yartys, M. Fichtner, *J. Alloys Compd.* **2020**, *817*, 153261.
[114] Q. Zhao, S. Stalin, L. A. Archer, *Joule* **2021**, *5*, 1119.
[115] A. M. Tripathi, W.-N. Su, B. J. Hwang, *Chem. Soc. Rev.* **2018**, *47*, 736.
[116] Y. Liang, H. Dong, D. Aurbach, Y. Yao, *Nat. Energy* **2020**, *5*, 646.
[117] F. Maroni, S. Dongmo, C. Gauckler, M. Marinaro, M. Wohlfahrt-Mehrens, *Batteries & Supercaps* **2021**, *4*, 1221.
[118] J. Shi, J. Zhang, J. Guo, J. Lu, *Nanoscale Horiz.* **2020**, *5*, 1467.
[119] Z. Lu, A. Schechter, M. Moshkovich, D. Aurbach, *J. Electroanal. Chem.* **1999**, *466*, 203.
[120] B. E. Hayden, E. Schweizer, R. Kötz, A. M. Bradshaw, *Surf. Sci.* **1981**, *111*, 26.
[121] Z. Zhao-Karger, M. E. G. Bardaji, O. Fuhr, M. Fichtner, *J. Mater. Chem. A* **2017**, *5*, 10815.
[122] L. A. Kibler, *Int. S. of Electrochem.* **2003**.
[123] M. Schlipf, F. Gygi, *Comput. Phys. Commun.* **2015**, *196*, 36.
[124] M. Löw, M. Guidat, J. Kim, M. M. May, Zenodo dataset for "The interfacial structure of InP(100) in contact with HCl and H2SO4 studied by reflection anisotropy spectroscopy" **2022**, DOI: 10.5281/zenodo.7410144.
[125] J. Kim, NOMAD dataset: RAS InP100 with Cl and H **2023**, DOI: 10.17172/NOMAD/2023.01.16-1.

Manuscript received: January 20, 2023
Revised manuscript received: February 23, 2023
Version of record online: ■■, ■■

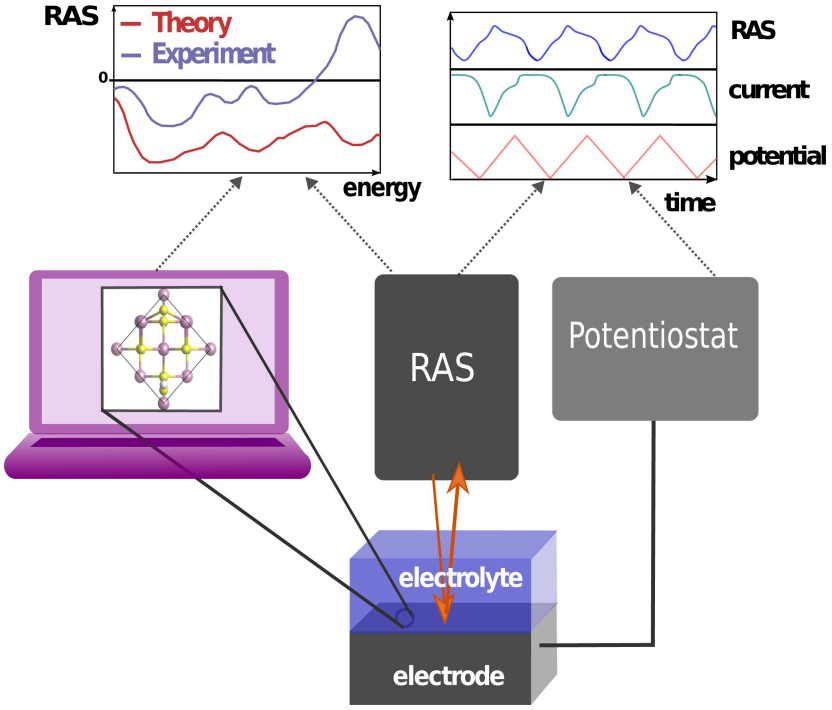

*M. Guidat, M. Löw, Dr. M. Kölbach, J. Kim, Dr. M. M. May**

1 – 18

Experimental and Computational Aspects of Electrochemical Reflection Anisotropy Spectroscopy: A Review

Understanding and controlling highly ordered electrochemical interfaces can be achieved by reflection anisotropy spectroscopy in parallel with electrochemical measurements. An in-depth understanding of experimental results from this spectroelectrochemical approach does, however, typically require a combination with computational spectroscopy.

RSC Advances

PAPER

View Article Online
View Journal | View Issue

Cite this: *RSC Adv.*, 2022, **12**, 32756

The interfacial structure of InP(100) in contact with HCl and H_2SO_4 studied by reflection anisotropy spectroscopy

Mario Löw, †[a] Margot Guidat, †[ab] Jongmin Kim [ab] and Matthias M. May *[ab]

Indium phosphide and derived compound semiconductors are materials often involved in high-efficiency solar water splitting due to their versatile opto-electronic properties. Surface corrosion, however, typically deteriorates the performance of photoelectrochemical solar cells based on this material class. It has been reported that (photo)electrochemical surface functionalisation protects the surface by combining etching and controlled corrosion. Nevertheless, the overall involved process is not fully understood. Therefore, access to the electrochemical interface structure under *operando* conditions is crucial for a more detailed understanding. One approach for gaining structural insight is the use of *operando* reflection anisotropy spectroscopy. This technique allows the time-resolved investigation of the interfacial structure while applying potentials in the electrolyte. In this study, p-doped InP(100) surfaces are cycled between anodic and cathodic potentials in two different electrolytes, hydrochloric acid and sulphuric acid. For low, 10 mM electrolyte concentrations, we observe a reversible processes related to the reduction of a surface oxide phase in the cathodic potential range which is reformed near open-circuit potentials. Higher concentrations of 0.5 N, however, already lead to initial surface corrosion.

Received 17th August 2022
Accepted 9th November 2022

DOI: 10.1039/d2ra05159a

rsc.li/rsc-advances

1 Introduction

Renewable energies will have to play a significant role in the future energy system. Due to the intermittency of wind or solar power, however, large-scale storage of harvested energy has to be realised, for instance, by electrochemical approaches.[1,2] One of the most significant scientific challenges here is understanding and controlling the electrochemical interface, where charge transfer and chemical reactions occur. The electrochemical interface of semiconductors, which are used in solar water splitting and battery applications, is a topic of intense research.[3–7] Yet while the surface structure under *operando* conditions is decisive for the performance, an atomistic picture of the interface is often not established. The last few years saw an increased effort of the community in the development and use of *in situ* and *operando* techniques to investigate these solid–liquid interfaces. Here, a common theme is that a complementary set of methods is typically required for the desired level of insight.[8–12]

The semiconductor indium phosphide (InP) has been studied intensively for use as a photocathode for solar water splitting,[13,14] but is also involved as a major ingredient in efficient photoelectrochemical multi-junction cells, where the top layer is often formed by an InP-based ternary compound semiconductor.[15,16] One of the main advantages of InP is the possibility to prepare surfaces with surface recombination velocities as low as 170 cm s^{-1}, which leads to an efficient carrier transport across the semiconductor–electrolyte interface and reduces photovoltage losses.[17,18] The versatile opto-electronic properties of InP-based semiconductors also render them platforms for other applications, for instance photonic devices.[19] In photoelectrochemical applications, however, the major challenge for InP is its surface corrosion and instability in aqueous solutions,[17] which then again increases surface charge-carrier recombination.[12] Approaches for surface passivation can, once identified, often be transferred to the more complex ternary compounds.[15,20]

This surface corrosion is best understood by investigating the system under operating conditions in the electrolyte. Ideally, it is then possible to design surface passivation approaches for InP.[14,21–24] Such a passivation layer should block (electro)chemical corrosion and ion transport over the solid–liquid interface while enabling efficient electron transfer. Previous investigations of InP in acidic electrolytes can be summarised as follows:[14,21–23,25] in the cathodic potential range in 0.5 N HCl and H_2SO_4, respectively, InP is reduced towards metallic indium at −0.553 V *vs.* (Ag/AgCl). In the case of HCl, the metallic In reacts further with adsorbed Cl-ions to InCl. An intermediate step that involves $InCl_3$ is also possible, yet unlikely due to its water-solubility. Simultaneously, the phosphorous is reduced to phosphine. In the anodic regions, parts of

[a]*Universität Ulm, Institute of Theoretical Chemistry, Ulm D-89081, Germany*
[b]*Universität Tübingen, Institute of Physical and Theoretical Chemistry, Tübingen D-72076, Germany. E-mail: matthias.may@uni-tuebingen.de*
† These authors contributed equally to this work.

the InCl are oxidised. However, a significant fraction remains on the surface, which results in the formation of a stable passivation layer after several electrochemical cycles that contains InCl (70 at%), $In(PO_3)_3$ (30 at%) and a layer of adsorbed Cl^- on the surface. In H_2SO_4, on the other hand, InP reacts to metallic indium and phosphine. However, the former is oxidised completely, and no stable passivation layer is observed. A possible way to obtain a stable passivation layer is by intermediate resting periods between the electrochemical cycles.[25] For the passivation layer formed in hydrochloric acid, subsequent Rhodium deposition leads to an efficient photocathode.[14,21] The treatment in an aqueous sodium sulphide solution, on the other hand, results in the removal of the native oxide and the formation of a passivation layer containing In–S and In–OH on the surface after one minute in the solution.[24]

Computational studies have reported on the structure and electronic properties of the pristine and oxidised InP surface using density-functional theory as well as molecular dynamics.[18,26,27] Wood *et al.*[18] investigated the interaction of gas-phase and liquid water with the pristine and oxygen-rich surfaces. Alvarado *et al.*[26,27] changed water coverage adsorbed on InP from single molecules to water film, and they found the OER and HER energetics to be modified due to the adsorption.

Methods used to experimentally study the formation of passivation layers on InP in different electrolytes comprise cyclic voltammetry, X-ray photoelectron spectroscopy (XPS), and on-line electrochemical mass spectrometry (OLEMS).[14,21–23,25] Depending on the conditions, under which surfaces are exposed to water or oxygen, the dominant pathways for surface (oxide) formation can become thermodynamically or kinetically driven.[28] Yet the question of whether these layers are well-ordered and to what extent their formation can be precisely controlled is still open. This knowledge could become instrumental for creating efficient solar water splitting cells.[15,29]

In this work, we study the interface of InP(100) with hydrochloric acid (HCl) and sulphuric acid (H_2SO_4) as electrolytes. Thereby we combine cyclic voltammetry, the standard tool of electrochemistry employed in the studies discussed above,[14,21–23,25] with reflection anisotropy spectroscopy (RAS). The latter is an optical technique sensitive to changes in surface chemistry, surface states, or surface reconstruction.[20,30] RAS enabled the investigation of adsorbates on InP,[20] but also metallic systems were already investigated in electrolytes.[31–33] We hereby show an electrolyte concentration-dependent reversibility of the cycling behaviour in HCl and H_2SO_4.

2 Experimental

Samples were prepared from p-doped InP(100) (Zn-doping of 4×10^{18} cm^{-3}), single-crystalline wafers with an offcut of $(0 \pm 0.5)°$ from CrysTec. The wafers with an epi-ready surface were cleaved and used without further pre-treatment. The samples were then mounted to a photoelectrochemical cell (PECC) from Zahner for the RAS measurement. For the electric contact, samples were back-contacted with a copper wire, fixed with silver resin (Ferro GmbH), and with some drops of GaIn eutectic (Sigma Aldrich). Pt and Ag/AgCl electrodes from Zahner were used as counter and reference electrodes, respectively. The cell was then filled with the desired electrolyte (HCl from VWR Chemicals and H_2SO_4 from Supelco). During measurements, the cell was degassed with argon. For the RA spectroscopy, an EpiRAS from Laytec was employed. The electrochemical measurements were controlled with a Princeton Applied Research VersaSTAT 3F potentiostat. Fig. 1 shows a schematic drawing of the cell.

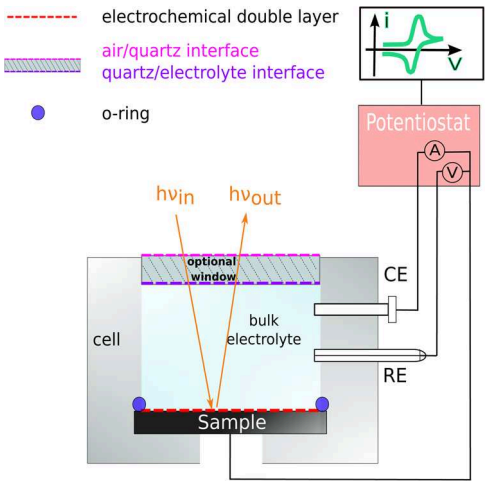

Fig. 1 Cross-section of the photoelectrochemical cell set-up for electrochemical RAS measurement. Here, WE is the InP working electrode, CE is the Pt-wire counter electrode, and RE is the Ag/AgCl reference electrode.

Reflection anisotropy spectroscopy was used here as a spectroelectrochemical method. RAS is a highly surface-sensitive tool that can investigate changes in surface chemistry, surface states, and surface reconstruction with a near-normal-incidence reflection set-up.[34] RAS is also used for controlling the growth during metal–organic chemical vapour deposition (MOCVD). The combination of the two methods allows to create highly ordered surfaces and interfaces with quantitative sub-monolayer control.[4,34–36] Furthermore, RAS is also employed to control layer-by-layer etching of multilayered semiconductors.[37]

For RAS, linearly polarised light impinges at near-normal incidence on the surface. The difference in the reflectivity, Δr, with respect to two orthogonal directions in the surface plane (x, y) is detected by analysis of the polarisation as a function of the photon energy, scaled with the overall reflectivity, r:

$$\mathrm{RAS} := \frac{\Delta r}{r} = \frac{2(r_x - r_y)}{r_x + r_y}; r \in \mathbb{C} \quad (1)$$

In the case of a crystal, where the bulk is optically isotropic – as for the (100) surfaces of zinc blende lattices here – there is no contribution to the signal from the bulk, but only from the (near) surface. Then, RAS becomes highly surface sensitive. This is a significant advantage to most other spectroscopies working with photons as those typically also probe a significant depth of the bulk material.[20,38,39] A baseline correction is applied to all the spectra using the signal of an optically isotropic Si(100) crystal

in water. This approach for baseline correction allows us to eliminate signals, that do not arise from the sample itself, but from optical components in the light-path that change the polarisation state. Additionally, we have calibrated the signal amplitude of our spectrometer with a Si(110) crystal following the standard procedure for the EpiRAS in a way that the peak at 3.46 eV exhibits an amplitude of 4 RAS units. We obtained a correction factor from this measurement, which we applied to all further measured spectra. No further numerical treatment of the data, such as peak fitting, was employed, we simply took the location of the extrema of the peaks. Cyclic voltammetry measurements were performed between −2 V and +1.5 V (*vs.* Ag/AgCl) with a scan rate of 0.05 V s^{-1}, starting from open circuit potential (OCP) towards the negative terminus for three cycles for low concentration (0.01 M) electrolyte, respectively. For higher-concentration electrolytes (0.5 N), the cyclic voltammogram (CV) was performed between −0.75 V and +0.45 V (*vs.* Ag/AgCl) with a scan rate of 0.05 V s^{-1}, starting from the OCP towards the negative terminus for ten cycles, respectively.

Further on, potentiostatic measurements were performed at the potentials of −2 V, −1 V, 0 V, and +1.5 V *vs.* Ag/AgCl, respectively. Potential step experiments were performed to investigate the stability of the surface at cathodic potentials. In this case, the potential was set to OCP for 10 s, then to −1 V for 30 s, then to OCP for 30 s, to −2 V for 30 s, and finally to OCP for 20 s. This cycle was then repeated two more times. During the electrochemical experiments, RA spectra were recorded continuously, or the anisotropy was measured time-resolved at fixed photon energy (transient mode).

For the computational spectroscopy, density-functional theory (DFT) calculations using the CP2K code[40] were first performed to obtain the relaxed structure of the slabs. The slab consists of 17 layers. To avoid spurious interactions between replica of the slab under 3D-periodic boundary conditions, we set a vacuum spacing of 20 Å between the slabs. Exchange and correlation effects were described by means of the generalised gradient approximation (GGA) using Perdew–Burke–Ernzerhof (PBE) parameterisation.[41] The plane-wave cutoff was set to 800 Ry. We used Goedecker–Teter–Hutter (GTH) pseudopotentials to represent core electrons and valence electrons. After the structural optimisation, the atomic coordinates were transferred to the plane wave/pseudopotential code QUANTUM ESPRESSO.[42] For these calculations, optimised norm-conserving Vanderbilt pseudopotentials were adopted.[43] The Brillouin zone (BZ) was sampled on a 10 × 10 × 1 k-grid with an energy cutoff of 60 Ry. The RAS calculations were performed using the Yambo code.[44,45] We employed the RPA-IP approach for the microscopic dielectric function. To correct the underestimated bandgap calculated by PBE, a scissor shift was adopted. In the RAS calculations, we used an experimental bulk dielectric function.[46]

3 Results & discussion

Fig. 2(a) shows the InP(100) spectra in 0.01 M hydrochloric and 0.01 M sulphuric acid, respectively, at OCP (around 0.2 V *vs.* Ag/AgCl) as well as the epi-ready crystal in air under ambient conditions without any pre-treatment. All three spectra show two positive peaks at 3.25 eV and 4.55 eV due to surface-modified bulk transitions.[20] The presence of electrolytes only slightly influences the RA spectra with an upwards shift in the RAS baseline, which can also arise from imperfect baseline correction. The noise in the high-energy region of the spectra is due to a reduced overall reflectivity from absorption and reflection losses in the electrolyte and at the air–electrolyte interface, respectively.

In the next step, different potentials were applied to investigate their effect on the optical anisotropy and hence the interfacial structure. To this end, we performed potentiostatic measurements at 0 V, −1 V, and −2 V in the cathodic range and +1.5 V in the anodic potential range *vs.* Ag/AgCl, respectively, during the acquisition of RA spectra. The RA spectra in Fig. 2(b) at anodic potentials shift towards more positive anisotropies. In contrast, RA spectra taken at cathodic potentials develop a negative peak for photon energies below 3 eV and the rest of the spectrum shifts to slightly more negative anisotropies. Additionally, the peak at 4.55 eV is much more intensive than at 0 V or OCP. These spectra suggest an ordered surface structure

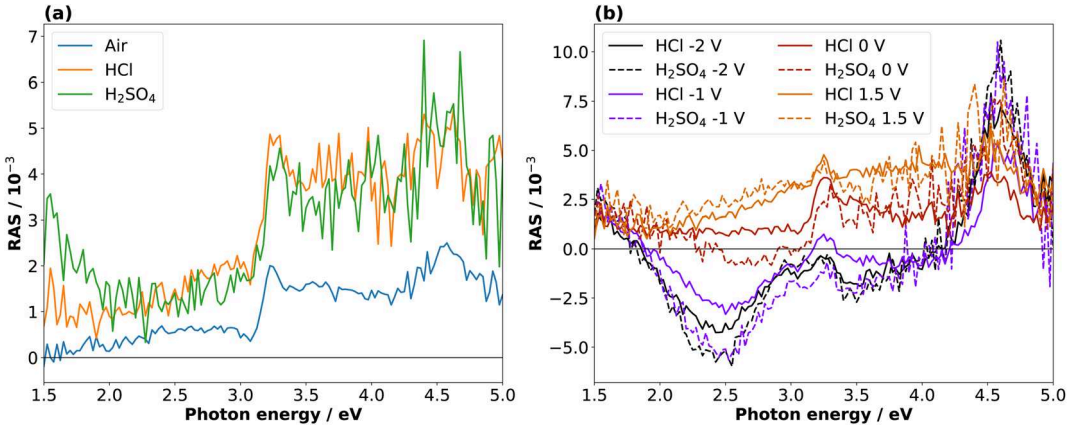

Fig. 2 (a) RA spectra of epi-ready InP(100) in air and immersed in 0.01 M HCl and H_2SO_4 at open-circuit potential. (b) RA spectra at −2 V, −1 V, 0 V and 1.5 V of the InP(100) surface in 0.01 M HCl (solid line) and 0.01 M H_2SO_4 (dashed line) solution.

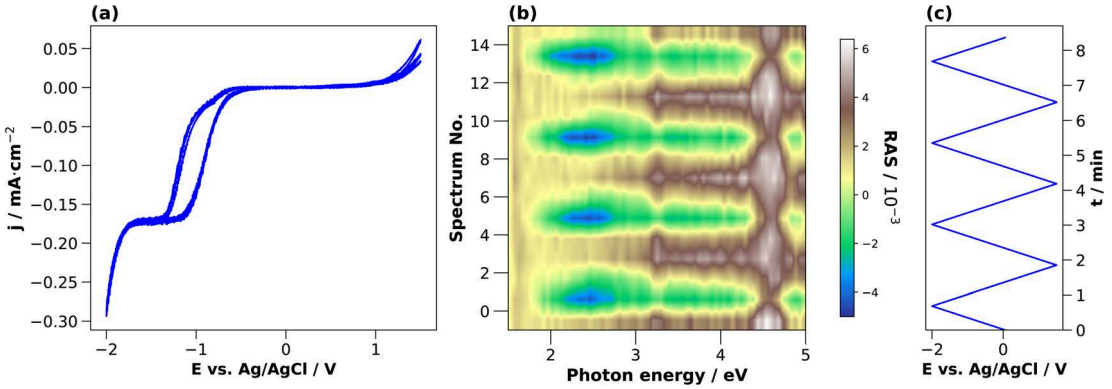

Fig. 3 Cyclic voltammograms of InP in 0.01 M HCl (a) with associated colour plot (b), where the RAS amplitude is colour-coded during continuous acquisition of spectra over time. The evolution of the applied potential over time with aligned *y*-axis is shown in (c). The potential scan from OCP was performed first towards −2 V and then to 1.5 V for 3 cycles, with a scan rate of 0.05 V s^{-1}.

in the cathodic and anodic potential ranges, but with different surface structure or composition. The similarity of the spectra at OCP or 0 V *vs.* Ag/AgCl with the epi-ready oxide indicate a similarity of the interface structure under these conditions.

To investigate the dynamic behaviour of the interface between these states during the cycling in the electrolyte, we changed the potential continuously between two terminals. The CV in 0.01 M HCl is shown in Fig. 3(a). In the cathodic region, the cathodic current density increases from around −0.4 V, reaches a plateau at −1.3 V, and increases further after −1.7 V. This current plateau, observed also for H_2SO_4, corresponds to the photocurrent from the white-light RAS measurement spot. Notable is a small deflection around −0.85 V that occurs only in the forward scan from OCP towards cathodic potentials. In the anodic region, there is an increase in the current density at potentials greater than 1 V. The first cycle shows the highest current density.

During this CV measurement, we continuously recorded RA spectra in the form of a 'colour plot'. The colour-coded signal amplitude during the CV is depicted in Fig. 3(b), showing reversible changes in the RA signal. The comparison with the applied potential in Fig. 3(c) shows that for cathodic potentials, there is a negative anisotropy at around 2.25 eV. In addition, there are significant changes of the optical anisotropy during the potential sweep at the photon energies 3.25 eV and around 4 eV, yet with qualitatively different behaviour. Yet as full spectra are recorded during a colour plot, the time resolution to track one specific spectral feature is relatively low. This can be alleviated by fixing the photon energy and tracking the signal over time with increased time-resolution in the transient mode. Yet before going into detail here, we first discuss the behaviour of InP in H_2SO_4.

The CV for 0.01 M H_2SO_4 in Fig. 4(b) shows that the cathodic current density increases beyond −0.5 V, reaches a plateau at −1.1 V and increases further beyond −1.4 V. In this case, however, the second step after −1.4 V is steeper than for HCl and simultaneously leads to a higher current density value at the potential terminus, where the current is dominated by the hydrogen evolution reaction.[25] For the first forward scan towards cathodic potentials, the cathodic current onset starts at −0.7 V, but at −0.8 V for the subsequent scans. Also here, a small deflection of the cathodic current is observed around −0.6 V. This is in the potential region where, albeit at higher electrolyte concentrations, the reduction of InP towards metallic indium and phosphine was reported at around −0.55 V *vs.* Ag/AgCl.[14,21–23] The cathodic current density at the potential terminus decreases from the first cycle on. Above +1 V, we observe an anodic current, which decreases over the three cycles. In the first cycle, a small oxidation wave can be observed at around +0.3 V, which is absent for the CV taken with HCl. According to the literature, this anodic peak could be due to the formation of indium phosphate.[47]

For higher time-resolution during the CV measurements, transients were recorded *operando* at the energies 2.25 eV, 3.25 eV, and 4.00 eV during a potential sweep with the same settings as for Fig. 3. The photon energies were chosen since changes in the spectra at different potentials in Fig. 2(b) and 3(b) are most pronounced here. These transient measurements enabled us to observe the potential-induced changes on the surface during cycling at higher time-resolution and evaluate the reversibility with respect to the interfacial structure. Fig. 4 shows the periodic changes of the anisotropy in these transients. The minimum of the optical anisotropy occurs under the application of a cathodic potential. In contrast, the maximum is associated with the anodic region. Shape and amplitude of the transients remain virtually constant for HCl, with the exception of the transients at 3.25 and 4 eV, which become more negative from the first cathodic half-scan to the subsequent ones. The case of H_2SO_4 shows distinct differences. Here, the negative extremum of the RA amplitude at 2.25 eV increases from cycle to cycle, yet not for the higher photon energies, which, similar to HCl, only show a slightly less negative amplitude in the first cathodic scan. From these different signal shapes at different potentials and electrolytes, we can try to deduce the reactions on the interface of InP with the respective electrolyte.

At the beginning of the experiment, the epi-ready InP(100) wafer is covered by a thin, well-defined oxide layer. In the presence of an acidic electrolyte, the oxide layer is expected to

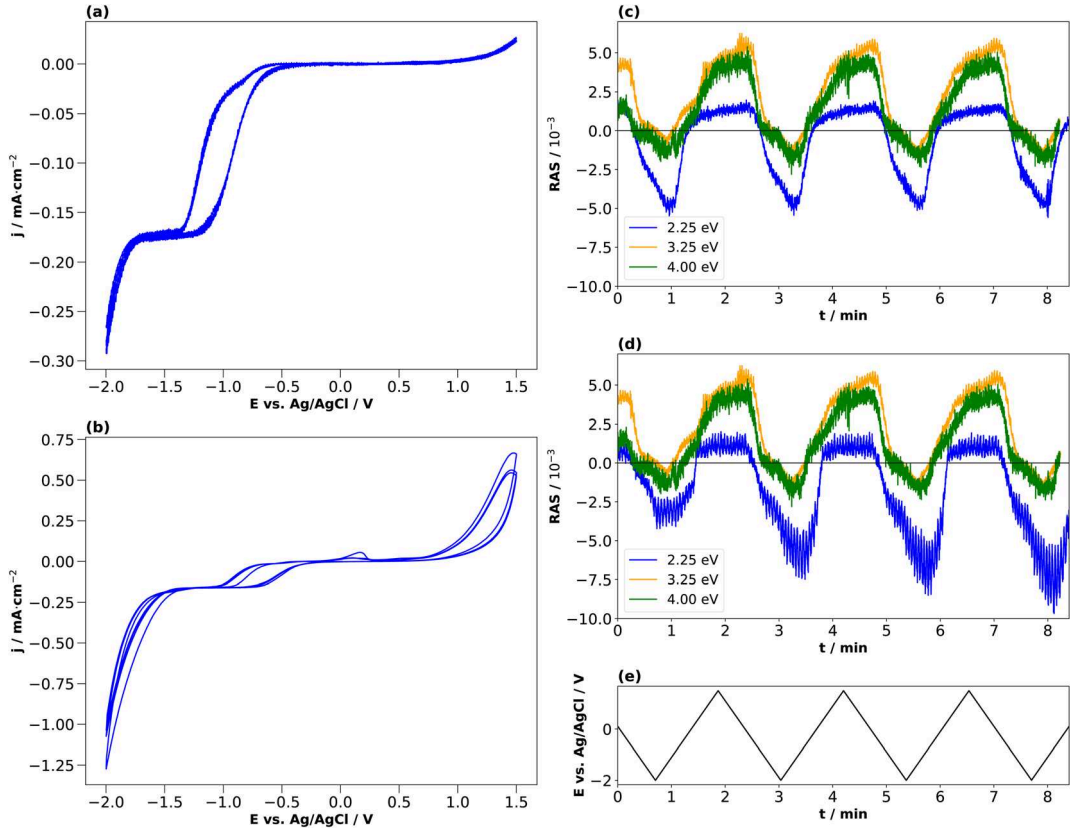

Fig. 4 Cyclic voltammograms of InP in 0.01 M (a) HCl with associated transients (c), and in 0.01 M (b) H_2SO_4 with associated transients (d). (e) Potential plotted against Ag/AgCl. Scan from OCP towards −2 V and than to 1.5 V for 3 cycles, with a scan rate of 0.05 V s^{-1}.

dissolve when scanning the potential from OCP towards the cathodic region.[14,21–23,25] The well-defined, reproducible RA spectrum that we observe at cathodic potentials indicates that this oxide-free layer is well-ordered. Yet the spectral shape does not clearly correspond to one of the main characteristic surface reconstructions of InP(100), the 'P-rich' $p(2 \times 2)/c(4 \times 2)$ reconstruction or the mixed-dimer 'In-rich' (2×4) reconstruction. Both these surfaces exhibit a pronounced negative anisotropy around 1.8–2 eV, associated with surface dimers,[20] while here, the peak observed here is located at 2.5 eV. The strong positive anisotropy around 4.5 eV, however, is a common feature with the In-rich surface.[20,30] Scanning back to OCP or 0 V *vs.* Ag/AgCl, the spectrum is again similar to the epi-ready oxide. This suggests a re-formation of the oxide phase in this potential region for both electrolytes. In both electrolytes, the negative anisotropies are slightly reduced for the first cycle, which could suggest that the re-formed oxide layer is of slightly different nature, possibly with a higher degree of ordering as indicated by the higher transient amplitudes. The observation that both CV and RAS transients remain then constant for HCl indicates a highly reversible process. This would be compatible with the adsorption of chloride on an In-terminated surface, leading to the formation of an InCl surface film starting from −0.55 V (Ag/AgCl),[22] which would also explain the differences at lower photon energies to H_2SO_4. The further change of the anisotropy at cathodic potentials beyond −1.5 V could then be related to the reordering of the (near-)interface water[26] or the adsorption of protons/hydrogen on the surface.

In H_2SO_4, only a fraction of the indium is expected to react with the sulphate ions because of sulphate's weaker interaction with InP compared to the chloride–InP interaction in HCl.[21,23,48] Therefore, metallic indium and $In_x(SO_4)_y$ species would be present at the interface. According to the literature, the metallic Indium and InCl compounds are partially oxidised to In^{3+} in the anodic potential range, forming Indium oxide, and Indium phosphate at high electrolyte concentrations.[22,23] Interestingly, the increasing amplitude of the negative anisotropy with ongoing cycling in the H_2SO_4 electrolyte is associated with a higher overpotential for the hydrogen evolution reaction.

In the literature, conditioning of InP for use as a photocathode was performed typically at higher electrolyte concentrations of 0.5 or 1 N, and these were also the concentrations used to study the resulting surface composition by photoelectron spectroscopy.[22,23] We therefore also applied the same approach to these higher electrolyte concentrations. Fig. 5(a) and (b) show the resulting cyclic voltammograms for both HCl and H_2SO_4. The CV changes its shape from cycle to cycle, effectively reducing the overpotential for the hydrogen evolution reaction, as observed similarly in the literature.[23]

Unlike for the lower concentrations, the amplitudes of the transients at 2.25 eV decrease over the cycles in the cathodic potential region. This occurs continuously for HCl, less so for

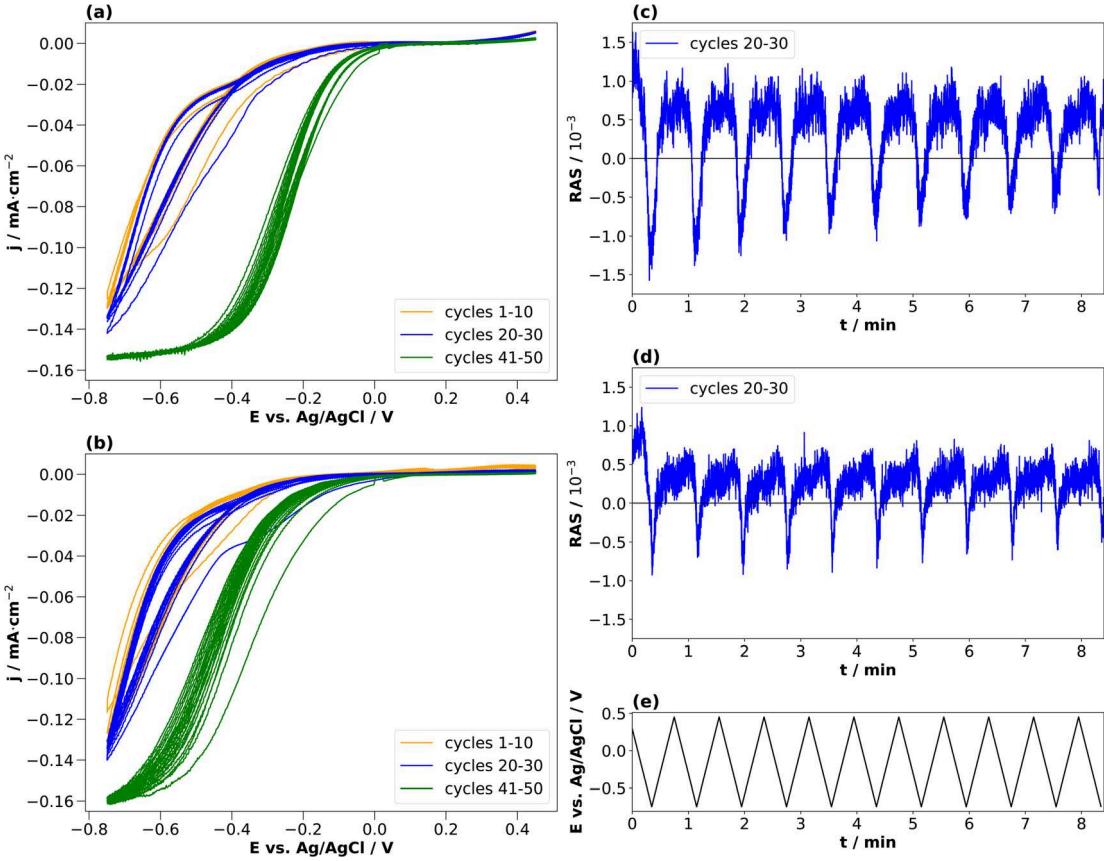

Fig. 5 Cyclic voltammograms of InP (a) HCl (0.5 M) and (b) H_2SO_4 (0.25 M) with corresponding transients at 2.25 eV for cycles 20–30 (c and d) and the applied potentials (e). Potential plotted against Ag/AgCl. Scan from open-circuit potential towards −0.75 V and then to +0.45 V with a scan rate of 0.05 V s^{-1}. The orange curve shows the cycles 1–10, the blue curve shows the cycles 20–30, and the green curve shows the cycles 41–50.

H_2SO_4. This hints towards a decreased interface ordering with ongoing cycles, consistent with inline XPS studies suggesting the formation of a layer of mixed oxides with a thickness in the order of a single or few nanometres.[21–23] Consequently, cycling in higher electrolyte concentrations induces slightly different surface reactions reducing the degree of ordering of the interface. A comparison with the literature on InP(100) in 0.5 M HCl[22,23] shows that the build-up of a passivation layer progressively transforms the surface into a relatively thick, amorphous layer. This lack of reversibility is observed through the evolution of the negative anisotropy in Fig. 5(c) and (d), decreasing from cycle to cycle. In HCl, the passivation layer is composed of InCl, indium phosphate and indium oxide.[22,23] In contrast, the passivation layer from cycling in H_2SO_4 consists of metallic In, $In_x(SO_4)_y$, indium phosphate and indium oxide.

For a more detailed insight, information on the exact surface composition would be instrumental, especially for the structurally well-ordered interface in lower electrolyte concentrations. Alas, in virtually all cases, RAS does not allow to directly derive composition and exact structure from experimental spectra alone, requiring either correlation with other techniques or computational spectroscopy.[49] A straightforward choice for probing the surface/interface composition is X-ray photoelectron spectroscopy. While XPS is almost as surface-sensitive as RAS, it does not probe the surface real-space structure, but rather the electronic structure. Furthermore, the sensitivity of XPS for light elements is strongly reduced, a limitation not found for RAS. With respect to information on the surface structure, the classical surface science method low-energy Electron Diffraction (LEED) could be considered related to RAS, yet the use of LEED is limited to ultra-high vacuum (UHV).

The application of standard XPS for electrochemical systems also requires samples prepared at the desired potential to be transferred from the electrolyte to UHV, which is experimentally challenging. Especially for ultra-thin interface layers, it is important to understand to what extent the surface created at a certain potential will be stable in the absence of applied potential and/or electrolyte. Therefore, we tested the stability of the newly formed interface at cathodic potentials through potential-step experiments during which transients were recorded. This experiment aims to assess the kinetics of formation and disintegration of the interface formed at −2 V and −1 V, respectively. Depending on how fast these changes occur, one can try to assess whether the stability window of the cathodically formed interface is large enough for transfer to UHV. Fig. 6 shows the resulting transients in both electrolytes at 2.25 eV.

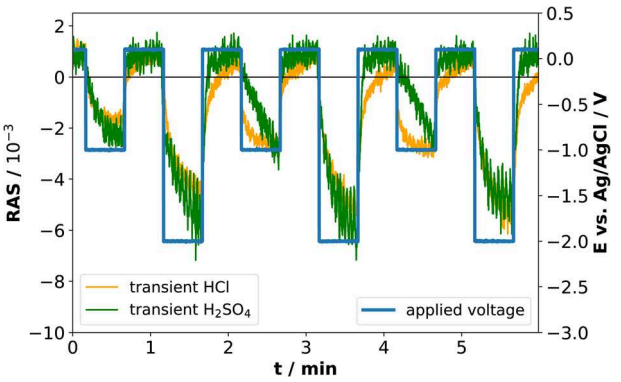

Fig. 6 Potential-step and transient measurements at 2.25 eV in 0.01 M HCl and in 0.01 M H_2SO_4.

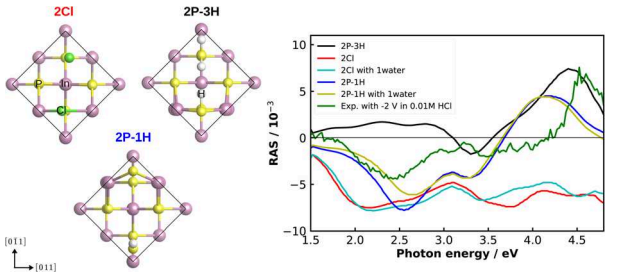

Fig. 7 Left: top view of the fully Cl-covered surface, as well as the surface with one and three adsorbed hydrogen atoms of InP(100) (2Cl, 2P–1H, 2P–3H, respectively). The black line indicates the surface unit cell. Right: computed and experimental (green) RAS of the InP(100) in contact with 0.01 M HCl solution under the applied potential of −2 V.

When the cathodic potential step is applied, the RAS amplitudes of the transient spectrum decrease towards its negative extremum in equilibrium, but with different time-constants. Especially for HCl at −1 V, there appears to be a fast process in addition to a slower signal decrease, while the transient in H_2SO_4 decreases more slowly. After setting the potential back to OCP, the anisotropy in H_2SO_4 changes back to the original value at OCP, while the process is slower in HCl. One of the two processes observed in HCl could be related to the formation and dissolution of the above-mentioned InCl layer, which is not present for the H_2SO_4 case. Yet the time-constants clearly indicate that the time-window for a transfer to XPS is very small and conclusive results would very likely require ambient-pressure XPS similar to ref. [28], but at different applied potentials.

As an alternative to correlation with another experimental method for a more detailed understanding of our experimental RA spectra, we performed computational RAS on structures that could be expected to be relevant for InP(100) in contact with an electrolyte. In Fig. 7, we compare the experimental RA spectrum of InP(100) in 0.01 M HCl at −2 V with calculated spectra. For the latter, we model three systems in which phosphorus atoms at the InP surface are fully substituted with chlorine, forming an InCl layer (termed 2Cl), and one or three hydrogen atoms are adsorbed on the surface (2P–1H and 2P–3H). We further consider adsorption of one water molecule on the 2Cl and 2P–1H structures, as water molecules can significantly alter the RAS signature.[49] When comparing computational to experimental RA spectra, it has to be noted that experimental surfaces would be expected to be not as 'perfect' as the computational structure, where all of the surface is in the same state. This would translate to lower intensities for the experimental spectra. We find that elements of the computed spectra for the 2Cl and 2P–1H, yet also for the 2P–3H surfaces resemble the experimental signature. The calculation for the 2Cl surface reveals a constantly negative anisotropy with negative peaks around 2.2 and 3.8 eV and a shoulder around 2.7 eV, the additional water molecule slightly modifies the spectrum, but the general shape is conserved. A noticeable difference to the experimental RA-signal is that the positive anisotropy at 4.5 eV does not appear in the calculated spectrum. For the case of 2P–1H, two pronounced negative anisotropies around 2.5 eV and 3.3 eV are observed. Unlike the 2Cl surface, the strong positive feature, which also arises in the experimental spectrum, is shown at 4.2 eV. Compared to the experiment, this peak is red-shifted by around 0.35 eV, while the minimum of the anisotropy is slightly blue-shifted and the shift increases with adsorbed water. The 2P–3H structure, on the other hand, displays a rather flat positive anisotropy up to 3 eV, a slight negative peak at 3.3 eV, and a strong positive anisotropy at around 4.4 eV. The latter feature is very similar to the high-energy peak of the experimental spectrum. In general, single water molecules do not play a crucial role for these spectra. Minor discrepancies between the experiment and calculations in terms of the energies would be expected from bandgap errors of the exchange-correlation functional and neglecting defects, oxidation, and domain boundaries on the surface. These initial results suggest a coexistence of H-terminated and Cl-terminated surface, which would lead to a superposition of the spectra of the respective structures. While the computational results give already a first hint towards the real surface structure, a surface phase diagram followed by computational spectroscopy of the – numerous – different structures is required to probe a higher fraction of the chemical space. In addition, multiple water layers and applied potentials might be required.[49] Due to the significant involved computational effort, however, this will have to be left to future work.

To summarise, our results indicate different mechanisms for the two electrolyte concentrations. The transients measurements of InP(100) in low acidic concentrations (0.01 M, Fig. 4) reveal persistently reversible changes in the surface ordering during cycling. Starting from open-circuit potential, a well-ordered, ultra-thin oxide layer appears to be dissolved and, in the case of HCl, replaced by a monolayer of InCl. The spectra found in the cathodic potential range show a strong negative anisotropy around 2.5 eV for both HCl and H_2SO_4, yet with slight differences. Hydrogen adsorption appears to be involved as well for both electrolytes. Setting the potential back to open-circuit, this oxide layer is re-formed and appears to exhibit a higher degree of ordering than the original, epi-ready oxide on the wafer as indicated by a slightly more pronounced spectrum after the first cycle. Also in the anodic potential range,

a spectrum different from OCP is found, but less distinct, which could indicate a lower degree of ordering in this potential range. The reversibility indicates, that potential cycling does not involve further etching of the surface, which is typically accompanied by a gradual loss of interface ordering. Potential cycling in higher electrolyte concentrations of 0.5 N, on the other hand, leads to a gradual change in the shape of the cyclic voltammograms, associated with a gradual loss of interface ordering, when the nm-thick mixture of oxides and phosphates[22,23,47] is formed.

4 Conclusions

Using *operando* electrochemical reflection anisotropy spectroscopy for the study of electrochemical InP(100) interfaces in contact with HCl and H_2SO_4, we find the potential-dependent formation of well-ordered InP–electrolyte interfaces for low electrolyte concentrations. Transient measurements indicate for both electrolytes that there is a reversible formation and removal of ultra-thin oxide layer, yet only in the case of low-concentration (0.01 M) electrolytes. In the case of higher-concentration electrolytes the interface gradually transitions into an unordered state.

Time-resolved potential step measurements show that the surface prepared at cathodic potentials is not stable when the potential is set back to OCP, which hampers the study of the exact chemical nature of this interface state by standard X-ray photoelectron spectroscopy. While initial results from computational RA spectroscopy corroborate the hypothesis that the structures formed in HCl under cathodic potentials involve InCl and adsorbed hydrogen, further computational studies, also under applied potentials, will have to be performed for a more definitive insight.

In summary, our study shows the potential of electrochemical reflection anisotropy spectroscopy for the preparation of well-structured interfaces in the electrolyte. These could then serve as a starting point for subsequent (photo)-electrochemical functionalisation, such as deposition of passivation layers and catalysts, to be used for solar-water-splitting devices.[15] As the process observed here for InP resembles the formation of solid–electrolyte interphases (SEI),[12] electrochemical RAS also has potential as a technique to gain a microscopic, time-resolved insight into SEI processes on battery electrodes.

Conflicts of interest

There are no conflicts to declare.

Acknowledgements

This work was funded by the Deutsche Forschungsgemeinschaft (DFG, German Research Foundation) under Germany's Excellence Strategy – EXC 2154 – project number 390874152 as well as DFG project number 434023472. We acknowledge the state of Baden-Württemberg, through bwHPC, and DFG through grant no. INST 40/575-1 FUGG (JUSTUS 2 cluster) for computational resources. We acknowledge support by the Open Access Publishing Fund of University of Tübingen.

References

1 A. Andrijanovits, H. Hoimoja and D. Vinnikov, *Elektron. Elektrotech.*, 2012, **118**, 21–26.
2 S. Ould Amrouche, D. Rekioua, T. Rekioua and S. Bacha, *Int. J. Hydrogen Energy*, 2016, **41**, 20914–20927.
3 J. Popovic, *Nat. Commun.*, 2021, **12**, 6240.
4 O. Supplie, M. M. May, S. Brückner, N. Brezhneva, T. Hannappel and E. V. Skorb, *Adv. Mater. Interfaces*, 2017, **4**, 1601118.
5 W. A. Smith, I. D. Sharp, N. C. Strandwitz and J. Bisquert, *Energy Environ. Sci.*, 2015, **8**, 2851–2862.
6 H. Gerischer, *Surf. Sci.*, 1969, **18**, 97–122.
7 H. Gerischer, *J. Phys. Chem.*, 1991, **95**, 1356–1359.
8 D. V. Esposito, J. B. Baxter, J. John, N. S. Lewis, T. P. Moffat, T. Ogitsu, G. D. O'Neil, T. A. Pham, A. A. Talin, J. M. Velazquez and B. C. Wood, *Energy Environ. Sci.*, 2015, **8**, 2863–2885.
9 A. M. Tripathi, W.-N. Su and B. J. Hwang, *Chem. Soc. Rev.*, 2018, **47**, 736–851.
10 J. Li and J. Gong, *Energy Environ. Sci.*, 2020, **13**, 3748–3779.
11 G. Gourdin and V. Doan-Nguyen, *Cell Rep. Phys. Sci.*, 2021, **2**, 100660.
12 M. M. May and W. Jaegermann, *Curr. Opin. Electrochem.*, 2022, **34**, 100968.
13 A. Heller, B. Miller, H. J. Lewerenz and K. J. Bachmann, *J. Am. Chem. Soc.*, 1980, **102**, 6555–6556.
14 A. G. Muñoz, C. Heine, H. W. Klemm, T. Hannappel, N. Szabo and H.-J. Lewerenz, *ECS Trans.*, 2011, **35**, 141–150.
15 M. M. May, H.-J. Lewerenz, D. Lackner, F. Dimroth and T. Hannappel, *Nat. Commun.*, 2015, **6**, 8286.
16 J. L. Young, M. A. Steiner, H. Döscher, R. M. France, J. A. Turner and T. G. Deutsch, *Nat. Energy*, 2017, **2**, 17028.
17 J. Tournet, Y. Lee, S. K. Karuturi, H. H. Tan and C. Jagadish, *ACS Energy Lett.*, 2020, **5**, 611–622.
18 B. C. Wood, E. Schwegler, W. I. Choi and T. Ogitsu, *J. Phys. Chem. C*, 2014, **118**, 1062–1070.
19 K. Vyas, D. H. G. Espinosa, D. Hutama, S. K. Jain, R. Mahjoub, E. Mobini, K. M. Awan, J. Lundeen and K. Dolgaleva, *Adv. Phys.: X*, 2022, **7**, 2097020.
20 M. M. May, H.-J. Lewerenz and T. Hannappel, *J. Phys. Chem. C*, 2014, **118**, 19032–19041.
21 A. G. Muñoz, C. Heine, M. Lublow, H. W. Klemm, N. Szabó, T. Hannappel and H.-J. Lewerenz, *ECS J. Solid State Sci. Technol.*, 2013, **2**, Q51–Q58.
22 H. Lewerenz and K. Schulte, *Electrochim. Acta*, 2002, **47**, 2639–2651.
23 K. Schulte and H. Lewerenz, *Electrochim. Acta*, 2002, **47**, 2633–2638.
24 M. V. Lebedev, Y. M. Serov, T. V. Lvova, R. Endo, T. Masuda and I. V. Sedova, *Appl. Surf. Sci.*, 2020, **533**, 147484.
25 A. Goryachev, L. Gao, R. P. J. van Veldhoven, J. E. M. Haverkort, J. P. Hofmann and E. J. M. Hensen, *Phys. Chem. Chem. Phys.*, 2018, **20**, 14242–14250.

26 R. Alvarado, I. Azahel and W. G. Schmidt, *ACS Omega*, 2022, **7**, 19355–19364.
27 R. Alvarado, I. Azahel, M. Karmo, E. Runge and W. G. Schmidt, *ACS Omega*, 2021, **6**, 6297–6304.
28 X. Zhang, T. A. Pham, T. Ogitsu, B. C. Wood and S. Ptasinska, *J. Phys. Chem. C*, 2020, **124**, 3196–3203.
29 W.-H. Cheng, M. H. Richter, M. M. May, J. Ohlmann, D. Lackner, F. Dimroth, T. Hannappel, H. A. Atwater and H.-J. Lewerenz, *ACS Energy Lett.*, 2018, **3**, 1795–1800.
30 O. Tereshchenko, D. Paget, P. Chiaradia, E. Placidi, J. Bonnet, F. Wiame and A. Taleb-Ibrahimi, *Surf. Sci.*, 2006, **600**, 3160–3166.
31 C. Goletti, G. Bussetti, A. Violante, B. Bonanni, M. Di Giovannantonio, G. Serrano, S. Breuer, K. Gentz and K. Wandelt, *J. Phys. Chem. C*, 2015, **119**, 1782–1790.
32 V. Mazine and Y. Borensztein, *Phys. Rev. Lett.*, 2002, **88**, 147403.
33 B. Sheridan, D. S. Martin, J. R. Power, S. D. Barrett, C. I. Smith, C. A. Lucas, R. J. Nichols and P. Weightman, *Phys. Rev. Lett.*, 2000, **85**, 4618–4621.
34 K. Haberland, P. Kurpas, M. Pristovsek, J.-T. Zettler, M. Weyers and W. Richter, *Appl. Phys. A: Mater. Sci. Process.*, 1999, **68**, 309–313.
35 J.-T. Zettler, K. Haberland, M. Zorn, M. Pristovsek, W. Richter, P. Kurpas and M. Weyers, *J. Cryst. Growth*, 1998, **195**, 151–162.
36 K. Christiansen, M. Luenenbuerger, B. Schineller, M. Heuken and H. Juergensen, *Opto-Electron. Rev.*, 2002, **10**(4), 237–242.
37 G. Sombrio, E. Oliveira, J. Strassner, J. Richter, C. Doering and H. Fouckhardt, *Micromachines*, 2021, **12**, 502.
38 P. Weightman, D. S. Martin, R. J. Cole and T. Farrell, *Rep. Prog. Phys.*, 2005, **68**, 1251–1341.
39 D. S. Martin and P. Weightman, *Surf. Rev. Lett.*, 2000, **07**, 389–397.
40 T. D. Kühne, M. Iannuzzi, M. Del Ben, V. V. Rybkin, P. Seewald, F. Stein, T. Laino, R. Z. Khaliullin, O. Schütt, F. Schiffmann, D. Golze, J. Wilhelm, S. Chulkov, M. H. Bani-Hashemian, V. Weber, U. Borštnik, M. Taillefumier, A. S. Jakobovits, A. Lazzaro, H. Pabst, T. Müller, R. Schade, M. Guidon, S. Andermatt, N. Holmberg, G. K. Schenter, A. Hehn, A. Bussy, F. Belleflamme, G. Tabacchi, A. Glöß, M. Lass, I. Bethune, C. J. Mundy, C. Plessl, M. Watkins, J. VandeVondele, M. Krack and J. Hutter, *J. Chem. Phys.*, 2020, **152**, 194103.
41 J. P. Perdew, K. Burke and M. Ernzerhof, *Phys. Rev. Lett.*, 1996, **77**, 3865–3868.
42 P. Giannozzi, S. Baroni, N. Bonini, M. Calandra, R. Car, C. Cavazzoni, D. Ceresoli, G. L. Chiarotti, M. Cococcioni, I. Dabo, A. D. Corso, S. de Gironcoli, S. Fabris, G. Fratesi, R. Gebauer, U. Gerstmann, C. Gougoussis, A. Kokalj, M. Lazzeri, L. Martin-Samos, N. Marzari, F. Mauri, R. Mazzarello, S. Paolini, A. Pasquarello, L. Paulatto, C. Sbraccia, S. Scandolo, G. Sclauzero, A. P. Seitsonen, A. Smogunov, P. Umari and R. M. Wentzcovitch, *J. Phys.: Condens. Matter*, 2009, **21**, 395502.
43 M. Schlipf and F. Gygi, *Comput. Phys. Commun.*, 2015, **196**, 36–44.
44 A. Marini, C. Hogan, M. Grüning and D. Varsano, *Comput. Phys. Commun.*, 2009, **180**, 1392–1403.
45 D. Sangalli, A. Ferretti, H. Miranda, C. Attaccalite, I. Marri, E. Cannuccia, P. Melo, M. Marsili, F. Paleari, A. Marrazzo, G. Prandini, P. Bonfà, M. O. Atambo, F. Affinito, M. Palummo, A. Molina-Sánchez, C. Hogan, M. Grüning, D. Varsano and A. Marini, *J. Phys.: Condens. Matter*, 2019, **31**, 325902.
46 D. E. Aspnes and A. A. Studna, *Phys. Rev. B: Condens. Matter Mater. Phys.*, 1983, **27**, 985–1009.
47 M. Muthuvel and J. Stickney, *J. Electrochem. Soc.*, 2006, **153**, C67.
48 H. J. Lewerenz, H. Gerischer and M. Lübke, *J. Electrochem. Soc.*, 1984, **131**, 100–104.
49 M. M. May and M. Sprik, *New J. Phys.*, 2018, **20**, 033031.

Cell Reports
Physical Science

CellPress
OPEN ACCESS

Article

Photoelectrochemical Schlenk cell functionalization of multi-junction water-splitting photoelectrodes

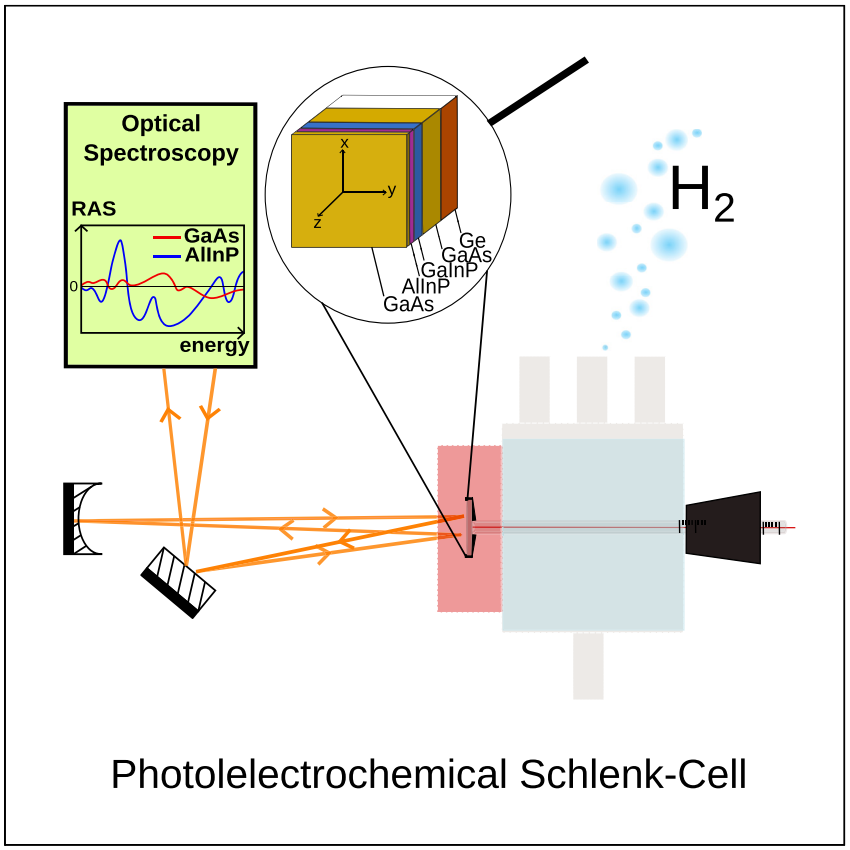

Schmitt et al. develop a flexible Schlenk cell setup for clean photoelectrochemical surface processing conditions with optical *in situ* control and performance benchmarking. They apply the versatile approach here on a photoelectrode for solar hydrogen production, resulting in solar-to-hydrogen efficiencies of up to 18%.

Erica A. Schmitt, Margot Guidat, Max Nusshör, ..., Daniel Lörch, Moritz Kölbach, Matthias M. May

matthias.may@uni-tuebingen.de

Highlights

Reproducible preparation and functionalization of water-splitting photoelectrodes

Solar-to-hydrogen efficiencies of up to 18.8% on increased electrode areas

Longer unbiased electrode lifetimes compared to similar previous work

In situ optical process control with reflection anisotropy spectroscopy

Schmitt et al., Cell Reports Physical Science 4, 101606
October 18, 2023
https://doi.org/10.1016/j.xcrp.2023.101606

Please cite this article in press as: Schmitt et al., Photoelectrochemical Schlenk cell functionalization of multi-junction water-splitting photoelectrodes, Cell Reports Physical Science (2023), https://doi.org/10.1016/j.xcrp.2023.101606

Cell Reports
Physical Science

Article

Photoelectrochemical Schlenk cell functionalization of multi-junction water-splitting photoelectrodes

Erica A. Schmitt,[1] Margot Guidat,[1] Max Nusshör,[1] Anna-Lena Renz,[1] Kristof Möller,[2] Marco Flieg,[1] Daniel Lörch,[1] Moritz Kölbach,[1] and Matthias M. May[1,3,*]

SUMMARY

Solar water splitting has the potential to significantly contribute to future greenhouse-gas-free fuels. In photoelectrochemical water splitting, the solar absorber is in direct contact with the aqueous electrolyte. This enables a higher level of device integration, but it also creates additional challenges when compared to decoupled photovoltaics-electrolysis approaches. Here, we report on the design of a photoelectrochemical Schlenk cell processing routine that allows photoelectrochemical interface functionalization under controlled conditions. Interface inhomogeneities that accelerate corrosion are hereby reduced, while the photoelectrochemical window layer from the functionalization reduces voltage and light absorption losses for the photoelectrode. Applied to a dual-junction GaInP/GaAs photoelectrode, we demonstrate solar-to-hydrogen efficiencies of up to 18.8% on increased electrode areas and longer unbiased electrode lifetimes compared to similar previous work. This general processing approach should be transferable to other systems where photoelectrochemical functionalization with optical *in situ* control is desirable.

INTRODUCTION

Generating hydrogen from solar energy is expected to be an important building block of our future carbon-free and sustainable energy supply and storage.[1,2] Even though this challenge has been widely discussed for many decades,[3,4] hydrogen production via water splitting is still quantitatively negligible compared to steam reforming from fossil fuels.[5]

While the currently most mature approach to produce solar hydrogen is to connect photovoltaic (PV) cells to an electrolyzer,[2,6,7] there are also more integrated approaches for solar water splitting. On an intermediate level of integration, the electrodes for the water-splitting reaction are separate electrodes that still allow heat exchange with the PV solar cell.[1,8] The highest degree of integration, which we pursue in the following, is reached in a photoelectrochemical (PEC) water-splitting approach, where the photoelectrode is immersed in the electrolyte and the front surface of the solar absorber is decorated with co-catalysts.[9–11] Here, the harvesting of solar photons and hydrogen evolution are combined in a single device, allowing for compact designs, low current densities, and—in principle—a low balance of system cost,[12,13] yet these come at the expense of complex challenges for the design of the involved interfaces. The direct approach has proven to be efficient[10,14–16] and could become a complementary technology to large-scale water

[1]Universität Tübingen, Institute of Physical and Theoretical Chemistry, Auf der Morgenstelle 15, 72076 Tübingen, Germany

[2]AZUR SPACE Solar Power GmbH, Theresienstraße 2, 74072 Heilbronn, Germany

[3]Lead contact

*Correspondence: matthias.may@uni-tuebingen.de

https://doi.org/10.1016/j.xcrp.2023.101606

electrolysis using PV-generated electricity. However, efficient and stable operation requires a very careful design of the solid-liquid interface, and so far, high performance combined with electrode lifetimes suitable for commercialization has not been achieved. The PEC approach implies that the minimum required photovoltage to be delivered by the device is given by the sum of the free energy of the desired reaction plus its overpotentials and that the solar-to-hydrogen (STH) efficiency only depends on the unassisted photocurrent. Together with the shape of the solar spectrum, this results in dual-junction photoabsorbers as the optimum in terms of efficiency.[15]

The higher efficiencies of multi-junction photoabsorbers do, however, come at the cost of increased device complexity and typically also more expensive materials, as in the case of the III-V material class. Here, approaches to integrate III-V top absorber(s) with a silicon substrate, which also acts as a bottom cell, promise to reduce costs toward commercial feasibility.[17,18] The demand for less-abundant material is hereby particularly lowered since the top absorber is typically more than two magnitudes thinner than the substrate material.

The high degree of integration for PEC processes is mainly based on the fact that the photoelectrode is in direct contact with the electrolyte. All beneficial characteristics of PEC water splitting with III-V semiconductors can only be taken advantage of if the semiconductor-electrolyte interface works at the same time as a charge-selective contact layer to reduce charge-carrier recombination and as a (electro)chemical passivation layer.[11] The latter serves to prevent corrosion and the correlated loss of efficiency. This can be achieved by suitable surface functionalization, for which intentional photocorrosion in a designated preparation environment can be used.[10] Furthermore, the semiconductor surface needs to be provided with a transparent catalyst layer, lowering the high overpotential of the water-splitting reaction. Finally, light absorption losses from the aqueous electrolyte[19] and ion transport losses need to be balanced.[20]

PEC *in situ* functionalization allows us to create electrode-electrolyte interfaces that meet the above-mentioned requirements resulting in the highest conversion efficiencies, yet electrode stabilities are still only in the order of less than a day.[10] One reason for the corrosion-induced failure of such photoelectrodes is localized surface inhomogeneities leading to the formation of pinholes in the protective layer.[21] Figure 1 shows such a case, where a particle on the surface was still present after wet-chemical etching and prior to functionalization, leading to catalyst deposition on top of the particle and a defective protection layer below. This is a well-known challenge in semiconductor processing and the reason for the use of cleanroom facilities in the semiconductor industry[22] but is also increasingly recognized in the electrocatalysis community.[23]

In this article, we introduce a PEC Schlenk cell processing that allows us to combine wet-chemical etching with optical *in situ* control, PEC functionalization, and PEC characterization in the same glass cell under inert conditions. The cell design offers a flexible handling with the opportunity to perform two- or three-electrode experiments and to vary the electrolyte layer thickness for balancing transport and optical losses. Process control is enabled via *in situ* reflection anisotropy spectroscopy, which is an established method to monitor epitaxial growth processes.[24] We apply this method to III-V-based multi-junctions, demonstrating high STH efficiencies of 18.8% on already significantly larger surface areas than reported previously and improved lifetimes.[14]

Please cite this article in press as: Schmitt et al., Photoelectrochemical Schlenk cell functionalization of multi-junction water-splitting photoelectrodes, Cell Reports Physical Science (2023), https://doi.org/10.1016/j.xcrp.2023.101606

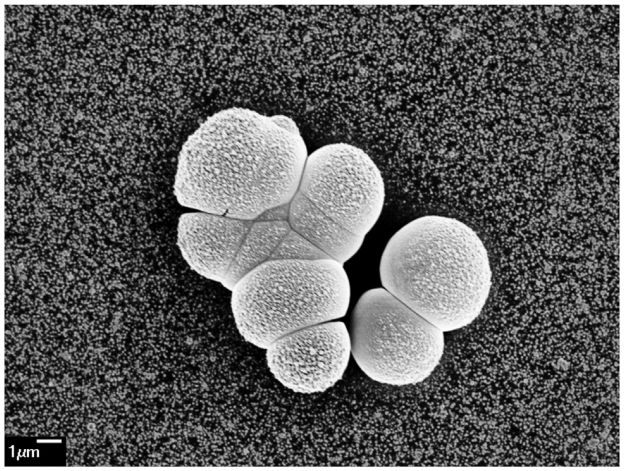

Figure 1. Contaminant on the window layer of the PEC cell

Scanning electron microscopy image of a photoelectrochemical cell surface after deposition of Rh nanoparticles under ambient conditions. The large particles in the middle, here probably fungal spores, constitute a typical contaminant from ambient air of biologic origin. This impedes surface functionalization and will result in a point of attack for (photo)corrosion. Scale bar: 1 μm.

RESULTS AND DISCUSSION

PEC Schlenk cell processing

To turn a dual-junction photoabsorber with an AlInP window layer into an efficient photoelectrode, three main process steps are required: the wet-chemical etching of the cap layer, the formation of a PEC window layer, and finally, the decoration of the surface with co-electrocatalysts. Here, the main purpose of the Schlenk cell processing is to establish well-defined process conditions, avoiding contamination that leads to surface inhomogeneities, pinholes, and ultimately corrosion. For well-conditioned samples, optical inspection during operation as well as postmortem analysis by scanning electron microscopy (SEM) reveals that corrosion sets in on only very few (typically 1–2) sites (see also Figure S11).[10] The identification of such rare sites by SEM prior to operation is not feasible, consequently allowing only qualitative statements. In our series of prepared samples, we could occasionally identify particles on top of surfaces prior to the introduction of the Schlenk cell processing but not thereafter. Practical considerations require the minimization of the cell volume to enable rapid change of process conditions. Furthermore, a variable electrolyte layer thickness is desirable to balance ion transport and light absorption losses in the electrolyte film above the sample.[20] The developed Schlenk cell depicted in Figure 2A fulfills these criteria and is based on a customized glass body, which is equipped with four inlets. The three inlets on top of the cell allow the flexible insertion of different electrodes and the necessary Schlenk valves to work under inert conditions. The horizontal inlet, depicted in a black color in Figure 2B, allows the insertion of working electrodes with a diameter up to 23 mm perpendicular to the quartz window. This is significantly larger than the areas reported for other high-efficiency, III-V-based PEC water splitting approaches, which were only in the range of 0.1–0.3 cm^2.[14,16] The working electrode is attached to a glass rod and inserted through a stopper with a hole. This allows for continuous adjustment of the distance between the working electrode and the quartz window and therefore the electrolyte layer in the light path. For relevant electrolyte layer thicknesses, the position of the working electrode (WE) will mostly be inside the cap holding the quartz window so that light scattering cannot artificially enhance

Please cite this article in press as: Schmitt et al., Photoelectrochemical Schlenk cell functionalization of multi-junction water-splitting photoelectrodes, Cell Reports Physical Science (2023), https://doi.org/10.1016/j.xcrp.2023.101606

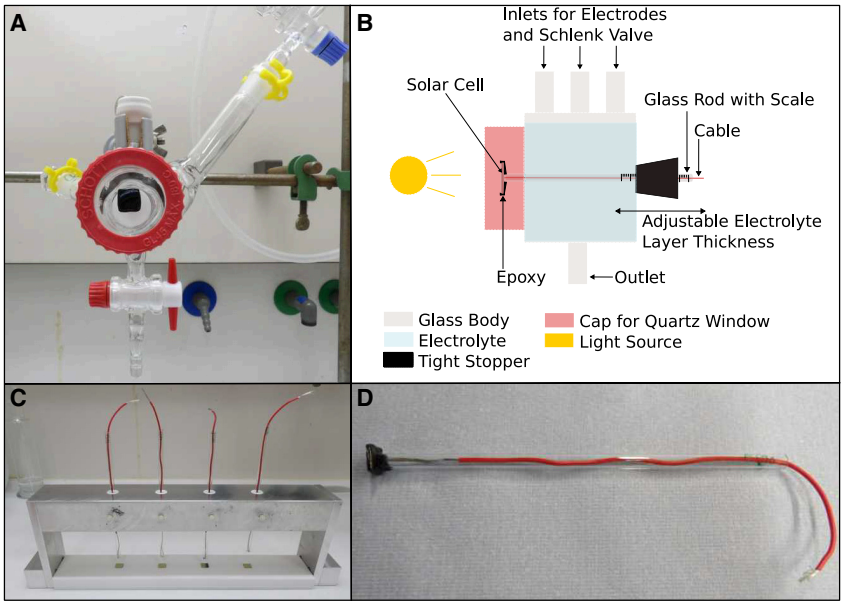

Figure 2. Photoelectrochemical Schlenk cell setup

(A) Schlenk glass cell with three inlets for Schlenk equipment and electrodes, horizontal inlet for the sample, and an outlet.

(B) Schematic drawing of the Schlenk glass cell in side view.

(C and D) Sample preparation in a customized stand (C) and prepared sample (D).

the STH efficiency. Also, the distance between the WE and the counter as well as a reference electrode can be adjusted.

For the PEC experiments, we use solar absorbers epitaxially grown on a Ge substrate. The bottom cell absorber material is GaAs (E_g = 1.4 eV), followed by the GaInP top absorber (E_g = 1.8 eV), as depicted in Figure 3. A thin AlInP window layer with a wide, indirect band gap of >2.2 eV serves as electron collector, which is finally covered by a protective cap layer of GaAs. The configuration is similar to III-V/Si dual-junction solar cells, which are currently under development but do not yet provide enough photovoltage for highly efficient operation due to charge-carrier recombination losses at the III-V/Si interface.[18] Yet as soon as photovoltages of the Si-based dual junctions have improved further toward their physical limit, our approach should be transferable to this less costly absorber class. This configuration merges the benefits of the more expensive but highly efficient III-V absorber materials and the scaled-up and hence less pricey technology of Si solar absorbers. It has to be noted that reducing processing costs is the main leverage for the scalability of III-V-related solar absorbers.[17] In terms of materials abundance, indium is the most critical element in our solar absorber stack. A comparison of the abundance in the continental earth crust with other popular materials for solar water splitting shows that indium is, for instance, more abundant than bismuth (the limiting ingredient of $BiVO_4$) and only slightly less abundant than iodine (often present in perovskites).[25]

The samples depicted in Figure 2 were prepared to suit the requirements of the PEC measurements in the PEC Schlenk cell. In Figure 2C, the preparation process in a customized stand is depicted to receive the samples as depicted in Figure 2D. The fixation in the stand ensures the parallel mounting of the photoelectrode and the quartz window.

Please cite this article in press as: Schmitt et al., Photoelectrochemical Schlenk cell functionalization of multi-junction water-splitting photoelectrodes, Cell Reports Physical Science (2023), https://doi.org/10.1016/j.xcrp.2023.101606

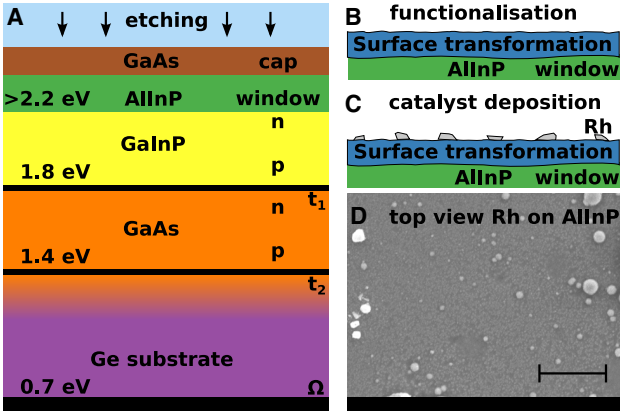

Figure 3. Layer stack of the photoelectrochemical solar cell

(A) Layer stack; t_1 and t_2 and Ω denote tunnel junctions and ohmic back contact, respectively; vertical arrows indicate selective chemical etching of the cap layer.

(B) Chemical and photoelectrochemical surface transformation of the AlInP window layer in an aqueous solution of $RhCl_3$.

(C) Photoelectrodeposition of electrocatalyst nanoparticles.

(D) Scanning electron microscope image of the surface after Rh catalyst deposition; scale bar: 1 μm. Adapted from May et al.[10]

Etching with optical *in situ* control

Before the catalyst is photoelectrochemically deposited on the surface of the photoabsorber, the protective GaAs cap layer must be removed in a manner that leaves a well-defined, homogeneous surface.[10] The purpose of the GaAs layer is to protect the solar absorber from damages due to moisture or mechanical influences prior to processing. In the case of a PV solar cell, the GaAs layer additionally forms a barrier between the electronic front contact and the AlInP window layer, preventing metal diffusion toward the bulk, forming undesired alloys. The thickness of the cap layer differs from 20 nm as a protection layer to 250 nm in a PV solar cell. The most common way to achieve the removal of this cap layer is wet-chemical etching.

Etching solutions made of H_2O_2, NH_4OH, and H_2O are widely used for a selective removal of GaAs.[26] In a previous related work, a 1:1:10 (H_2O_2 NH_4OH:H_2O) volume ratio was used to etch the GaAs cap layer within 5 s.[10] For the preparation of the etching solution, aqueous solutions of H_2O_2 and NH_3 were used, and the stated concentration of NH_4OH refers to the initial concentration of NH_3 before any protonation has occurred. The etching process is believed to consist of two steps: the oxidation of GaAs by the oxidizing agent H_2O_2 and the dissolution of the oxides by the dissolving agent NH_4OH.[27] Therefore, the etching solution must have a pH value between 10.1 and 12 to ensure that no residual Ga oxides are present on the surface after etching (pH <10.1) and to prevent H_2O_2 dissociation (pH $>$ 12). Furthermore, the time of etching should be long enough to be resolved by the optical *in situ* probe. Hence, the volume ratio of the etching solution of 1:1:200 (H_2O_2 NH_4OH:H_2O) was chosen to fulfill these two conditions.

A careful choice of the etching solution allows us to realize a highly selective etching, i.e., the etching rate ratio of the topmost layer to the layer below must typically be greater than five,[26] which minimizes etching into the underlying window layer. Furthermore, the choice of the solution should also allow for isotropic etching to result in a homogeneously etched surface. Here, etch process optimization can benefit from real-time *in situ* monitoring. For a well-defined control of the

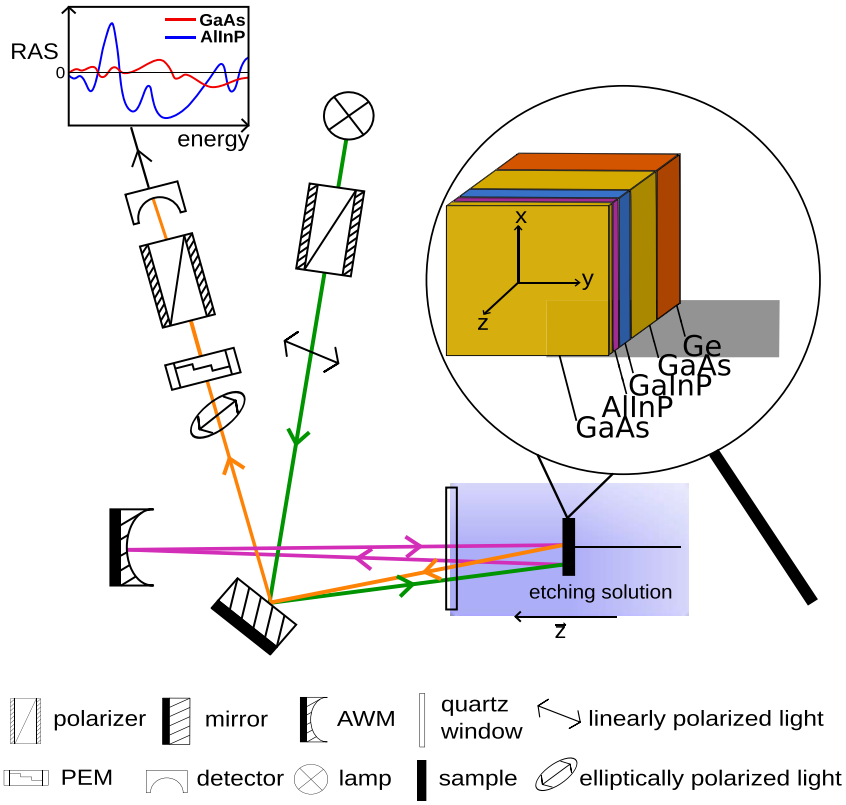

Figure 4. *In situ* electrochemical RAS setup for the PEC Schlenk cell

Schematic of the RAS setup used to monitor the etching and functionalization process of the photoelectrode in solution.

solid-liquid interface evolution, the characterization technique considered should be surface sensitive and non-destructive and should offer a reasonable time resolution to observe the transition from one material layer to another. Reflection anisotropy spectroscopy falls within the available techniques that fulfill these requirements.[28,29] Its principle is illustrated in Figure 4, and the setup is detailed in the experimental procedures. In short, reflection anisotropy spectroscopy (RAS) is a linear optical technique that measures the optical in-plane anisotropy in a simple near-normal incidence reflection geometry. More specifically, it probes the difference in reflectivity, Δr, between two orthogonal directions, x and y, of the surface plane, normalized by the mean overall reflectivity (Equation 1). RAS is sensitive to changes in surface composition, surface structure, environment at the interface, electric fields, and internal strain, which is, in principle, beneficial but also renders signal analysis complex.[28] For heteroepitaxial samples, another degree of complexity is added, as layers from different buried heterointerfaces can also contribute to the signal.

$$\text{RAS} : = \frac{\Delta r}{r} = 2 \cdot \frac{r_x - r_y}{r_x + r_y} \qquad \text{(Equation 1)}$$

To determine the etching time, we fit the time-resolved signal, the transient, with a sigmoid function given in Equation 2, adapted from Sombrio et al.[30] The photon energy for the transient is chosen in such a way that no Fabry-Perot oscillations are present, and a sigmoid decrease of the anisotropy value is observed. τ is a time constant, and t_0 corresponds to the time of the inflection point of the transient.

Please cite this article in press as: Schmitt et al., Photoelectrochemical Schlenk cell functionalization of multi-junction water-splitting photoelectrodes, Cell Reports Physical Science (2023), https://doi.org/10.1016/j.xcrp.2023.101606

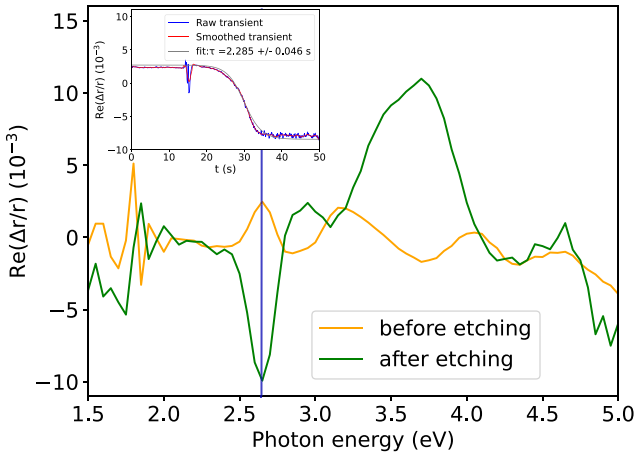

Figure 5. RA spectra of the photoelectrode before and after etching

RA spectra of the photoelectrode before and after etching. The orange and green curves correspond to GaAs and AlInP termination, respectively. The inset shows the time-resolved optical anisotropy at a photon energy of 2.6 eV during etching and the corresponding curve fit to determine the etch time.

RAS_i and RAS_f are the anisotropy values at the beginning and the end of the etching process, respectively.

$$f(t) = \frac{RAS_i - RAS_f}{1+\exp\left(\frac{t - t_0}{\tau}\right)} + RAS_f \qquad \text{(Equation 2)}$$

The etching time is then defined as the time during which the growth rate of the function f is less than 97%:

$$\frac{f(t) - f(t_i)}{f(t_\infty) - f(t_i)} \leq 0.97. \qquad \text{(Equation 3)}$$

The RA spectra of the solar absorber in water, prior to and after the etching process, are shown in Figure 5. The orange and green spectra correspond to GaAs and AlInP, respectively. The GaAs spectrum resembles an n-type, oxidized GaAs(100) surface.[31,32] The main features of the GaAs RA spectrum are found at the E1 and E1 + δ E1 critical points at around 2.6 and 3.2 eV, respectively. The AlInP spectrum is well distinguishable from the one of GaAs, especially around 2.6 and 3.7 eV, where it shows two main characteristic peaks. For this reason, to control the etching process, a transient is measured at 2.6 eV, where the anisotropy is expected to significantly drop. The etch monitoring is illustrated in the inset of Figure 5. The high signal-to-noise ratio of the time-resolved anisotropy and the large anisotropy drop between 20 and 35 s allow for a well-defined etch process monitoring with RAS. The artifact present at around 15 s corresponds to the addition of etching solution from the bottom to the top of the sample. To facilitate fitting of the transient with a higher precision, the latter is smoothed with a Savitzky-Golay filter. Smoothed transients are then fitted with Equation 2, and the etching time is determined with Equation 3. Over five different etched samples, a mean etching time of 14.8 s with a standard deviation of 1.6 s is determined, and no traces of residual GaAs were found (see also Figure S1). It is therefore possible to precisely control the removal of the GaAs cap layer in the time domain by *in situ* RAS monitoring without the requirement of time-consuming *ex situ* analysis. Assessment of the structural quality of the obtained surface is straightforwardly possible on a fingerprint basis from the

spectrum, which would change upon modifications in structure and composition at the surface. Sample or process agent contamination, but also changes in ambient illumination, can impact the etching process kinetics and the final results.[33,34] Hence, evaluating both spectra and transients is highly desirable for the control of the resulting interfacial properties. Our results suggest that the method could also be instrumental for wet-(electro)chemical processing of other crystalline materials.

Variable water layer thickness

The absorption of light by water-based electrolytes is a well-known challenge for PEC water splitting. As the effect is most pronounced in the near-infrared (IR) region, it is especially relevant for high-efficiency multi-junction photoelectrodes, which comprise absorbers with band gaps below 1.5 eV.[15,19,35,36] An example is depicted in Figure S2A, showing simulations assuming the AM1.5G spectrum traveling through a water layer of 10 and 50 mm thickness in comparison with the genuine AM1.5G spectrum.[20] However, a thin electrolyte layer with accordingly low absorption induces significant overpotential losses from ion transport. Hence, an optimum exists that counter-balances losses from light absorption and ion transport. In the case of a dual junction with a Si bottom cell, simulations showed that the theoretical optimum for the water layer thickness between the photoelectrode and the quartz window is about 5 mm, yet this also depends on the electrolyte and the exact electrode configuration.[20] Our setup allows us to continuously vary the electrolyte layer thickness, adapting an optimum thickness as a function of electrolyte conductivity and absorber band gaps. Figure S3A shows a variation of the water layer thickness between 1 and 30 mm for a triple junction with an active Ge bottom cell, where the effect is more pronounced than for the dual junctions. The experimental data for the unbiased, two-electrode case lies in between the modeled losses displayed in Figure S3B, which is to be expected, as our model neglects effects of electrode geometries impacting transport overpotentials but also diode non-idealities. Our results on the water layer thickness for the triple junction deviate to some extent from the results of Moon et al.,[36] who find their best results for the same type of solar absorber with 2 mm water layer thickness. This might, however, be due to their different light source, which does not allow such a fine-grained tuning, or their TiO_2-coated layer stack with decreased transparency or reduced anti-reflective properties, as they also find a reduced overall current density. In the following, we employ an electrolyte thickness of 5 mm for the dual-junction absorbers.

Surface functionalization and water-splitting performance

After wet-chemical etching of the dual-junction solar absorbers, the AlInP window layer, which is not intrinsically stable in an aqueous electrolyte, was functionalized photoelectrochemically and decorated with Rh nanoparticles as co-electrocatalysts in a procedure adapted from May et al.[10] The functionalization results in a mixture of phosphites, phosphates, and oxides that exhibit a suitable band alignment and improved electrochemical stability.[10] The processed dual-junction samples typically had an active area of around 0.75 cm^2 due to epoxy resin covering the edges of the initially squared 1 cm^2 samples. They were then subject to benchmarking under chopped AM1.5G illumination using a multi-LED solar simulator Wavelabs Sinus-220 with integrated spectrometer. Figure 6 shows the current densities over time in a two-electrode setup without bias voltage (see also Video S1 for typical operation conditions).

We observe an initial STH efficiency of 18%, and the efficiency is kept > 15% for more than 40 min for the champion sample B (see Table 1). The presented samples A, B, C, and D were prepared and measured consecutively. The underlying assumption for the determination of the STH efficiency from the photocurrent is a near-unity

Cell Reports
Physical Science
Article

CellPress
OPEN ACCESS

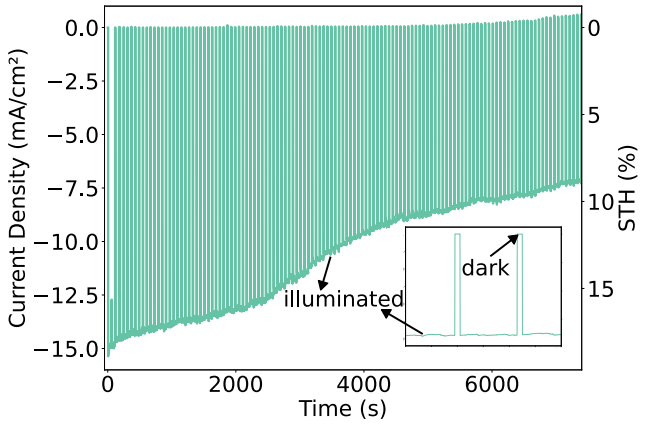

Figure 6. Current density of champion sample B

Current density of champion sample B measured in the described PEC cell after surface functionalization ibidem (0 V vs. IrO_x CE, simulated chopped AM1.5G, 1 M $HClO_4$). The inset exemplary shows the current density during three illuminated and two dark periods.

Faradaic efficiency. This can, however, be justified by the stack of thin epitaxial layers, as the dissolution of the AlInP window layer (<50 nm) would directly lead to a breakdown of photovoltage due to charge-carrier recombination with drastic reduction of the current density.[10] Assuming a cathodic dissolution of AlInP releasing PH_3, a charge of about 20 mC/cm^2 would be required to dissolve the complete window layer of 20 nm thickness. With the measured current densities, this charge would be transferred in less than 2 s, which justifies the assumption of a near-unity Faradaic efficiency. Slow corrosion still leads to a degradation of the photocurrent density, and after 100 min, the photocurrent transients around the dark periods start to show the typical spikes associated with the onset of charge-carrier recombination.[37] To assess the time evolution of photodegradation more quantitatively, we employ the STH_i definition,[35] giving the average performance of the photoelectrode on a logarithmic time axis as defined in Equation 4, taking into account only the time of illumination. The results for a sequence of samples are shown in Table 1 and Figure S4.

$$STH_i = \frac{1}{10^i}\int_0^{10^i} STH(t)dt \qquad \text{(Equation 4)}$$

As already noted above, surface inhomogeneities from epitaxial growth, sample handling (Figure 1), or additionally grown protection layers can greatly accelerate surface corrosion.[10,21] The probability for such defects grows with the sample area, and consequently, sample sizes in the literature for high-efficiency, immersed photoelectrodes were often only in the order of 0.1–0.3 cm^2.[14,16] Yet also in our case, surface corrosion remains the major challenge to be addressed by further improvements of the surface functionalization routine or the combination with complementary protection layers. Such protection layers need to be, just like the catalyst, optically transparent, provide excellent electron transport properties, and be chemically stable in an acidic environment. A material that, in principle, meets these requirements is crystalline, atomic layer-deposited (ALD) TiO_2.[38] Still, challenges such as the formation of pinholes and the energetic alignment between these ALD interlayers, the underlying absorbers, and the overlying catalyst are often performance limiting and therefore the subjects of current research. From the electrolyte side, the reduction of acidity can be considered for further stability improvements, while the efficiency will be lowered here due to transport overpotentials.[20]

Please cite this article in press as: Schmitt et al., Photoelectrochemical Schlenk cell functionalization of multi-junction water-splitting photoelectrodes, Cell Reports Physical Science (2023), https://doi.org/10.1016/j.xcrp.2023.101606

Table 1. STH_i efficiencies for four samples values derived from unbiased, two-electrode operation under simulated AM1.5G illumination, rounded down to one decimal place

Time (s)	(%)	A	B	C	D
1	STH_0	18.1	18.0	16.2	18.8
10	STH_1	17.5	17.9	16.0	16.6
100	STH_2	16.6	17.5	15.6	13.7
1,000	STH_3	15.2	16.7	14.9	12.9

Samples were prepared under similar conditions and in succession. See also Table S1 and Figure S4.

Degradation in the investigated samples can be observed with the removal of Rh catalyst particles from the absorber surface as depicted in the SEM picture of sample D in Figure S9. Removal of catalyst nanoparticles can be induced by the mechanical stress from the formation of hydrogen bubbles. This problem could be approached by the use of surfactants, which reduce bubble sizes,[9,10] yet such surfactants also need to be inert. Another reason for the Rh removal can be corrosion of the underlying window layer, which is observed in the X-ray photoelectron spectroscopy (XPS) measurements in Figures S6–S8. Here, we observe that the AlInP signatures partially vanish after extended operation of the PEC cell, indicating the dissolution of the window layer. While an increase of the catalyst loading would therefore also be a route toward increased stability of the device, this does, beyond a threshold, also increase light absorption by the catalyst layer and hence reduce efficiency.[35]

To summarize, the PEC Schlenk cell processing presented in this work enables PEC surface functionalization under well-controlled conditions, avoiding a glovebox or cleanroom facilities. An optical *in situ* process control using RAS was implemented and allows us to further improve reproducibility and quantification of sample-to-sample variations. We could exemplarily demonstrate the benefits of the method by achieving high STH efficiencies of up to 18.8% of an immersed PEC system. The active sample areas are already significantly larger than previously reported (at 19.3% STH) for a similarly processed system where only 30 min of unbiased water splitting was demonstrated,[14] which can probably, at least to some extent, be attributed to improved homogeneity of the overall processing here (see also Figure S10). The flexibility of the setup, in principle, allows for further spectroelectrochemical methods to be employed, such as IR or Raman spectroscopy. The variable electrolyte top layer thickness allows us to set the optimum distance to the front window, which depends on the electrolyte, the (bottom) absorber, and the geometry of the setup with respect to the placement of the counter-electrode. Surface treatments after (bulk) synthesis are also common for other materials, such as the CoPi photoelectrodeposition on $BiVO_4$,[39] and hence the approach could also be beneficial for material classes beyond III-V. For future product analysis and the prevention of gas crossover, we will further adapt the setup to include a membrane assembly between the electrodes. While ultimately, outdoor efficiency benchmarking should also be envisaged,[40] our results are already a first step toward scaling up PEC photoelectrode processing, which will be required for realistic application cases.

EXPERIMENTAL PROCEDURES

Resource availability

Lead contact

Further information and requests for resources should be directed to and will be fulfilled by the lead contact, Matthias M. May (matthias.may@uni-tuebingen.de).

Please cite this article in press as: Schmitt et al., Photoelectrochemical Schlenk cell functionalization of multi-junction water-splitting photoelectrodes, Cell Reports Physical Science (2023), https://doi.org/10.1016/j.xcrp.2023.101606

Materials availability

This study did not generate new unique reagents.

Data and code availability

The data that support the findings of this study are openly available on Zenodo at https://doi.org/10.5281/zenodo.8279703.

RAS

The RA spectra were measured with an RA spectrometer (EpiRAS from Laytec) equipped with a Xenon light source. The setup used for the *in situ* etching monitoring is illustrated in Figure 4. To allow RAS measurements of the surface of the photoabsorber mounted vertically in the glass cell, a mirror is placed below the spectrometer at an angle of 45° and in front of the sample. The light, initially linearly polarized, is reflected on the mirror and reaches the sample (green light path). An eventual imperfect vertical position of the sample is corrected by an anti-wobble mirror (AWM) after the first reflection of the light on the surface (pink light path). After the second reflection on the photoelectrode, the light, now elliptically polarized due to the optical anisotropy, reaches the detector of the spectrometer.

The reference spectrum of the epitaxial layer stack, corresponding to the GaAs-terminated surface, was taken in water during the cleaning process of the cell. For the etch monitoring, a solution of 1:1:200 (H_2O_2:NH_4OH:H_2O; H_2O_2 supplied by Merck 30%, NH_4OH supplied by Merck 25%) was prepared. Before starting the transient, the PEC cell was filled with the etching solution just below the bottom of the electrode. 10 s after the start of the transient, the electrode was fully covered with the etching solution. 30 s after the sample was fully covered, the etching solution was removed. The spectral signature of AlInP can slightly vary depending on the time of contact of the etching solution with the surface of the PEC cell. To avoid significant variation of the AlInP spectrum and to prevent the etching of AlInP by the residual etching solution present on the surface of the electrode, the PEC cell was rinsed three times with ultra-pure water within 1 min after the etching process was completed. The spectrum after etching was measured in water during the third cleaning step. Note that for all spectra, a baseline correction is applied to the RA spectra and to the transient by subtracting the sum of two spectra where the sample has been rotated by 90° in between.

Sample preparation

A glass rod was cut to length, followed by the insertion of a copper cable. The glass rod was then fixed in the customized steel stand. The 1 × 1 cm^2 solar absorber was positioned underneath the rod on a PTFE mount. The wire was then connected to the backside gold contact of the photoelectrode with silver resin. Afterward, the glass rod was attached to the absorber with epoxy resin "Epoxies 10–3046" (Epoxies Etc.). The epoxy was cured for 30 min at ambient conditions. Finally, the gold back contact, the sample edges, and the skinned wire were fully covered with epoxy and left to dry at ambient conditions over night. To avoid pinholes, the epoxy-covered areas were then fully covered again and left to cure for 24 h at ambient conditions. The absorbers from AZUR SPACE were based on their commercial "TJ Solar Cell 3G30C - Advanced" epitaxial structure with a bottom-up monocrystalline layer stack of Ge (band gap 0.7 eV), GaAs (1.4 eV), and GaInP (1.8 eV) and an intentionally reduced GaAs-cap layer thickness of 20 nm to simplify and support the *in situ* etching procedure prior to functionalization. Under PV operation, these triple-junction cells deliver an open-circuit voltage of ca. 2.35 V,

resulting in an expected open-circuit voltage for the dual junction of about 1.9 V (see also Figure S5) after subtraction of the voltage of the Ge bottom cell (0.45 V).

Surface functionalization

For the etching, the sample was first inserted into the Schlenk cell. Next, the pressure in the cell was reduced, and it was flushed with N_2 three times. Afterward, and after every preparation step, the cell was cleaned with water (MilliQ grade) under an N_2 counterflow two times. The surface functionalization was adapted from May et al.[10] For the surface functionalization and deposition of Rh nanoparticles of sample A, a 0.5 mM aqueous solution of $RhCl_3$ (99.98%, Sigma Aldrich) and 0.5 M KCl (99.997%, Alfa Aesar) was used. For samples B and C, a 5 mM aqueous solution was used, and for sample D, a 2.5 mM aqueous solution of $RhCl_3$ (99.98%, Sigma Aldrich) and 0.5 M KCl (99.997%, Alfa Aesar) was used. The deposition was performed in a three-electrode setup with the sample as a WE, a glassy carbon counter-electrode (>99.9% carbon, carbon rod electrode 6/60 mm, redox.me), and an Ag/AgCl reference electrode (913 pH Meter, Metrohm). The samples were treated in the $RhCl_3$ solution under open-circuit potential and 100 s illumination (AM1.5G). The light source was a Wavelabs Sinus-220 LED solar simulator with integrated spectrometer for automated spectral correction.

Chronoamperometry

The setup for determination of the current density was a two-electrode setup with an IrO_x counter-electrode (4 cm^2, IrO_x on a titanium mesh with 12 g Ir/m^2, Metakem) at 0 V bias voltage, controlled by a Zahner ZenniumPro potentiostat. The Sinus-220 solar simulator provided the AM1.5G spectrum at the location of the glass cell. The spectral mismatch of this light source is <5% (A++), and the uniformity fulfills the requirements of class A+. The spectral range is 400–1,100 nm. The Schlenk cell was equipped with a quartz plate as the front window. The electrolyte was 1 M $HClO_4$. The determination of the active sample surface was carried out with the software ImageJ.[41] The area was determined five times from one picture to form an average value. For the sample measured in Figure 6, the average size determined with that is 0.76 $\pm$ 0.01 cm^2.

SUPPLEMENTAL INFORMATION

Supplemental information can be found online at https://doi.org/10.1016/j.xcrp.2023.101606.

ACKNOWLEDGMENTS

This work was supported by the German Bundesministerium für Bildung und Forschung (BMBF), projects "H2Demo" (no. 03SF0619K) and "NETPEC" (no. 01LS2103A), as well as the German Research Foundation (DFG) under project number 434023472. The Schlenk cell was manufactured in pleasant cooperation with the University of Tübingen glassblower Thomas Nieß. The absorbers were kindly provided by AZUR SPACE.

AUTHOR CONTRIBUTIONS

The project was developed by M.M.M. and the experimental design by M.K., E.A.S., M.G., M.F., D.L., and M.M.M. The experiments were conducted by E.A.S., M.G., M.N., and A.-L.R. The code for the PEC model was implemented by M.M.M. and M.K. The modification of the photoabsorber epitaxy was introduced by K.M. E.A.S., M.G., and M.M.M. wrote the manuscript.

Cell Reports
Physical Science
Article

CellPress
OPEN ACCESS

DECLARATION OF INTERESTS

The authors declare no competing interests.

INCLUSION AND DIVERSITY

We support inclusive, diverse, and equitable conduct of research.

Received: May 31, 2023
Revised: August 4, 2023
Accepted: September 7, 2023
Published: October 2, 2023

REFERENCES

1. Jacobsson, T.J., Fjällström, V., Edoff, M., and Edvinsson, T. (2014). Sustainable solar hydrogen production: from photoelectrochemical cells to PV-electrolyzers and back again. Energy Environ. Sci. *7*, 2056–2070. https://doi.org/10.1039/C4EE00754A.

2. Turner, J.A. (2004). Sustainable Hydrogen Production. Science *305*, 972–974. https://doi.org/10.1126/science.1103197.

3. Ciamician, G. (1912). The Photochemistry of the Future. Science *36*, 385–394. https://doi.org/10.1126/science.36.926.385.

4. Fujishima, A., and Honda, K. (1972). Electrochemical Photolysis of Water at a Semiconductor Electrode. Nature *238*, 37–38. https://doi.org/10.1038/238037a0.

5. Bermudez, J.M., Evangelopoulou, S., and Pavan, F.I.E.A. (2022). Hydrogen, Iea (IEA). License: CC BY 4.0. https://www.iea.org/reports/hydrogen. Hydrogen - Energy systems overview. Accessed.

6. Calnan, S., Bagacki, R., Bao, F., Dorbandt, I., Kemppainen, E., Schary, C., Schlatmann, R., Leonardi, M., Lombardo, S.A., Milazzo, R.G., et al. (2021). Development of various photovoltaic-driven water electrolysis technologies for green solar hydrogen generation. Sol. RRL *6*, 2100479. https://doi.org/10.1002/solr.202100479.

7. van de Krol, R., and Parkinson, B.A. (2017). Perspectives on the photoelectrochemical storage of solar energy. MRS Energy Sust *4*, 13. https://doi.org/10.1557/mre.2017.15.

8. Kölbach, M., Rehfeld, K., and May, M.M. (2021). Efficiency gains for thermally coupled solar hydrogen production in extreme cold. Energy Environ. Sci. *14*, 4410–4417. https://doi.org/10.1039/D1EE00650A.

9. Khaselev, O., and Turner, J.A. (1998). A monolithic photovoltaic-photoelectrochemical device for hydrogen production via water splitting. Science *280*, 425–427. https://doi.org/10.1126/science.280.5362.425.

10. May, M.M., Lewerenz, H.J., Lackner, D., Dimroth, F., and Hannappel, T. (2015). Efficient direct solar-to-hydrogen conversion by in situ interface transformation of a tandem structure. Nat. Commun. *6*, 8286. https://doi.org/10.1038/ncomms9286.

11. Schleuning, M., Ahmet, I.Y., van de Krol, R., and May, M.M. (2022). The role of selective contacts and built-in field for charge separation and transport in photoelectrochemical devices. Sust. En. Fuels *6*, 3701–3716. https://doi.org/10.1039/D2SE00562J.

12. Pinaud, B.A., Benck, J.D., Seitz, L.C., Forman, A.J., Chen, Z., Deutsch, T.G., James, B.D., Baum, K.N., Baum, G.N., Ardo, S., et al. (2013). Technical and economic feasibility of centralized facilities for solar hydrogen production via photocatalysis and photoelectrochemistry. Energy Environ. Sci. *6*, 1983. https://doi.org/10.1039/c3ee40831k.

13. Song, H., Luo, S., Huang, H., Deng, B., and Ye, J. (2022). Solar-driven hydrogen production: Recent advances, challenges, and future perspectives. ACS Energy Lett. *7*, 1043–1065. https://doi.org/10.1021/acsenergylett.1c02591.

14. Cheng, W.H., Richter, M.H., May, M.M., Ohlmann, J., Lackner, D., Dimroth, F., Hannappel, T., Atwater, H.A., and Lewerenz, H.J. (2018). Monolithic Photoelectrochemical Device for Direct Water Splitting with 19% Efficiency. ACS Energy Lett. *3*, 1795–1800. https://doi.org/10.1021/acsenergylett.8b00920.

15. May, M.M., Döscher, H., and Turner, J.A. (2018). Chapter 12:High-efficiency Water Splitting Systems. In Integrated Solar Fuel Generators (The Royal Society of Chemistry), pp. 454–499. chapter 12. https://doi.org/10.1039/9781788010313-00454.

16. Young, J.L., Steiner, M.A., Döscher, H., France, R.M., Turner, J.A., and Deutsch, T. (2017). Direct solar-to-hydrogen conversion via inverted metamorphic multi-junction semiconductor architectures. Nat. Energy *2*, 17028. https://doi.org/10.1038/nenergy.2017.28.

17. Cariou, R., Benick, J., Feldmann, F., Höhn, O., Hauser, H., Beutel, P., Razek, N., Wimplinger, M., Bläsi, B., Lackner, D., et al. (2018). III–V-on-silicon solar cells reaching 33% photoconversion efficiency in two-terminal configuration. Nat. Energy *3*, 326–333. https://doi.org/10.1038/s41560-018-0125-0.

18. Hermle, M., Feldmann, F., Bivour, M., Goldschmidt, J.C., and Glunz, S.W. (2020). Passivating contacts and tandem concepts: Approaches for the highest silicon-based solar cell efficiencies. Appl. Phys. Rev. *7*, 021305. https://doi.org/10.1063/1.5139202.

19. Parkinson, B. (1982). An evaluation of various configurations for photoelectrochemical photovoltaic solar cells. Sol. Cell. *6*, 177–189. https://doi.org/10.1016/0379-6787(82)90065-5.

20. Kölbach, M., Özen, C., Höhn, O., Lackner, D., Feifel, M., Abdi, F.F., and May, M.M. (2021). Counterbalancing light absorption and ionic transport losses in the electrolyte for integrated solar water splitting with III–V/Si dual-junctions. Appl. Phys. Lett. *119*, 083904. https://doi.org/10.1063/5.0060700.

21. Didden, A., Hillebrand, P., Dam, B., and van de Krol, R. (2015). Photocorrosion mechanism of TiO_2-coated photoanodes. Int. J. Photoenergy *2015*, 1–8. https://doi.org/10.1155/2015/457980.

22. Ma, Z., Liu, X., and Zhang, T. (2021). Measurement and optimization on the energy consumption of fans in semiconductor cleanrooms. Build. Environ. *197*, 107842. https://doi.org/10.1016/j.buildenv.2021.107842.

23. Wei, C., Rao, R.R., Peng, J., Huang, B., Stephens, I.E.L., Risch, M., Xu, Z.J., and Shao-Horn, Y. (2019). Recommended Practices and Benchmark Activity for Hydrogen and Oxygen Electrocatalysis in Water Splitting and Fuel Cells. Adv. Mater. *31*, 1806296. https://doi.org/10.1002/adma.201806296.

24. Haberland, K., Kurpas, P., Pristovsek, M., Zettler, J.T., Weyers, M., and Richter, W. (1999). Spectroscopic process sensors in MOVPE device production. Appl. Phys. A: Mater. Sci. Process. *68*, 309–313. https://doi.org/10.1007/s003390050893.

25. Haynes, W.M., Lide, D.R., Bruno, T.J. (Eds.)CRC Handbook of Chemistry and Physics. 97 ed., CRC Press. https://doi.org/10.1201/9781315380476.

26. Clawson, A. (2001). Guide to references on III–V semiconductor chemical etching. Mater. Sci. Eng. R Rep. *31*, 1–438. https://doi.org/10.1016/S0927-796X(00)00027-9.

27. Bryce, C., and Berk, D. (1996). Kinetics of gaas dissolution in H_2O_2-NH_4OH-H_2O solutions. Ind. Eng. Chem. Res. *35*, 4464–4470. https://doi.org/10.1021/ie960278t.

28. Guidat, M., Löw, M., Kölbach, M., Kim, J., and May, M.M. (2023). Experimental and computational aspects of electrochemical reflection anisotropy spectroscopy: A review. Chemelectrochem *10*, e202300027. https://doi.org/10.1002/celc.202300027.

29. Richter, W., and Zettler, J.T. (1996). Real-time analysis of III–V-semiconductor epitaxial growth. Appl. Surf. Sci. *100–101*, 465–477. https://doi.org/10.1016/0169-4332(96)00321-2.

30. Sombrio, G., Oliveira, E., Strassner, J., Richter, J., Doering, C., and Fouckhardt, H. (2021). Doped or Quantum-Dot Layers as In Situ Etch-Stop Indicators for III/V Semiconductor Reactive Ion Etching (RIE) Using Reflectance Anisotropy Spectroscopy (RAS). Micromachines *12*, 502. https://doi.org/10.3390/mi12050502.

31. Acosta-Ortiz, S., and Lastras-Martínez, A. (1987). Measurements of above-bandgap optical anisotropies in the (0 0 1) surface of GaAs. Solid State Commun. *64*, 809–811. https://doi.org/10.1016/0038-1098(87)90706-X.

32. Sobiesierski, Z., Westwood, D.I., and Elliott, M. (1997). Reflectance anisotropy spectra from Si δ-doped GaAs(001): Correlation of linear electro-optic effect with integrated surface field. Phys. Rev. B *56*, 15277–15281. https://doi.org/10.1103/PhysRevB.56.15277.

33. Li, X. (2012). Metal assisted chemical etching for high aspect ratio nanostructures: A review of characteristics and applications in photovoltaics. Curr. Opin. Solid State Mater. Sci. *16*, 71–81. https://doi.org/10.1016/j.cossms.2011.11.002.

34. Srivastava, R.P., and Khang, D.Y. (2021). Structuring of Si into Multiple Scales by Metal-Assisted Chemical Etching. Adv. Mater. *33*, 2005932. https://doi.org/10.1002/adma.202005932.

35. May, M.M., Lackner, D., Ohlmann, J., Dimroth, F., van de Krol, R., Hannappel, T., and Schwarzburg, K. (2017). On the benchmarking of multi-junction photoelectrochemical fuel generating devices. Sust. En. Fuels *1*, 492–503. https://doi.org/10.1039/C6SE00083E.

36. Moon, C., Seger, B., Vesborg, P.C.K., Hansen, O., and Chorkendorff, I. (2020). Wireless photoelectrochemical water splitting using triple-junction solar cell protected by TiO_2. Cell Rep. Phys. Sci. *1*, 100261. https://doi.org/10.1016/j.xcrp.2020.100261.

37. Peter, L., Li, J., and Peat, R. (1984). Surface recombination at semiconductor electrodes: Part I. Transient and steady-state photocurrents. J. Electroanal. Chem. Interfacial Electrochem. *165*, 29–40. https://doi.org/10.1016/S0022-0728(84)80084-4.

38. Lin, Y., Kapadia, R., Yang, J., Zheng, M., Chen, K., Hettick, M., Yin, X., Battaglia, C., Sharp, I.D., Ager, J.W., and Javey, A. (2015). Role of TiO_2surface passivation on improving the performance of p-InP photocathodes. J. Phys. Chem. C *119*, 2308–2313. https://doi.org/10.1021/jp5107313.

39. Ma, Y., Le Formal, F., Kafizas, A., Pendlebury, S.R., and Durrant, J.R. (2015). Efficient suppression of back electron/hole recombination in cobalt phosphate surface-modified undoped bismuth vanadate photoanodes. J. Mater. Chem. A *3*, 20649–20657. https://doi.org/10.1039/C5TA05826K.

40. Ben-Naim, M., Aldridge, C.W., Steiner, M.A., Nielander, A.C., Deustch, T.G., Young, J.L., and Jaramillo, T.F. (2022). Demonstration of photoreactor platform for on-sun unassisted photoelectrochemical hydrogen generation with tandem III-V photoelectrodes. Chem Catal. *2*, 195–209. https://doi.org/10.1016/j.checat.2021.12.013.

41. Abràmoff, M.D., Magalhães, P.J., and Ram, S.J. (2004). Image processing with imagej. Biophot. Int. *11*, 36–42.

Batteries & Supercaps

Research Article
doi.org/10.1002/batt.202300394

Chemistry Europe
European Chemical Societies Publishing

www.batteries-supercaps.org

Special Collection

In Situ Monitoring of the Al(110)-[EMImCl]:$AlCl_3$ Interface by Reflection Anisotropy Spectroscopy

Margot Guidat[+],*[a] Fatemehsadat Rahide[+],[b] Mario Löw,[c] Jongmin Kim,[a] Helmut Ehrenberg,[b] Sonia Dsoke,[b] and Matthias M. May[a]

Recently, Al-batteries (AlBs) have become promising candidates for post-lithium batteries, with [EMImCl]:$AlCl_3$ (1:1.5) as the most commonly used electrolyte. However, progress in the development of AlBs is currently hindered by the lack of understanding of its solid-electrolyte interface. Monitoring the structure of this interface under operational conditions by complementary spectroscopy could help to identify and overcome bottlenecks of the system. Reflection anisotropy spectroscopy (RAS), an optical *in situ* technique, provides access to physical and chemical properties of electrochemical interfaces on an atomistic level. Herein, we report the first example of RAS as an *in situ* characterization technique for non-aqueous battery systems, investigating an Al(110)-based model system. During chemical pre-treatment in [EMImCl]:$AlCl_3$, the Al(110) surface passivation film is modified. The oxide film is partially etched while an inhomogeneous passivation layer forms, increasing the surface roughness. Upon electrochemical cycling, applied potential-dependent oscillations of the anisotropy are observed and demonstrate the applicability of RAS to monitor phenomena such as plating/stripping and surface passivation in real-time.

Introduction

Al-batteries are a promising class among the post-lithium systems as they provide high specific power and energy.[1–3] Al is abundant, inexpensive, and recyclable, and it can provide a high theoretical volumetric capacity (8046 mAh cm^{-3}), making it a suitable anode material.[3,4] The condition of the Al electrode substrate plays an important role in the performance of rechargeable AlBs.[4] The Al surface is initially covered by a passivation layer consisting of an amorphous, ion/electron blocking oxide (Al_2O_3).[5] Although this oxide layer suppresses dendrite formation[6] and leads to an increased electrode/electrolyte interface stability,[4] it may also hinder the aluminum plating and stripping in non-acidic and non-corrosive $AlCl_3$-free electrolytes, due to the low electronic and ionic conductivities of the latter.[4,7]

The [EMImCl]:$AlCl_3$ Ionic Liquids (IL) remain the most commonly used electrolytes in the field of AlBs. When the ratio of $AlCl_3$ to [EMImCl] is higher than 1, the presence of $Al_2Cl_7^-$ and $AlCl_4^-$ species as well as the Lewis acidity in the electrolyte medium contribute to the corrosivity of the IL. $AlCl_3$ also increases the electrolyte's sensitivity to humidity.[1,8] The replacement of IL electrolytes by non-corrosive electrolytes is therefore crucial and currently constitutes a bottleneck in the field of AlBs since plating and stripping of $AlCl_3$-free electrolytes on Al substrates encounters severe issues such as side reactions and surface passivation.[9–13] It is consequently necessary to modify the electrode/electrolyte interfaces for $AlCl_3$-free electrolytes to partially remove the oxide layer, allowing both the formation of the contact between electrolyte and the Al surface and the prevention of dendrite growth.

Numerous approaches for Al surface pre-treatment and designing the Al-electrolyte interface have, via *in situ* and *ex situ* characterization like *in situ* optical microscopy and X-ray photoelectron spectroscopy (XPS), already shown to improve the cycling stability and hinder dendrite formation.[14–16] The immersion pre-treatment of the Al substrate in IL has been regarded as an efficient strategy to partially remove the inactive oxide layer (Al_2O_3) covering the Al substrate and to activate the Al electrode for subsequent electrochemical cycling in IL electrolytes.[5,17,18] However, the partial removal of the Al_2O_3 layer has not proven to be sufficient to allow subsequent electrochemical cycling in $AlCl_3$-free electrolytes.[19] Several hypotheses could explain the origin of the absence of plating and stripping

[a] M. Guidat,[+] J. Kim, Dr. M. M. May
Institute of Physical and Theoretical Chemistry
Universität Tübingen
Auf der Morgenstelle 15
72076 Tübingen, Germany
E-mail: margot.guidat@uni-tuebingen.de

[b] F. Rahide,[+] Prof. H. Ehrenberg, Dr. S. Dsoke
Institute for Applied Materials (IAM)
Karlsruhe Institute of Technology (KIT)
Hermann-von-Helmholtz-Platz 1
76344 Eggenstein-Leopoldshafen, Germany

[c] M. Löw
Institute of Theoretical Chemistry
Universität Ulm
Lise-Meitner-Str. 16
89081 Ulm, Germany

[+] These authors contributed equally.

Supporting information for this article is available on the WWW under https://doi.org/10.1002/batt.202300394

Special Collection This publication is part of a joint Special Collection dedicated to Post-Lithium Storage, featuring contributions published in Advanced Energy Materials, Batteries & Supercaps, and ChemSusChem.

in $AlCl_3$-free electrolytes comprising a non-effective pre-treatment in IL, an oxide layer reformation inside the glovebox between pre-treatment and cycling or an oxide layer reformation after immersion in non-corrosive electrolytes.[2,18] Earlier studies have already claimed that the instability and the irregular nature of the Al-IL solid-electrolyte interphase (SEI) render the pre-treatment in IL inefficient.[19]

These findings and hypotheses can, in principle, be probed by *in situ* reflection anisotropy spectroscopy (RAS). Since the latter operates at near normal-incidence reflection, its setup makes it (rather) straightforward to integrate with other techniques.[20,21] RAS, as a non-destructive optical surface analysis can, for instance, provide more insight into the evolution of the surface either during immersion pre-treatment or during electrochemical cycling inside a glovebox. In battery research, RAS has the potential to give insight into SEI formation, metal stripping/plating, as well as ion transport processes. In the working principle of RAS, linearly polarized light impinges at near-normal incidence on a single-crystalline surface.[21,22] The difference in reflectivity, Δr, with respect to two orthogonal directions in the surface plane (x, y) is then measured and scaled with the mean reflectivity, r. The surface's anisotropy can be determined according to Equation (1):

$$\mathrm{RAS}: \frac{\Delta r}{r} = 2 \cdot \frac{r_x - r_y}{r_x + r_y} \quad (1)$$

The anisotropy of the signal can arise from both the surface and the bulk of the sample due to the penetration depth of light in the material. In the case of cubic crystals with isotropic bulk, it is possible to exclusively get information about the surface. With such a technique, changes in surface structure and surface chemistry can be studied with a time resolution of about 10 ms. Furthermore, real-time monitoring in an electrochemical environment is possible.[22] Since RAS is restricted to single crystals, the present study focuses on the evolution of Al(110) in the IL electrolyte. Previous work on the corrosion of Al foils in the presence of HCl under galvanostatic conditions has revealed that the evolution of the surface morphology and the evolution of the etching pits depends significantly on the initial morphology of the surface, its impurities and the composition of the surface oxide.[23] Performing experiments with Al single crystals allows working with surfaces that are initially highly pure with a very low surface roughness (<0.1 nm) and a smooth and homogeneous oxide layer on top. For a more detailed understanding of RA-spectra, it is necessary to complement RAS with other surface-sensitive techniques such as XPS and scanning tunneling microscopy (STM), or computational RAS.

In this study, we first establish the experimental and computational spectra of Al(110) surfaces with different surface terminations or in different environments. In a second part, we monitor the evolution of the oxide layer upon pre-treatment in IL (1:1.5) by *in situ* RAS and we correlate the results with computational RAS, scanning electron microscopy (SEM) and energy-dispersive X-ray analysis (EDX). The third section investigates the possibility to use *in situ* RAS to study the Al(110)-IL (1:1.5) interface during electrochemical cycling. The experimental work presented here provides the first application of RAS on a battery system.

Results and Discussion

Computational and experimental Al(110) reference spectra

A previous study has already investigated RA-spectra of clean Al(110) surfaces prepared in an ultra-high vacuum environment as well as oxygenated Al(110) surfaces.[24] It was found that the characteristic anisotropic peak at about 1.5 eV is related to bulk Al(110) (interband transition), and is weakly affected by surface oxidation. The latter reduces the strength of the peak at 1.5 eV and shifts it to 1.45 eV. After 50 Langmuir of oxygen coverage, the oxide layer becomes amorphous and optically isotropic. Hence, above this amount of coverage, no meaningful changes in the anisotropy intensities can be detected anymore. Due to the strong anisotropy arising from its bulk, studying a (110) crystalline surface by RAS is to some extent reducing its surface-sensitivity because both bulk and surface anisotropy contribute to the RA-spectrum. However, (110) remains the orientation of choice compared to the commonly used (100) and (111) surfaces, where the surface is isotropic and, therefore, does not contribute to the RA-spectrum.

To understand the sensitivity of the RA-spectra to oxygen coverage, we model Al(110) surfaces with different amounts of O atoms on top, i.e., coverage of half a monolayer (0.5 ML) and one monolayer (1 ML). Figure 1a presents the computed RA-spectra of the clean and covered Al(110) surfaces. Similar to the experimental and theoretical results of Herrmann et al., our calculation of the clean surface yields a pronounced peak at 1.48 eV.[24] However, our calculated RA-spectrum is more similar to their experimental spectrum.[24] For instance, we find a negative anisotropy at 1.2 eV, which is also shown in their experimental spectrum, but is not observed in their theoretical result.[24] In principle, we and Herrmann et al. carried out first-principles calculations within the generalized gradient approximation, and also employed the same method for the calculation of the dielectric function, i.e. the IP-RPA approach. The main difference is the number of layers of the Al(110) surface. We and they modeled 21 and 16 layers, respectively. A different study revealed that the thickness of the slab has an effect on the RAS spectrum.[25] In addition, they used a computed bulk dielectric function for the RAS calculation, while an experimental one was adopted in our calculations. Note that by increasing the oxygen coverage, the negative peak at 1.2 eV is slightly shifted to lower energies, while the intensity of the characteristic peak at 1.48 eV is proportionally reduced.

Since the oxygen concentration inside our glovebox is in the order of 0.5 ppm, the Al crystal can, due to its high reactivity, be considered to be passivated with an oxide layer. Thus, it is appropriate to compare an experimental spectrum with a theoretical spectrum corresponding to Al(110) with at least one oxygen monolayer on top.

Research Article
doi.org/10.1002/batt.202300394
Chemistry Europe
European Chemical Societies Publishing

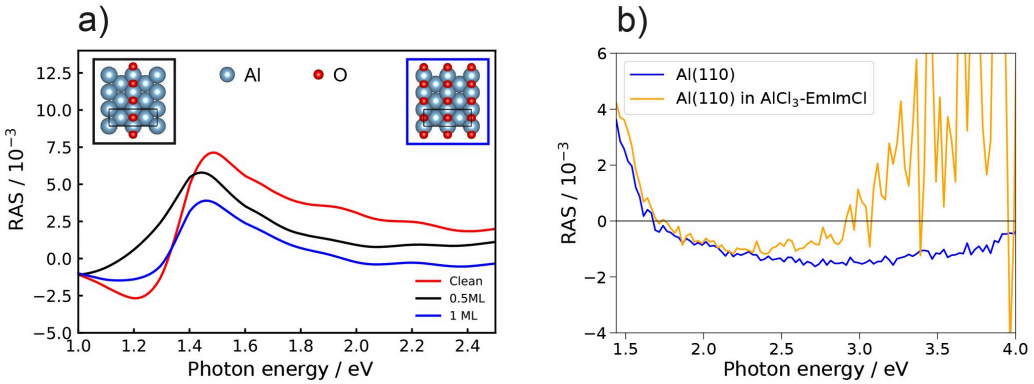

Figure 1. (a) Computed RA-spectra of the clean Al(110) (red), half monolayer (black) and monolayer (blue) coverage of O atoms on the surface. The insets show a top view of the 0.5 ML and 1 ML structures covered with oxygen. Oxygen and Aluminium atoms are depicted in red and light blue, respectively. The unit cells are indicated by the black lines. (b) Reference spectra of the Al(110) surface in Argon atmosphere and of the Al(110)-IL interface directly after immersion.

Figure 1b shows the experimental reference RA-spectra corresponding to the Al(110) surface and the Al(110)-IL interface. The reference spectrum of the as-received Al(110) crystal shows the same characteristics as the theoretical spectrum shown in Figure 1a. The anisotropy intensity is similar to the one of a monolayer oxygen coverage, suggesting that an oxide layer of about one monolayer passivates the Al surface. Since the resolution of the RA-spectra is significantly impacted by the setup, i.e. by the presence of a thick and coloured electrolyte layer, the data presented in this paper have a low signal-to-noise ratio. In particular, the spectrum of Al(110) in the IL suffers from a low signal-to-noise ratio beyond 3.0 eV due to the light absorption from the electrolyte at these energies. Moreover, due to the energy-range limitation of the spectrometer, it is not possible to access energies below 1.44 eV. Therefore, all the following graphics are restricted to an energy range between 1.44 and 2.5 eV, which allows better visibility of the area of interest. Figure 1b exhibits a small anisotropy offset already in the energy range of 1.44–3.0 eV when Al(110) is immersed in IL. Since the bulk electrolyte is not expected to be structured and should, therefore, not contribute to the optical anisotropy in this energy range, the anisotropic offset is expected to originate from an imperfect baseline correction or from a linear electro-optic effect from structured electrolyte molecules acting as dipoles at the near-Al surface. Further explanations are the dependence of the chemical interactions between the surface and the electrolyte, resulting in a modification in the morphology or composition of the surface.

Surface pre-treatment

For the surface pre-treatment, continuous RA-spectra (colourplot) were recorded over the time for 2 h of immersion of the Al crystal C1 in IL and are presented in Figure 2a. On the colourplot (CP), changes related to the peak at 1.5 eV are observed upon immersion. The width of the peak is conserved, but its anisotropy drops in the first phase before increasing

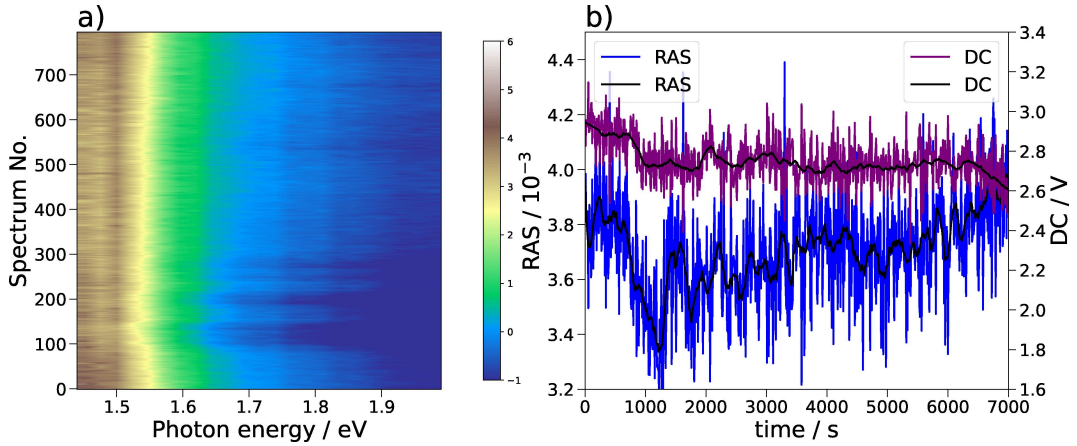

Figure 2. (a) Colourplot (CP) of Al(110) upon immersion in IL for 2 h. (b) Transient at 1.49 eV extracted from the CP. The purple and blue curves correspond to the evolution of the anisotropy and the reflectance over the time, respectively. The black curves correspond to the transients data filtered with a Savitzky–Golay filter.

Research Article
doi.org/10.1002/batt.202300394
Chemistry Europe
European Chemical Societies Publishing

slightly above its initial value. For better visibility on the trend of the CP, a transient at 1.49 eV together with the reflectance (proportional to the DC signal) over the time at 1.49 eV are extracted and shown in Figure 2b. Here, the decrease in the anisotropy and the reflectance until the first half hour of the pre-treatment is noticeable, i.e. the interface deteriorates over time. The loss in the interface ordering is expected to originate from partial oxide layer removal and electrolyte decomposition. Previous studies have shown that after immersion or cycling of Al in IL, the Al surface contains a trace amount of chlorine from residual electrolyte that adsorbs on the oxide layer.[26,27] Furthermore, due to trace amounts of water originating from the glovebox atmosphere, $AlCl_3$ undergoes a hydrolysis leading to the formation of $Al(OH)_3$, Al_2O_3, and HCl, which can affect the Al-IL interface.[26] In the second phase, the anisotropy rises until slightly above its initial value at the end of the pre-treatment, meaning that the ordering at the interface. The rupture of the oxide film that partially dissolves in the electrolyte and then leads to the appearance of active sites on the surface would explain the increase of the RA intensity at the end of the pre-treatment. Concerning the DC signal, it progressively decreases until the end of the pre-treatment, confirming that the increase in ordering at the interface does no occur homogeneously over the surface plane and that some areas of the interface keep deteriorating. The formed solid electrolyte interface consisting of the byproducts of the IL electrolyte and repassivated Al_2O_3 oxide film on the Al surface complicates the interpretation of the RA-spectra. Hence, we will in the following refer to the layers present on the Al surface as the passivation layer. To minimize the contribution of the electrolyte film to the spectra, a comparison of spectra and SEM pictures taken before and after pre-treatment (in the absence of electrolyte) is shown in Figure 3.

Figure 3a–b compares the RA-spectra and the DC signals of the Al(110) surface before and after pre-treatment in IL, as well as the relative ratio of the RA-spectrum taken after pre-treatment, divided by the one taken before pre-treatment and the difference between the DC signals. The DC signal is proportional to the reflectance of the Al surface and correlating it with the anisotropy can help understanding the surface evolution. In Figure 1a, apparent changes in the peak at 1.5 eV between non-treated and treated surfaces are displayed. An increase of the anisotropy after pre-treatment is observed. According to the results discussed in Figure 1a, this increase indicates a reduction in oxygen coverage. A comparison of the RA-intensities between the theoretical and experimental spectra suggests that the crystal is initially covered by about one monolayer of oxygen. After pre-treatment, the anisotropy maintains a value between 4 and 5 at 1.5 eV, suggesting that the surface is still partially covered by oxygen after pre-treatment. Taking into account the oxygen content from the glovebox atmosphere, it is to be expected that surfaces re-oxidize after pre-treatment.

For a better understanding, the evolution of the anisotropy is compared to the evolution of the DC signal before and after pre-treatment (Figure 3b). An increase in reflectance and anisotropy implies, according to Figure 1a, a progressive removal of an oxide layer, leaving behind a cleaner surface. However, as depicted in Figure 3a–b, the DC signal decreases after pre-treatment while the RAS signal increases, which is a typical signature of surface roughening. Moreover, it is important to notice that both the RA-spectra ratio and DC signals difference lead to a rather constant value over the whole photon energy range. It suggests that either the surface is getting rougher, rather than its passivation layer reduced or the increase in surface in-homogeneity is more prominent in the evolution of the RA-spectrum than the reduction in the passivation layer thickness. These observations are in agreement with the conclusions from Natishan et al. on the reaction mechanism between chlorine and Al/Al_2O_3 in chlorine-containing electrolytes.[28] They demonstrated that after its adsorption on Al_2O_3, Cl^- is incorporated into the bulk of the oxide and moves towards the oxide/metal interface. Afterwards, Cl^- reaches the oxide/metal interface leading to blister formation and rupture of Al_2O_3 oxide film. The rupture of the oxide film, however, occurs only locally and leads to a heterogeneous, porous oxide layer with pitting corrosion. Assuming a similar mechanism on the oxidized Al(110) surface in the presence of

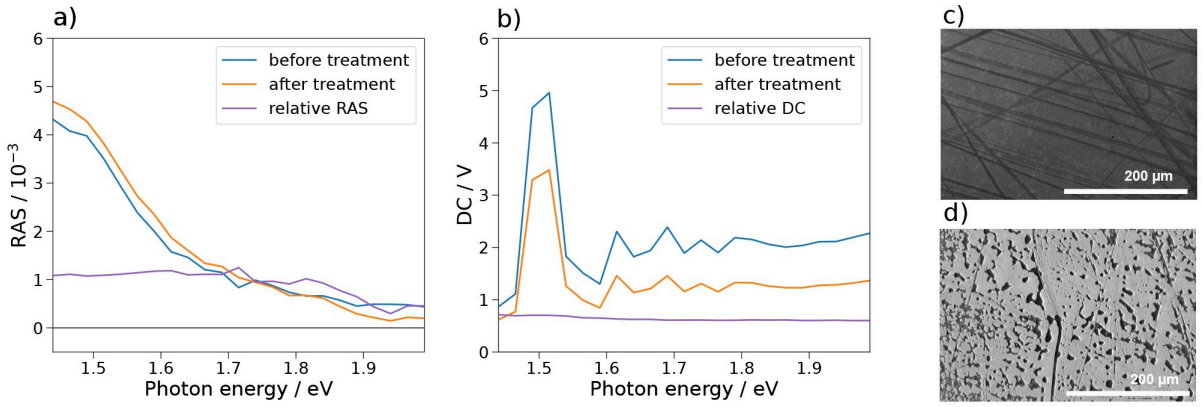

Figure 3. RA-spectra and their ratio (a) and DC signals and their absolute difference (b) of Al(110) surface before and after pre-treatment in IL. (c) and (d) provide the SEM pictures taken before and after pre-treatment, respectively.

Research Article
doi.org/10.1002/batt.202300394
Chemistry Europe
European Chemical Societies Publishing

$Al_2Cl_7^-$ and $AlCl_4^-$ species would explain why not only the surface roughness increases, leading to an overall increase in the anisotropy, but also the anisotropy increases at around 1.5 eV due to the appearance of clean Al(110) surface spots. This interpretation implies that the surface is getting inhomogeneous on a microscopic scale.

To complement our findings from the RAS data, SEM pictures and EDX analysis were performed on the Al crystal after it was pre-treated and clean-connect transferred to the SEM chamber. Figure 3c–d compares the SEM pictures of the crystal before (as received from the supplier) and after pre-treatment, respectively. On the picture from Figure 3c, the as-received Al surface presents some scratches from the last polishing steps performed by the supplying company during the surface preparationof the crystal. The surface also contains particles of less than 1 μm in size composed of SiO_2. Since the last polishing step for Al crystals usually involves the use of a SiO_2 particle suspension, the presence of these particles is also attributed to residuals from the surface preparation process.[29] Figure 3d differs considerably from 3c in morphology and composition. The picture taken after pre-treatment shows an inhomogeneous surface made of a gray matrix with dark puddles on top. Displayed on Figures S2, S3 and Table S1, the EDX analysis of the same area indicates that grey matrix is composed almost exclusively of Al with low amounts of C, O and Cl (below 1 atomic weight %), while the dark areas present significant amounts of C (6–7 weight %), O (3–4 weight %), N (2–4 weight %) and Cl (4–5 weight %) and a decrease in Al content. It indicates that the pre-treatment of Al in the IL leads to the emergence of active site areas and areas where the electrolyte decomposes and adds on to the initial surface oxide layer. These results match our RAS interpretation as well as those of earlier studies.[9,19]

The change in anisotropy and reflectance upon surface pre-treatment indicates that RAS is sensitive to the evolution of the Al(110) surface in IL and allows *in situ* access. Yet the formed interface/interphase is very complex and the interpretation of the spectra is not straightforward. Furthermore, since our spectrometer averages over the whole measurement spot of several mm^2, the measurements average over in-plane surface inhomogeneities. Therefore, it is not possible to disentangle if the changes in the anisotropy over the pre-treatment are homogeneously distributed on the surface or are a sum of contributions from inhomogeneous areas on the surface. A parallel *in situ* investigation with reflection anisotropy microscopy (RAM) would provide a better spatial resolution and allow the elucidation of the different contributions. However, it would require, in addition to the spectrometer detector and the UV-visible light source, the inclusion of a camera, an objective lens, and a laser light source. Combining spectroscopy and microscopy is not achievable with our commercially available spectrometer but could, in principle, be implemented in a custom-build reflection anisotropy setup. Although they are currently limited to single-wavelength studies, RAM or 2D-surface optical reflectance (2D-SOR) have already demonstrated surfaces monitoring with spatial resolutions of about 5–10 μm.[30,31]

Electrochemical cycling

In the previous section, the pre-treatment of the Al(110) single crystals in IL monitored by RAS has shown that RAS is sensitive to the Al surface evolution. This suggests that it should be feasible to study *in situ* the Al(110)-IL interface/interphase during plating and stripping with RAS. To compare the electrochemical cycling behaviour of Al single crystals with the one of Al foil – which is commonly used in the AlBs community and shown in Figure S4 – Al(110) crystal number 2 (C2) is cycled in the photoelectrochemical (PEC) cell at a scan rate of 20 mV/s in a potential range allowing full Al stripping. In parallel with the cyclic voltammetry (CV), a CP is recorded at a speed that four spectra are obtained during one full potential cycle. The experimental procedure is illustrated in Figure S1. The CVs depicted in Figure 4 resemble the one with Al-foil taken in similar conditions (Figure S4), indicating that the behaviour of a (110)-oriented Al surface during electrochemical cycling is comparable to a polycrystalline Al surface. The evolution of the surface roughness observed in the RA-spectra over the experimental series can first be understood from the evolution of the CVs. Over the experimental series, the stripping peak on the CV around 0.28 V vs. Al gets more pronounced. This phenomenon is attributed to a progressive Al plating and stripping from a nanocrystalline to microcrystalline form of Al,[32] i.e. the surface is getting rougher. Thus, if the structure of the surface evolves upon cycling with an increasing amount of Al plated and stripped in a microcrystalline form, the plating and stripping occur in a more defined manner, and the variation of the anisotropy is supposed to be higher. However, because of the high scan rate and the large energy range chosen for this set of experiments, the time resolution is too low to observe a trend related to plating and stripping on the CPs recorded in parallel to the CVs (Figure S5).

During the experimental series, the CVs were recorded on both treated and untreated Al(110). As described in the pre-treatment section, when the Al(110) electrode is immersed in IL, the native Al_2O_3 film covering the Al single crystal undergoes a transformation, resulting in a porous film composed of an inner

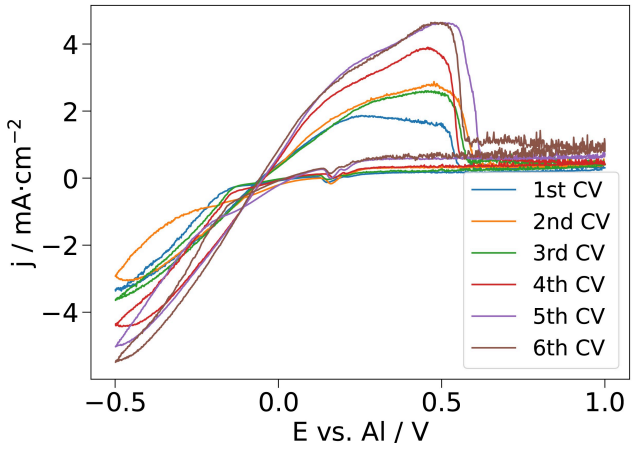

Figure 4. Last cycles of 6 CV experiments measured between −0.5 to 1 V vs. Al at 20 mV/s for 10 cycles.

Research Article
doi.org/10.1002/batt.202300394
Chemistry Europe
European Chemical Societies Publishing

layer enriched with oxides and an outer layer made of both inorganic and organic materials. According to the literature, the partial removal and the reduction in thickness of the Al_2O_3 film makes it easier for charge carriers and ions to move between the Al electrode and the electrolyte.[9,27,33,34] Figure S6 provides insights into the electrochemical behaviour of pre-treated and unpre-treated Al(110) C2 in IL under the same cycling conditions as the one of Figure 4. Specifically, it illustrates notable differences in CVs of these electrodes and their implications for the Al plating and stripping processes.

When examining the CVs of not pre-treated Al(110) in Figure S6a, it is apparent that as the cycle number increases, the current density responsible for Al plating and stripping keeps increasing. This fluctuation indicates an unstable electrode-electrolyte interface, which has a detrimental effect on the plating and stripping processes. This trend aligns with the literature, where it is stated that Al plating and stripping peaks tend to be smaller and less predictable during the initial cycles, but become more reversible with continued cycling, typically around the second or third cycle.[35,36] The native Al_2O_3 film delays the activation of the anode and makes it more challenging to reach a reversible regime, resulting in a significant over-potential.[2,37] Therefore, the result confirms that the presence of the Al_2O_3 film can act as a barrier, limiting the effective interaction between the Al electrode and the electrolyte, and reducing the efficiency of the electrochemical system.[9,36]

In Figure S6b, the maximum of the stripping peaks initially decreases over the first cycles before reaching a stable value. This is an indicator for an efficient modification or removal of the Al_2O_3 oxide layer, which is known to play a crucial role in these electrochemical processes. Hence, the porous surface film formed during the immersion pre-treatment seems to have a beneficial impact on the electrode's performance.[9]

A further set of experiments was performed on a second Al(110) crystal (C3) and was monitored with higher temporal spectroscopic resolution than for C2. In this second experimental series, Al(110) C3 is first pre-treated according to the procedure described in the experimental section. For the cycling performance, the Raman cell from rhd instruments (rhd cell) is used, where a thinner electrolyte layer is present on top of the crystal surface, reducing light absorption from the electrolyte in comparison to the PEC cell. Compared to the previous experiment series (with PEC cell), the cell is cycled at lower scan rates of 2.5 mV/s, and RAS is measured in parallel with higher temporal resolution, as depicted in Figure 5 for a potential range between −0.25 and 0.25 V vs. Al. The potential range of the CV shown in Figure 5a and 5c does not allow for complete Al stripping, but a more detailed *in situ* investigation of the surface during plating and stripping is possible from the spectroscopic side, i. e. about 20 spectra are measured per cycle, as shown in Figure 5b and 5c.

Plotting the applied voltage as a function of the time together with the CP is a systematic way to probe potential direct correlations between the electrochemical and optical measurements. In the case of systems with a high degree of ordering, such as InP in contact with low-concentration acidic electrolytes, there are clear visual correlations between the cyclic potential and the oscillations of the RA-values.[38] For Al in IL, a more complex and less ordered system, plotting the applied voltage with the CP simply helps deducing that they do exhibit a directly apparent correlation and that more extensive analysis of the CP is required. For better visibility of the anisotropy features, transients at 1.49 eV are extracted from the CPs. Figure 6 presents the electrochemical cycling of Al(110) sample C2 between −0.25 to 0.25 V vs. Al (a) and between −0.5 and 0.5 V vs. Al (b), plotted over time together with a transient and a DC-signal extracted from the CP at 1.49 eV.

To reduce the background noise from the transients shown in Figure 6, and to identify if there is a feature correlated to plating and stripping, the transients are filtered by Fast Fourier transform (FFT). The FFT-filtered transient from Figure 6a was extracted from the CP of Figure 5b at 1.49 eV and exhibits an increasing trend in the first cycles. While the anisotropy progressively decreases after the third cycle, small oscillations with a period matching the cycling period of the potential start to appear. The periods of the potential applied during the

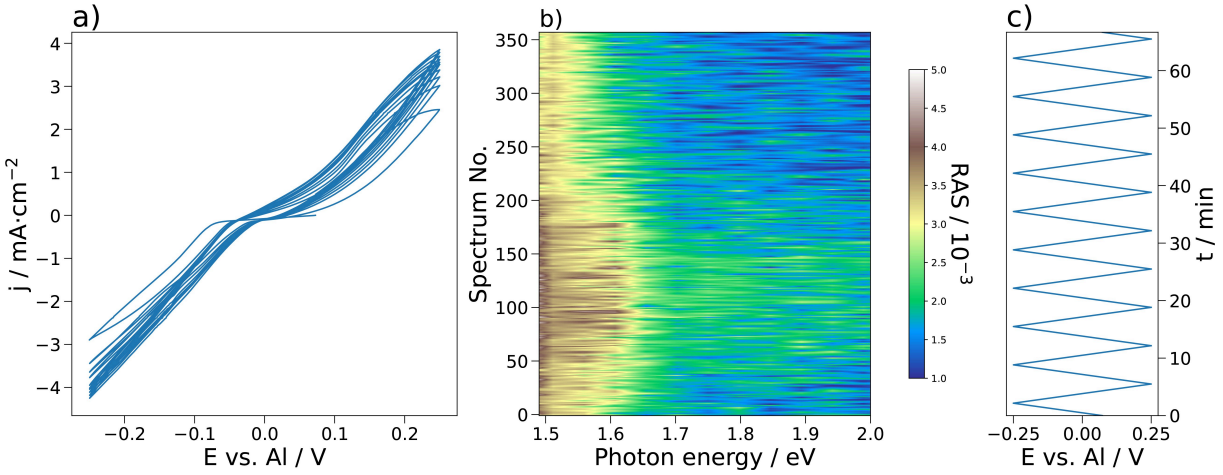

Figure 5. (a) CV between −0.25 and 0.25 V vs. Al for 10 cycles at 2.5 mV/s. (b) CP measured in parallel to CV. (c) applied voltage with respect to the time.

Research Article
doi.org/10.1002/batt.202300394
Chemistry Europe
European Chemical Societies Publishing

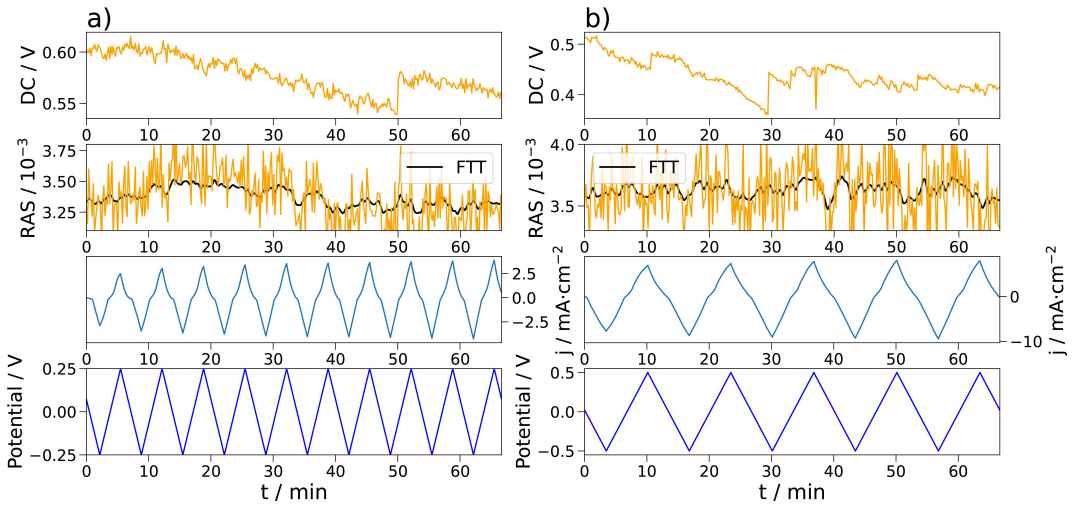

Figure 6. DC signal and transients at 1.49 eV extracted from a CP measured during (a) CV between −0.25 and 0.25 V at a scan speed of 2.5 mV/s for 10 cycles and (b) CV between −0.5 and 0.5 V at 2.5 mV/s for 5 cycles. The black curves correspond to the FFT-filtered transients.

experiments shown in Figure 6a–b are 2.5 and 1.25 mHz, respectively.

Figure 7a shows again the original transient of Figure 6a while its Fourier spectrum is shown in Figure 7b. The DC value at 0 Hz has been discredited due to its high amplitude as compared to the other peaks. The second most dominant peak is observed at 2.5 mHz, which corresponds to the oscillation period of the applied potential. The same conclusion is drawn when examining the FFT of the original transient of Figure 6b: the most prominent peak is observed at 1.25 mHz, i.e. the period of the applied potential (Figure S8).

The presence of these peaks justifies the application of an exponential filter to the data and confirms that the oscillations observed in the transient can be correlated with the applied potential. When correlating the RAS oscillations in Figure 6a with the corresponding CV, the local minima of the oscillations are located shortly after the local maxima in the anodic current. Oscillations of the RAS intensity are also present on the transient from Figure 6b for which the potential range of the CV was broader. However, the period of the oscillations is less well-defined than for the narrower potential range. This indicates that, depending on the potential range in which Al is cycled, the plating and stripping process is more or less ordered. Between −0.25 to 0.25 V, small oscillations emerge with increasing cycle number, meaning that the process is most probably happening homogeneously at the surface and in a layer-by-layer manner.

Between −0.5 and 0.5 V, the build-up and build-down of an anisotropy are less defined, indicating that the process occurs on a larger scale and that the surface is getting rough. The DC signals globally decrease over time, but exhibit some features, i.e. at 50 minutes in Figure 6a and at 10 and 30 minutes in Figure 6b. There are significant changes in the transients at the time of these features, meaning that they are not associated with composition or structural change, but that they can be attributed to surface etching. The progressive surface etching

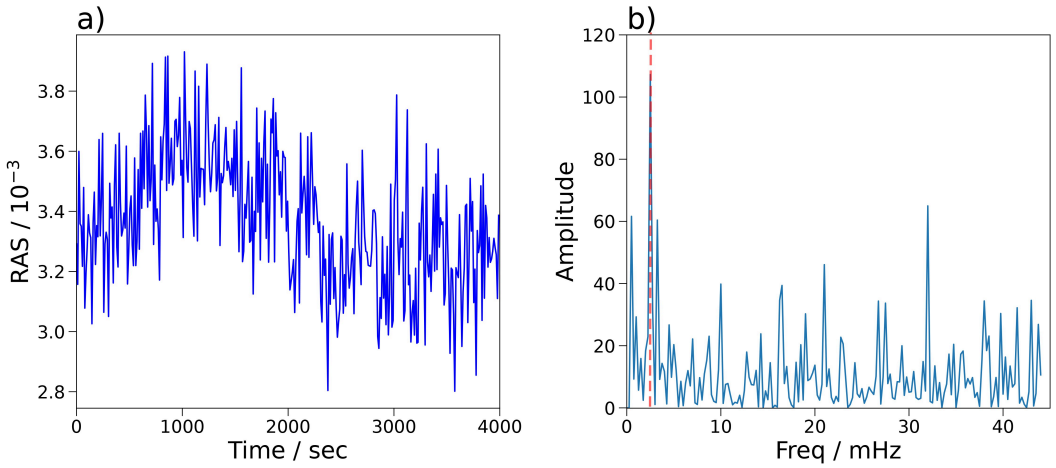

Figure 7. (a) Transient at 1.49 eV extracted from the CP from Figure 6(a) and 6(b). The corresponding Fourier spectrum. The red dashed line marks the predominant frequency of the spectrum at 2.5 mHz.

indicates that the stripping/plating is uneven. Al is more stripped than plated, and depending on the potential range used, more or less cycles are needed to fully etch one aluminum layer. Between −0.25 and 0.25 V, only one step-wise increase in the DC signal is observed, while between −0.5 and 0.5 V, 2 step-wise increases can be observed before the process becomes too ill-defined and it is not possible to distinguish features from etching anymore. Hence, the potential range and the scan rate also have an impact on the occurrence of surface etching.

While in this study both single- and poly-crystalline substrates have comparable CVs, using different crystal orientations can result in different cycling performance. This difference in structural form can impact the physical properties of the deposited Al, such as its grain size, grain boundaries, and defect density. This impacts the nucleation and growth of Al deposits, altering the overall electrochemical behaviour. Dendrite formation during Al electrodeposition depends on factors like surface properties of the aluminum substrate, electrolyte, and cycling conditions, and results from inhomogeneous current distribution, ion concentration variations, and defects.[39–41] Single crystals offer defined nucleation sites, promoting or inhibiting dendrite growth based on their surface orientation. As displayed in Figure S7, dendrites were observed on the SEM images of the crystal C2 taken after the experimental series described in Figure S1 was conducted. It means that, depending on the electrochemical conditions, an Al 110-orientation is prone to dendrite growth in a [EMImCl]:$AlCl_3$ (1:1.5) electrolyte. Structural changes from nanocrystalline to microcrystalline aluminum can influence dendrite formation as well. Microcrystalline structures reduce nucleation sites, but may have defects that promote dendrites. Al(110) sample C3 was cycled in smaller potential ranges (where plating/stripping in the nanocrystalline form of Al is predominant) and at lower scan rates than the crystal C2. Unlike for the ones of C3, the SEM images from Figure S7 of C2 present dendrites, meaning that the dendrite growth is favoured by a microcrystalline surface structure.

These findings show that RAS can be used as a probe to study electrochemical interfaces of battery systems comprising stripping/plating, SEI formation, and dendrite growth. Note that since the interfaces of battery systems remain very challenging and are still at an early stage of investigation and comprehension, interpretation and conclusion from RAS investigation should be accompanied by complementary techniques such as XPS, STM, and 2D-SOR. Nevertheless, this study gives a glimpse into the potential of electrochemical RAS as a complementary tool for the study of battery-electrolyte interfaces and interphases. Specifically, it enlightens the etching process and morphological changes at the Al(110)-IL interface during electrochemical conditioning.

Conclusions

In this work, we introduced RAS as an *in situ* technique of the Al(110)-electrolyte interface monitoring for battery applications. We particularly showed that the surface pre-treatment in [EMImCl]:$AlCl_3$ affects the reflectance at the interface and the anisotropic feature of the Al(110) spectrum related to its oxide passivation layer. In the electrolyte, although the Al surface globally deteriorates due to electrolyte decomposition and swelling of the passivation layer, a localized surface ordering progressively rises over the pre-treatment. Comparison of the surface before and after pre-treatment with the computed spectra and with post-mortem SEM/EDX analysis allows deducing a combination of a partial decrease in the passivation layer thickness and the appearance of active sites with an overall increase in surface roughness/inhomogeneities. Al stripping/plating from the [EMImCl]:$AlCl_3$ electrolyte on Al(110) single crystals is comparable to polycrystalline Al foil and evolves from nanocrystalline to a microcrystalline form of Al. The CVs of the pre-treated Al(110) electrode exhibit a faster stabilization of Al plating and stripping peaks compared to those of untreated Al(110). This observation suggests that for an Al crystal with a 110-orientation, the pre-treatment has a positive effect on the Al plating and stripping performances.

The presence of oscillations of the anisotropy during plating and stripping was only observed in a low potential range. It suggests that, depending on the potential range, the stripping and plating process is more or less ordered. Cycling in a potential range, where Al plating and stripping in the nanocrystalline form is predominant, occurs in a more defined manner than cycling in a potential range where Al plating and stripping in the microcrystalline form is preponderant.

Yet the Al-[EMImCl]:$AlCl_3$ interface remains very complex, and the use of [EMImCl]:$AlCl_3$ for a high $AlCl_3$/[EMImCl] ratio is highly corrosive and therefore not sustainable for long-term battery operation. This study emphasizes that RAS is a potential tool to follow the build-up of a conductive and protective film which is required for the implementation of non-acidic, non-aqueous electrolytes.[9] A natural progression of this work is to improve the pre-treatment of noisy signals. As an alternative, focusing on advanced light sources could increase signal-to-noise ratios.

Experimental

Materials and electrolyte preparation

The Al(110) single crystals were purchased from Mateck (purity of 99,999%, diameter of 10 mm, and thickness of 3 mm) and are denoted as C1, C2 and C3. In the study, [EMImCl]:$AlCl_3$ (1:1.5) was prepared by slowly adding aluminum chloride ($AlCl_3$) (Anhydrous, Sigma–Aldrich, 99.99%) to 1-Ethyl-3-methylimidazolium chloride (EMImCl) (Sigma–Aldrich, >95%) while stirring using a magnetic stirring bar at room temperature (28 to 30 C) inside an argon-filled glovebox (MBraun, <0.5 ppm O_2, <0.5 ppm H_2O). Anhydrous Acetonitrile (99.8%) has been purchased from Sigma–Aldrich.

Al surface pre-treatment

All handling and preparation of Al(110) occurred inside an argon-filled glovebox. The Al electrode surface modification has been achieved by immersion for 2 hours in 6 mL of [EMImCl]:$AlCl_3$ (1:1.5)

electrolyte. Spectra were taken prior to, during and after surface pre-treatment, in the absence and presence of electrolyte. After each measurement, the Al(110) was cleaned and washed several times with anhydrous acetonitrile inside the glovebox before the RA spectrum was measured.

Electrochemical setup and technique

All electrochemical experiments were performed inside an argon-filled glovebox. For the electrochemical measurement, a photo-electrochemical cell (PEC cell) from Zahner was used for C2 and a Raman cell from rhd instruments was used for C3. For the PEC cell, Al wire as a pseudo reference electrode Alfa Aesar (0.5 mm diameter, 99.9999% purity) and glassy carbon as counter electrode (redox.me) were respectively polished with SiC paper (400 P WS FLEX 16) and 250 nm diamond polishing suspension (rhd instruments) before each electrochemical setup. The PEC and the rhd cell were filled with 9 and 3 ml of [EMImCl]:$AlCl_3$ (1:1.5), respectively. For the RA spectroscopy, an EpiRAS from Laytec was employed. The electrochemical measurements were controlled with a Princeton Applied Research VersaSTAT 3F potentiostat and a Gamry Instruments (Interface 5000E). To perform the measurements, the RA-spectrometer was installed on top of the glovebox. A quartz window placed in the sealing of the glovebox, between the setup and the spectrometer, allowed light transmission. The electrochemical cell was placed under the window on top of a hexapod (Physik Instrumente H-840 Hexapod), which allowed for rotating, inclining, and translating the cell to align it with the lightpath. For the SEM/EDX measurements the Apero 2 from Thermo Fisher Scientific with the clean connect system was used, enabling transport of the sample from the glovebox to the SEM without breaking the inert environment. The SEM/EDX measurements were done with a 10 kV electron beam and a beam current of 26 nA. The experimental series performed with C2 are detailed in Figure S1.

Baseline correction and FFT

A baseline correction was applied to some spectra, using a Si(100) crystal immersed in the electrolyte. The transients from Figure 7 are filtered by Fast Fourier transform (FFT) with an exponential filter of a factor of -0.5.

Computational

To obtain theoretically derived RAS, we firstly performed density-functional theory (DFT) calculations with Quantum Espresso (QE).[42] In the QE, we adopted the optimized norm-conserving Vanderbilt pseudopotentials. The sampling of the Brillouin zone (BZ) was performed with a 40×120×1 **k**-grid for our investigated systems. An energy cutoff of 50 Ry was used. For the exchange-correlation functional, we employed the generalized gradient approximation (GGA) in the Perdew–Burke–Ernzerhof (PBE) parametrization. The subsequent RAS calculations were carried out using the Yambo code.[43,44] Here, we used the IP-RPA method to compute the dielectric function of our investigated slabs.

Supporting Information

The authors have cited additional references within the Supporting Information.[10,46]

Acknowledgements

The authors would like to thank Dr. Marcel Drüschler, Dr. Sebastian Kranz, and Dr. Benedikt Huber from the rhd instruments company for their scientific support and assistance in battery cell setup supplies. We also thank Dr. Holger Euchner for his help in the revision of the manuscript. This work was funded by the Deutsche Forschungsgemeinschaft (DFG, German Research Foundation) under Germany's Excellence Strategy – EXC 2154 – project number 390874152 as well as DFG project number 434023472. We acknowledge the state of Baden-Württemberg, through bwHPC, and DFG through grant no. INST 40/575-1 FUGG (JUSTUS 2 cluster) for computational resources. Open Access funding enabled and organized by Projekt DEAL.

Conflict of Interests

There are no conflicts to declare.

Data Availability Statement

The data that support the findings of this study are openly available on Zenodo at https://doi.org/10.5281/zenodo.10000855, Ref. [45].

Keywords: aluminum · battery · electrochemistry · interfaces · spectroscopy

[1] B. Craig, T. Schoetz, A. Cruden, C. Ponce de Leon, *Renewable Sustainable Energy Rev.* **2020**, *133*, 110100.
[2] Q. Li, N. J. Bjerrum, *J. Power Sources* **2002**, *110*, 1.
[3] E.-S. Lee, S.-H. Huh, S.-H. Lee, S.-H. Yu, *ACS Sustainable Chem. Eng.* **2023**, *11*, 2014.
[4] X. Zhang, R. Lv, W. Tang, G. Li, A. Wang, A. Dong, X. Liu, J. Luo, *Adv. Funct. Mater.* **2020**, *30*, 2004187.
[5] S. K. Das, S. Mahapatra, H. Lahan, *J. Mater. Chem. A* **2017**, *5*, 6347.
[6] C. Schütter, A. Bothe, A. Balducci, *Electrochim. Acta* **2020**, *331*, 135421.
[7] M. Chiku, S. Matsumura, H. Takeda, E. Higuchi, H. Inoue, *J. Electrochem. Soc.* **2017**, *164*, A1841.
[8] J.-K. Chang, S.-Y. Chen, W.-T. Tsai, M.-J. Deng, I.-W. Sun, *Electrochem. Commun.* **2007**, *9*, 1602.
[9] L. C. Loaiza, N. Lindahl, P. Johansson, *J. Electrochem. Soc.* **2023**, *170*, 030512.
[10] T. Mandai, P. Johansson, *J. Mater. Chem. A* **2015**, *3*, 12230.
[11] Z. Slim, E. J. Menke, *Batteries & Supercaps* **2023**, *6*, e202300164.
[12] X. Wen, J. Zhang, H. Luo, J. Shi, C. Tsay, H. Jiang, Y.-H. Lin, M. A. Schroeder, K. Xu, J. Guo, *J. Phys. Chem. Lett.* **2021**, *12*, 5903.
[13] H. Wang, S. Gu, Y. Bai, S. Chen, F. Wu, C. Wu, *ACS Appl. Mater. Interfaces* **2016**, *8*, 27444.
[14] S. Varshney, M. Oded, S. Remennik, V. Gutkin, U. Banin, *Small* **2023**, *19*, 2304478.
[15] R. Tao, H. Fu, C. Gao, L. Fan, E. Xie, W. Lyu, J. Zhou, B. Lu, *Adv. Funct. Mater.* **2023**, 2303072.
[16] S. He, J. Wang, X. Zhang, W. Chu, S. Zhao, D. He, M. Zhu, H. Yu, *J. Mater. Chem. A* **2023**, *11*, 17020.
[17] F. Wu, N. Zhu, Y. Bai, Y. Gao, C. Wu, *Green Energy & Environ.* **2018**, *3*, 71.
[18] H. Wang, S. Gu, Y. Bai, S. Chen, F. Wu, C. Wu, *ACS Appl. Mater. Interfaces* **2016**, *8*, 27444.
[19] T. Dong, K. L. Ng, Y. Wang, O. Voznyy, G. Azimi, *Adv. Energy Mater.* **2021**, *11*, 2100077.

[20] K. Haberland, P. Kurpas, M. Pristovsek, J.-T. Zettler, M. Weyers, W. Richter, *Appl. Phys. A Mater. Sci. Process.* **1999**, *68*, 309.
[21] P. Weightman, D. S. Martin, R. J. Cole, T. Farrell, *Rep. Prog. Phys.* **2005**, *68*, 1251.
[22] M. Guidat, M. Löw, M. Kölbach, J. Kim, M. M. May, *ChemElectroChem* **2023**, *10*, e202300027.
[23] J. Scherer, O. Magnussen, T. Ebel, R. Behm, *Corros. Sci.* **1999**, *41*, 35.
[24] T. Herrmann, M. Gensch, M. J. G. Lee, A. I. Shkrebtii, N. Esser, W. Richter, P. Hofmann, *Phys. Rev. B* **2004**, *69*, 165406.
[25] C. Hogan, O. Pulci, P. Gori, F. Bechstedt, D. S. Martin, E. E. Barritt, A. Curcella, G. Prevot, Y. Borensztein, *Phys. Rev. B* **2018**, *97*, 195407.
[26] S. Poetz, P. Handel, G. Fauler, B. Fuchsbichler, M. Schmuck, S. Koller, *RSC Adv.* **2014**, *4*, 6685.
[27] D.-M. She, W.-L. Song, J. He, N. Li, H. Chen, S. Jiao, D. Fang, *J. Electrochem. Soc.* **2020**, *167*, 130530.
[28] P. M. Natishan, W. E. O'Grady, *J. Electrochem. Soc.* **2014**, *161*, C421.
[29] *Buehler Sum Met: The Sum Of Our Experience*, Buehler, Lake Bluff, Il, 4th edition **2018**.
[30] C. Punckt, F. S. Merkt, H. H. Rotermund, *New J. Phys.* **2007**, *9*, 213.
[31] S. Pfaff, A. Larsson, D. Orlov, G. S. Harlow, G. Abbondanza, W. Linpé, L. Rämisch, S. M. Gericke, J. Zetter-berg, E. Lundgren, *ACS Appl. Mater. Interfaces* **2021**, *13*, 19530.
[32] R. Böttcher, S. Mai, A. Ispas, A. Bund, *J. Electrochem. Soc.* **2020**, *167*, 102516.
[33] D. Pradhan, D. Mantha, R. Reddy, *Electrochim. Acta* **2009**, *54*, 6661.
[34] H. Yang, F. Wu, Y. Bai, C. Wu, *J. Energy Chem.* **2020**, *45*, 98.
[35] S. Xia, X. Zhang, K. Huang, Y.-L. Chen, Y. Wu, *J. Electroanal. Chem.* **2015**, *757*.
[36] O. M. Ylivaara, X. Liu, L. Kilpi, J. Lyytinen, D. Schneider, M. Laitinen, J. Julin, S. Ali, S. Sintonen, M. Berdova, E. Haimi, T. Sajavaara, H. Ronkainen, H. Lipsanen, J. Koskinen, S.-P. Hannula, R. L. Puurunen, *Thin Solid Films* **2014**, *552*, 124.
[37] M. Jiang, C. Fu, P. Meng, J. Ren, J. Wang, J. Bu, A. Dong, J. Zhang, W. Xiao, B. Sun, *J. Adv. Mater.* **2022**, *34*, 2102026.
[38] M. Löw, M. Guidat, J. Kim, M. M. May, *RSC Adv.* **2022**, *12*, 32756.
[39] N. Sabi, K. Palanisamy, F. Rahide, S. Daboss, C. Kranz, S. Dsoke, *Batteries & Supercaps* **2023**, *6*, e202300298.
[40] N. Li, D. She, K. Zhang, H.-S. Chen, W.-L. Song, S. Jiao, *ChemSusChem* **2022**, *15*, e202201390.
[41] T. Schoetz, O. Leung, C. P. De Leon, C. Zaleski, I. Efimov, *J. Electrochem. Soc.* **2020**, *167*, 040516.
[42] P. Giannozzi, S. Baroni, N. Bonini, M. Calandra, R. Car, C. Cavazzoni, D. Ceresoli, G. L. Chiarotti, M. Cococcioni, I. Dabo, A. D. Corso, S. de Gironcoli, S. Fabris, G. Fratesi, R. Gebauer, U. Gerstmann, C. Gougoussis, A. Kokalj, M. Lazzeri, L. Martin-Samos, N. Marzari, F. Mauri, R. Mazzarello, S. Paolini, A. Pasquarello, L. Paulatto, C. Sbraccia, S. Scandolo, G. Sclauzero, A. P. Seitsonen, A. Smogunov, P. Umari, R. M. Wentzcovitch, *J. Phys. Condens. Matter* **2009**, *21*, 395502.
[43] A. Marini, C. Hogan, M. Grüning, D. Varsano, *Comput. Phys. Commun.* **2009**, *180*, 1392.
[44] D. Sangalli, A. Ferretti, H. Miranda, C. Attaccalite, I. Marri, E. Cannuccia, P. Melo, M. Marsili, F. Paleari, A. Marrazzo, G. Prandini, P. Bonfà, M. O. Atambo, F. Affinito, M. Palummo, A. Molina-Sánchez, C. Hogan, M. Grüning, D. Varsano, A. Marini, *J. Phys. Condens. Matter* **2019**, *31*, 325902.
[45] M. Guidat, F. Rahide, M. Loew, J. Kim, H. Ehrenberg, S. Dsoke, M. M. May, *Zenodo dataset* **2023**, DOI:10.5281/zenodo.10000854.
[46] F. Rahide, E. Zemlyanushin, G.-M. Bosch, S. Dsoke, *J. Electrochem. Soc.* **2023**, *170*, 030546.

Manuscript received: September 11, 2023
Revised manuscript received: October 10, 2023
Accepted manuscript online: October 13, 2023
Version of record online: November 14, 2023

Name: M. Eng. Margot Guidat

Declaration of Originality

Hereby, I confirm that the submitted doctoral thesis:

- was written by me,
- was written using only the references mentioned where appropriate,
- was not examined before nor has it been published.

I also confirm that the electronic and printed versions are identical in content and format.

Place, Date . . . . . Signature . . . . . .